

# The Aerosol Limb Imager

A Thesis Submitted to the  
College of Graduate Studies and Research  
In Partial Fulfillment of the Requirements  
for the Degree of Doctor of Philosophy  
In the Department of Physics and Engineering Physics

University of Saskatchewan  
Saskatoon

By

Brenden J. Elash

### **Permission to Use**

In presenting this thesis in partial fulfilment of the requirements for a Postgraduate degree from the University of Saskatchewan, I agree that the Libraries of this University may make it freely available for inspection. I further agree that permission for copying of this thesis in any manner, in whole or in part, for scholarly purposes may be granted by the professor or professors who supervised my thesis work or, in their absence, by the Head of the Department or the Dean of the College in which my thesis work was done. It is understood that any copying or publication or use of this thesis or parts thereof for financial gain shall not be allowed without my written permission. It is also understood that due recognition shall be given to me and to the University of Saskatchewan in any scholarly use which may be made of any material in my thesis.

Requests for permission to copy or to make other use of material in this thesis in whole or part should be addressed to:

Head of the Department of Physics and Engineering Physics

University of Saskatchewan

Saskatoon, Saskatchewan S7N 5E2

## ABSTRACT

Stratospheric aerosol has been measured globally from satellite platforms over the past three decades. The variability of the natural and anthropogenic sources and resulting effect on climate make continued and improved measurements a priority. Yet, few satellite instruments capable of measuring stratospheric aerosol currently exist, with a lack of planned missions to fill the gap left by the ultimate loss of current instruments. The Aerosol Limb Imager (ALI) is an optical remote sensing instrument designed to image scattered sunlight from the atmospheric limb. These measurements are used to retrieve spatially resolved information of the stratospheric aerosol distribution, including spectral extinction coefficient and particle size. Here we present the design, development and test results of an ALI prototype. The instrument design uses a large aperture Acousto-Optic Tunable Filter (AOTF) to image the sunlit stratospheric limb in a selectable narrow wavelength band ranging from the visible to the near infrared. Through the nature of the AOTF operation, ALI measures one orientation of the polarized limb radiance, rather than the historically observed total radiance. A modelling study on the impact of this approach on the retrievals shows that while there is no distinct advantage to the linearly polarized measurement, there are also no clear disadvantages assuming the somewhat lower overall signal levels can be handled in the instrument design or operation.

The long term goal of this work is the eventual realization of ALI on a satellite platform in low earth orbit, where it can provide high spatial resolution observations, both in the vertical and cross-track dimensions. The ALI prototype was tested on a stratospheric balloon flight from the Canadian Space Agency (CSA) launch facility in Timmins, Canada, in September 2014. Preliminary analysis of the hyperspectral images indicate that the radiance measurements are of high quality, and these are used to successfully retrieve vertical profiles of stratospheric aerosol extinction coefficient from 650–950 nm, along with one moment of the particle size distribution.

## ACKNOWLEDGMENTS

The work presented here would not be possible without the contributions of many individuals and organizations. Without them I would not have been able to partake in this educational journey through optics and atmospheric science. I would like to thank the Institute for Space and Atmospheric Studies, the University of Saskatchewan, the Natural Sciences and Engineering Research Council, the Centre National d'Etudes Spatiales, and the Canadian Space Agency for their financial support.

Members of my research team have been monumental to assisting in the completion of this project. Thanks to Paul Loewen for building and testing the electronics for ALI; Seth Dueck for creating the polarized version of SASKTRAN-HR as well as the guidance given using the polarized model; Landon Rieger for help and advice in using the retrieval package; Dr. Nick Lloyd for his assistance in the designing and testing of the flight software; and Dr. Douglas Degenstein for overall advice and knowledge during the project.

To my supervisor, Dr. Adam Bourassa, I would extend a sincere thanks for the wonderful opportunity to work alongside him in this endeavor. Without his guidance, knowledge, and enthusiasm this project would not be what it became.

Finally, I would like to thanks my family and friends for their support throughout this work.

*To my family: Johanna, Kaitlyn, Chris, and Amy*

## TABLE OF CONTENTS

	<u>page</u>
<b>ABSTRACT.....</b>	<b>iii</b>
<b>ACKNOWLEDGMENTS .....</b>	<b>iv</b>
<b>LIST OF TABLES .....</b>	<b>x</b>
<b>LIST OF FIGURES .....</b>	<b>xi</b>
<b>LIST OF ABBREVIATIONS .....</b>	<b>xix</b>
<b>1 INTRODUCTION.....</b>	<b>1</b>
<b>2 BACKGROUND .....</b>	<b>6</b>
2.1 Introduction.....	6
2.2 Stratospheric Aerosol.....	9
2.2.1 Aerosol Sources .....	10
2.2.2 Aerosol Microphysics .....	11
2.2.3 Climate Effects.....	14
2.3 Aerosol Measurements.....	15
2.3.1 In-situ Measurements .....	15
2.3.2 Occultation .....	16
2.3.3 Lidar .....	17
2.3.4 Limb Scatter .....	19
2.4 Radiative Transfer.....	22
2.4.1 Scalar Radiative Transfer .....	22
2.4.2 Vector Radiative Transfer .....	26
2.4.3 Rayleigh Scattering .....	28
2.4.4 Mie Scattering .....	28
2.4.5 SASKTRAN Radiative Transfer Model .....	31
2.5 Inversion Techniques .....	32
2.5.1 Optimal Estimation .....	33
2.5.2 Levenberg-Marquardt .....	34
2.5.3 Multiplicative Algebraic Reconstruction Technique .....	35
2.6 ALI Prototype Instrument and Stratospheric Balloon Flight.....	35
2.6.1 ALI Specifications .....	36
<b>3 INSTRUMENT DESIGN .....</b>	<b>38</b>
3.1 Introduction.....	38
3.2 AOTF Theory and Background .....	38
3.2.1 Solution to the Acoustic Equation .....	39
3.2.2 Diffraction Efficiency .....	44
3.2.3 Diffraction Angle .....	45
3.2.4 Tuning Curve .....	48

3.3 Optical Chain Development.....	50
3.3.1 AOTF Operation .....	51
3.3.2 Telecentric System Prototype .....	53
3.3.3 Telescopic System Prototype .....	60
3.3.4 ALI Optical Design .....	65
3.3.5 Correction to the Optical Design.....	70
3.4 Opto-Mechanical Design and Thermal Balancing.....	72
3.4.1 Opto-Mechanical Design .....	72
3.4.2 Baffle Design .....	77
3.4.3 Light Tight Case.....	82
3.4.4 Thermal Considerations .....	82
<b>4 CALIBRATIONS AND CONTROL SOFTWARE.....</b>	<b>85</b>
4.1 Introduction.....	85
4.2 Control Software .....	85
4.3 AOTF Calibration .....	89
4.3.1 Tuning Curve Analysis .....	89
4.3.2 Point Spread Function .....	92
4.3.3 Diffraction Efficiency .....	93
4.4 ALI Calibrations and System Test.....	94
4.4.1 Exposure Time Determination .....	94
4.4.2 DC Offset Removal.....	96
4.4.3 Dark Current Correction .....	98
4.4.4 Stray Light Calibration.....	99
4.4.5 Relative Flat-Fielding Correction .....	100
4.5 Integrated Testing .....	103
<b>5 STRATOSPHERIC BALLOON FLIGHT AND AEROSOL RETRIEVALS .....</b>	<b>105</b>
5.1 Stratospheric Balloon Flight .....	105
5.1.1 Preflight Preparations .....	105
5.1.2 Balloon Flight .....	108
5.2 Limb Measurements.....	112
5.3 Aerosol Retrievals.....	119
5.3.1 Aerosol Extinction Retrieval Methodology .....	119
5.3.2 Particle Size Retrieval Methodology .....	124
5.3.3 Aerosol Extinction Retrievals .....	128
5.3.4 A Sample Particle Size Retrieval .....	132
<b>6 THE SENSITIVITY TO POLARIZATION IN STRATOSPHERIC AEROSOL RETRIEVALS FROM LIMB SCATTERED MEASUREMENTS .....</b>	<b>134</b>
6.1 Background and Forward Model .....	135
6.1.1 Polarized Scattered Sunlight and Stratospheric Aerosols .....	135
6.1.2 SASKTRAN-HR Model .....	139
6.1.3 Model Scenarios.....	140

6.2 Methodology .....	143
6.3 Analysis.....	147
6.3.1 Difference in Scalar Retrievals using a Scalar or Vector Model .....	147
6.3.2 Fraction of Limb Signal due to Aerosol.....	149
6.3.3 Potential for Retrieval Bias .....	154
6.3.4 Precision Analysis.....	156
6.4 Conclusions of the modelling study.....	160
<b>7 CONCLUSION .....</b>	<b>162</b>
7.1 Summary .....	162
7.2 Contributions of This Work .....	164
7.3 Outlook, Recommendations and Future Challenges.....	165
<b>LIST OF REFERENCES.....</b>	<b>170</b>
<b>A HARDWARE COMPONENTS.....</b>	<b>183</b>
A.1 ALI Optical Components .....	183
A.1.1 Optical Lenses.....	183
A.1.2 Polarizers.....	183
A.1.3 AOTF .....	184
A.2 ALI Opto-Mechanical and Electrical Components.....	185
A.2.1 RF Driver .....	185
A.2.2 QSI CCD Camera.....	185
A.2.3 OCELOT Computer .....	185
A.2.4 Opto-Mechanical Pieces.....	186
A.3 Calibration Equipment .....	187
A.3.1 Horiba iHR 320 spectrometer .....	187
A.3.2 Synapse CCD Detector .....	187
<b>B ALI SOFTWARE COMMANDS .....</b>	<b>188</b>
B.1 List of Commands for ALI Software .....	188
B.1.1 EnableScience.....	189
B.1.2 DisableScience .....	189
B.1.3 EnableRF .....	189
B.1.4 DisableRF .....	190
B.1.5 EnableAutoSendStats .....	190
B.1.6 DisableAutoSendStats .....	190
B.1.7 SetScienceMode .....	190
B.1.8 ReloadConfig.....	191
B.1.9 LdCusCnf .....	191
B.1.10 LdCusExp .....	191
B.1.11 GetFile .....	192
B.1.12 EndCurrentScienceCycle.....	192
B.1.13 SetExposureScaleFactor .....	192

B.1.14 UpdateExposureTimeCurve .....	192
B.1.15 EnableCheckRfTemps .....	193
B.1.16 DisableCheckRfTemps .....	193
B.1.17 ResetHousekeeping .....	193
B.1.18 DumpConfig .....	193
B.1.19 SetBitsPerSecond .....	193
B.1.20 EnableAutomation .....	194
B.1.21 DisableAutomation .....	194
B.1.22 SetAutomationTimeout .....	194
B.1.23 EnableGps .....	194
B.1.24 DisableGps .....	194
B.1.25 EnablePulse .....	194
B.1.26 DisablePulse .....	194
<b>B.2 List of ALI Science Modes .....</b>	<b>195</b>
B.2.1 Invalid Mode .....	195
B.2.2 Calibration Mode .....	195
B.2.3 Aerosol Mode .....	196
B.2.4 H <sub>2</sub> O Mode .....	196
B.2.5 O <sub>2</sub> Mode .....	197
B.2.6 Custom Mode .....	198
B.2.7 Aerosol Constant Exposure Time Mode .....	198
<b>B.3 List of ALI Exposure Modes .....</b>	<b>198</b>
B.3.1 Invalid Mode .....	198
B.3.2 Calibrated Exposure Mode .....	199
B.3.3 Custom Exposure Mode .....	199

## LIST OF TABLES

<u>Table</u>	<u>page</u>
<b>Table 3-1:</b> Telecentric Test System Optical specifications .....	55
<b>Table 3-2:</b> Telescopic Prototype System Optical Parameters .....	62
<b>Table 3-3:</b> Final ALI optical specifications.....	68
<b>Table 3-4:</b> Revised ALI optical specifications .....	71
<b>Table 4-1:</b> Location of ALI temperature sensors. ....	88
<b>Table 4-2:</b> Estimated balloon flight exposure times.....	96
<b>Table 6-1:</b> Different particle size distributions used to test the sensitivity of the aerosol retrieval. ....	142
<b>Table 6-2:</b> The SSA dependence of the normalized co-variance for the horizontal and vertical polarization retrievals. The given numbers are the mean with the standard deviation for each geometry across all wavelengths. Note that the SSA of 90° for the vertical polarization has been removed due to the poor signal in this region.....	158
<b>Table A-1:</b> Lens used in ALI and their specifications. ....	183
<b>Table A-2:</b> AOTF Specifications. ....	184
<b>Table A-3:</b> QSI CCD camera specifications. ....	185
<b>Table A-4:</b> Opto-mechanical components used in ALI .....	186
<b>Table A-5:</b> Horiba iHR 320 spectrometer specifications .....	187
<b>Table A-6:</b> Synapse CCD Detector Specifications .....	187
<b>Table B-1:</b> ALI operational science modes.....	195
<b>Table B-2:</b> ALI calibration science mode specifications. ....	196
<b>Table B-3:</b> ALI aerosol science mode specifications.....	196
<b>Table B-4:</b> ALI H <sub>2</sub> O science mode specifications. ....	197
<b>Table B-5:</b> ALI O <sub>2</sub> science mode specifications. ....	197
<b>Table B-6:</b> ALI operational exposure time modes. ....	198

## LIST OF FIGURES

<u>Figure</u>	<u>page</u>
<b>Figure 2-1:</b> Sample log-normal distribution for typical non-volcanic stratospheric aerosol.	12
<b>Figure 2-2:</b> Bimodal particle size distributions fits from OPC. (a) Distributions from a volcanic period after the Mount Pinatubo eruption recorded in 1993. (b) Distributions from a background aerosol period recorded in 1999. Both of the aerosol distribution measurement are from 20 km altitude with the solid line being the fine mode and the dashed line is the coarse mode. Figure is recreated from Figure 5 of <i>Deshler et al.</i> (2003).	13
<b>Figure 2-3:</b> An occultation instrument monitoring the atmosphere by scanning the atmosphere by looking directly at the sun.	17
<b>Figure 2-4:</b> Lidar instrument showing measurements in both the nadir and off-nadir lines of sight.	18
<b>Figure 2-5:</b> Limb scattering geometry measurement for an instrument where single and multiple scattering events occur.	20
<b>Figure 2-6:</b> (a) Change in extinction for Rayleigh and Mie scattering over wavelength. The Mie scattering uses a log-normal distribution with a mode width of 1.6 and a mode radius of 0.08 $\mu\text{m}$ . (b) The first term of scattering matrix, $P_{11}(\theta)$ , for Rayleigh and Mie scattering cross scattering angle.	31
<b>Figure 3-1:</b> Geometry for the AOTF wave derivation assuming the acoustic wave is along the x-axis and the AO interaction occurs along the z axis over an interaction length, L. The parameters $r_i$ , $k_i$ , and $\theta_i$ are the position vector, wave vector, and angle of the incident electric field and similarly for the diffracted electric field. Figure recreated from <i>Xu and Stroud</i> (1992)	41
<b>Figure 3-2:</b> A standard non-collinear AOTF experiential set up. The crystal is assumed to be infinitely long in the y direction. Figure recreated after <i>Guenther</i> (1990) number 14B-1	47
<b>Figure 3-3:</b> General Layout of an AOTF. A randomly polarized incoming light source hits the front surface of the birefringent crystal. The black bar below the crystal is the piezoelectric transducer that produces the RF signal and forms the acoustic wave represented by the grey arrow. The momentum matching Bragg diffraction occurs and monochromatic polarized light (-1 order) exits the AOTF at a constant angle with the 0th order and +1 order being blocked by an optical stop	47
<b>Figure 3-4:</b> The wave vectors generated by the AOTF experiment set up in Figure 3-2. From the above figure $k_e$ and $k_o$ are the wave vectors of the extraordinary and	

ordinary axis of the AOTF crystal. Originally published as Figure 1 in *Elash et al.* (2016).....49

**Figure 3-5:** (a) An AOTF undergoing Bragg diffraction with an unpolarized input incident wave with a RF wave applied represented by the arrow. After the diffraction event four output signals are formed: the zeroth order and first order ordinary (o) and extraordinary (e) signals. However the only optical path that remains at a constant angle no matter the applied RF wavelength is the first order extraordinary diffracted signal. (b) Two linear polarizers are added to the system, the first linear polarizer removes the ordinary polarization from the outputs with the dotted lines and the second linear polarizer removes undiffracted extraordinary light shown by the dashed line. This configuration is the “AOTF-on” state. (c) The system in (b) without a RF wave so no Bragg diffraction is occurring. Once again the first linear polarizer removes the ordinary polarization represented by the dotted line and the second linear polarizer removes the extraordinary light shown by the dashed line. This configuration is the “AOTF-off” state. Originally published as Figure 2 in *Elash et al.* (2016).....52

**Figure 3-6:** A standard paraxial ray tracing diagram. The aperture is located to make the system telecentric in the image plane and f is the focal length of the lens. ....53

**Figure 3-7:** Ray Tracing diagram simulation of the telecentric lens system preformed using Code V. The elements in the system are the following: (1) Optical Stop and telecentric aperture. (2) 100 mm focal length plano-convex lens. (3) Brimrose AOTF. (4) 100 mm focal length plano-convex lens. (5) Telecentric Aperture. (6) 75.6 mm focal length plano-convex lens. (7) Imaging plane. It should be noted that the x and y scales are not the same in this image. Also, in the lab a polarizer is added in front and behind the AOTF as well as prisms after the AOTF.....54

**Figure 3-8:** Quantum efficiency of the Kodak KAF-1603ME contained within the QSI CCD camera is represented by blue curve. Quantum efficiency provided by QSI Scientific. (<http://www.qsimaging.com/616-overview.html>) .....56

**Figure 3-9:** The effect on the optical path of converging light bundles as they pass through a material of index of refraction  $n(\lambda)$ . When the index of refraction strongly depends on wavelength, as in the AOTF, the optical path length can experience great changes that alters the focal point of the system.....57

**Figure 3-10:** Code V simulation of the spot size for the telecentric system at focus at 800 nm. The spots are shown for 0.0, 1.5 and 2.6 degree fields of view at 600 nm (blue) and 800 nm (green). The full spot sizes for the 600 nm spots are 0.16, 0.22, and 0.25 mm for 0.0, 1.5, and 2.6 degrees fields respectively, with the corresponding 800 nm spot sizes being 0.024, 0.053, 0.094 mm. The black circles represent the Airy disk for each specific wavelength and FOV. .....58

<b>Figure 3-11:</b> The top left is the original test image used for the telecentric experiment. The top right, bottom left, and bottom right are the images recorded through the telecentric system at 650, 750, and 850 nm. The system is focused at 800 nm.....	60
<b>Figure 3-12:</b> Ray Tracing diagram of the telescopic lens system simulated by Code V. The elements in the system are the following: (1) 100 mm focal length plano-convex lens. (2) Location where field stop is located to limit stray light (3) 100 mm focal length plano-convex lens. (4) Brimrose AOTF. (5) 75.6 mm focal length plano-convex lens. (6) Imaging plane. It should be noted that the x and y scales are not the same as Figure 3-7. Also, in the lab a polarizer is added in front and behind the AOTF.....	61
<b>Figure 3-13:</b> Vertical displacement of a collimated bundle of light cause by a material of index of refraction $n(\lambda)$ .....	62
<b>Figure 3-14:</b> Code V simulation of the spot size for the telescopic system. The spots are shown for 0.0, 1.5 and 3.0° fields of view at 600 nm (blue) and 800 nm (green). The full spot sizes for the 600 nm spots are 0.004, 0.045, and 0.122 mm for 0.0, 1.5, and 3.0° fields respectively, with the corresponding 800 nm spot sizes being 0.096, 0.081, 0.047 mm. The black circles represent the Airy disk for 600 nm wavelength and each FOV. ....	64
<b>Figure 3-15:</b> The top left is the original test image used for the telescopic experiment. The top right, bottom left, and bottom right are the images recorded through the telescopic system at 650, 750, and 850 nm. The system is focused at 800 nm. ....	65
<b>Figure 3-16:</b> Final optical design for ALI with a Code V ray tracing diagram. The elements in the system are: (1) 150 mm focal length plano-convex lens. (2) Field stop. (3) 100 mm focal length plano-convex lens. (4) Vertical (extraordinary) linear polarizer. (5) Brimrose AOTF. (6) Horizontal (ordinary) linear polarizer. (7) 50.4 mm focal length bi-convex lens. (8) Imaging plane. Originally published as Figure 4 in <i>Elash et al.</i> (2016). ....	66
<b>Figure 3-17:</b> MTF analysis performed by Code V for the final ALI design used in the balloon campaign. The 7 pixel running average corresponds to a spatial frequency of 15.5 cycles/mm.....	68
<b>Figure 3-18:</b> The final optical layout of ALI's optical chain from the top and profile perspectives with the components being the following: (1) 150 mm plano-convex lens with 25.4 mm diameter. (2) Field Stop. (3) 100 mm plano-convex lens with 50.8 mm diameter. (4) Optical rail system. (5) Vertical (extraordinary) linear polarizer. (6) Brimrose AOTF. (7) Rotation Stage. (8) Horizontal (ordinary) linear polarizer. (9) 50 mm bi-convex lens with 25.4 mm diameter. (10) QSI 616s CCD camera. (11) Optical rail. ....	75

<b>Figure 3-19:</b> The custom mounting hardware design to mount the AOTF and QSI CCD camera into ALI's opto-mechanical design. Left: Custom AOTF mounting hardware. Right: The five piece QSI CCD camera mounting hardware. ....	76
<b>Figure 3-20:</b> ALI opto-mechanical system with three degree horizontal tilt and designed baffle discussed in section 3.4.2. Originally published as Figure 5 in <i>Elash et al.</i> (2016).....	76
<b>Figure 3-21:</b> (a) Start of the optical baffle geometry method. The red lines are the marginal rays and the green line is the first ray that can enter the system without encountering at least three surfaces. (b) The first internal vane has been added and the location of the next vane is being determined. (c) The second internal baffle has been added and since the green line intersects with the critical baffle no more baffles are required. (d) Additional interior vanes and an external vane have been added to ensure a height to pitch ratio of 0.5 to improve the baffle's capabilities to reduce stray light. ....	79
<b>Figure 3-22:</b> A cross-section view of the ALI baffle system. All dimensions on the drawing are in millimeters and the sloped black lines represent the 6 degree FOV.....	80
<b>Figure 3-23:</b> ALI baffle vain profile. Dimensions are in millimeters.....	81
<b>Figure 3-24:</b> Final ALI optical and opto-mechanical assembly.....	81
<b>Figure 3-25:</b> ALI optical system with light tight case attached. Three degree horizontal tilt not present in this image. ....	82
<b>Figure 4-1:</b> A complete flow diagram showing interaction between all the of ALI software modules on board the ALI flight computer.....	86
<b>Figure 4-2:</b> Telecentric test experiential setup for AOTF parameter determination. All lenses and apertures are represented by the vertical lines.....	90
<b>Figure 4-3:</b> (a) A row averaged image taken from the AOTF of the point spread function when the tuning frequency of the AOTF was at 124.96 MHz. (b) The FWHM for each of the determined wavelengths for the AOTF. The FWHM at 600 nm is 1.5 nm and as the wavelengths get longer the FWHM increases to 4.9 nm at 1080 nm. (c) The calibration curves for the AOTF RF versus the diffracted wavelength which contains the data points recorded and fit curves. (d) The percent error with respect to the measured frequency for the two best fit curves in the previous panel. Originally published as Figure 6 in <i>Elash et al.</i> (2016).....	91
<b>Figure 4-4:</b> Simulated scalar radiances from the SASKTRAN-HR in blue and red with the radiance on the left side and the scaling factor in black with the value on the right side. ....	95

<b>Figure 4-5:</b> The DC offset curve (Equation 4.5) is seen in black where the lab and flight calibration data is shown in blue. The counts on the vertical axis are the counts that need to be removed to account for the DC offset.	97
<b>Figure 4-6:</b> The dark current from the calibration images over a series of camera temperatures and exposure times.	98
<b>Figure 4-7:</b> A calibration image after stray light removal has been performed where the measured wavelength is 750 nm with a 1 second exposure time. Vignetting can be seen as moving away from center of the image. Additionally the last 1° of the horizontal FOV on the right side is lost due to strong contamination from reflections within the system. Originally published as Figure 7 in <i>Elash et al. (2016)</i> .	99
<b>Figure 4-8:</b> The blackbody emittance curve from Equation 4.6 normalized to 775 nm.	101
<b>Figure 4-9:</b> The flat fielding coefficients for 750 nm.	102
<b>Figure 5-1:</b> The QSI CCD with the panel that covers the vacuum seal removed. The orange o-ring seen in the cavity is removed from the chamber to break the vacuum seal on detector.	107
<b>Figure 5-2:</b> The ALI instrument is mounted on board the CARMEN-2 gondola (top shelf on the right). ALI located next to SHOW. ALI has a cover over the optical entrance to protect the instrument from dust and other contaminates. Thermal insulation has been added to the instrument exterior. Some of the reflective covering was blacked out to not cause additional stray light into SHOW optical path.	108
<b>Figure 5-3:</b> (a) The GPS data from ALI during the Nimbus 7 mission generated via Google Earth. The colour of the line represents the absolute speed of the gondola during the mission and the blue, green, red colours represent speeds of approximately 10, 70, and 140 km/h. Important landmarks are noted on the image. The end of mission represents the end of the data collection. No GPS data was collected from ALI after power down. The location of image 208 is the red label. (b) The temperature and altitude profiles from the Nimbus 7 flight. The time of image 208 is shown by the cyan vertical line and first light measured by ALI occurs at the magenta vertical line. Originally published as Figure 8 in <i>Elash et al. (2016)</i> .	110
<b>Figure 5-4:</b> During the flight the calibrated exposure times was updated. The blue curve represents the exposure times from the ground calibration and the red curve is the recalibration during the flight. The black curve is the percent change in between the pre-flight calibrated results and the during flight calibration.	111
<b>Figure 5-5:</b> Stray light removal technique was performed using image 208 which is a 750 nm measurement. The top panel is the image after the DC offset has been removed from the measurement. The middle panel is the associated AOTF-off image and stray light features are seen in the upper right of the image as well as light being registered in the entire right side of the image. The final panel is the first	

panel minus the second panel and the abnormal gradient has been removed from the final image, leaving a cleaner radiance profile. ....115

**Figure 5-6:** (a) Final calibrated 750 nm image, taken at 13:57 UTC located at 48.55°N, 80.00°W with a SZA and SSA of 63° and 98° respectively. The horizontal FOV is 30 km.(b) The same 750 nm image with the mean of the profile removed from the image leaving the residual signal that shows thin clouds in the troposphere. Originally published as Figure 9 in *Elash et al.* (2016).....116

**Figure 5-7:** Averaged ALI relative radiance vectors from 12 of the 13 wavelengths from the Nimbus 7 flight. Each panel presents the radiance vectors from a different wavelength measured which is denoted in the top right corner. The dashed lines are radiance profiles where the SZA is greater than 90° and solid lines are profile where the SZA is less than 90°. Originally published as Figure 10 in *Elash et al.* (2016).....117

**Figure 5-8:** Relative radiances spectrally from 650 nm to 950 nm as measured from ALI at approximately 14:20 UTC consisting of images number 204 to 216 looking 90° in the azimuth from the sun facing southwards. These spectral profiles are presented at several tangent altitudes with a horizontal look direction of 0°. The shading represents the error on the radiances. Originally published as Figure 11 in *Elash et al.* (2016).....118

**Figure 5-9:** (a) The black, blue, red curves represent the measurement vector,  $y$ , first term of Equation 5.5, and second term of Equation 5.5 using image 208 (b) A collection of all of the measurement vectors at 750 nm during the mission with a SZA less than 90°. (c) Image 208 measurement vector with associated error represented by the shading. ....120

**Figure 5-10:** Reproduced from Figure 4 of *Rieger et al.* (2014). For OSIRIS scan 6432001 aerosol measurement vectors were calculated at 22.5 km. (A) The three size distributions used in the study. (B) The measurement vectors calculated via the SASKTRAN simulation (C) The relative percent difference of the fine and representative distributions with respect to the bimodal distribution. A 1% error is the radiance yields an uncertainty in the bimodal measurement vector shown by the grey shading. ....125

**Figure 5-11:** Mie scattering cross section at 750 nm computed with the optical properties of the SASKTRAN-HR engine. This variation of the cross section with respect to the mode radius and width allows for some determination of the particle size distribution through the Angström exponent. ....126

**Figure 5-12:** An example of three aerosol retrievals from images 206, 208, and 214, with center wavelengths of 750, 850, and 950 nm respectively are vertically displayed in the figure from top to bottom. The left column shows the measurement vector,  $y$ , in black with the retrieved forward model,  $F$ , in blue. The center column shows the ratio of the measurement vector over forward model known as  $\gamma$  and is the scaling factor between the ALI measurement and the forward model. For both of

the first two columns, the black line is barely visible due to the very good agreement of the forward model. The final column is ALI aerosol extinction in blue with the associated error represented by the light blue shading. ....129

**Figure 5-13:** Left is the retrieved aerosol extinction profiles from the last complete imaging cycle consisting of images 205 to 216 from the  $0.0^\circ$  horizontal line-of-sight. Right is the 750 nm ALI aerosol extinction in blue with its error represented by the shading compared to the 750 nm extinction measured by OSIRIS in red with its error represented by the shading. Originally published as Figure 12 in *Elash et al.* (2016). ....130

**Figure 5-14:** (a) Image 208 (750 nm) re-retrieved using an albedo of 0 and 1 compared to the original albedo used from OSIRIS. (b) Using the determined zenith pointing error from section 5.2, image 208 is retrieved again using the maximum possible pointing error compared to the original. ....132

**Figure 5-15:** The left panel shows the convergence of two sample particle size retrievals, blue and red represent an initial state of  $0.08$  and  $0.12 \mu\text{m}$  mode radius respectively. Both initial states converge to the same value over approximately 3 iterations in the particle size retrieval method. The middle panel shows the final Angström exponents determined from images 204-216. The shading represents the error associated with the least squares fit. The right panel shows a typical least squares fit of the retrieved extinction values over wavelength to determine the Angström exponent at model altitude of 14.5 km. Originally published as Figure 13 in *Elash et al.* (2016). ....133

**Figure 6-1:** (Top) The fraction of a linear polarization (left is horizontal and right is vertical) over the total radiance for molecular air density. (Bottom) The change in the fraction of linear polarization between an atmosphere that contains aerosol and one with only molecular air density. ....139

**Figure 6-2:** The two aerosol profiles used in this study. The blue is a background aerosol extinction levels, and the red curve is a representative aerosol profile after the Nabro eruption. ....142

**Figure 6-3:** Percent differences between the vector retrieved aerosol extinction profiles and the scalar retrieval from simulated total radiance measurements. Each column represents a different particle size distribution (see Table 6-1). ....148

**Figure 6-4:** (Top) For a horizontal (left) or vertical (right) linear polarization the percent of the signal that is attributed to aerosol,  $\delta$ . (Bottom) The change in the fraction of the limb signal due to aerosol when compared to the total radiance for the horizontal (left) and vertical (right) polarization ( $\Delta\delta$ ). The simulation uses a geometry of SZA= $45^\circ$  and SSA= $60^\circ$ , with the albedo being 0 and the aerosol state the background profile with particle size distribution 1. Take note the red-blue scale is non-symmetric. ....150

<b>Figure 6-5:</b> Dependence of the fraction of the limb spectra due to aerosol on solar scattering angle (left panels) for total radiance (top), horizontal polarization (middle) and vertical polarization (bottom), and the magnitude of the radiance for each case (right panels). Note the low signal near SSA of 90 degrees for the vertical polarization which would be problematic for terminator orbits. ....	151
<b>Figure 6-6:</b> The ratio of the linearly polarized radiance to the total radiance for horizontal (left) and vertical (right) orientations. Note that the scale for each plot is different. The simulation was performed with a SSA of 60 degrees with volcanic aerosol loading for a tangent altitude of 20 km. ....	152
<b>Figure 6-7:</b> The mean percent difference between the retrieved aerosol extinction profile with an assumed particle size distribution and the true state corresponding to the indicated particle size distribution (see Table 6-1). Error bars represent one standard deviation of the variability across all viewing geometries. Results shown are for 750 nm and 20 km altitude.....	155
<b>Figure 6-8:</b> The wavelength dependence of the co-variance for the horizontal and vertical polarization retrievals normalized to the total radiance case. The faded line represent one standard deviation of the variability encountered across all input parameters. The top panel is for an instrument design and/or operation that compensates for changing signal levels with polarization and viewing geometry, and the bottom panel is for uncompensated measurements.....	157
<b>Figure A-1:</b> The transmission and extinction ratios of the LPVIS100 used in ALI. ....	184
<b>Figure A-2:</b> Typical Spectral response of a Synapse CCD Detector as provided by Jobin-Yvon.....	187

## LIST OF ABBREVIATIONS

ALI	Aerosol Limb Imager
ALTIUS	Atmospheric Limb Tracker for the Investigation of the Upcoming Stratosphere
AO	Acousto-Optic
AOTF	Acousto-Optical Tunable Filter
BEO	Back End Optics
CALIPSO	Cloud-Aerosol Lidar and Infrared Path_nder Satellite Observations
CATS	Cloud Aerosol Transport System
CCD	Charged-Coupled Device
CNES	Centre National d'Etudes Spatiales
CSA	Canadian Space Agency
DC	Direct Current
FEO	Front End Optics
FOV	Field of View
FWHM	Full Width Half Max
GPS	Global Positioning System
ICESat	Ice, Cloud, and land Elevation Satellite
IR	InfraRed
MART	Multiplicative Algebraic Reconstruction Technique
MTF	Modular Transfer Function
NASA	National Aeronautics and Space Administration
NIR	Near InfraRed
OMPS	Ozone Mapping and Pro_le Suite
OPC	Optical Particle Counter
OSIRIS	Optical Spectrograph and Infra-Red Imaging System
RF	Radio Frequency
SAGE	Stratospheric Aerosol and Gas Experiments
SASKTRAN-HR	SASKTRAN High Resolution
SCIAMACHY	SCanning Imaging Absorption spectroMeter for Atmospheric CHartographY
SME	Solar Mesosphere Experiment
SNR	Signal to Noise Ratio
UTLS	Upper Troposphere and Lower Stratosphere

# CHAPTER 1

## INTRODUCTION

The atmosphere of the Earth is a dynamic, evolving system with complex composition. The concentration of various atmospheric species is dependent upon altitude, geographical location, season, and time of day. These species interact with light and absorb, scatter, and re-emit the radiation originating from the sun. Using spectroscopy, concentrations of different species can be determined to discover the composition of the atmosphere. Over a period of time, changes to the composition caused by natural and anthropogenic sources can be used to infer processes and trends, some of which are causes or effects of climate change. One particularly important species in terms of the radiative balance of the Earth is aerosol in the stratosphere. These aerosols are typically submicron-sized droplets of sulfuric acid and water that scatter solar radiation away from earth, effectively increasing the planetary albedo and causing a cooling effect of the surface temperature. Source gasses that form these aerosols can arise from the burning of fossil fuels, biomass burning, and natural marine processes and form a relatively stable layer of aerosol in the stratosphere, often referred to as the “background” layer (*Kremser et al.*, 2016). Large and unpredictable perturbations of this layer occur after large volcanic eruptions that can inject large quantities of sulfur dioxide directly into the stratosphere where it oxidizes and forms aerosol droplets. The variability of the aerosol layer in terms of particle size, composition and its spatial and temporal distributions, makes it both challenging and critical to measure and understand. This so-called “persistently variable” aerosol layer has been linked to a significant reduction in the global-warming from greenhouse gases that would have occurred (*Solomon et al.*, 2011), and have played a role in understanding the “emergence of healing” of the ozone layer in the Antarctic (*Solomon et al.*, 2016).

Instrumentation has been deployed over the past several decades to monitor the atmospheric state from the ground, within the atmosphere, and from orbit using many different methods. As progress is made towards understanding the process and trends in atmospheric composition through these observations, the scientific questions inevitably probe deeper into more detailed and smaller scale structures requiring both high spatial and temporal resolution measurements as well as global coverage. This evolution provides ever more challenging requirements for new measurements and hence new instrumentation to provide these observations. Advancements in optical and detector technology combined with the increasing ease of access to space means that the capabilities of the future generation of satellite instruments will be able to tackle the driving scientific needs for precision, accuracy and resolution with global coverage.

Stratospheric aerosol in particular has been monitored globally from satellite platforms since the 1970s. The “gold-standard” remote sensing method is solar occultation, most notably used by the NASA SAGE (Stratospheric Aerosol and Gas Experiment) (*Russell and McCormick, 1989; Thomason and Taha, 2003*) series of satellite missions. Solar occultation instruments directly measure the spectral attenuation of sunlight as it passes through the atmosphere and through this acquire accurate vertical profiles of the aerosol extinction coefficient; however, the occultation technique is inherently limited in the number of observations that can be acquired per day due to the simple fact that the measurement is made only when the satellite instrument observes a sunrise or sunset from orbit. More recently other remote sensing techniques have been used successfully from space to measure stratospheric aerosol. One such technique is the measurement of limb scattered sunlight, which is performed by the Canadian OSIRIS (Optical Spectrograph and InfraRed Imaging System) (*Llewellyn et al., 2004*) instrument onboard the Odin spacecraft. The observation of limb scattered sunlight achieves greater temporal and spatial coverage since the

measurement only requires sunlit conditions. Other techniques have also been successfully used for stratospheric aerosol measurement from space including lidar, stellar occultation and thermal emission, and the combination of various data sets has provided a rich monitoring record of the highly variable aerosol load. However, the current satellite instruments capable of these measurements are operating well past their design lifetimes and very few satellite missions with stratospheric measurement capability are planned. Active discussions are underway in the scientific community about an upcoming gap in stratospheric measurements and the requirements for future measurements of stratospheric aerosol, and in particular the readiness for observations of the next big volcanic eruption (*Kremser et al.*, 2016).

In this thesis work, the design and test flight of a new passive remote sensing instrument, named the Aerosol Limb Imager (ALI), is presented. The long term goal of the work is the eventual realization of the ALI instrument on a small- or micro-satellite platform. ALI is designed to use novel acousto-optic filtering technology to image limb scattered sunlight for the retrieval of high resolution stratospheric aerosol extinction distributions, both vertically and horizontally. The horizontal dimension of the image, when observed from a moving satellite or aircraft platform is often referred to as the cross-track dimension. The hyperspectral approach to the ALI design provides the capability for this cross-track coverage of the limb, which is a feature that to our knowledge has never been performed from an atmospheric composition instrument. This will provide an especially powerful observation set for studying the transport and evolution of often ultra-thin and variable aerosol layers. As part of this work, a prototype of the ALI instrument was developed for proof-of-concept measurements from stratospheric balloon, and a test flight of this prototype occurred from the Canadian Space Agency launch facility in Timmins, Ontario, in 2014.

This flight was the first known test of a large-aperture imaging quality acousto-optic filter from a stratospheric balloon, providing important space-flight heritage for the technology.

This thesis presents the motivational background and design of the ALI instrument, the results from the stratospheric balloon test flight, and concludes with a systematic modelling study on the effect of polarization on the aerosol measurement. The work covers a wide range of topics and as such the necessary background material is diverse and multidisciplinary. Chapter 2 outlines the relevant background physics of the atmosphere, with a focus on stratospheric aerosol. This includes its discovery, sources and microphysical properties, and a discussion about the importance of aerosol in the atmosphere including the effect on climate. Following this, an overview of the different techniques used to measure aerosols is presented including both in-situ and remote sensing methods. Particular attention is paid to the limb scattering method, which is the technique used by the ALI instrument. This chapter concludes with a survey of atmospheric radiative transfer and inversion theory, which encompasses the core physics for understanding and interpreting remote sensing observations. This discussion starts with the traditional scalar equations and moves into the more complete polarized, or vector, theory needed for this work. An overview of the comprehensive radiative transfer model developed at the University of Saskatchewan, which is called SASKTRAN (*Bourassa et al.*, 2008) and is used extensively within this work, is provided along with a brief survey of standard inverse methods to determine atmospheric parameters from remote sensing measurements.

Chapter 3 begins with an overview of the Acousto-Optic Tunable Filter (AOTF), which is the novel filtering device at the core of the ALI design. The background physics and practical application of this device are covered with a focus on the advantages and disadvantages of using this technology in space-based remote sensing applications. Following this is a detailed discussion

of the optical design trade-offs specific to the ALI requirements, and the testing of the chosen optical system design. Chapter 4 details the calibration and performance of the prototype instrument as well as an overview of the control software developed for the stratospheric balloon flight.

Chapter 5 is a presentation of the ALI test flight on a stratospheric balloon in Timmins, Ontario in 2014. The results from the measurements recorded from the flight are presented including calibrated images, retrieved aerosol extinction profiles, a precision estimate, and a retrieval of the particle size distribution from the acquired spectral information. These results are then compared to current coincident satellite measurements.

Finally, the use of the AOTF technology means that ALI inherently measures the linearly polarized radiance, whereas existing satellite instruments that provide the measurement and algorithm heritage are purposefully designed to measure the total radiance with insensitivity to the polarization state. Thus the thesis includes a systematic study, presented in Chapter 6, to determine the full effect of the polarized measurement on the aerosol retrieval capability from simulated satellite-based polarized measurements.

## CHAPTER 2

## BACKGROUND

### 2.1 Introduction

Stratospheric aerosol plays an important role in the global radiative forcing balance by scattering solar irradiation and causing an overall cooling effect that depends on the particle size distribution and the concentration (*Kiehl and Briegleb*, 1993; *Stocker et al.*, 2013). These climate effects are an important and recent focus of research due to the potential contribution of stratospheric aerosol to the so-called global warming hiatus (*Solomon et al.*, 2011; *Haywood et al.*, 2014; *Fyfe et al.*, 2013) and efforts to quantify the variability and trends in the global stratospheric aerosol load are underway with various ground-based and satellite data sets (e.g. *Rieger et al.*, 2015; *Ridley et al.*, 2014).

Since its discovery with stratospheric balloon observations (*Junge et al.*, 1961), stratospheric aerosol has been measured with various techniques, although due to the variability of physical composition and particle size, the observations are always limited to some degree and no single measurement technique can fully determine the full range of aerosol properties unambiguously. In-situ balloon observations continue to be used and have provided highly valuable data sets, including most notably the long time series of Optical Particle Counter (OPC) measurements from Laramie, WY (*Deshler et al.*, 2003; 2008; *Kovilakam et al.*, 2015). Aircraft-borne nephelometers (*Beuttell and Brewer*, 1949; *Charlson et al.*, 1969) acquire detailed in-situ measurements, providing, for example, plume composition (*Murphy et al.*, 2014), but are spatially limited to the aircraft track. Ground based lidars have been used to do detailed studies of the extent of volcanic aerosol plumes (*Chazette et al.*, 1995; *Sawamura et al.*, 2012) and provide valuable insight into long term local variability and trends in the aerosol layer. For example, lidar observations were used by *Hofmann et al.* (2009) to first report the observed increase in stratospheric aerosol over

approximately the last decade. However, the global distribution, which can only really be obtained with satellite observations, provides invaluable insight into aerosol processes and variability. A good example of this is the use of satellite observations by *Vernier et al.* (2011b) to determine that the increased stratospheric aerosol load reported by *Hofmann et al.* (2009) was in fact due to a series of relatively minor, mostly tropical, volcanic eruptions.

Several recent studies have highlighted the requirement for continued global stratospheric aerosol observations and especially the need to resolve, both vertically and horizontally, aerosol in the lowermost stratosphere and the upper troposphere. This is the case for tracking the evolution of aerosol from volcanic eruptions, which can have a substantial effect on the aerosol optical depth in the lowermost stratosphere (*Ridley et al.*, 2014; *Andersson et al.*, 2015). Furthering the understanding of the transport of aerosol near and across the tropopause would also benefit from higher spatial and temporal resolution observations. This is evident in the case of volcanic plumes, such as that from Nabro in 2011, the transport and origin of which has been studied extensively and the conclusions are somewhat controversial (*Bourassa et al.*, 2012c; 2013; *Vernier et al.*, 2013; *Fromm et al.*, 2013; 2014; *Fairlie et al.*, 2014; *Clarisso et al.*, 2014). However, this is also the case for the formation of background-level aerosol, particularly in the region of the Asian and North American monsoons, which have been identified as a source of substantial, seasonal and highly structured aerosol formation from precursor tropospheric source gases (*Vernier et al.*, 2011a; *Neely et al.*, 2014; *Thomason and Vernier*, 2013).

Continued stratospheric aerosol observations from space are drastically needed though few, if any, planned missions with such capability are underway. In this work, we present the design and test of a prototype instrument for potential future satellite-based stratospheric aerosol observation. The Aerosol Limb Imager (ALI) concept is a relatively small, low-cost, low-power, passive

instrument, suitable for microsatellite deployment with the capability to provide high spatial resolution measurements, both vertically and horizontally, of the visible/NIR aerosol extinction coefficient. The basic idea is to leverage the clear advantages of the limb scatter technique as a passive, and therefore low mass and low power, means to obtain daily global coverage, with a two dimensional hyperspectral imager for filling cross-track observation.

The ALI instrument concept is built around the use of an Acousto-Optic Tunable Filter (AOTF), which is a novel filtering technology that provides the ability to rapidly select the central wavelength of an image with no moving parts. These filters, which have recently been developed as large aperture imaging quality devices, operate very efficiently in the red and near infrared spectral range, which is a well matched spectral range for limb scatter sensitivity to aerosol and cloud (*Rieger et al.*, 2014). Additionally, the spectral bandpass of the AOTF, which is typically between 3-6 nm at these wavelengths, is very suitable for the broadband scattering characteristics of the aerosol limb signal. The two dimensional imaging nature of the design provides the capability to achieve at least sub-kilometer resolution at the tangent point, which is on the order of the scale size of the upper troposphere and lower stratosphere (UTLS) aerosol features mentioned above.

It should be noted that the basic instrument design concept of ALI is very similar to that of the Atmospheric Limb Tracker for the Investigation of the Upcoming Stratosphere (ALTIUS) (*Dekemper et al.*, 2012, *Fussen et al.*, 2016), which is a Belgian instrument concept from the Belgian Institute for Space Aeronomy (BIRA) and has been recently selected for small satellite deployment by the European Space Agency. ALTIUS is designed to measure limb scattered sunlight; however, it also has solar, stellar, and planetary occultation modes and is scientifically

focused on trace gas measurements, particularly for ozone, whereas ALI is optimized for aerosol observation from limb scattering observations.

## 2.2 Stratospheric Aerosol

In the late 18<sup>th</sup> century, it was known that atmospheric temperature decreased with altitude and a theory had been raised that at a specific altitude the temperature must eventually go to absolute zero (*Hoinka*, 1997). This led to a series of balloon campaigns, which were noisy and unreliable due to the technology available, to discover this mysterious altitude in the atmosphere. However, in the late 19<sup>th</sup> century the technology used in these sounding balloons had improved to a point where the atmospheric temperature could be accurately measured and it was found that at approximately 12 km an inversion point occurs where the temperature starts to increase and thus the tropopause, which separates the troposphere and the stratosphere, was discovered. The stratosphere is the region of the atmosphere above this temperature inversion point where atmospheric temperature increases. The tropopause, which is the lower bound of the stratosphere, ranges in altitude from approximately 10 km to 16 km from the high latitudes to the tropics (*Andrews*, 1987), and extends up to approximately 50 km. It is a thermodynamically stable and fairly dry (*Boucher*, 2015) region of the atmosphere, and the characteristic stability of the stratosphere limits vertical transport, leading to long lifetimes, spanning from months to years, for non-volatile species (*Volk et al.*, 1997; *Brasseur and Solomon*, 2005)

The stratosphere undergoes exchange of air with the troposphere through a series of dynamical processes including tropical convection, polar vortices, and tropopause folding (*Holton et al.*, 1995). Meridional circulation within the stratosphere is dominated by the slow Brewer-Dobson circulation, although zonal circulation, *i.e.* along a constant latitude, is much faster (*Plumb and Eluszkiewicz*, 1999) and tends to cause zonal symmetry of composition. The transport of gases emitted from sources on the surface, or chemically created in the troposphere, through the

tropopause and into the stratosphere is an important aspect of stratospheric composition. This is the case for stratospheric aerosol where the oxidation of sulfur-bearing compounds, transported from the troposphere to the stratosphere, forms the aerosol layer discovered by *Junge et al.* (1961) with stratospheric balloon sondes measurements. These aerosols are primarily droplets of hydrated sulfuric acid ( $H_2SO_4$ ) formed from the oxidation of sulfur-containing source gases, primary OCS and  $SO_2$  (*Brock et al.*, 1995). This stable layer of aerosol exists in the stratosphere from the altitude of the tropopause to approximately 30 km.

### **2.2.1 Aerosol Sources**

The source gases that eventually form stratospheric aerosol are emitted or produced in the troposphere through both natural and anthropogenic processes. These sulfur sources enter the atmosphere in various ways and undergo a chain of chemical reactions to form sulfate aerosol within the stratosphere.

One primary source of atmospheric sulfur is OCS, which originates from natural marine processes, biomass burning, and industrial processes (*Kettle et al.*, 2002; *Notholt et al.*, 2003). OCS has a long lifetime in the troposphere and low solubility allowing for a significant portion to reach the stratosphere where some of it oxidizes and hydrates to form sulfate aerosol ( $H_2SO_4$ ) where it contributes to the background aerosol layer (*Crutzen*, 1976).

Another important source of atmospheric sulfur is sulfur dioxide ( $SO_2$ ), which originates in the troposphere through the burning of fossil fuels.  $SO_2$  has a short lifetime in the troposphere, and its concentration varies regionally; however, this emitted  $SO_2$  still can enter the stratosphere through transport processes and contribute to the background aerosol layer (*Thomason and Peter*, 2006). A second source of  $SO_2$  is from volcanic eruptions; which, although highly variable in location and time, can inject a large amount of sulfur directly into the stratosphere. Volcanic eruptions can inject such large amounts of sulfur that they in fact dominate the variability of the stratospheric

aerosol layer, essentially episodically perturbing the background levels. This volcanic enhancement of the aerosol layer occurred on a massive level following the volcanic eruptions of El Chichon in 1982 (12-20 Tg of SO<sub>2</sub>) (*McCormick and Swissler, 1983; Hofmann and Rosen, 1983*) and Mount Pinatubo in 1991 (20-30 Tg of SO<sub>2</sub>) (*McCormick and Veiga, 1992*). However, after the Mount Pinatubo eruption a volcanically quiescent period occurred where aerosol layers returned to background until the early 2000's. Following this period, a series of relatively minor, mostly tropical, volcanic eruptions have increased the background aerosol layer in the amount of 4-7% per year from 2000 to 2009 (*Vernier et al., 2011b*). These small eruptions have continued to the present day and include eruptions such as Kasatochi (1.2-2.2 Tg of SO<sub>2</sub>) in 2008 (*Prata et al., 2010*), Nabro (1.0- 1.5 Tg of SO<sub>2</sub>) in 2011 (*Clarisse et al., 2016*), Kelut (0.1-0.3 Tg of SO<sub>2</sub>) in 2014, and Calbuco (0.2 -0.5 Tg of SO<sub>2</sub>) in 2015 (*Carn et al., 2016*). The enhancement of the aerosol layer from these eruptions is well captured in the satellite record (*Rieger et al., 2015*).

### 2.2.2 Aerosol Microphysics

These sulfur source gases undergo a series of chemical reactions and are converted into molecular H<sub>2</sub>SO<sub>4</sub> that then nucleates and condenses to form liquid droplets of approximately 25% H<sub>2</sub>O and 75% H<sub>2</sub>SO<sub>4</sub> (*Rossen, 1971; Wang et al., 1989*). These spherical droplets coagulate into various sizes distributed between approximately 0.05 to 1.0 μm, depending on the various contributions and stages of the processes of nucleation, evaporation and condensation (*Junge et al. 1961; Brock et al., 1995; Bingen et al., 2004*). A log-normal distribution is often used to approximate the distribution of particle radii, *r*, in the form of

$$\frac{dn(r)}{dr} = \frac{n_0}{r \ln(\sigma_g) (2\pi)^{1/2}} \exp\left(-\frac{\ln^2(r/r_g)}{2 \ln^2(\sigma_g)}\right) \quad (2.1)$$

where *n*<sub>0</sub> is the aerosol number density, *r*<sub>g</sub> is the mode radius, and *σ*<sub>g</sub> is the mode width (*Jäger and Hofmann, 1991; Hamill et al. 1997*). In this case, the particle radii are distributed normally

over the logarithm of the radius. For a typical non-volcanic background aerosol, with a mode radius and mode width of 0.08  $\mu\text{m}$  and 1.6 respectively (Deshler, 2003), the log-normal distribution is shown in Figure 2-1.

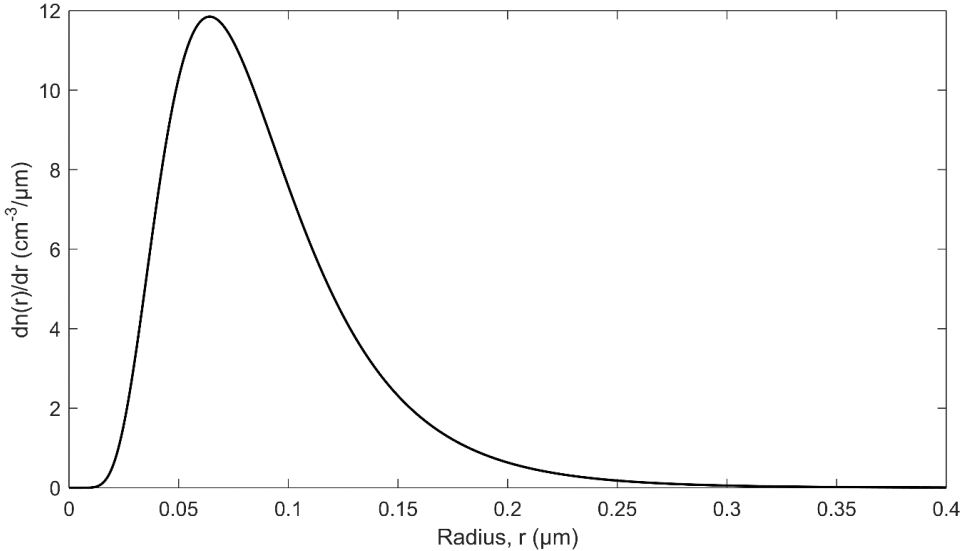


**Figure 2-1:** Sample log-normal distribution for typical non-volcanic stratospheric aerosol.

Optical Particle Counters (OPC) have been used on board stratospheric balloon flights from Laramie, Wyoming over the past 40 years to make *in situ* measurements of aerosol particle sizes in bins between 0.15 to 2.0  $\mu\text{m}$  (Deshler *et al.*, 2003). These measurements provide a valuable and unique long term set of size-resolved measurements of sulfate aerosol. These particle size distributions are primarily unimodal during non-volcanic periods and the log-normal distribution given in Equation 2.1 can be used to approximate background period particle sizes. But during volcanic episodes, a bimodal log-normal distribution of aerosol particles, which includes what is referred to fine and coarse modes, is more representative of the measured distributions (Deshler *et al.*, 2003; 2008; Kovilakam *et al.*, 2015). The coarse mode has larger particles than the fine mode and complicates the determination of aerosol microphysical parameters since the number of required parameters has increased to six: a number density for both the fine and coarse mode, two

mode radii, and two mode widths. Figure 5 from *Deshler et al.* (2003), recreated in Figure 2-2, demonstrates two bimodal particle size distributions from balloon OPC measurements. The first distribution is from a volcanic period in 1993 after the Mount Pinatubo eruption and another from a background period in 1999. It should be noted that even though a bimodal distribution is found for the background case in Figure 2-2, the number density of the coarse mode is very small and can generally be ignored in non-volcanic periods so a unimodal approximation is typically sufficient.

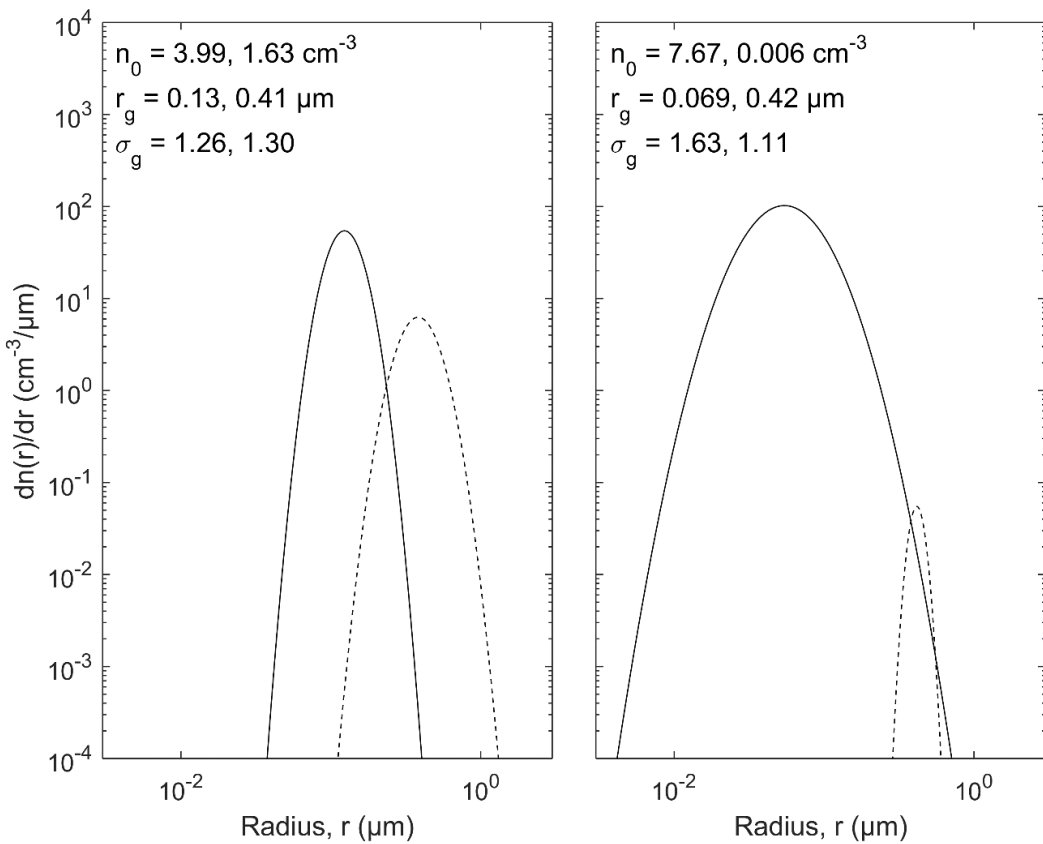


**Figure 2-2:** Bimodal particle size distributions fits from OPC. (a) Distributions from a volcanic period after the Mount Pinatubo eruption recorded in 1993. (b) Distributions from a background aerosol period recorded in 1999. Both of the aerosol distribution measurement are from 20 km altitude with the solid line being the fine mode and the dashed line is the coarse mode. Figure is recreated from Figure 5 of *Deshler et al.* (2003).

### 2.2.3 Climate Effects

Stratospheric aerosol can have several effects on the climate of the planet, and particularly due to the variability of the volcanic contribution, there is a large amount of uncertainty in the overall effect (*Solomon et al.*, 2007). Through the so-called “direct effect”, aerosol particles scatter incoming visible solar radiation away from earth increasing the albedo causing a cooling of the surface of the planet (*Lacis et al.*, 1992). The albedo is the amount of incoming solar irradiance that is reflected back to space. A secondary direct effect from aerosols, which is highly dependent on aerosol particle size distribution, is a greenhouse-like effect that is caused by scattering of infrared radiation emitted from the earth’s surface (*Kiehl and Briegleb*, 1993). Aerosol also introduces a so-called “indirect effect” to the radiative balance. This is also known as the cloud albedo effect. This is caused by condensation of water onto existing aerosol particles. These become cloud condensation nuclei and stimulate cloud formation, which leads to an increase of the planetary albedo, which then also contributes to cooling the planet's surface. These types of cloud forming particles also tend to increase the overall lifetime of the cloud, increasing the overall cloud coverage and thus increasing the planetary albedo (*Charlson et al.*, 1992). Overall, the cooling effect of the aerosol particles dominates the warming effect and cools the surface of the planet (*Solomon et al.*, 2011).

During background periods without substantial volcanic contribution to the aerosol load the cooling effect from stratospheric aerosols is very small, but this greatly changes during periods of volcanic activity where the layer concentrations can be significantly enhanced. After the eruption of Mount Pinatubo in 1991 the sulfate aerosol load was increased by 5 to 10 fold causing cooling of the lower atmosphere by  $0.5^{\circ}\text{C}$  (*McCormick et al.* 1995; *Soden et al.*, 2002) and 0.1 to  $0.3^{\circ}\text{C}$  on the surface (*Thompson et al.*, 2009; *Canty et al.*, 2013). The surface temperatures did not return to pre-Pinatubo level until approximately three years after the eruption as the atmosphere

filtered out the additional aerosol (*Hansen et al.*, 1996). More recently, a series of small to moderate volcanic eruptions have increased the background stratospheric aerosol layer (*Vernier et al.*, 2011b). This additional volcanic aerosol load has been proposed to be linked to a larger effect of decreased warming, known sometimes as the global warming hiatus (*Solomon et al.*, 2011; *Haywood et al.*, 2014; *Fyfe et al.*, 2013).

### **2.3 Aerosol Measurements**

There are essentially three fundamental approaches to measuring atmospheric aerosol: ground based systems, *in-situ* measurements, and satellite based remote sensing. Each of these methods has certain strengths and the combination of data from all three approaches is essential for the future. Ground based and *in-situ* measurements typically provide detailed information about a specific localized area. Global coverage can only really be obtained with satellite measurements, but these are essentially always information-limited by the remote sensing technique. Ground-based, *in-situ* and satellite measurements have important roles in monitoring the planet's aerosol content and each of these methods have inherent advantages and disadvantages. An overview is given here on some of the common methods for stratospheric aerosol measurements in order to place the ALI requirements and design in context.

#### **2.3.1 In-situ Measurements**

In-situ measurement are typically performed using balloon- or aircraft-based platforms. In-situ balloon instruments directly measure aerosol particles during the ascent and can determine the height profile of the particle size distribution. The OPC is an active instrument that uses a light source internal to the device to optically count aerosol particles. This type of instrument has been launched from Laramie, Wyoming since 1971, and has successfully measured aerosol mixing ratio and particle size distributions (*Deshler et al.*, 2003; 2008; *Kovilakam et al.*, 2015) on many flights since that time. Similarly, aircrafts have been used to carry nephelometers to acquire detailed in-

situ measurements (*Beuttell and Brewer*, 1949; *Charlson et al.*, 1969) including plume composition (*Murphy et al.*, 2014) but are limited spatially to the aircraft track.

### 2.3.2 Occultation

Satellite instrumentation capable of measuring stratospheric aerosol has been in use since the 1970s, beginning with limb sounding solar occultation measurements. The viewing geometry of this technique is shown in Figure 2-3. Solar occultation measurements have provided a reliable, accurate and essentially continuous long term record of vertically resolved aerosol extinction coefficient measurements, mostly from the series of Stratospheric Aerosol and Gas Experiment (SAGE) instruments including SAGE I in 1979, SAGE II in 1984, and SAGE III in 2001 (*Russell and McCormick*, 1989; *Thomason and Taha*, 2003). These SAGE measurements, which have a vertical resolution of approximately 1 km, have generally compared well with ground-based and in-situ measurements, although there are challenges associated with determining microphysical parameters and comparison between instruments can be challenging (*Russell and McCormick*, 1989; *Kovilakam et al.*, 2015). However, solar occultation is generally a robust and stable technique as it directly measures atmospheric optical depth, along with the exo-atmospheric solar spectrum with each scan, allowing for straightforward retrieval of aerosol extinction coefficients (*Damadeo et al.*, 2013). The major drawback to occultation instruments is that a sunrise or sunset event is required to perform a measurement limiting the number of scans per day to 16-48 measurements depending on the orbit.

The series of SAGE missions came to an end in 2006 with the failure of SAGE III. The occultation measurements from the currently operational MAESTRO and ACE-Imager instruments on SciSat (*McElroy et al.*, 2007; *Gilbert et al.*, 2007) have had some success producing stratospheric aerosol extinction products (*Vanhellemont et al.*, 2008; *Sioris et al.*, 2010).

Furthermore, a manifestation of SAGE III is planned for deployment on the International Space Station in 2016 (*Cisewski et al.*, 2014) to continue the valuable occultation-based aerosol record.

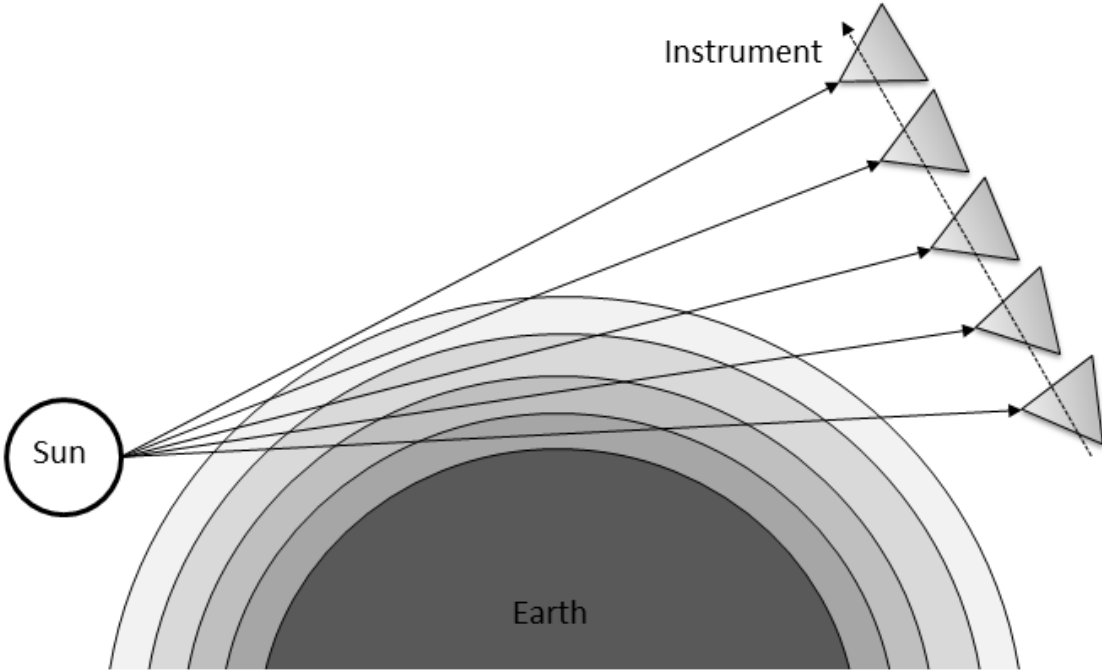


**Figure 2-3:** An occultation instrument monitoring the atmosphere by scanning the atmosphere by looking directly at the sun.

### 2.3.3 Lidar

A method known as lidar can determine atmospheric parameters through the pulsing of a laser and the subsequent measurement of the intensity of the backscattered light at different wavelengths and polarizations. Lidar has been used at ground based facilities to measure aerosol layers dating back to the 1960s (*Fiocco and Grams*, 1964) and are still used today. More recently lidar instruments have been used on satellite missions including the Ice, Cloud, and land Elevation Satellite (ICESat) from 2002 to 2010 (*Schutz et al.*, 2005) and Cloud-Aerosol Lidar and Infrared Pathfinder Satellite Observations (CALIPSO) which launched in 2006 (*Winker et al.*, 2007). More recently Cloud Aerosol Transport System (CATS) (*Chuang et al.*, 2013) has been mounted on the international space station in 2015 with a three year planned mission. Traditionally lidar

instruments observed in the nadir or zenith directions (*i.e.* straight down or up); however, some instruments are mounted slightly off-nadir. Both orientations are shown in Figure 2-4 for a space based geometry. Lidar measurements have been used to make highly spatially resolved measurements of aerosol plumes from volcanic eruptions (*Chazette et al.*, 1995; *Sawamura et al.*, 2012) as well as monitoring long term trends (*Hofmann et al.*, 2009).

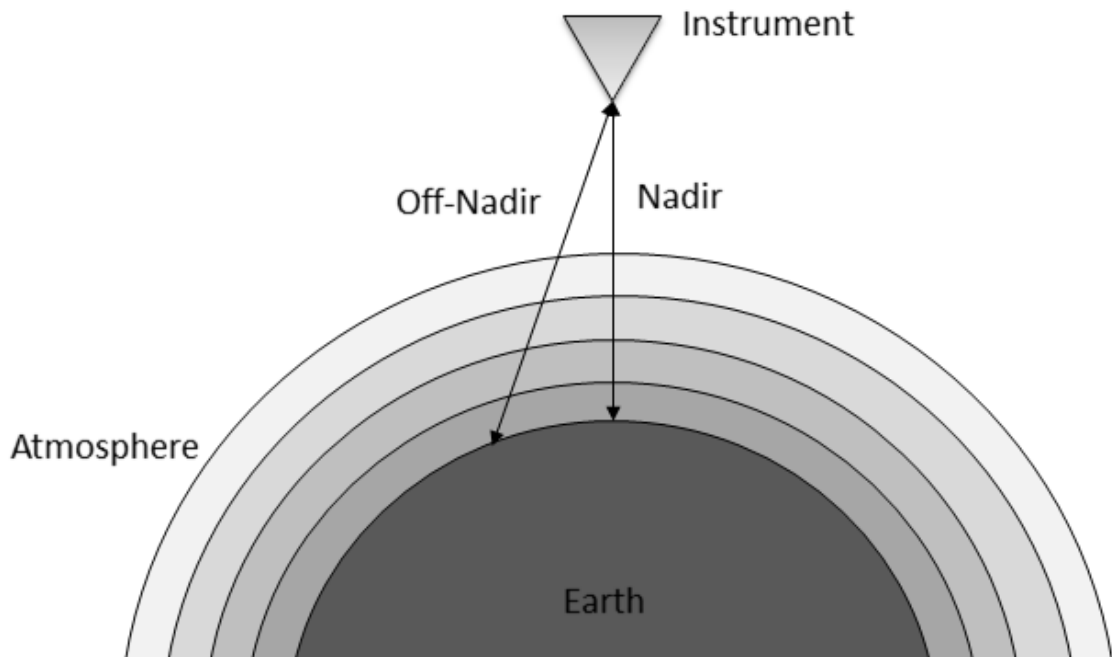


**Figure 2-4:** Lidar instrument showing measurements in both the nadir and off-nadir lines of sight.

One of the most notable lidar instruments for stratospheric aerosol measurements is CALIPSO, which is a joint mission developed between the National Aeronautics and Space Administration (NASA) and the Centre National d'Etudes Spatiales (CNES) of the United States and France respectively. It uses a two wavelength polarized lidar system to achieve high resolution aerosol and cloud retrievals along the satellite's orbital track with global coverage from 82°S to 82°N (*Young and Vaughan*, 2009). CALIPSO nominally measures backscatter profiles approximately every 300 m along track with approximately 200 m vertical resolution. However, the stratospheric

backscatter signal is weak and requires averaging of only the night time measurements over several days, typically yielding resolutions of 0.5 km vertically and 500 km horizontally (*Vernier et al*, 2011b). Additionally, the uncertainty in the calibration with respect to the molecular background is on the order of the stratospheric aerosol signal and leads to a potential bias in the stratospheric measurements (*Rogers et al.*, 2011). CALIPSO was launched in 2006 and although it is presently still operational, it is operating beyond its design lifetime.

### **2.3.4 Limb Scatter**

The limb scatter technique has an observing geometry that is similar to occultation but measures sunlight light that is scattered into the line of sight of the instrument from atmospheric interactions rather than directly observing the sun. These scattering interactions can include both single and multiple scattering events. Single scattering occurs when light from the sun interacts with a particle in the atmosphere and scatters it directly into the line of sight of the instrument. Multiple scatter is when the photon undergoes several scattering events before entering the line of sight. This can include scattering from multiple particles in the atmosphere and scattering from the ground surface. In general, these events can occur any number of times before entering the instrument. The geometry for the limb scatter technique is shown in Figure 2-5 along with the fundamental angles used to describe this condition. All angles are defined from the tangent point, which is the point where the distance between the line of sight and the surface of the earth is minimized, represented by the black dot. The Solar Zenith Angle (SZA) is the angle between the local vertical and the direction of the sun; the Solar Scattering Angle (SSA) is the defined to be the angle between the direction of the sun and the line of sight; and the Solar Azimuth Angle (SAA) is the angle between the projection of the sun direction onto the horizontal plane at the tangent point and the line of sight.

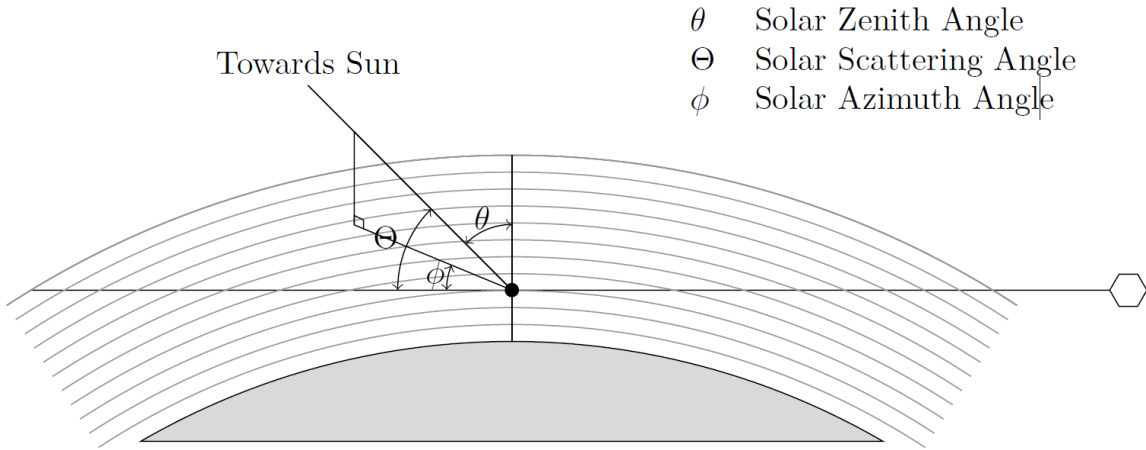


**Figure 2-5:** Limb scattering geometry measurement for an instrument where single and multiple scattering events occur.

The limb scatter method yields relatively good vertical resolution, comparable to occultation, and allows for measurements to be taken during any daylight period; however, it requires the use of a complex forward model to calculate the scattering events along with typically some *a priori* knowledge of the aerosol scattering cross section in order to retrieve the extinction coefficient profile. The model needs to accurately determine the effect of multiple scattering since it consists of 10-50% of the measured signal depending of the specific geometry and wavelength (*Oikarinen et al., 1999*). Furthermore, due to the complex nature of the problem; a large amount of computational time and memory is required for an accurate calculation.

The first use of limb scatter was on the Solar Mesosphere Explorer (SME) (*Barth et al., 1983*) to measure mesospheric ozone profiles in 1981. Much later, other limb scatter instruments were launched into low earth orbit that had the capability to determine aerosol extinction including the Optical Spectrograph and InfraRed Imaging System (OSIRIS) launched on the Odin satellite in 2001 (*Llewellyn et al., 2004*) and the SCanning Imaging Absorption spectrometer for Atmospheric CHartographY (SCIAMACHY) on Envisat launched in 2002 (*Bovensmann et al., 1999*). Both of

these instruments are scanning grating spectrometers with a single line-of-sight and scan the atmosphere vertically to complete a vertical profile measurement.

The OSIRIS version 5.07 data product provides 750 nm aerosol extinction profiles at approximately 2 km vertical resolution (*Bourassa et al.*, 2007) and has been shown to agree relatively well, generally within 30%, with SAGE II and SAGE III occultation measurements (*Bourassa et al.*, 2012b; *Rieger et al.*, 2015). The SCIAMACHY instrument uses a retrieval technique essentially similar to OSIRIS to retrieve aerosol profiles at 750 nm with approximately 3 km vertical resolution (*Ernst et al.*, 2012; *von Savigny et al.*, 2015). However SCIAMACHY observations ceased with the demise of Envisat in 2012 and although OSIRIS continues to operate, it is now in the sixteenth year of a mission designed for two years.

The most recently launched limb scatter instrument is the Ozone Mapping Profiler Suite Limb Profiler (OMPS-LP) on the Suomi-NPP satellite in 2011. Although similar in spectral range and vertical resolution to OSIRIS, OMPS-LP is an imaging spectrometer that vertically images the limb in a single measurement. The imaging capability of OMPS-LP provides a decrease in the time required to obtain a limb profile and so increases the along track sampling. Recent work on the feasibility of aerosol retrieval from OMPS-LP measurements show promising results (*Rault and Loughman*, 2013).

An instrument that is currently under development for a European Space Agency satellite mission is ALTIUS (*Dekemper et al.*, 2012, *Fussen et al.*, 2016), which is a concept from the Belgium Institute for Space Aeronomy. ALTIUS is designed to image limb scattered sunlight, both vertically and horizontally across the track through the use of Acousto-Optic Tunable Filter (AOTF) technology (see section 3.2). ALTIUS is also designed to have solar, stellar, and planetary occultation modes. ALTIUS is scientifically focused on trace gas measurements, particularly for

ozone and the instrument has three hardware channels, each channel with a separate AOTF, overall measuring wavelengths from 250-2000 nm. These measurements could eventually be used for aerosol extinction retrieval.

The limb scatter technique is the one selected for the ALI instrument in this thesis work. The limb scatter technique was selected for ALI due to the potential for global coverage, high vertical resolution and the high quality of aerosol extinction retrieval as proven the OSIRIS heritage. Like ALTUIS, ALI also uses an AOTF to spectrally image the limb scattered signal. As discussed in detail in Chapter 3, the hyperspectral imaging nature of the ALI design with the AOTF allows for rapid image collection for the retrieval of high spatial resolution aerosol extinction.

## 2.4 Radiative Transfer

The use of the limb scatter technique requires a detailed understanding of radiative transfer, and the modeling of the complex scattering interactions of light within the atmosphere is somewhat involved. In this section, a necessary overview of scalar radiative transfer is provided, followed by the necessary modifications to the theory to form the polarized radiative transfer equation. A description of scattering interactions important to aerosols is also developed. Finally, an overview of the SASKTRAN radiative transfer model used within this work is provided.

### 2.4.1 Scalar Radiative Transfer

The following presents a derivation of radiative transfer equations for the atmosphere in terms of the scalar radiance, a theory which does not account for polarization. In order to accurately discuss radiative transfer, a coordinate system must first be defined. If we assume that a ray of light,  $I$ , is propagating in a given direction,  $\hat{\Omega}$ , and starts at a location,  $s_0$ , with the initial position of  $\mathbf{r}_0$ , then the position of the ray along the path direction can be completely defined by its path length,  $s$ . The basis of path length is used to define the radiative transfer equations.

The fundamental theory for radiative transfer is known as the Beer-Lambert law. The law describes the change in intensity or radiance of light,  $dI$ , as it interacts with a thin layer of space or atmosphere,  $ds$ . The thin layer has particles which affect the attenuation of the light which is dependent on the number of particles,  $n$ , and the particle cross section,  $\sigma$ . If there are several different particles, the attenuation is a summation of the number densities and cross sections. The Beer-Lambert Law describes the change in radiance along the path

$$\frac{dI(s)}{ds} = -I(s) \sum_i n_i(s) \sigma_i(s). \quad (2.2)$$

The extinction of light by particles is a measure of the loss of light over a given distance and is defined as

$$k(s) = \sum_i n_i(s) \sigma_i(s). \quad (2.3)$$

Integrating Equation 2.2 forms the following result

$$I(s_1) = I(s_0) e^{-\int_{s_0}^{s_1} k(s') ds'}. \quad (2.4)$$

The optical depth,  $\tau(s)$ , is defined as the extinction over the path length simplifying Equation 2.4 to

$$I(s_1) = I(s_0) e^{-\tau(s)}. \quad (2.5)$$

The above gives the radiance at point  $s_1$  after it has gone through attenuation from  $s_0$ .

Although this form of the Beer-Lambert's Law is useful for describing the loss of light through scattering or absorbing from an initial source though a medium, in the atmosphere we must also account for incoming light that is scattered into the line of sight from other directions or directly emitted from particles along the path. To account for this additional source of light a source term,  $J$ , is added to Equation 2.2 to yield

$$\frac{dI(s)}{ds} = k(s)(J(s) - I(s)). \quad (2.6)$$

Using the fact that the change in optical depth is defined as

$$d\tau = -k(s)ds \quad (2.7)$$

Equation 2.6 is rearrange into

$$\frac{dI(\tau)}{d\tau} = I(\tau) - J(\tau). \quad (2.8)$$

Using the following derivative

$$\frac{d}{d\tau}(I(\tau)e^{-\tau}) = \frac{dI(\tau)}{d\tau}e^{-\tau} - I(\tau)e^{-\tau} \quad (2.9)$$

and substituting it into Equation 2.8 yields

$$\frac{d}{d\tau}(I(\tau)e^{-\tau}) = -J(s)e^{-\tau}. \quad (2.10)$$

This form can now be integrated over the optical depth giving

$$I(\tau)e^{-\tau} - I(\tau_0)e^{-\tau_0} = - \int_{\tau_0}^{\tau} J(\tau')e^{-\tau'}d\tau'. \quad (2.11)$$

Selecting the reference point at the observer to be  $\tau_0 = s_0 k(s_0) = 0$  and converting the equation back to path lengths yields

$$I(s_0) = I(s)e^{-\tau(s)} + \int_s^{s_0} k(s')J(s')e^{-\tau(s')}ds' \quad (2.12)$$

which gives the radiance as seen from an observer at a point,  $s$ , along the line of sight.

In the atmosphere there are three sources of additional radiation that contribute to the source term: thermal emissions, photochemical reactions, and scattered light. For wavelengths from the visible to the near infrared (*i.e.* wavelengths less than 2  $\mu\text{m}$ ) there is negligible contribution from thermal emissions. Furthermore, as long as distinct wavelengths where photochemical reactions

emit are avoided this source term can also be ignored. This leaves scattering as the only significant source of light to be added into the line of sight. The source term for scattered sunlight is given by

$$J(s, \hat{\Omega}) = \frac{k_{scat}(s)}{k(s)} \int_{4\pi} I(s, \hat{\Omega}') p(s, \theta) d\hat{\Omega}'. \quad (2.13)$$

The diffuse radiance is given by  $I(s, \hat{\Omega}')$  and is the radiation scattered into the line of sight from all directions. The phase function,  $p(s, \theta)$ , described the probability that a ray of light is scattered from a direction,  $\hat{\Omega}'$ , into the line of sight propagation direction,  $\hat{\Omega}$ . The scattering angle,  $\theta$ , is defined as

$$\cos(\theta) = \hat{\Omega}' \cdot \hat{\Omega}. \quad (2.14)$$

Lastly,  $k_{scat}(s)$  is the extinction only caused by scattering and not absorption. The term  $\frac{k_{scat}(s)}{k(s)}$  only allows the fraction of particles that scatter radiation, and not absorb it, to contribute to the source term.

As a final note, the calculation of the diffuse radiance is what makes this a computationally heavy problem. To completely solve for the diffuse radiance, the radiance at every point in the atmosphere must be determined. Furthermore, the light can be scattered multiple times in the atmosphere, requiring a diffuse radiance for each order of scatter. Each successive scattering adds smaller contributions to the final radiance at the observer. Through this iterative process the full multiple scatter solution to the radiative transfer equation is

$$I(s_0) = \sum_{i=1}^{\infty} [I_i(s)] e^{-\tau(s)} + \int_s^0 k(s') \sum_{i=1}^{\infty} [J_i(s')] e^{-\tau(s')} ds'. \quad (2.15)$$

The multiple scatter term is calculated for each successive order until the contribution is sufficiently small to be negligible.

### 2.4.2 Vector Radiative Transfer

The scalar radiative transfer equation works well for systems that do not measure polarized light as the effect of polarization on the total radiance is small. However, for instruments that measure polarized light, a vector radiative transfer equation is required. Before polarization can even be discussed, a method to quantify polarization must be defined. The general framework for this analysis is the Stokes vectors. The Stokes vectors are given as

$$\mathbf{I} = \begin{bmatrix} I \\ Q \\ U \\ V \end{bmatrix}, \quad (2.16)$$

where  $I$  is the scalar or total radiance,  $Q$  is the difference between horizontal polarization to vertical polarization,  $U$  is the difference between  $+45^\circ$  diagonal polarization to  $-45^\circ$  polarization, and  $V$  is the difference between the counter clockwise circular polarization to clockwise polarization (*Bickel and Bailey, 1985*). Using a reference frame where the local x-axis is defined to be the horizontal polarization leads to the following definition for the Stokes vector

$$\begin{aligned} I &= \langle E_x \rangle^2 + \langle E_y \rangle^2 \\ Q &= \langle E_x \rangle^2 - \langle E_y \rangle^2 \\ U &= 2\text{Re}(\langle E_x \rangle \langle E_y^* \rangle) \\ V &= 2\text{Im}(\langle E_x \rangle \langle E_y^* \rangle) \end{aligned} \quad (2.17)$$

The electric field aligned with the x and y-axis are  $E_x$  and  $E_y$  respectively, the star is the complex conjugate, and Re and Im are the “real part of” and “imaginary part of” respectively. The degree of polarization can be determined with the Stokes vectors. If the equality  $I^2 = Q^2 + U^2 + V^2$  holds true then the light is fully polarized, otherwise it is only partially polarized if  $I^2 > Q^2 + U^2 + V^2$ .

With the addition of polarization, the radiative transfer and source term equations (Equations 2.12 and 2.13) need to be rewritten with the polarization state included. The polarized radiative transfer equation are

$$\mathbf{I}(s_0) = \mathbf{I}(s)e^{-\tau(s)} + \int_s^0 k(s') \mathbf{J}(s') e^{-\tau(s')} ds' \quad (2.18)$$

$$\mathbf{J}(s, \hat{\Omega}) = \frac{k_{scat}(s)}{k(s)} \int_{4\pi} \mathbf{L}(\theta_2) \mathbf{P}(s, \theta) \mathbf{L}(\theta_1) \mathbf{I}(s, \hat{\Omega}') d\hat{\Omega}', \quad (2.19)$$

which are the vector radiative transfer and source term equations respectively (*Mishchenko et al.*, 2002). With polarization a scattering reference frame is defined and incoming radiance is rotated into the scattering frame multiplied by the scattering matrix,  $\mathbf{P}(s, \theta)$ , then returned to the original propagation frame. The rotation matrix is defined as

$$\mathbf{L}(\theta) = \begin{bmatrix} 1 & 0 & 0 & 0 \\ 0 & \cos(2\theta) & \sin(2\theta) & 0 \\ 0 & -\sin(2\theta) & \cos(2\theta) & 0 \\ 0 & 0 & 0 & 1 \end{bmatrix} \quad (2.20)$$

where  $\theta$  is the angle between the propagation and scattering reference frames. The radiance and the source terms are now Stokes vectors in 4 by 1 matrices and the scattering matrix,  $\mathbf{P}(s, \theta)$ , is a 4 by 4 tensor that is related to the probability of the incoming light to be scattered in the propagation direction with a specific polarization. As a note, the operation of  $\mathbf{L}(\theta_2) \mathbf{P}(s, \theta) \mathbf{L}(\theta_1)$  is commonly referred to as the phase matrix. The polarization equation adds extra computation and memory consumption since the polarization must be computed at each scattering in the radiative transfer equation, which is nontrivial, and stored in memory, essentially four times the size of a standard scalar radiance calculation.

With the complete vector polarized radiative transfer expression the two scattering interactions that pertain to determining aerosol are described. The first interaction is Rayleigh scattering, which defines the scattering process from the molecular atmosphere, and Mie scattering, which determines how incoming light scatters from spherical particles, *i.e.* a model for stratospheric aerosol scattering.

### 2.4.3 Rayleigh Scattering

Rayleigh scatter is the scattering process by the molecular background atmosphere, *i.e.* by molecules of the air. The first calculation of molecular atmospheric scattering cross sections was by Lord Rayleigh where he assumed the molecules were dielectric spheres with radii much less than the wavelength of the light (*Rayleigh*, 1899). Later, the King correction was added to the Rayleigh scattering cross section,  $\sigma_{ray}$ , to yield the following expression

$$\sigma_{ray} = \frac{128\pi^5 \alpha_0^2}{3\lambda^4} \frac{6 + 3\rho_n}{6 - 7\rho_n}, \quad (2.21)$$

which is highly dependent on wavelength,  $\lambda$ . The parameters  $\alpha_0$  and  $\rho_n$  are the volume polarizability, given per unit volume, and the depolarization ratio, which is unitless (*Sneep and Ubachs*, 2005). The depolarization ratio is the ratio of the intensity of light perpendicular to the reference frame over the intensity of light aligned with the reference frame.

The other important quantity for scattering is the scattering matrix, which is analogous to the scattering phase function in the scalar theory. For Rayleigh scattering, the vector model scattering matrix is given by the Rayleigh-Gans approximation (*Mishchenko et al.*, 2002)

$$\mathbf{P}(\theta) = \frac{3}{4} \begin{bmatrix} 1 + \cos^2 \theta & -\sin^2 \theta & 0 & 0 \\ -\sin^2 \theta & 1 + \cos^2 \theta & 0 & 0 \\ 0 & 0 & 2\cos\theta & 0 \\ 0 & 0 & 0 & 2\cos\theta \end{bmatrix}. \quad (2.22)$$

Each component of the scattering matrix itself is smoothly varying and analytically determined, which allows for easy and accurate calculation of Rayleigh scattering.

### 2.4.4 Mie Scattering

For larger particles, like sulfate aerosol, Rayleigh scattering no longer holds since the size of the particles is on the order of the wavelength and Mie scattering must be used. *Mie* (1908) solved Maxwell's equations for scattering from a dielectric sphere in a general sense with a solution using

a series of spherical Bessel and Henkel functions. Only the fundamental Mie scatter equation is presented here but a full derivation of Mie scatter can be found in *van de Hulst* (1957). The scattering cross section from Mie theory is given by

$$\sigma_{mie} = \frac{2\pi}{k^2 r^2} \sum_{l=1}^{\infty} (2l+1) (|a_l|^2 + |b_l|^2), \quad (2.23)$$

where  $k$  is the wavenumber,  $r$  is the particle radius and the coefficients  $a_l$  and  $b_l$  are given by

$$a_l = \frac{\Psi'_l(nkr)\Psi_l(kr) - n\Psi_n(nkr)\Psi'_l(kr)}{\Psi'_l(nkr)\zeta_l(kr) - n\Psi_l(mkr)\zeta'_l(kr)}, \quad (2.24)$$

$$b_l = \frac{n\Psi'_l(nkr)\Psi_l(kr) - \Psi_n(nkr)\Psi'_l(kr)}{n\Psi'_l(nkr)\zeta_l(kr) - \Psi_l(mkr)\zeta'_l(kr)}. \quad (2.25)$$

The index of refraction of the particle is given by  $n$ , and  $\Psi_l$  and  $\zeta_l$  are the normalized half-integer order Bessel functions of the first kind and Henkel functions of the second kind respectively. The scattering matrix for Mie scatter for a vector solution has the following form (*Hansen and Travis*, 1974)

$$\mathbf{P}(\theta) = \frac{2\pi}{k^2 \sigma_{mie}} \begin{bmatrix} S_1 S_1^* + S_2 S_2^* & S_1 S_1^* - S_2 S_2^* & 0 & 0 \\ S_1 S_1^* - S_2 S_2^* & S_1 S_1^* + S_2 S_2^* & 0 & 0 \\ 0 & 0 & S_1 S_2^* + S_2 S_1^* & i(S_1 S_2^* + S_2 S_1^*) \\ 0 & 0 & -i(S_1 S_2^* + S_2 S_1^*) & S_1 S_2^* + S_2 S_1^* \end{bmatrix}. \quad (2.26)$$

The terms in the scattering matrix,  $S_1$  and  $S_2$ , are known as the amplitude functions and are given by

$$S_1(\theta) = \sum_{l=1}^{\infty} \frac{2l+1}{l(l+1)} \left[ a_l \frac{1}{\sin\theta} + b_l \frac{d}{d\theta} \right] P_l^1(\cos\theta), \quad (2.27)$$

$$S_2(\theta) = \sum_{l=1}^{\infty} \frac{2l+1}{l(l+1)} \left[ b_l \frac{1}{\sin\theta} + a_l \frac{d}{d\theta} \right] P_l^1(\cos\theta), \quad (2.28)$$

where  $P_l^1$  are the Legendre polynomials.

In the atmosphere, various particle sizes occur and a log-normal distribution (Equation 2.1) is assumed for aerosols. In order to determine an effective scattering cross-section, a weighted average over the particle radius is performed

$$\sigma_{eff} = \frac{\int_0^{\infty} \sigma_{mie}(r)n(r)dr}{\int_0^{\infty} n(r)dr}. \quad (2.29)$$

The weighted average is similarly performed to determine the effective phase matrix for a particle size distribution.

There are stark differences between Rayleigh and Mie scattering cross sections and scattering matrices. Using standard atmospheric conditions, a comparisons of the extinctions and thus the scattering cross sections as a function of wavelength are shown in Figure 2-6a. The “wavelength to the fourth” dependence is shown for Rayleigh scattering, in blue, (Equation 2.21) whereas Mie scattering, in red, has a flatter spectral dependence, which changes with particle size. Due to this difference, the contribution of Mie scattering becomes more predominant as wavelength increases. The terms of the scattering phase matrix are also radically different for the two scattering processes (Figure 2-6b). For the first term of the scattering matrix,  $P_{11}(\theta)$ , the Rayleigh term is smooth with even forward and back scattering and decreases at  $90^\circ$  scattering angle. The scattering term for Mie on the other hand has a strong tendency for forward scattering compared with much lower values for scattering angles past  $90^\circ$ . Further, for certain wavelengths and size parameters the Mie phase matrix can have oscillations super-imposed onto the curve making the phase matrix even more complex than Rayleigh scattering.

It should be noted that although the theory is well understood, the calculation of the Mie scattering cross sections and phase matrices in practice is computationally intensive since the terms consist of infinite sums of Bessel and Henkel functions. Comprehensive work done by *Wiscombe*

(1980) has allowed for accurate and efficient computation of the Mie scattering coefficients, and these are used within the modelling work presented here.

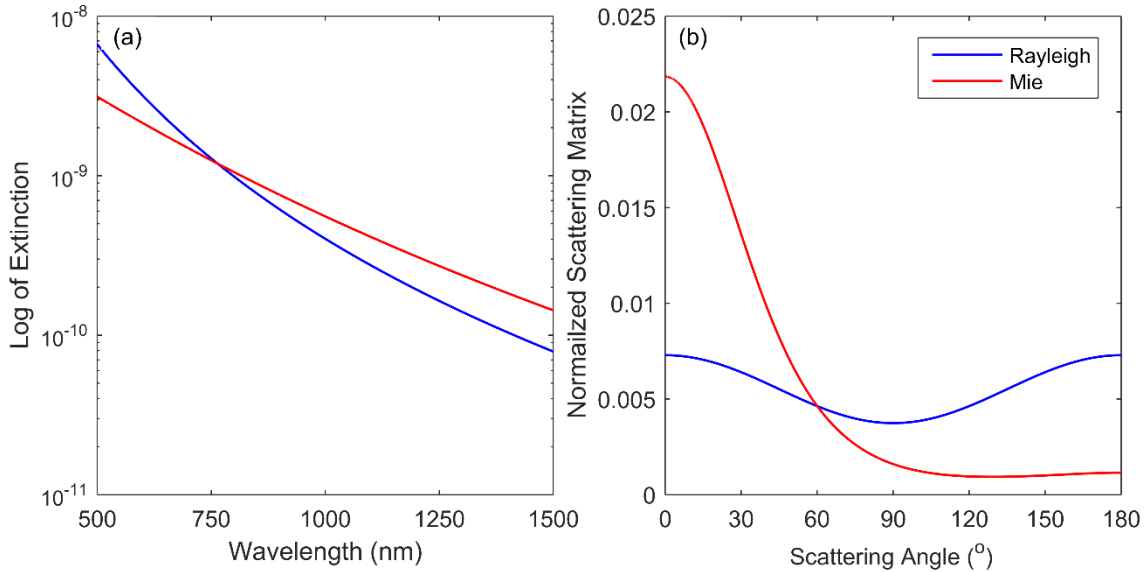


**Figure 2-6:** (a) Change in extinction for Rayleigh and Mie scattering over wavelength. The Mie scattering uses a log-normal distribution with a mode width of 1.6 and a mode radius of 0.08  $\mu\text{m}$ . (b) The first term of scattering matrix,  $P_{11}(\theta)$ , for Rayleigh and Mie scattering cross scattering angle.

#### 2.4.5 SASKTRAN Radiative Transfer Model

The SASKTRAN radiative transfer was first developed to solve the scalar radiative transfer equation in a fully spherical atmosphere for both single and multiple scattering with a one dimensional atmosphere, *i.e.* considering the variation in altitude only (Bourassa *et al.*, 2008). The first source term,  $J_1$ , is the light from the sun attenuated and scattered into the instrument line of sight, and it is assumed the incoming solar irradiance encounters the earth in parallel randomly polarized rays. To include higher order terms, a successive orders method is used to simulate second, third and higher orders of scattering within the atmospheric model. Another important assumption in the SASKTRAN model is that the ground reflection is assumed to have a depolarizing Lambertian distribution, which will evenly distribute the incoming radiance evenly in all outgoing directions with the efficiency of the planetary albedo.

Recent upgrades have been performed on SASKTRAN and have led to a new solver, or “engine” known as SASKTRAN High Resolution or SASKTRAN-HR (Zawada *et al.*, 2015) which has expanded the model capabilities to be able to perform radiative transfer calculations with a fully three dimensional atmosphere. This update allows the model to vary the atmospheric concentrations in not just the vertical direction, like the original SASKTRAN, but in both of the horizontal geometries (*i.e.* latitude and longitude), allowing for more accurate modelling of the variation of atmospheric parameters along the instrument line of sight and the potential for tomographic inversions.

The most important update to the SASKTRAN-HR model for this thesis work is the capability to calculate the vector or polarized radiances (Dueck *et al.*, 2016). Solving the vector radiative transfer equation allows for SASKTRAN to compute the Stokes vectors in the reference frame of the model, which can then be rotated into any desired instrument frame of reference. The polarization algorithm implemented in SASKTRAN-HR provides polarized calculations up to a user-specified number of orders of scattering, with all successive orders approximated as randomly polarized.

## 2.5 Inversion Techniques

Remote sensing methods indirectly measure the desired atmosphere state and require a method to be able to transform the measurement into the desired physical atmospheric quantity. This process is known as a measurement “inversion”, “retrieval”, or more generally as the inverse problem. A measurement vector,  $\mathbf{y}$ , is constructed from the spectral radiance that has sensitivity to the desired physical parameter while reducing sensitivity to other physical parameters as much as possible. A forward model (for example in this case SASKTRAN-HR),  $\mathbf{F}(\mathbf{x}, \mathbf{b})$  is used to compute the measurement vector using an input atmospheric state,  $\mathbf{b}$ , and desired physical

parameter state,  $\mathbf{x}$ . The length of the measurement vector and state vector are  $m$  and  $n$  respectively. It is important to note that the length of the measurement vector and state vector do not have to be the same. This leads to the following formation

$$\mathbf{y} = \mathbf{F}(\mathbf{x}, \mathbf{b}) + \boldsymbol{\epsilon}, \quad (2.30)$$

where  $\boldsymbol{\epsilon}$ , is the measurement noise. This is the equation that needs to be inverted to yield the desired atmospheric state.

The inverse is found directly if it is assumed that there is no measurement error and the problem is linear. Using an initial guess or *a priori*,  $\mathbf{x}_a$ , the retrieved parameter state can be found through

$$\mathbf{y} = \mathbf{K}(\mathbf{x} - \mathbf{x}_a) + \mathbf{F}(\mathbf{x}_a, \mathbf{b}), \quad (2.31)$$

$$\hat{\mathbf{x}} = \mathbf{x}_a + \mathbf{K}^{-1}(\mathbf{y} - \mathbf{F}(\mathbf{x}_a, \mathbf{b})). \quad (2.32)$$

The Jacobian is represented by  $\mathbf{K}$ , and is the partial derivative of the forward model to the state vector. The Jacobian is an  $m \times n$  matrix. However, remote sensing methods are generally non-linear and contain measurement noise; additionally numerical approximations are usually used to calculate the forward model and Jacobian in realistic time frames. These issues make the direct method generally ineffective and iterative methods are used. This section will briefly cover common methods used for atmospheric inversions.

### 2.5.1 Optimal Estimation

Very commonly in atmospheric remote sensing, a Bayesian approach is used to update the atmospheric state, and this is known as optimal estimation (Rodgers, 2000). This method uses statistical knowledge of the *a priori* and state parameter with measurement noise to determine the probability that the state parameter is  $\mathbf{x}$  given a measurement of  $\mathbf{y}$ , and is given by

$$P(\mathbf{x}|\mathbf{y}) = \frac{P(\mathbf{y}|\mathbf{x})P(\mathbf{x})}{P(\mathbf{y})}. \quad (2.33)$$

A solution is found by maximizing the probability of  $P(\mathbf{x}|\mathbf{y})$ . If it can be assumed that the covariance of the measurement vector and *a priori* have a Gaussian distribution, the above can be solved to yield

$$\hat{\mathbf{x}} = \mathbf{x}_a + \mathbf{S}_a \mathbf{K}^T (\mathbf{K} \mathbf{S}_a \mathbf{K}^T + \mathbf{S}_\epsilon)^{-1} (\mathbf{y} - \mathbf{K} \mathbf{x}_a). \quad (2.34)$$

The covariance matrices of the *a priori* and measurement error are  $\mathbf{S}_a$  and  $\mathbf{S}_\epsilon$  respectively. For non-linear problems, this equation is iterated until a converged solution is found. It should be noted that if the covariance of the *a priori* is unknown or is not well modeled by a Gaussian distribution this method can provide less “optimal” results.

## 2.5.2 Levenberg-Marquardt

The Gauss-Newton iterative method has been classically used to solve for non-linear inversion problems. However, if the initial guess is far from the solution and if the solution space is not well described by a quadratic the method will fail. *Levenberg* (1944) proposed another method for the non-linear least squares fit that was later modified by *Marquardt* (1963) given as

$$\hat{\mathbf{x}}^{(n+1)} = \hat{\mathbf{x}}^{(n)} + (\mathbf{K} \mathbf{K}^T + \gamma^{(n)} \mathbf{D})^{-1} \mathbf{K}^T (\mathbf{y} - \mathbf{F}(\hat{\mathbf{x}}^{(n)}, \mathbf{b})), \quad (2.35)$$

and is known as the Levenberg-Marquardt algorithm. The damping factor,  $\gamma$ , reduces the step size in iteration to keep the problem in a linear region. If this damping factor is small the method approaches the Gauss-Newton method whereas if  $\gamma$  is large the method steps down the direction of the gradient descent. The diagonal matrix,  $\mathbf{D}$ , is a scaling matrix for the damping factor since the state vector may have different dimensions and magnitudes resulting in the benefit of larger step sizes in more linear areas of the solution space. However, the determination of the damping factor can be difficult to determine from numerical methods and usually an ad hoc method is used.

### 2.5.3 Multiplicative Algebraic Reconstruction Technique

The Multiplicative Algebraic Reconstruction Technique (MART), which is used for the operational processing of the OSIRIS data products, is a form of relaxation techniques similar to the well-known Chahine relaxation (*Chahine, 1970*). The MART algorithm has the modification of a weighting matrix,  $\mathbf{W}$ , which relates the importance of each measurement vector,  $k$ , and tangent altitude,  $j$ , to each retrieved state altitude,  $i$ . The algorithm is given by

$$\hat{x}_i^{(n+1)} = \hat{x}_i^{(n)} \sum_k \sum_j \frac{y_{jk}}{F_{jk}(\mathbf{x}^{(n)}, \mathbf{b})} W_{ijk}. \quad (2.36)$$

Unlike the previous methods, this method allows for computation of the state vector without the computation of the Jacobian or any matrix inversions allowing for a fast and efficient algorithm. In the OSIRIS aerosol algorithm, only one spectral measurement vector is used (*Bourassa et al., 2007; 2012b*) and the measurement vector summation over  $k$  from Equation 2.36 can be dropped.

## 2.6 ALI Prototype Instrument and Stratospheric Balloon Flight

The work presented in this thesis is focused on the development of the Aerosol Limb Imager (ALI). The core concept of ALI is to use the limb scatter technique together with a rapid hyperspectral imaging design approach to ultimately provide global coverage of highly spatially resolved and accurate observations of stratospheric aerosol. The central design feature of ALI is the use of the novel AOTF technology, which provides the ability to rapidly select a filtered wavelength with no moving parts, an ideal feature for space application. AOTFs have recently been developed with large apertures and high quality crystals allowing for imaging capabilities. The AOTF technology operates efficiently in the red and near infrared region of the spectrum, which is well-matched for limb scatter sensitivity to aerosol and clouds (*Rieger et al., 2014*) and

has a typical spectral bandpass of 3-6 nm, which is ideal for the broadband scattering characteristics of aerosol.

### **2.6.1 ALI Specifications**

As mentioned previously, the ultimate goal of this work is the eventual realization of ALI on a future satellite mission. However, for the prototype design and test work presented here, the available flight opportunity was on a stratospheric balloon. This choice of test platform has resulted in some specific design decisions for the prototype that would ultimately require revision for a satellite-based implementation.

Stratospheric balloon flights provide a stable float altitude of 35 km. This results in a minimum vertical field of view for ALI of  $6^\circ$  in order to image the limb from the ground to the float altitude. For a satellite platform the required field of view would be substantially reduced to approximately  $1^\circ$  in order to cover the same range. The structural features in the aerosol distribution discussed in section 2.2 are generally less than one kilometer vertically and to resolve these features a minimum spatial resolution of 250 m is required. For this design, similar specifications are used for the horizontal (cross-track) direction.

Spectrally, aerosol scattering is a broadband phenomenon with spectrally smooth scattering cross sections such that high spectral resolution is not required; however, a large spectral range is desirable. Particle size sensitivity in limb scattering increases from the visible to the near infrared (*Rieger et al.*, 2014). When combined with the single octave range capability of the AOTF, ALI is designed to measure the 600-1200 nm spectral range. Since the aerosol (Mie) scattering cross section varies slowly with wavelength, measurements every 25-50 nm within the range are required. Furthermore, this slow varying cross section also allows for low spectral resolution with a spectral bandpass requirement of less than 10 nm.

The nature of imaging limb scattering results in a situation where the lower altitudes have high signal and the upper altitudes have low signal. Therefore signal to noise levels are the most important at the high altitudes due to the exponential signal drop-off. The highest measurement altitudes (*i.e.* 30-35 km) require that the signal to noise ratio must remain above 5 to be able to use these high altitude measurements to determine aerosol extinction. Additionally, the system should be able to take a single image with an exposure time on the order of a second or less to achieve a high measurements density.

Finally, due to the limitations of the stratospheric balloon platform both mass, power consumption, and thermal ranges are a concern. The balloon platform can only sustain so much mass and has a limited amount of power. As such, the total mass of ALI must remain below 50 kg and power consumption below 80 W. Furthermore, the thermal environment of the balloon at stratospheric altitudes is challenging with ambient temperatures that are colder than -40°C. Additionally, heating from direct sunlight cause large thermal gradients in the instrument resulting in concerns of overheating. In order to mitigate these concerns ALI must be thermally stable within all equipment's standard operating ranges.

# CHAPTER 3

## INSTRUMENT DESIGN<sup>1</sup>

### **3.1 Introduction**

Aerosol is an important component in the climate balance and new instruments with the capability of measuring aerosol with high resolution and accuracy are required for the near future. These instruments will need to have the ability to determine both aerosol concentration as well as particle size information to better understand the effect of aerosol on the global climate. This chapter discusses the ALI instrument with the goal of measuring high quality aerosol profiles to fulfill the need of future scientific monitoring. The design of ALI is covered from the initial planning to the completed optical and opto-mechanical system. First, a discussion of the Acousto-Optical Tunable Filter (AOTF) is presented that covers the solution of the wave equation, diffraction efficiency, output diffracted angle, and tuning curve. Following is a discussion of the trade-offs of the two primary optical design layouts considered for the instrument. Then the final optical specifications of the chosen design are presented along with the opto-mechanical aspects of the instrument

### **3.2 AOTF Theory and Background**

The fundamental piece of technology used in the ALI design is an AOTF, which provides tunable narrow band filtering of an incident optical signal with fast response times and no moving parts. The use of AOTF technology for space based initiatives is only recently possible due to the recent advances in creating AOTFs with the ability to maintain imaging quality performance over wide acceptance angles. This section discusses the theory behind the AOTF.

---

<sup>1</sup> Portion of sections 3.3.1, 3.3.2, 3.3.3, and 3.3.4 as well as Figure 3-4, Figure 3-5, Figure 3-16, and Figure 3-20 were originally published in *Elash et al. (2016)*

### 3.2.1 Solution to the Acoustic Equation

The AOTF is a device that through phonon-phonon interaction and a Bragg-like diffraction process allows a broadband light source to be filtered and the output can be captured as an image. Two primary types of AOTFs exist, collinear (*i.e.* the acoustic wave is aligned with the incident beam, (*Harris and Wallace, 1969*)) and non-collinear (*i.e.* the acoustic wave and the optical beam do not propagate collinearly in the crystal, (*Chang, 1977*)) configurations, and both use an optically anisotropic medium (*Saito and Yano, 1976*). An anisotropic medium is a material that is transparent and has a different index of refraction based upon the polarization state of the incoming light and its propagation direction, commonly called birefringence. For imaging purposes, a wide aperture is required and such AOTFs have been developed (*Gass and Sambles, 1991*) and are currently readily available.

To effectively utilize an AOTF in a precision optical instrument, it is imperative to understand the detailed principle of operation. The AOTF produces a phenomena known as an Acousto-Optic (AO) effect, which describes the interaction between sound and light waves within the medium, generally a crystal. The AOTF used in this work operates in the Bragg diffraction regime which will be assumed for this derivation. Understanding the interactions between the light and the sound (acoustic) waves within the crystal leads to an understanding of the functionality of the device. For an AO interaction within the AOTF there are three fundamental signals: the first two are light waves that are represented by an incident and diffracted (or filtered) electric fields and the third is a sound wave that is generated by an applied Radio Frequency (RF) wave. Solving the AO wave equation for an AOTF will determine the form of the incident and diffracted waves in terms of optical and medium parameters. This is useful to determine the primary characteristics of the operation of the device such as diffraction efficiency and wavelength calibration. The RF wave exerts a stress on the crystal within the AOTF and this stress is the basis of the AO wave equation.

The derivation starts with the determination of the AO wave equation starting from Maxwell's equations. Amperes law and Faradays law are the foundation for the wave equation and are presented as

$$\nabla \times \mathbf{E} + \frac{\partial \mathbf{B}}{\partial t} = 0 \quad (3.1)$$

$$\nabla \times \frac{\mathbf{B}}{\mu} = \mathbf{J} + \frac{\partial(\epsilon \mathbf{E})}{\partial t} \quad (3.2)$$

where  $\mathbf{E}$  is an electric field,  $\mathbf{B}$  is an magnetic field,  $\mathbf{J}$  is the current density,  $\mu$  is the permeability, and  $\epsilon$  is the permittivity. By taking the curl of the Equation 3.1, combining it with Equation 3.2, and assuming that the AOTF crystal is non-conductive (*i.e.*  $\mathbf{J} = 0$ ) along with the identity  $\nabla \times (\nabla \times \mathbf{E}) = \nabla(\nabla \cdot \mathbf{E}) - \nabla^2 \mathbf{E}$  and assuming the crystal has no net charge (*i.e.*  $\nabla \cdot \mathbf{E} = 0$ ) gives the simplified wave equation in the form

$$\nabla^2 \mathbf{E} = \mu_0 \frac{\partial^2(\epsilon \mathbf{E})}{\partial t^2}. \quad (3.3)$$

The RF or sound wave creates a stress wave within the crystal that causes a modulation within the crystal effecting the dielectric permittivity. Since the dielectric permittivity is not a constant with time, it induces a susceptibility yielding the following form

$$\nabla^2 \mathbf{E} - \mu_0 \epsilon \frac{\partial^2 \mathbf{E}}{\partial t^2} = \frac{\mu_0}{\epsilon_0} \frac{\partial^2 \mathbf{P}}{\partial t^2} \quad (3.4)$$

where  $\mathbf{P}$  is the induced polarization due to the stress in the AO medium given by  $\mathbf{P} = \epsilon_0 \Delta \chi \mathbf{E}$  and  $\Delta \chi$  is the change in the susceptibility. It is important to note that if the input electric field is linearly polarized (*i.e.* ordinary polarization) then the stimulated electric field has a different linear polarization state (*i.e.* extraordinary polarization) (Voloshinov, 1996). It is standard to define the input electric field as the incident field and output electric field as the diffracted field. Remembering that the crystal is birefringent, the indices of refraction for the two wave fronts will

differ. Using this standard, the susceptibility is given by  $\Delta\chi = -n_i^2 n_d^2 p \mathbf{S}$  where  $n_i$  and  $n_d$  are the indices of refraction for the incident and diffracted electric fields and  $p$  is the elasto-optic coefficient which is dependent on medium and orientation of the crystal used, and  $\mathbf{S}$  is the strain wave induced by the acoustic wave. As mentioned earlier a solution for this equation is presented in the Bragg region meaning only first order diffraction effects are considered.

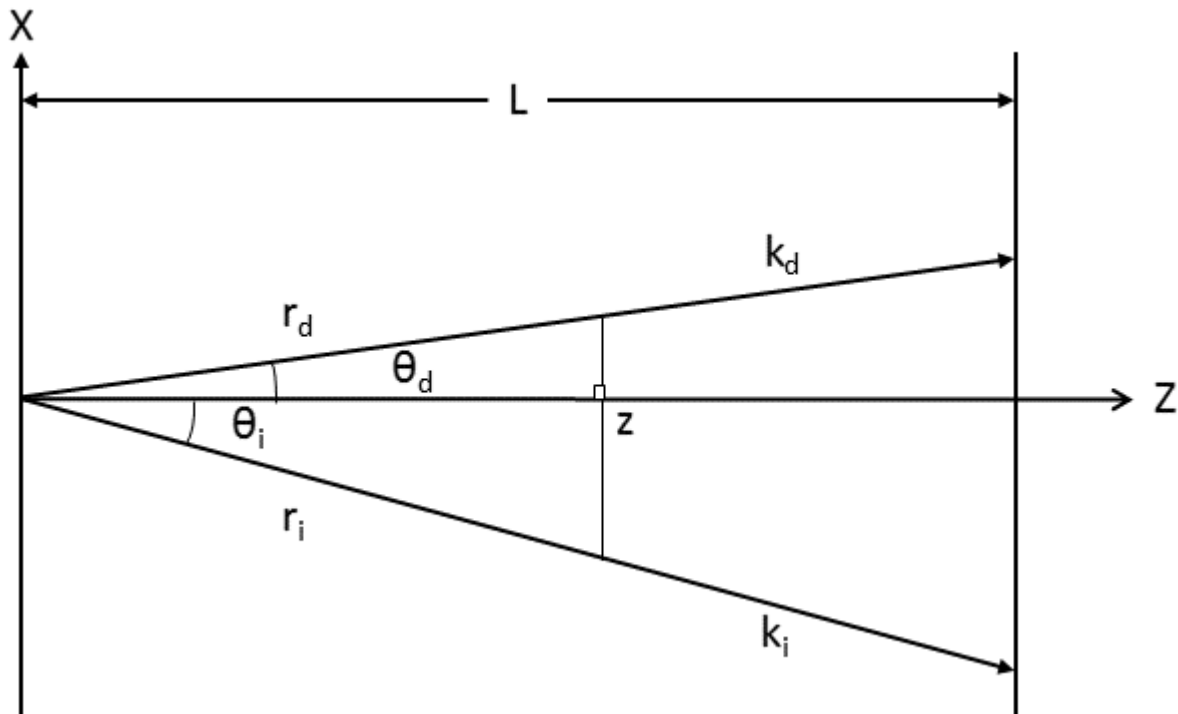


**Figure 3-1:** Geometry for the AOTF wave derivation assuming the acoustic wave is along the x-axis and the AO interaction occurs along the z axis over an interaction length,  $L$ . The parameters  $r_i$ ,  $k_i$ , and  $\theta_i$  are the position vector, wave vector, and angle of the incident electric field and similarly for the diffracted electric field. Figure recreated from Xu and Stroud (1992)

Assuming the incoming electric field is a plane wave, which is valid since most wave fronts enter the device with a large radius of curvature, the above differential equation can be solved. A standard acousto-optical geometry is used in the solution and is shown in Figure 3-1. The acoustic wave is propagating in the x direction of the crystal causing a stress wave which leads to the modulation of the index of refraction within the acoustic region of the crystal denoted by  $L$ . The

system is orientated such that the acousto interaction occurs along on the z axis and the electric field entering the device is a plane wave described by

$$\mathbf{E}_i(\mathbf{r}, t) = \frac{1}{2} \mathbf{E}_i(z) \exp[j(\omega_i t - \mathbf{k}_i \cdot \mathbf{r})] \quad (3.5)$$

and the diffracted electric field is described as

$$\mathbf{E}_d(\mathbf{r}, t) = \frac{1}{2} \mathbf{E}_d(z) \exp[j(\omega_d t - \mathbf{k}_d \cdot \mathbf{r})] \quad (3.6)$$

where  $\omega$  and  $\mathbf{k}$  are the angular frequencies and wave vectors for the incident and diffracted beams.

The modulation caused by the acoustic wave is a strain on the crystal given as

$$\mathbf{S}(\mathbf{r}, t) = \frac{1}{2} \mathbf{S}(z) \exp[j(\Omega t - \boldsymbol{\kappa} \cdot \mathbf{r})] \quad (3.7)$$

where  $\Omega$  is the angular frequency of the RF wave, and  $\boldsymbol{\kappa}$  is the acoustic wave vector.

Equations 3.5 through 3.7 are used to determine the coupled wave equations by using them in the acoustic wave equation, Equation 3.4. The induced polarization is formed by the incident wave interacting with the strain wave resulting in  $\mathbf{P} = \epsilon_0 \Delta \chi \mathbf{E}$ . The polarization wave will in turn stimulate the diffracted electric field yielding the first half of the coupled equations in the form

$$\frac{dE_d(z)}{dz} - j\Delta k E_d(z) = -j \frac{n_i^2 k_d}{4 \cos \theta_d} p S E_i(z) \exp[j(\mathbf{k}_d - \mathbf{k}_i - \boldsymbol{\kappa}) \cdot \mathbf{r}] \quad (3.8)$$

$$\frac{dE_d(z)}{dz} - j\Delta k E_d(z) = j \frac{v_i}{2L} E_i(z) \exp[j(\mathbf{k}_d - \mathbf{k}_i - \boldsymbol{\kappa}) \cdot \mathbf{r}]$$

where  $\Delta k$  is the difference between the group and phase wave vectors of the diffracted electric field,  $L$  is the length of the AO interaction, and  $v_i = -n_i^2 k_d p S L / 2 \cos(\theta_d)$ . However, once the interaction between the incident electric field forms the diffracted field, the diffracted field in turn interacts to form a polarization wave that stimulates the incident wave yielding the second coupled equation

$$\frac{dE_i(z)}{dz} = -j \frac{n_d^2 k_i}{4 \cos \theta_i} p S^* E_d(z) \exp[j(\mathbf{k}_i - \mathbf{k}_d - \boldsymbol{\kappa}) \cdot \mathbf{r}] \quad (3.9)$$

$$\frac{dE_i(z)}{dz} = j \frac{v_d}{2L} E_d(z) \exp[j(\mathbf{k}_i - \mathbf{k}_d - \boldsymbol{\kappa}) \cdot \mathbf{r}],$$

with  $v_i = -n_d^2 k_i p S L / 2 \cos(\theta_i)$ . From the previous coupled equations, a very crucial concept for the operation of the AOTF is revealed known as the momentum matching criteria. The value of the exponential term needs to be very small or equal to zero (*i.e.*  $\mathbf{k}_i = \mathbf{k}_d \pm \boldsymbol{\kappa}$ ) for the previous coupled equations to have a useful solution. The momentum matching criteria is an important result and will be used to find the tuning curve and diffraction angle within the AOTF. For efficient Bragg diffraction, the geometry is set up such that the difference of the wave vectors for the incident electric field is small or zero. Finally,  $v_i$  and  $v_d$  are the optical phase shift and the effective optical phase shift is defined as  $v_{id}^2 = v_i v_d$ .

Solving the coupled wave equations assuming momentum matching criteria yields the following solutions

$$E_i(z) = \exp\left(j \frac{\Delta k}{2} z\right) \left( A_1 \cos \frac{Tz}{L} + A_2 \sin \frac{Tz}{L} \right) \quad (3.10)$$

$$E_d(z) = \exp\left(j \frac{\Delta k}{2} z\right) \left( B_1 \cos \frac{Tz}{L} + B_2 \sin \frac{Tz}{L} \right) \quad (3.11)$$

where  $T = \left(v_i v_d + \frac{\Delta k^2}{4}\right)^{\frac{1}{2}}$  which is a function of the inverse of wavelength. It should be noted that the angular frequency of the diffracted wavelength is  $\omega_i \pm \Omega$  through the coupled interaction. To find the unknown coefficients, the boundary conditions of the system, are used

$$E_i(0) = E_i, \quad E'_i(0) = 0, \quad E_d(0) = 0, \quad E'_d(0) = \frac{v_i}{2L} E_i. \quad (3.12)$$

Solving for the coefficients yields

$$\mathbf{E}_i(z) = E_i \exp\left(j \frac{\Delta k}{2} z\right) \left( \cos \frac{Tz}{L} - j \frac{\Delta k L}{2T} \sin \frac{Tz}{L} \right) \quad (3.13)$$

$$\mathbf{E}_d(z) = E_i \exp\left(j \frac{\Delta k}{2} z\right) \left( \frac{v_i}{2T} \sin \frac{Tz}{L} \right). \quad (3.14)$$

With the completed forms of the incident and diffracted fields the diffraction efficiency and the shape of the point spread function can be determined.

### 3.2.2 Diffraction Efficiency

The diffraction efficiency,  $\eta$ , of the AOTF is ratio of the energy of the incident electric field compared to the energy of the diffracted electric field at the end of the acoustic interaction region given by

$$\eta = \frac{|E_d(L)|^2}{|E_i(0)|^2} = \left(\frac{v_i}{2}\right)^2 \left(\frac{\sin T}{T}\right)^2 \cong \left(\frac{v_{id}}{2}\right)^2 \left(\frac{\sin T}{T}\right)^2. \quad (3.15)$$

This form yields the common “sinc”-squared function shape for the spectral Point Spread Function (PSF) of an AOTF. The PSF describes the spectral bandwidth of the filtering capabilities of the device and is the limiting factor of the spectral resolution of the AOTF. For ALI, this limit must be sufficiently small enough (approximately less than 10 nm) to be able to accurately resolve aerosol from atmospheric measurements. Additionally, this form can be altered to better identify how to increase the diffraction efficiency of an AOTF. The diffraction efficiency is converted into a form that uses the RF driving power assuming exact momentum matching (*i.e.*  $\Delta k = 0$ ) and that assumes the interaction occurs within a birefringent medium. The RF driving power is the amplitude at which the piezoelectric transducer pumps the RF signal into the AO medium. The average energy flow of the acoustic power is defined by

$$P_a = \frac{\rho v^3 S^2 H L}{2} \quad (3.16)$$

where  $\rho$  is mass density of the medium,  $v$  is the acoustic velocity in the crystal,  $H$  and  $L$  is the height and length of the acoustic wave interaction region. Another variable that is useful is the acousto-optic figure of merit,  $M_2$ , which is completely determined by the medium properties defined by

$$M_2 = \frac{n_i^3 n_d^3 p^2}{\rho v^3} \quad (3.17)$$

and is a measure of how efficiently a medium can undergo the AO effect.

Using Equations 3.16 and 3.17 along with the definition of  $T$  and rearranging Equation 3.15 yields the following for the diffraction efficiency

$$\eta = \sin^2 \left( \frac{\pi}{\lambda \sqrt{\cos \theta_i \cos \theta_d}} \sqrt{\frac{M_2 L P_a}{2H}} \right). \quad (3.18)$$

Thus, the efficiency of the diffraction at a wavelength,  $\lambda$ , can be optimized through design considerations. First, a medium should be picked that yields the largest possible AO figure of merit. Second, the active region of the AO interaction should be narrow and long increasing the  $L/H$  ratio. And lastly, the driving power of the RF wave should be large enough to drive the argument of the sinusoid function in Equation 3.18 towards  $\pi$ . It should be noted that increasing the RF power beyond a certain limit can have the possibility of deceasing the AOTF diffraction efficiency (*Xu and Shroud, 1992*).

### 3.2.3 Diffraction Angle

Although the wave equations are useful in determining the diffraction efficiency, PSF, and the form of the electric fields, these relations do not determine two useful and practical parameters: the angle of the diffracted wave, and the relation between the acoustic wave frequency and the diffracted wavelength, known as the tuning curve (covered in section 3.2.4). Instead the momentum matching criteria realized through Equations 3.8 and 3.9 are used.

The diffraction angle is analyzed using the interaction between the acoustic sound wave and the light wave by

$$\mathbf{k}_i = \mathbf{k}_d \pm \boldsymbol{\kappa} \quad (3.19)$$

known as the momentum matching criteria. For this analysis, only the +1 order diffraction interaction is performed although a similar analysis can be performed for the -1 case. The wave vectors are defined as

$$|\mathbf{k}_i| = \frac{2\pi n_i}{\lambda}, \quad (3.20)$$

$$|\mathbf{k}_d| = \frac{2\pi n_d}{\lambda}, \quad (3.21)$$

$$|\boldsymbol{\kappa}| = \frac{2\pi F}{v}. \quad (3.22)$$

The RF frequency is given by  $F$  which is related to the angular frequency by  $\Omega = 2\pi F$  and the speed of the acoustic wave within the crystal is given by  $v$ . It is assumed that the extraordinary light undergoes the momentum matching through the device.

A standard acousto optical experimental setup, which can be seen in Figure 3-2, is used to determine the diffraction angle. Using Equation 3.19, the x component of the wave vector is

$$k_x = k_i \sin \theta_i = k_d \sin \theta_d + \kappa \quad (3.23)$$

and the magnitude of the diffracted wave vector is

$$k_d = \frac{\omega_d}{c} = \frac{\omega_i - \Omega}{c}. \quad (3.24)$$

Combining the results from Equation 3.23 and Equation 3.24 the angular deviation of the diffracted source is

$$\sin \theta_d = \frac{c(k_i \sin \theta_i - \kappa)}{\omega_i - \Omega}. \quad (3.25)$$

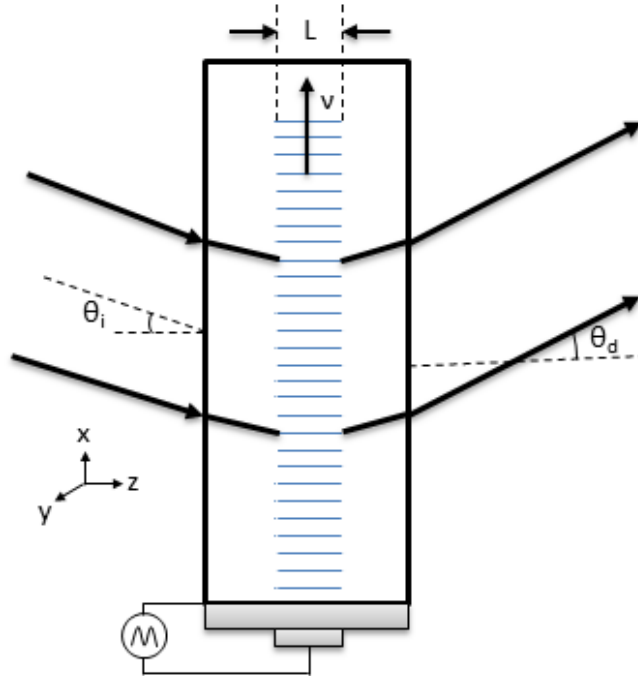


**Figure 3-2:** A standard non-collinear AOTF experiential set up. The crystal is assumed to be infinitely long in the y direction. Figure recreated after Guenther (1990) number 14B-1.

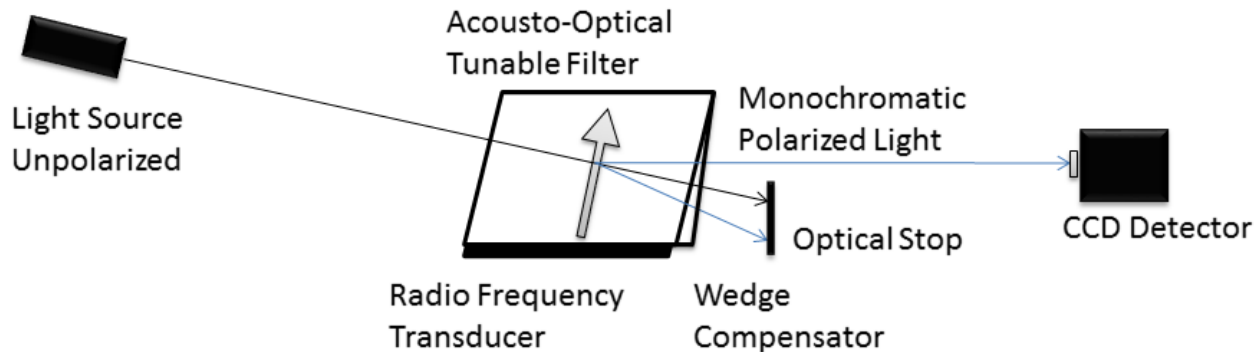


**Figure 3-3:** General Layout of an AOTF. A randomly polarized incoming light source hits the front surface of the birefringent crystal. The black bar below the crystal is the piezoelectric transducer that produces the RF signal and forms the acoustic wave represented by the grey arrow. The momentum matching Bragg diffraction occurs and monochromatic polarized light (-1 order) exits the AOTF at a constant angle with the 0th order and +1 order being blocked by an optical stop.

An important consequence of this relationship is that the diffracted light leaves the AOTF at a different angle depending on the RF. This translates to angular movement of the diffracted beam

as the filtered wavelength is scanned. In order for the device to be usable in an imaging optical system, the diffracted light should leave the device following the same path independent of selected wavelength. Thus, a crystal wedge or compensator is fashioned to the back of the device to compensate for this effect using a correcting prism-like effect causing the diffracted beam to always leave the device at the same angle. A general optical layout with the deflection in the optical path and an attached compensating wedge is shown in Figure 3-3.

### 3.2.4 Tuning Curve

The tuning curve is the AOTF relationship between the diffracted wavelength and the applied RF. The analysis is performed using the momentum matching criteria stated in Equation 3.19. Figure 3-4 shows the wave vectors in a tellurium oxide ( $\text{TeO}_2$ ) crystal in a birefringent orientation where  $\alpha$  is the propagation angle of the acoustic wave with respect to the crystal orientation.

The wave vector diagram can be used to define the incident and diffracted indices of refraction in terms of the ordinary and extraordinary indices of refraction in the following

$$n_i = \left( \frac{\sin^2(\theta_i + \alpha)}{n_e^2} + \frac{\cos^2(\theta_i + \alpha)}{n_o^2} \right)^{-\frac{1}{2}}, \quad (3.26)$$

$$n_d = n_o. \quad (3.27)$$

If the difference in the index of refraction is small, as it is for  $\text{TeO}_2$ , Equation 3.26 can be approximated as (*Voloshinov et al., 2007*)

$$n_i = n_o + \Delta n \sin^2(\theta_i + \alpha), \quad (3.28)$$

where  $\Delta n$  is the difference between the extraordinary and ordinary indices of refraction (*i.e.*  $\Delta n = n_e - n_o$ ). The wave vectors, seen in Figure 3-4, of the system need to follow the momentum matching criteria from Equation 3.19. Separating the wave vectors into their directional

components with respect to the propagation angle,  $\alpha$ , the tangential and perpendicular directions respectively are

$$k_i \cos \theta_i = k_d \cos \theta_d, \quad (3.29)$$

$$k_i \sin \theta_i - \kappa = k_d \sin \theta_d. \quad (3.30)$$

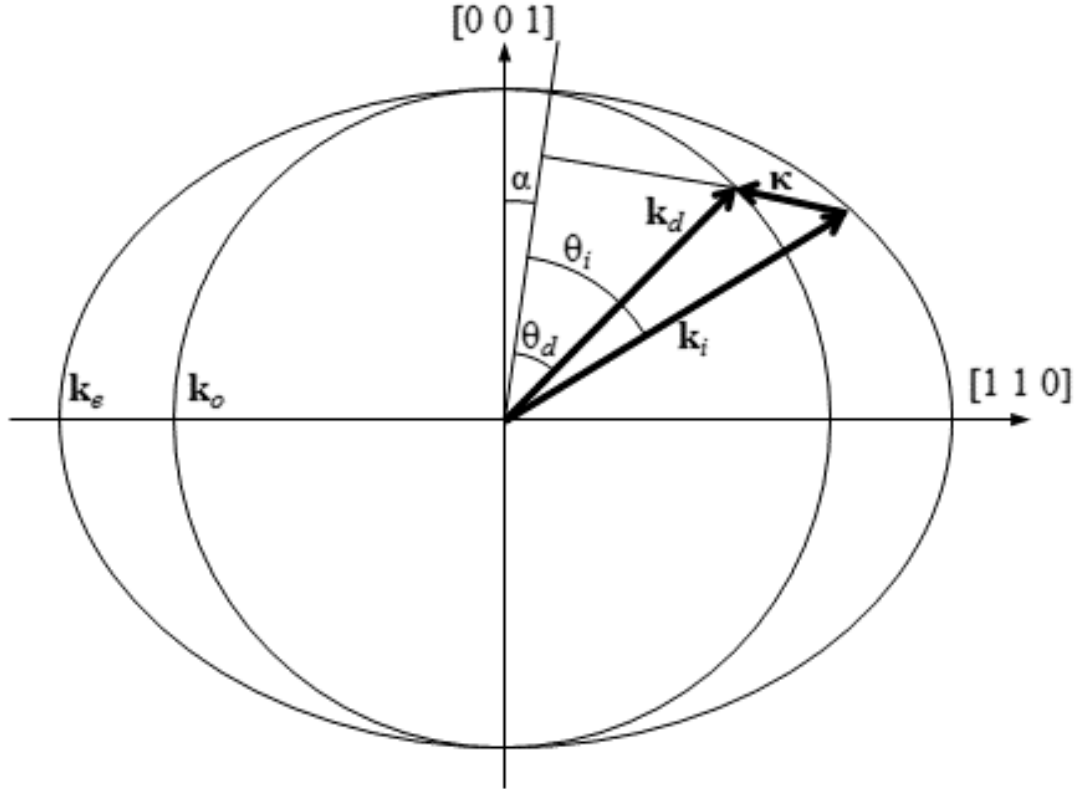


**Figure 3-4:** The wave vectors generated by the AOTF experiment set up in Figure 3-2. From the above figure  $k_e$  and  $k_o$  are the wave vectors of the extraordinary and ordinary axis of the AOTF crystal. Originally published as Figure 1 in Elash *et al.* (2016).

The tangential and perpendicular directions of the wave vector can be used in combination with the wave vectors definitions (Equations 3.20-3.22, and 3.29-3.30) to yield

$$\lambda = \frac{v}{F} \left[ n_i \sin \theta_i - (n_o^2 - n_i^2 \cos^2 \theta_i)^{\frac{1}{2}} \right]. \quad (3.31)$$

The above can be approximated as

$$\lambda = \frac{\Delta n v}{F} \frac{\sin^2(\theta_i + \alpha)}{\sin \theta_i} \quad (3.32)$$

assuming difference in indices of refraction is small (Equation 3.28) (*Voloshinov and Mosquera, 2006*). This equation has several implications to the operation of the device that affect the design possibilities in an imaging system. First, the wavelength diffracted by the AOTF is inversely related to frequency of the RF wave. Second, the wavelength of the diffracted signal is dependent on the angle of incidence of the incoming wave. Therefore, passing a signal through the AOTF at different incident angles results in different outgoing, or diffracted, wavelengths. Also, through the described interaction, the diffracted light goes through a 90° rotation in polarization (*Voloshinov, 1996*). Finally, it is important to note that the indices of refraction are sensitive to temperature changes which can alter the tuning curve calibrations, generally corresponding to a 1 nm change per 10 °C for TeO<sub>2</sub>. This theory of AOTF operation provides the foundation to utilize the device in a spectral imaging system for limb scatter measurements of stratospheric aerosol.

### **3.3 Optical Chain Development**

The ALI design goal for the stratospheric balloon prototype presented in this work is a simple optical system with commercial off-the-shelf components that is capable of imaging the stratospheric limb a single wavelength at a time through the use of an AOTF. However, the AOTF operation requires important instrument design considerations to optimize its operation and performance (*Suhre et al., 2004*). First, a brief overview of AOTF operational states is discussed. Then an introduction to the two optical design layouts considered for ALI is presented followed by an overview of the finalized ALI optical design. The final design as built is capable of imaging the stratospheric limb with a spatial resolution of 200 m for both vertical and cross-track dimensions over the wavelength range of 650-950 nm. This range is slightly smaller than the original specifications and is a consequence of the usable range of the chosen detector due to

quantum efficiency limitations. Code V optical design software was used to assist in the designing and analyzing the performance of both of the optical designs and final optical system.

### **3.3.1 AOTF Operation**

This section describes the two fundamental states of the AOTF used throughout the rest of this work but first is the general operation of the device itself. The general operation of the AOTF is shown in Figure 3-5a. An RF wave is applied and there is one input, the unpolarized broadband incident ray, and four output signals. The birefringence of the crystal splits the zeroth order ordinary and extraordinary polarizations into two separate outputs. The RF wave interacts with the incoming radiance to form the first order extraordinary and ordinary diffracted beams with polarizations rotated by 90°. Further, only the first order extraordinary polarization remains at a consistent angle as the RF is scanned due to the compensation mentioned in section 3.2.3.

In practice, the first order extraordinary beam is imaged and the removal of the unwanted beams is desired to achieve high quality low contamination images. As such, a linear polarizer is always placed in front of the AOTF to remove the ordinary polarization and a linear polarizer is placed behind the AOTF to remove the zeroth order extraordinary polarization. When an RF wave is applied to the crystal with the polarizers, as seen in Figure 3-5b, the AOTF is considered to be in the on or “AOTF-on” state with only the first order extraordinary wave passing through the system. When an RF wave is not applied to the crystal and the polarizers are present, as seen in Figure 3-5c, the AOTF is considered to be in the off or “AOTF-off” state with no outputs from the system. These two states, “AOTF-on” and “AOTF-off” are used throughout the remainder of this work to describe these two operational modes of the system.

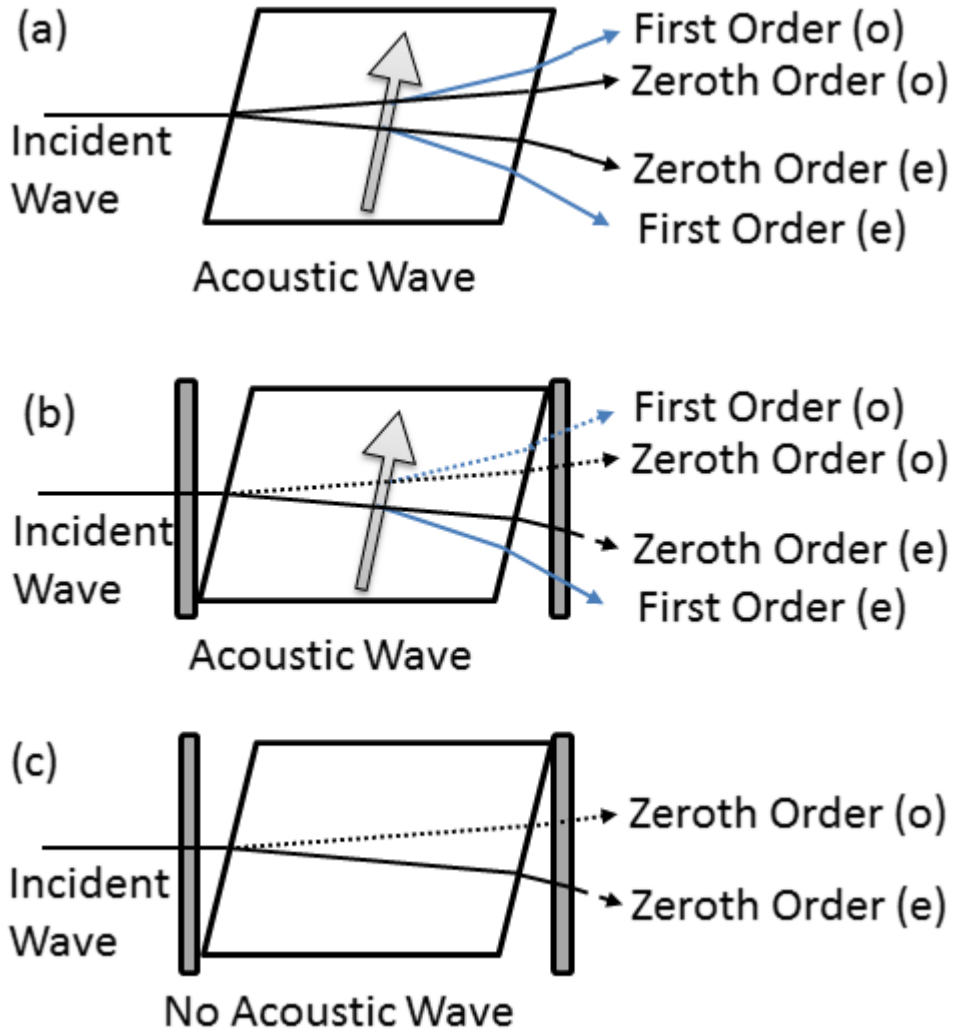


**Figure 3-5:** (a) An AOTF undergoing Bragg diffraction with an unpolarized input incident wave with a RF wave applied represented by the arrow. After the diffraction event four output signals are formed: the zeroth order and first order ordinary (o) and extraordinary (e) signals. However the only optical path that remains at a constant angle no matter the applied RF wavelength is the first order extraordinary diffracted signal. (b) Two linear polarizers are added to the system, the first linear polarizer removes the ordinary polarization from the outputs with the dotted lines and the second linear polarizer removes undiffracted extraordinary light shown by the dashed line. This configuration is the “AOTF-on” state. (c) The system in (b) without a RF wave so no Bragg diffraction is occurring. Once again the first linear polarizer removes the ordinary polarization represented by the dotted line and the second linear polarizer removes the extraordinary light shown by the dashed line. This configuration is the “AOTF-off” state. Originally published as Figure 2 in Elash *et al.* (2016).

An AOTF for the ALI prototype was acquired from Brimrose of America (model number TEAFI10-0.6-1.0-MSD) with a DC-powered Gooch and Housego RF driver (model number

64020-200-2ADMDFS-A). This particular AOTF has a large 10 mm by 10 mm aperture and is an imaging quality crystal. It is tuned for a spectral range of 600 nm to 1200 nm, which corresponds to an RF range of 156 to 75 MHz. The spectral resolution is approximately 1.6 nm at 633 nm and broadens to about 6.3 nm at 1153 nm with an approximate diffraction efficiency of 60% across the spectral range. The AOTF is made from a tellurium dioxide ( $\text{TeO}_2$ ) birefringent crystal. The extraordinary light is diffracted at  $2.7^\circ$  from the optical axis of the device with a minimum separation angle of  $6.4^\circ$  between the zeroth and first order. The acceptance angle is  $2^\circ$  from the normal, which defines the angular spread of the incident beam for which the AOTF provides diffraction within the rated efficiency limit (Xu and Shroud, 1992). A detailed overview of the AOTF specifications can be found in appendix A.1.3.

### 3.3.2 Telecentric System Prototype

The first optical system considered for ALI is a telecentric system, which is known as a system that images without perspective. Before the telecentric design is discussed a basic explanation of a telecentric system is provided.

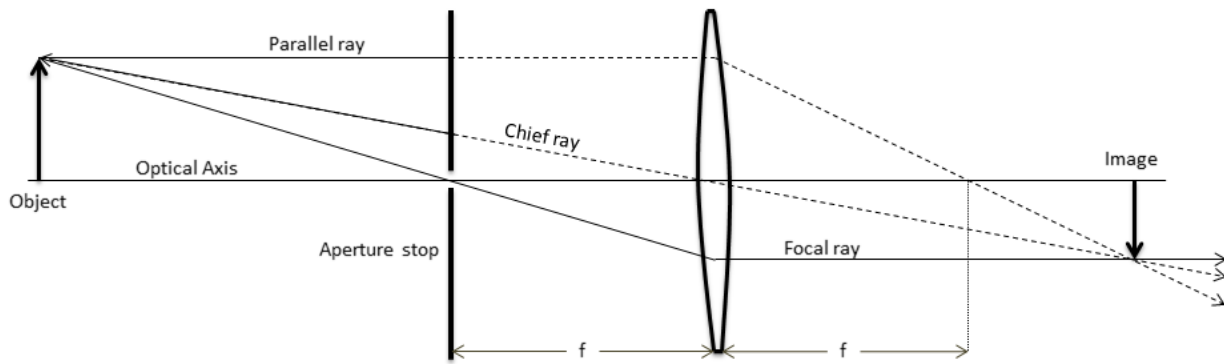


**Figure 3-6:** A standard paraxial ray tracing diagram. The aperture is located to make the system telecentric in the image plane and  $f$  is the focal length of the lens.

To describe the concept behind the telecentric system, a basic ray tracing image is shown in Figure 3-6 where three paraxial rays are drawn using a simple biconvex lens. To make this simple

biconvex system telecentric in image space, an aperture is added to the system on the object side at the focal point of the lens. The theoretical idea is to have an aperture so small that only the focal ray can pass through it. All of the other rays, including the chief and parallel ray, are blocked from entering the system. Now the image is only defined by a single ray and it is in focus everywhere on the image side of the system, and therefore the system has infinite depth of field. However, an aperture that is so small proposes a few problems in practice. First, such a small size would cause diffraction effects that would dominate the imaging qualities of the system. Second, such a small aperture would let so little signal through that very long exposure times would be needed to meet the required Signal to Noise Ratio (SNR). So in practice a larger aperture is used at the focal point. Now the system no longer has an infinite depth of field, but still retains a large depth of field and the image remains almost the same size no matter where the image plane is located. It should be noted that a telecentric system in object space can be created by putting the aperture on the image side of the lens causing the object to always be the same size in the image no matter where it is physically located.

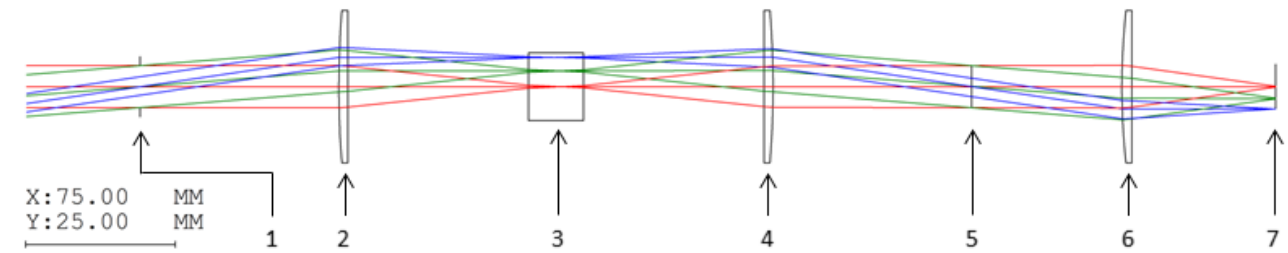


**Figure 3-7:** Ray Tracing diagram simulation of the telecentric lens system preformed using Code V. The elements in the system are the following: (1) Optical Stop and telecentric aperture. (2) 100 mm focal length plano-convex lens. (3) Brimrose AOTF. (4) 100 mm focal length plano-convex lens. (5) Telecentric Aperture. (6) 75.6 mm focal length plano-convex lens. (7) Imaging plane. It should be noted that the x and y scales are not the same in this image. Also, in the lab a polarizer is added in front and behind the AOTF as well as prisms after the AOTF.

A telecentric layout in both image and object space has advantages and disadvantages for the imaging quality of the AOTF system. An advantage is since the wavelength filtered by the AOTF

is dependent on the incident angle (Equation 3.32), and as shown in the ray tracing diagram (Figure 3-7), all lines of sight enter with approximately the same angular spread, so the filtered image has constant wavelength and spectral point spread function across the image plane. However, two problems result with this system. First, the focus of the final image depends on wavelength, which is discussed below in greater detail. As well, this method is sensitive to any surface defects of the crystal since the light enters the crystal in focused bundles.

A test optical system was designed with telecentric Front End Optics (FEO) in both object and image space and with Back End Optics (BEO) designed to resize the image to fit on a CCD detector. A list of the specifications can be seen in Table 3-1 and a ray tracing diagram from a Code V simulation is shown in Figure 3-7. Here the AOTF optical aperture of 10 mm by 10 mm is the field stop of the system. This is obviously a physical limit of the device and causes the Field Of View (FOV) to be limited in this design. In order to image the vertical limb from the ground to float altitude of a stratospheric balloon, typically 35 km, a  $6^\circ$  FOV is required. Also, using standard 100 mm focal length lenses, the rays of light from each line of sight enter the AOTF at the maximum acceptance angle, which is  $2^\circ$ . This allows the maximum amount of light to enter the device to achieve highest possible throughput.

**Table 3-1:** Telecentric Test System Optical specifications

Parameter	Value
Effective focal length (mm)	75.6
Front End Optics Magnification	1.00
Back End Optics Magnification	0.756
Field Of View ( $^\circ$ )	5.7 x 5.7
F-number	14.28

The image is focused on a 16-bit digital QSI 616 CCD with 1536x1024 pixels and a mechanical shutter that allows an integration time between 0.01 seconds to 240 minutes. The CCD chip itself

is a Kodak KAF-1603ME with micro lenses to improve the quantum efficiency of the device and its spectral characteristics can be seen by the blue curve in Figure 3-8.

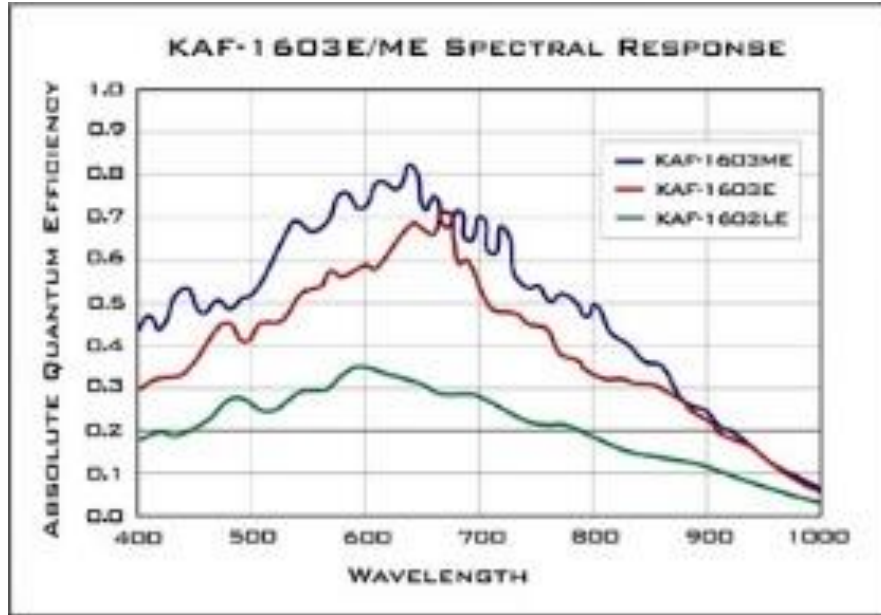


**Figure 3-8:** Quantum efficiency of the Kodak KAF-1603ME contained within the QSI CCD camera is represented by blue curve. Quantum efficiency provided by QSI Scientific. (<http://www.qsimaging.com/616-overview.html>)

The overall design has several aspects that make it a good system for imaging. First, all of the bundles of light entering the AOTF have the same angular spread. As seen in Equation 3.32, the diffracted wavelength depends on the incoming angle. With the telecentric layout all points of the imaging plane have the same angular dependence so the entire image is of the same wavelength and have the similar spectral PSF.

However, despite its benefits, there are a few drawbacks to consider in the design as well. First, the optical path between the two 100 mm focal length lens is 200 mm in air for the prototype, however the AOTF is made of tellurium dioxide ( $\text{TeO}_2$ ) or paratellurite and has a high index of refraction and dispersion given by (*Uchida, 1971*)

$$n_o^2 = 1 + \frac{2.584\lambda^2}{\lambda^2 - 0.1342^2} + \frac{1.157\lambda^2}{\lambda^2 - 0.2638^2}, \quad (3.33)$$

$$n_e^2 = 1 + \frac{2.823\lambda^2}{\lambda^2 - 0.1342^2} + \frac{1.542\lambda^2}{\lambda^2 - 0.2631^2}, \quad (3.34)$$

for the ordinary and extraordinary polarizations respectively. The high dispersive property, or Abbe number results in a change in the distance in the optical path,  $d$ , given by

$$d = \frac{n(\lambda) - 1}{n(\lambda)} t, \quad (3.35)$$

where  $n(\lambda)$  is the index of refraction with a wavelength dependence and  $t$  is the thickness of the crystal. The AOTF crystal causes the optical path in air to be lengthened by  $d$ , as can be seen in Figure 3-9. In order to compensate, the length  $d$  must be added to the path to account for the discrepancy, however the adjustment can only be compensated for a specific wavelength and thus a defocusing of the image plane occurs for other wavelengths.

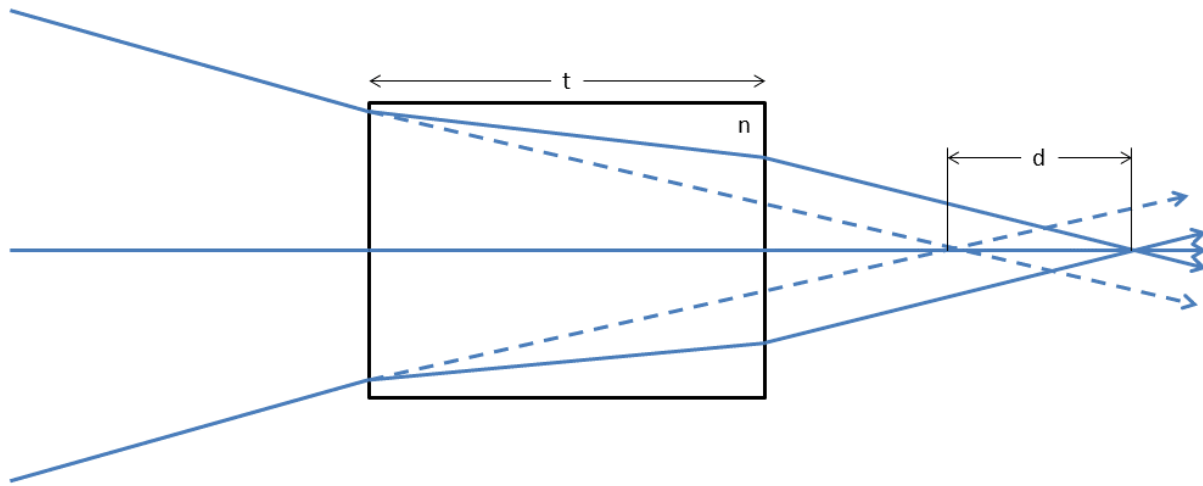


**Figure 3-9:** The effect on the optical path of converging light bundles as they pass through a material of index of refraction  $n(\lambda)$ . When the index of refraction strongly depends on wavelength, as in the AOTF, the optical path length can experience great changes that alters the focal point of the system.

The severity of this problem can be seen in Figure 3-10 from a Code V simulation of the spot size of the optical system which was optimally focused for 800 nm. In this simulation, a grid of rays was passed through the system for each FOV and using ray tracing the final location for each

FOV on the image plane were determined. The black circles represent the Airy disks, which are the minimum possible spot size possible due to diffraction for each wavelength of light. The spot sizes at 800 nm are on the order of 24  $\mu\text{m}$  at the center, which is diffraction limited, and 94  $\mu\text{m}$  at the edge of the FOV. However, for the same optical layout the 600 nm spot sizes are all greater than 160  $\mu\text{m}$  which causes a noticeable blurring in the recorded image. For a system using a telecentric system, this defocusing of the image plane would require additional compensating optics to correct the change in the path length or the detector of the system would need to be actively moved as wavelength is scanned. However, the f-number could be increased to increase the system's depth of field to reduce the defocusing effect caused by the AOTF, but the same effect causes a reduction in signal throughout leading to longer exposure times.

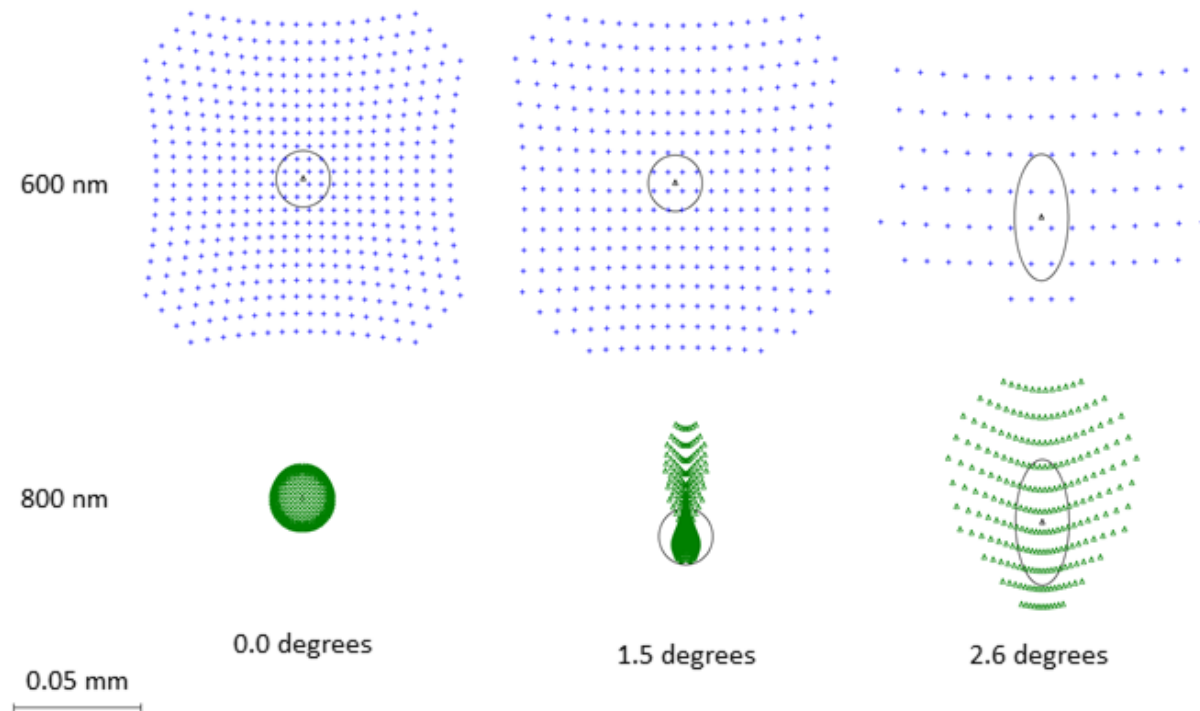


**Figure 3-10:** Code V simulation of the spot size for the telecentric system at focus at 800 nm. The spots are shown for 0.0, 1.5 and 2.6 degree fields of view at 600 nm (blue) and 800 nm (green). The full spot sizes for the 600 nm spots are 0.16, 0.22, and 0.25 mm for 0.0, 1.5, and 2.6 degrees fields respectively, with the corresponding 800 nm spot sizes being 0.024, 0.053, 0.094 mm. The black circles represent the Airy disk for each specific wavelength and FOV.

The telecentric system was breadboarded in the lab and used to image EIA 1956 standard resolution chart and the results of the test can be seen in Figure 3-11. The experimental set up was similar to the system in Figure 3-7 except for two fundamental differences. The Code V software can perform analysis for only one polarization and neglects the bend in the optical axis caused by the AOTF. However, these two issues can be dealt with sufficiently in the lab. The unwanted polarization was removed by adding a polarizer before and after the AOTF (Figure 3-5b and Figure 3-5c). The light that is actively diffracted through the AOTF is the light that enters the AOTF crystal with extraordinary polarization. The polarizer before the device stops the ordinary polarization from entering the AOTF and the second polarizer, orientated 90° to the first, on the posterior of the AOTF is used to only let the diffracted extraordinary light through and removes the non-diffracted extraordinary polarization light. As mentioned in section 3.2.4, the polarization of the diffraction beam is rotated by 90° (*Voloshinov, 1996*). The second issue to be handled is that the AOTF bends the optical path by 2.7°. Two prisms were added after the AOTF to straighten out the optical path; the optical path past the prisms is parallel to the original optical path and is offset by approximately a millimeter which then obscures a small part of the FOV. The resolution chart was positioned so that the loss of the FOV due to the prism compensation was accounted for by a shift in the vertical location of the resolution chart.

The two images were taken, an “AOTF-off” and “AOTF-on” image, every 25 nm at wavelengths between 600 and 1000 nm using 30 second exposures imaged on the QSI CCD camera. The “AOTF-off” image was subtracted from the “AOTF-on” image to approximately remove the detector dark current, DC offset, and stray light. Three sample images can be seen in Figure 3-11 with the optics focused at 800 nm. The image blurring that was simulated in the spot size diagram can be easily noticed in the 650 nm wavelength image. At this wavelength the center

lines of the resolution chart cannot be resolved from each other. A unique line can be resolved every 2 pixels in the center of the 750 nm image which corresponds to 150 m resolution at the tangent point from the balloon platform, and a 4-5 pixel resolution near the edge corresponding to about a 200 m resolution. Also due to the efficiencies of the CCD and decreased reflectivity of the chart at the longer wavelengths of light, the SNR of the 850 nm image in the bottom right panel is rather low; this can be observed in the grainy quality of the image.

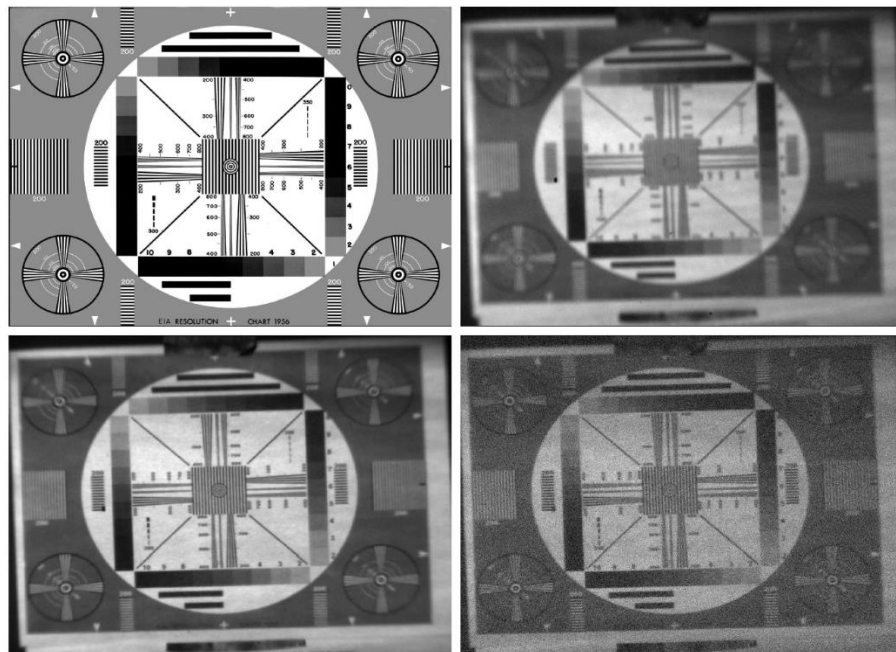


**Figure 3-11:** The top left is the original test image used for the telecentric experiment. The top right, bottom left, and bottom right are the images recorded through the telecentric system at 650, 750, and 850 nm. The system is focused at 800 nm.

### 3.3.3 Telescopic System Prototype

The second optical system layout considered for the ALI prototype is a telescopic optical system configuration consisting of a standard telescope for the FEO with a focusing lens for the BEO. The front lens, known as the objective lens, is used to focus an object at infinity to the focal point of the lens, then a second lens, the eyepiece is used to increase the optical power of the system, that is to increase the angular size of the image with respect to the angular size of the object. The

eyepiece lens is located at a combined distance of the focal lengths of both the objective and eyepiece and causes the image to be focused at infinity. However for our system the telescope is used to focus the light in order to enter the AOTF at an angle less than its acceptance angle as well as to reject light rays outside of the desired FOV. The light from each line of sight in the telescopic system enters the AOTF collimated and is focused though the BEO onto the QSI 616 CCD discussed in section 3.3.2. A detailed simulation Code V layout and ray tracing of the optical design can be seen in Figure 3-12.

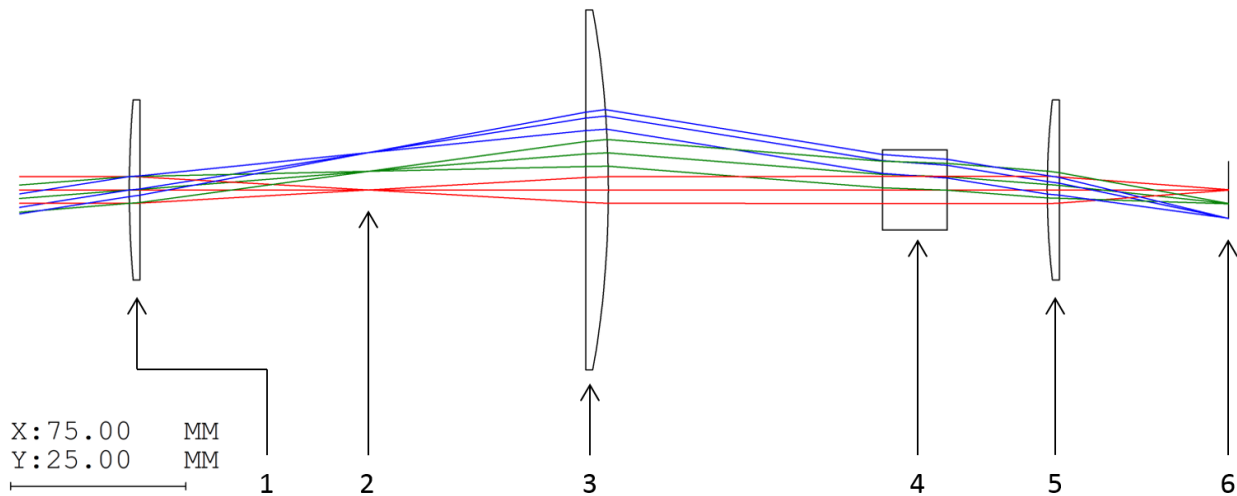


**Figure 3-12:** Ray Tracing diagram of the telescopic lens system simulated by Code V. The elements in the system are the following: (1) 100 mm focal length plano-convex lens. (2) Location where field stop is located to limit stray light (3) 100 mm focal length plano-convex lens. (4) Brimrose AOTF. (5) 75.6 mm focal length plano-convex lens. (6) Imaging plane. It should be noted that the x and y scales are not the same as Figure 3-7. Also, in the lab a polarizer is added in front and behind the AOTF as well as prisms behind the AOTF.

The telescopic prototype was designed with as many similar components and specifications as possible to the telecentric prototype in order to allow accurate comparisons of the systems without major optical effects and aberrations caused by using different materials, sizes, and focal length lenses. The optical specifications of this system are given in Table 3-2. However, there are a few fundamental differences. First, the aperture stop is located at the front lens which limits the rays

of light that can enter the system, unlike the telecentric design that has a front aperture stop at the focal length of the first lens.

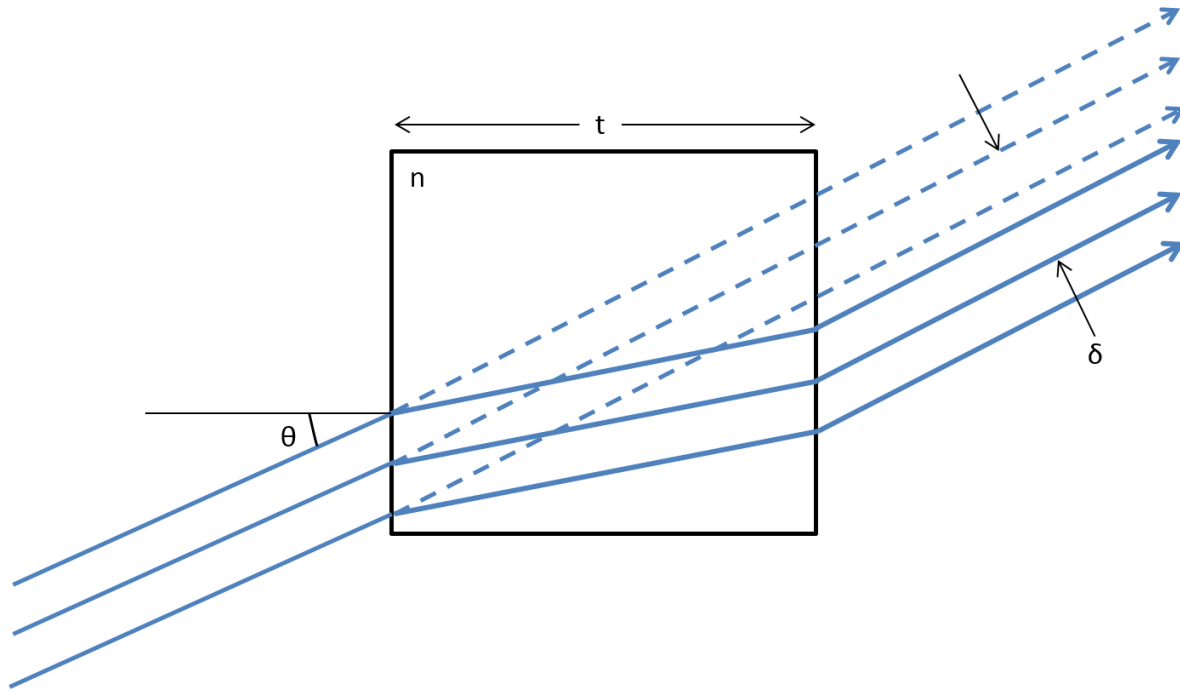


**Figure 3-13:** Vertical displacement of a collimated bundle of light cause by a material of index of refraction  $n(\lambda)$ .

**Table 3-2:** Telescopic Prototype System Optical Parameters.

Parameter	Value
Effective focal length (mm)	75.6
Front End Optics Magnification	1.00
Back End Optics Magnification	0.756
Field Of View (°)	6.0 x 6.0
F-number	20

The second fundamental change to the optical system is that the AOTF now has collimated light passing through the device, unlike the telecentric system, and this has impacts that both improve and degrade the imaging quality of the system. First, the primary light passing through the AOTF from a single line of sight enters the AOTF at the same angle, so the image has a smaller spectral PSF than the telecentric counterpart; however, each line of sight is diffracted with a different

fundamental wavelength due to the angular dependence in the AOTF Bragg diffraction wavelength determination (Equation 3.32). Thus the final image has a smaller spectral bandpass but there is a wavelength gradient radiating out from the center of the image. Second, since the light passes through the AOTF collimated, the focal point of the image no longer changes with wavelength. Instead, a lateral displacement of each line of sight occurs based on the angle of incidence and the diffracted wavelength which causes a slight magnification of the image. The lateral displacement that occurs is given by the following relation (*Fischer et al.*, 2008)

$$\delta = n(\lambda) - 1 \frac{t\theta}{n(\lambda)} \quad (3.36)$$

where  $\delta$  is the displacement from the original path and  $t$  is the thickness of the material; causing a slight magnification change based on the wavelength of the light being diffracted and  $\theta$  is the incident angle on the crystal. However, this wavelength dependent change is at worst 50 micrometers for the test configuration. The effect can be seen in Figure 3-13. The last change to the system is the focusing power it possesses, as can be seen in the spot diagrams in Figure 3-14. The change in spot size due to wavelength is primarily due to the chromatic aberrations of the optical lenses. If it is desired to remove the chromatic aberration one option is to replace the lenses with mirrors in the flight version, the second option is to use achromatic doublets. The system is diffraction limited for 600 nm for all lines of sight and for 800 nm at 3.0 degrees. Also the difference in location of the spot sizes is caused by the magnification effect discussed above.

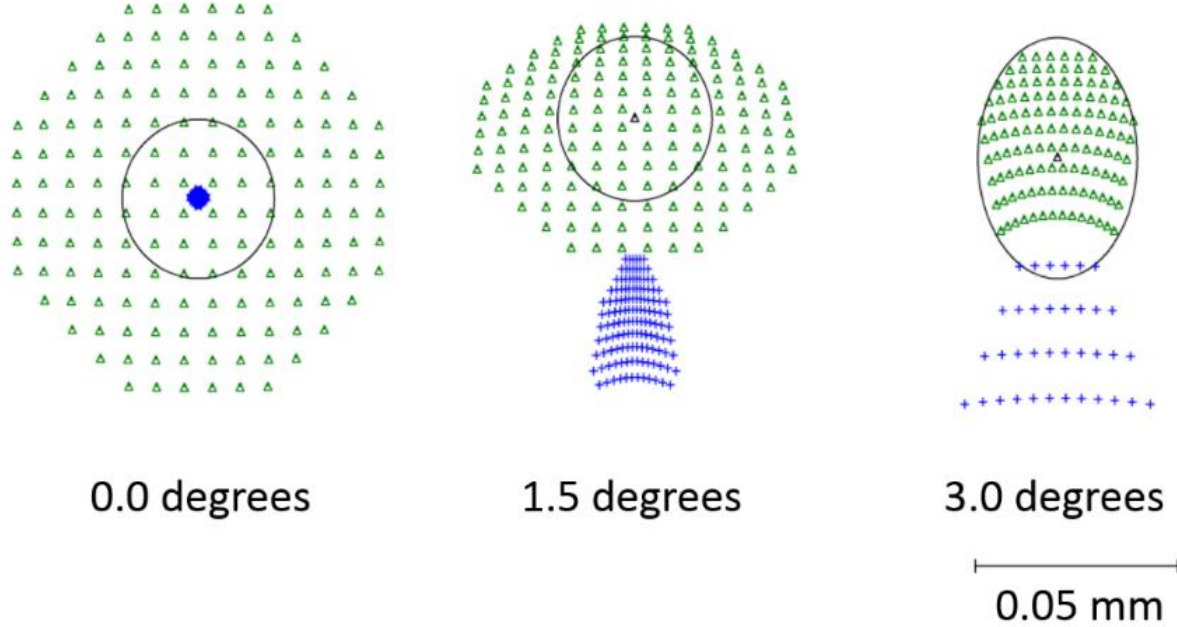


**Figure 3-14:** Code V simulation of the spot size for the telescopic system. The spots are shown for 0.0, 1.5 and 3.0° fields of view at 600 nm (blue) and 800 nm (green). The full spot sizes for the 600 nm spots are 0.004, 0.045, and 0.122 mm for 0.0, 1.5, and 3.0° fields respectively, with the corresponding 800 nm spot sizes being 0.096, 0.081, 0.047 mm. The black circles represent the Airy disk for 600 nm wavelength and each FOV.

An experimental resolution test was assembled with the telescopic system with two polarizers and prisms added to the optical chain in the similar fashion to the section 3.3.2 experimental set up. The QSI CCD was also used with the same 30 second integration time. The results of this test can be seen in Figure 3-15. Once again the image at 750 nm is the sharpest of the three but the center lines of the EIA 1956 test chart are distinguishable at all of the wavelengths. The blurring of the 650 nm image is caused by the chromatic aberrations of the lens and the prisms. Furthermore the prisms are removed in the final design reducing the aberrations. Also, the magnification issue discussed above is relatively insignificant in the test images and the small changes can be accounted for in the calibration of the final instrument. Lastly, the detector efficiency and the resolution target's poor reflectivity in the NIR causes the 850 nm image to also have a low SNR.

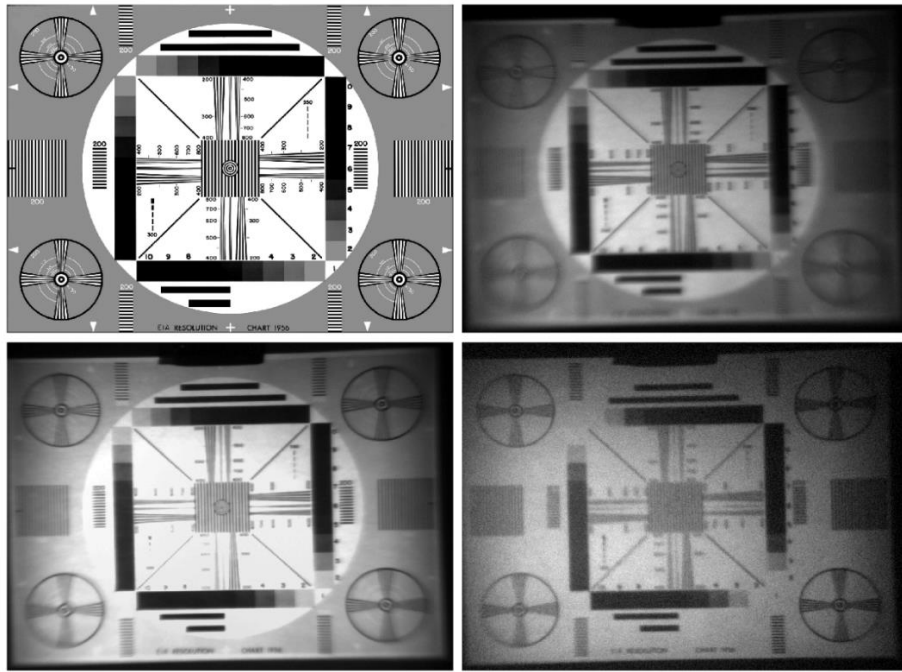


**Figure 3-15:** The top left is the original test image used for the telescopic experiment. The top right, bottom left, and bottom right are the images recorded through the telescopic system at 650, 750, and 850 nm. The system is focused at 800 nm.

### 3.3.4 ALI Optical Design

In light of the requirements for imaging aerosol, we have chosen a telescopic design for the ALI prototype. Since the wavelength gradient across the image is small compared to the slowly varying aerosol scattering cross section, the fixed image plane is preferable for the improvement it provides in spatial imaging, particularly as we desired to use as simple as possible an optical design.

We used a very simple three lens optical layout with commercial off-the-shelf components. Two lenses before the AOTF form a simple telescope for the Front End Optics (FEO), and a single focusing lens behind the AOTF comprises the Back End Optics (BEO). The AOTF is oriented such that the detected image is formed from the diffracted beam of the vertically polarized, *i.e.* extraordinary, light (defined at the entrance aperture). A linear polarizer (ThorLabs model number LPVIS100, see Appendix A.1.2) with an extinction ratio greater than  $10^5$  is placed at the back of

the FEO to remove the incoming horizontal, or ordinary, polarized beam. The diffracted extraordinary beam undergoes a  $90^\circ$  rotation in polarization so a second linear polarizer, oriented at  $90^\circ$  to the first, is used after the AOTF but before the BEO to remove the undiffracted beam. This is shown schematically in Figure 3-5b. Note that even with the high extinction ratio of the polarizers, a not insignificant fraction of light that is intended to be blocked passes through the system. The diffracted extraordinary signal comprises at most a  $\sim 10$  nm bandpass fraction of one polarization such that the unabsorbed broadband signal from the polarizers can be on the same order of intensity as the diffracted signal. This unabsorbed signal, if not mitigated, can significantly reduce the instruments sensitivity to the desired signal.

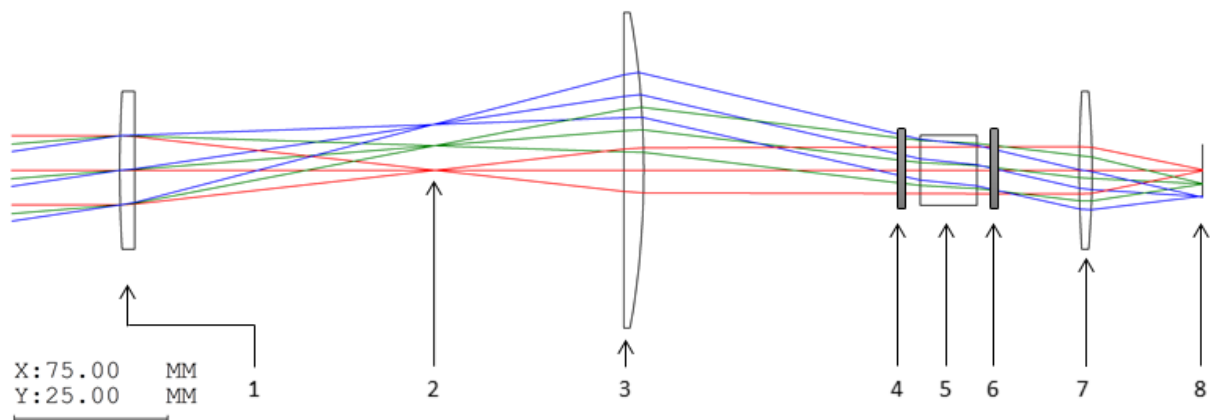


**Figure 3-16:** Final optical design for ALI with a Code V ray tracing diagram. The elements in the system are: (1) 150 mm focal length plano-convex lens. (2) Field stop. (3) 100 mm focal length plano-convex lens. (4) Vertical (extraordinary) linear polarizer. (5) Brimrose AOTF. (6) Horizontal (ordinary) linear polarizer. (7) 50.4 mm focal length bi-convex lens. (8) Imaging plane. Originally published as Figure 4 in Elash *et al.* (2016).

The extraordinary diffracted light is  $2.7^\circ$  from the optical axis and to compensate, the entire optical chain after the AOTF is mechanically aligned with this direction. The BEO forms the image of the signal on a QSI 616s 16 bit CCD with 1536 by 1024 pixels. A ray tracing diagram for the ALI optical system was created using the Code V optical design software and can be seen in Figure 3-16. No corrections were attempted to reduce chromatic or spherical aberrations within

the system and the system does exhibit some coma due to a large FOV and the curvature of the lenses near the edge of the FOV. Analysis with Code V shows that the distortion due to these effects across the center two degrees of the FOV is a change of less than 1% across the entire wavelength range. The final one degree shows a distortion of less than 4%. Finally the lateral displacement in the telescopic test configuration has been reduced in the final design to be on the order of a micrometer and is considered negligible.

An analysis was also performed to determine the minimum resolution required to achieve a Modular Transfer Function (MTF) of 0.3 across the entire FOV for all wavelengths (*Smith, 2000*). The MTF is an optical measure of the system's ability to resolve line pairs per millimeter where a line pair is a white line followed by a black line. Generally, increasing line pairs per millimeter leads to a circumstance where the system can no longer resolve the lines. The MTF can be found computationally through (*Fischer et al., 2008*)

$$MTF(f) = \frac{I(f)_{max} - I(f)_{min}}{I(f)_{max} + I(f)_{min}}, \quad (3.37)$$

where the MTF is dependent on the frequency,  $f$ , of the line pairs,  $I(f)_{max}$  is the maximum intensity of the measured pair, and  $I(f)_{min}$  is the minimum. The MTF can vary differently with respect to tangential and radial directions of the optic system. To obtain a minimum MTF of 0.3 across the entire field, except for the  $3^\circ$  tangential or perpendicular FOV, a seven pixel running average is required, corresponding to a MTF frequency of 15.5 line pairs per millimeter. The  $3^\circ$  tangential field being below the detection threshold of 0.3 is not a large concern since the SNR is low at the edges of the FOV and primality results in a loss of cross-track resolution at the ground and float altitude tangent points which are not critical for analysis. Furthermore, when the FOV is  $2.7^\circ$  from the normal the tangential component is above the 0.3 MTF threshold. The MTF analysis

of ALI can be seen in Figure 3-17. Overall, this corresponds to an average vertical and horizontal resolution of 210 m across the entire ALI FOV at the tangent point.

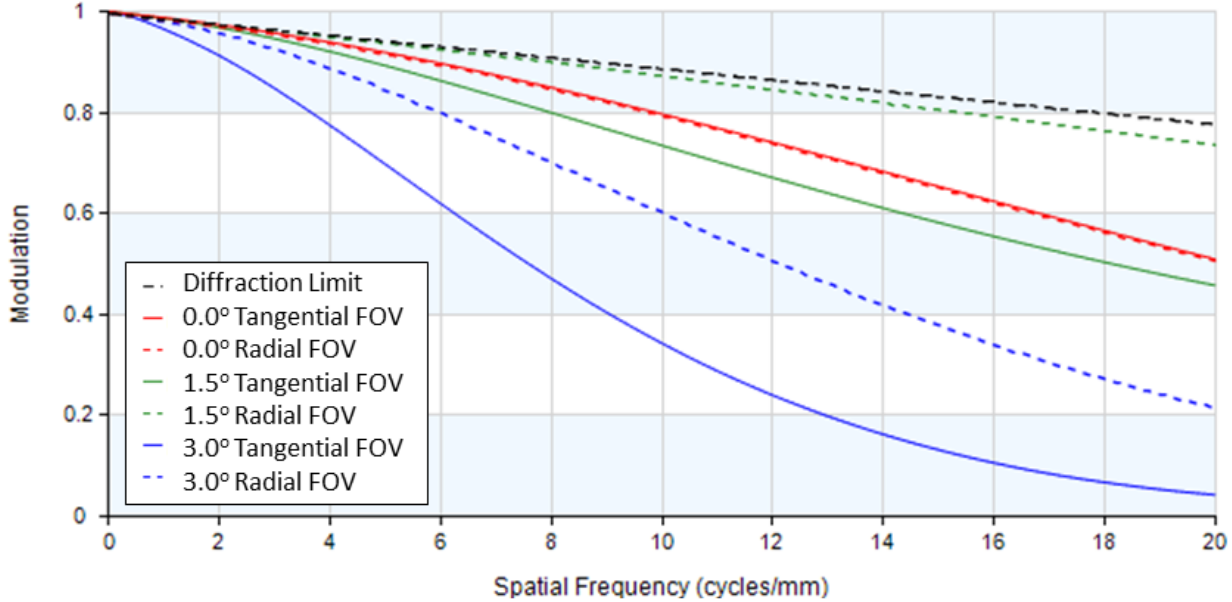


**Figure 3-17:** MTF analysis performed by Code V for the final ALI design used in the balloon campaign. The 7 pixel running average corresponds to a spatial frequency of 15.5 cycles/mm.

**Table 3-3: Final ALI optical specifications**

Parameter	Value
Effective focal length (mm)	74.3
Front end magnification	0.67
Back end magnification	1.27
Entrance Pupil (mm)	9.91
Field of view (°)	6.0 x 5.0
F-number	7.5
Image size (mm)	9 x 7.5
Image size (pixels)	1000 x 800
Resolved image size (averaged pixels)	143 x 114
Spectral range (nm)	650-950

A tolerance study was also performed with Code V to assess the capability of the system within the tolerances of the mounting equipment. Through a Monte Carlo method, the Code V analysis

perturbs the placement and shape of the optical components within the system and computes the change in the MTF on the image plane. This analysis determines what optical misalignments or defects will degrade the performance of the system. It was found that the ALI design was relatively insensitive to the tolerances of commercial off-the-shelf component used.

An experiment to determine the exposure times and entrance pupil of ALI is discussed in detail in the calibration section of Chapter 4, but for design purposes it is important to note here that the ALI entrance pupil was selected at 9.91 mm to yield estimated flight exposure times on the order of one second. Furthermore, a demagnification in the FEO and a magnification in the BEO was added to further increase the light throughput to help reduce the exposure times. A summary of the optical specification for the ALI prototype is given in Table 3-3. It is also important to note that a detector could not be acquired with sufficient capability to capture the entire desired range 600-1200 nm due to basic limitations of silicon technology. This required a reduction in the desired spectral range to 650-950 nm. Although high quality aerosol extinction measurements can still be made with this spectral range as evidenced by the OSIRIS data product heritage this limitation means that the ALI prototype does not have the desired sensitivity to particle size distribution. However, even with this spectral range some particle size information can still be retrieved as evidenced in Chapter 5.

It should be noted that our choice of a telescopic optical layout for ALI is actually the opposite choice of that made for the ALTIUS design, which uses a telecentric optical layout. For that instrument, the need for spectral resolution for trace gas retrieval makes the decision to use telecentric optics quite clear (*Dekemper et al.*, 2012, *Fussen et al.*, 2016). Even given that basic design difference, the overall optical specifications are quite similar between the ALI and ALITUS prototype instruments (again see Table 3-3 for ALI specifications), although two key differences

are noted. First, by using a telescopic layout the maximum FOV for ALI is determined by choosing lenses to ensure light enters ALI within the acceptance angle of the AOTF. This allows for a larger possible FOV than with a telecentric system where the field view is defined by the aperture of the AOTF. Second, the f-number for ALTIUS is 14.32 compared to 7.5 for ALI, which allows ALI to increase light throughput at the cost of slightly higher aberrations in the final image. *Dekemper et al.* (2012) reports that the visible channel of ALTIUS was breadboarded and tested by taking ground based measurements of a smoke stack plume. They used the measurements to retrieve NO<sub>2</sub> slant column density using 10 second exposure times; although, they note that an increase in measurement frequency would improve the instrument capabilities. This also factored into our decision to use telescopic optics to increase throughput for ALI.

A final selection for the optical design of ALI was presented in this section as well the justifications used to determine the result. For ALI, the telescopic system was deemed to be the better option for the purpose of dedicated measurements of aerosol extinction.

### **3.3.5 Correction to the Optical Design**

It should be noted a correction to the optical design is required that was discovered during the analysis of the data after the instrument campaign. The 3° half-angle FOV signal enters the AOTF at an angle of 2.2° from the normal and the acceptance angle of the AOTF is 2.0°. This results in a great loss of diffraction efficiency for approximately the last half degree of the FOV. This error was created when decreasing the f-number of the system to 7.5 to reduce the exposure times, remembering that lower f-numbers have higher light throughput, by adding a FEO magnification. However, this increase in throughput is overcompensated by the loss in diffraction efficiency of the AOTF in the last half degree of the FOV overall resulting in a lower SNR. To rectify this problem a slight change to the optical system is suggested in this section while still using commercial off-the-shelf components.

The main issue is in regard to the front end magnification and the suggested solution revolves around keeping a similar optical layout with a smaller demagnification in the FEO, and a compensating demagnification with the BEO to maintain the same final image size. This is performed by replacing the first lens or objective lens of the telescope (element 1 in Figure 3-16) by a 125 mm focal length plano-convex lens and compensating the optics such that the distance between the first two lenses is the sum of the two focal lengths of the telescope. The back end lens is also replaced with a 62.9 mm bi-convex lens. This results in the 3° half-angle FOV entering the AOTF at 1.6° well within the acceptance angle of the AOTF. A table of the revised specifications can be found in Table 3-4.

**Table 3-4:** Revised ALI optical specifications

Parameter	Value
Effective focal length (mm)	78.9
Front end magnification	0.80
Back end magnification	0.98
Entrance Pupil (mm)	9.91
Field of view (°)	6.0 x 5.0
F-number	8.0
Image size (mm)	8.5 x 7.1
Image size (pixels)	945 x 789
Resolved image size (averaged pixels)	135 x 114
Spectral range (nm)	650-950

This change results in several secondary changes to the system. First, the f-number is increased up to 8.0 which reduces the throughput of the system overall but the last half of a degree of the FOV becomes brighter helping to reduce the vignetting and SNR drop off near the edge of the measured images. Second, the size of the image on the CCD is reduced in size which should decrease the resolution of the instrument. However, the decrease is partially offset by the larger f-

number which reduces the system aberration thereby resulting in a final average vertical and horizontal resolution of 260 m.

### **3.4 Opto-Mechanical Design and Thermal Balancing**

Upon the finalization of the optical design of ALI, an appropriate opto-mechanical and thermal system was required for test flight on a stratospheric balloon. This section gives an overview of the hardware used to transform ALI from a laboratory breadboard to a flight model prototype. The opto-mechanical design section discusses the optical mounting approach within the system, stray light reduction, as well as the addition of a light tight case. Following is a brief overview of the thermal concerns in the system and how the prototype was designed to minimize the thermal risks.

#### **3.4.1 Opto-Mechanical Design**

The opto-mechanical system needed to be able to withstand the stresses applied to the system during the launch of the stratospheric balloon and to withstand the large thermal changes experienced during the flight in order to keep the optics in the system aligned and in focus. Furthermore, the system had to also meet safety factors for torque and shock forces on the instrument so that it could not become detached from the gondola during the flight. These strict regulations were in place to verify the safety of CNES workers who launch the balloon as well as citizens below the gondola during flight.

Consideration for thermal expansion and contraction of the opto-mechanical components also had to be considered when choosing materials to house the optical lenses housing system in order to reduce the chance of any torques arising in the optical chain from thermal expansion. To reduce this effect, a consistent material was picked for the complete optical housing so all materials would have the same thermal response to the environment. The chosen material was aluminum since it is commonly used in space-based instruments and platforms because of its strength, light weight, and relatively inexpensive cost.

Housing of the optics also required some consideration. Commonly, space-based instrumentation uses a solid piece of material that is machined into the shape required and weight-relieved by machining contours into the surfaces. However, this method is relatively expensive and not within the budget for this prototype project. The most sensible option was to design an optical rail system primarily from off-the-shelf components from optical manufacturers, which would allow the flexibility to be able to make slight modifications to the design at relatively low cost. Some particularly challenging mounting issues were tackled with small custom machined parts. The drawback, or trade-off, with only using off-the-shelf components is that it is more difficult to guarantee and maintain the alignment of the system.

Using components from ThorLabs, Edmund Optics, Newport, and McMaster-Carr, an opto-mechanical case and mounting system was designed for the ALI prototype. The optical rail system is shown in Figure 3-18. A single sturdy wide optical rail, element 11, was used as the system base since it has the whole optical chain plus a baffle (discussed in section 3.4.2) mounted to it and would have a low susceptibility to torsion. This rail would serve as a base for all the optical mounting. The opto-mechanical chain was connected to the rail using rigid optical aluminum rods. For the optical chain, an optical cage system was used since the four rods surrounding the optic mounts provided a rigid framework that would still allow for fine tuning of the optical elements. The optical cage is element 4 in Figure 3-18. Once the aligning of the optical system was completed, the components were glued into place with a suitable epoxy to prevent slippage during transportation and launch.

During the testing of the breadboard optical system in the lab, two prisms were used to account for the deviation in the optical chain caused by the AOTF. These prisms were removed in the final

design by bending the BEO of the optical chain by  $2.7^\circ$  through a rotation stage (element 7). The removal of the prisms further reduced distortions within the system as mentioned in section 3.3.4.

It should be mentioned that optical lenses for ALI were selected for the final system with the addition of antireflection coatings. The coatings increased the systems efficiency as well as reduced internal reflections. From ThorLabs, a B-type antireflection coating was ordered for the lenses, which reduces reflection from each lens surface down to an average of less than 0.50% from 650 to 1050 nm instead of an approximately 8% loss per surface from an uncoated lenses. The lenses also had a 1% tolerance in the focal length and were made from grade A NBK7 glass.

A selection of linear polarizers were considered for elements 5 and 8 in the opto-mechanical system. However, the wavelength range of ALI made standard polarizers difficult to procure and greatly limited the possible choices. A nanoparticle linear film polarizer from ThorLabs was eventually selected (model number LPVIS100, see Appendix A.1.2) since it has an extinction ratio better than  $10^5$  for 650 to 1200 nm, completely covering the operating range. The extinction ratio is defined by the ratio between the maximum transmission when the polarizer's axis is aligned with a linearly polarized incident signal to the maximum transmission after the polarizer has been rotated by  $90^\circ$ .

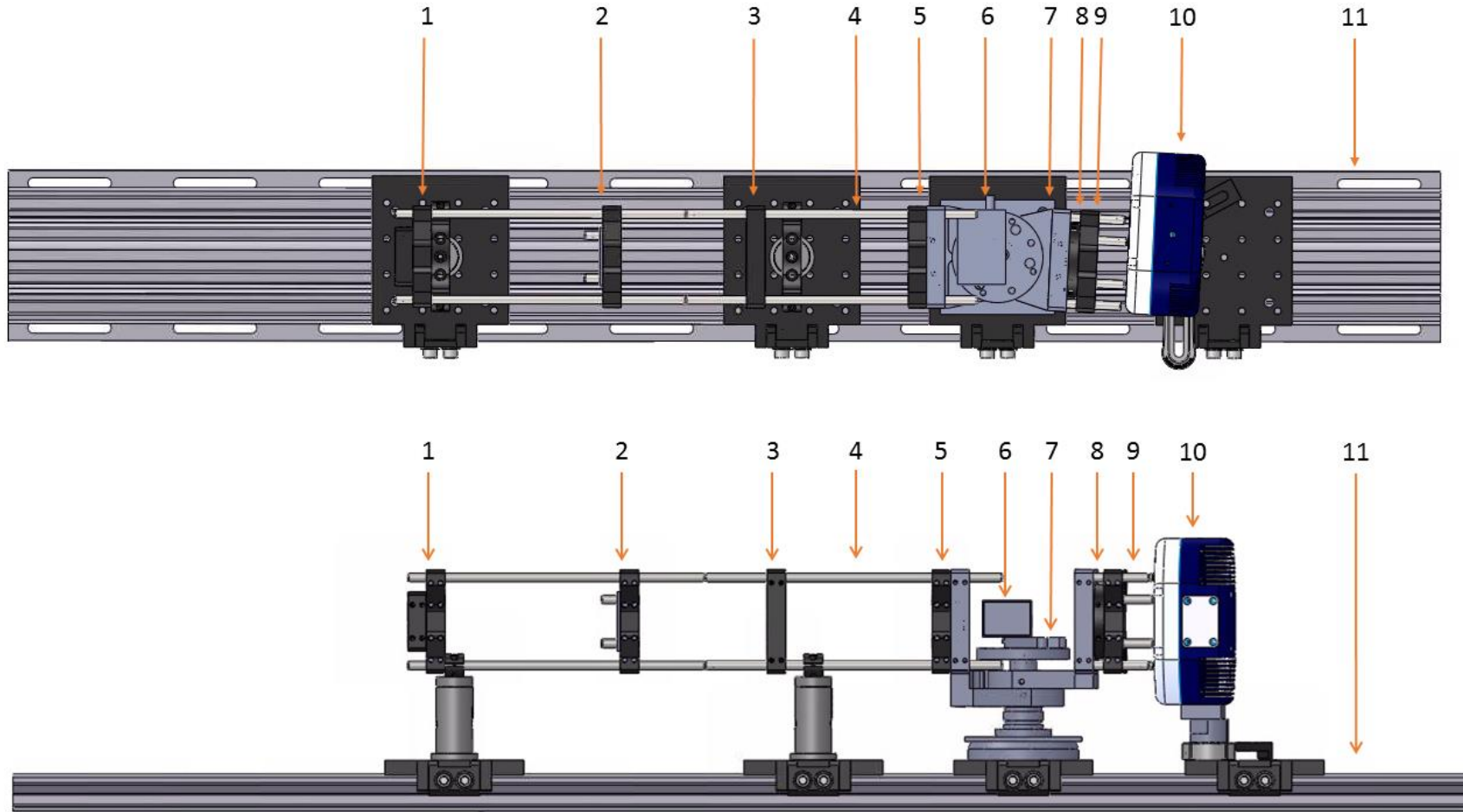


**Figure 3-18:** The final optical layout of ALI's optical chain from the top and profile perspectives with the components being the following: (1) 150 mm plano-convex lens with 25.4 mm diameter. (2) Field Stop. (3) 100 mm plano-convex lens with 50.8 mm diameter. (4) Optical rail system. (5) Vertical (extraordinary) linear polarizer. (6) Brimrose AOTF. (7) Rotation Stage. (8) Horizontal (ordinary) linear polarizer. (9) 50 mm bi-convex lens with 25.4 mm diameter. (10) QSI 616s CCD camera. (11) Optical rail.

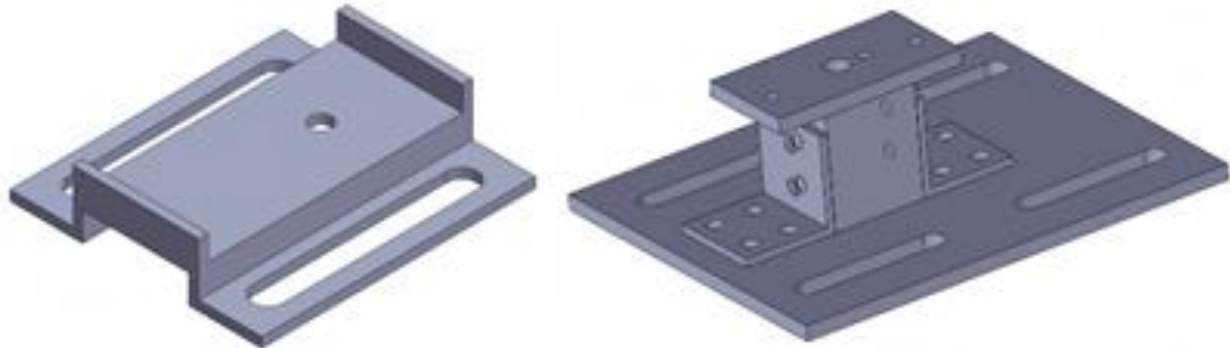


**Figure 3-19:** The custom mounting hardware design to mount the AOTF and QSI CCD camera into ALI's opto-mechanical design. Left: Custom AOTF mounting hardware. Right: The five piece QSI CCD camera mounting hardware.

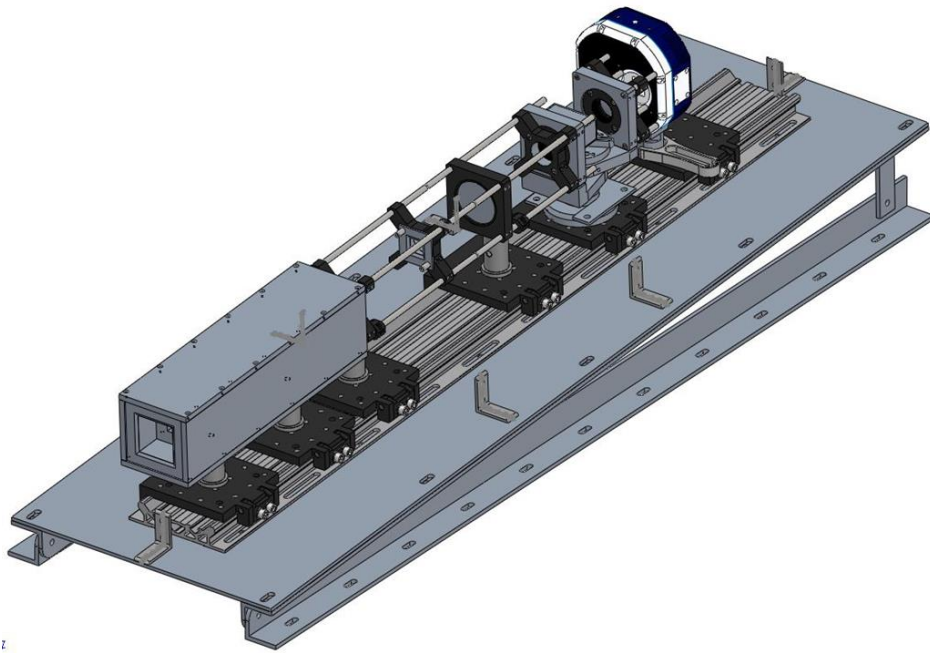


**Figure 3-20:** ALI opto-mechanical system with three degree horizontal tilt and designed baffle discussed in section 3.4.2. Originally published as Figure 5 in *Elash et al. (2016)*.

For the opto-mechanical design special consideration had to be given to mounting the AOTF and CCD camera. Both of these elements are non-standard sizes in optics and no pre-existing components could be purchased to mount these pieces. Therefore custom mounting hardware had

to be used to rigidly mount these components. Both components were designed through the use of the SolidWorks design software and can be seen in Figure 3-19.

The ALI system was tilted three degrees from the horizontal so that the symmetric FOV of the instrument from the balloon flight geometry would measure from the ground to the balloon float altitude. A SolidWorks rendition of ALI with the three degree tilt from the horizontal can be seen in Figure 3-20.

Finally, mounting hardware was tested through stress analysis calculations done by the CSA to verify that the safety factor of the system was met. ALI passed all safety requirements for the stratospheric balloon launch.

### **3.4.2 Baffle Design**

A major concern with any optical instrument is the presence of unwanted or stray light. Two types of stray light are commonly defined: internal and out-of-field stray light. Internal stray light is unwanted light that passes through the system through scattering, reflections, or imperfections in optical elements. Out-of-field stray light is light that enters the optical path but originates from outside of the FOV. A long standing concern in the design of limb scatter instruments is the effective rejection of out-of-field stray light. This is due to the bright surface very near to the targeted limb in combination with the exponentially dropping limb signal with tangent altitude. For ALI test observations from the stratospheric balloon, a front end baffle was incorporated.

When designing a baffle several design aspects need to be determined. Consideration must be given to the length and width of the baffle as a larger, well-designed baffle is able to more efficiently remove out-of-field light but increases the size, mass, and cost of the instrument. Furthermore, the number of vanes in the baffle design must be considered. More vanes help to remove additional out-of-field light but each vane adds an edge that light can scatter off which

may introduce more stray light into the system. A balance must be met with the size and number of vanes in the ALI baffle to best remove out-of-field stray light.

The first point of the discussion is the height and width of the baffle. In a baffle system, the larger the baffle is by cross-sectional area the better the baffle can be designed to reduce stray light. However, there is a limited amount of space to build the ALI instrument and the baffle must share space with optics, electronics and power systems; and as such, a size that fit these constraints had to be selected. An internal height and width of 70.00 mm was chosen since this was the size of the optical rails used to house the optical chain and the instrument could not be any taller than the height of the optical rail to meet size constraints.

The length is also limited by the space available, as well as the FOV and entrance aperture size. The baffle must be short enough so that the size of the FOV does not become larger than the cross-section of the baffle. To maximize the effectiveness of the baffle the longest possible length that could be accommodated was selected. This length is 300 mm with 250 mm for the primary baffle and 50 mm dedicated for an external baffle to reduce surface reflections.

Also, one always needs to make sure the optical stop located within the baffle is placed at the same location as the optical design. If the location of the optical stop is changed from the baffle design, it affects the performance of the instrument itself. If the optical stop is moved further from the optical design specifications, the FOV remains the same but limits the amount of light that enters the system. Thus changing the overall f-number of the system either increases the exposure times or decreases the SNR. In the other case, the optical stop is moved closer to the optical system and the opposite problem occurs. More light enters the system than the system was designed for causing an excess of stray light and rendering the baffle ineffective.

The baffle system is designed such that it minimizes the percentage of out-of-field stray light that enters the system without encountering at least three baffle surfaces. This method, the optimal baffle geometry, is a standard used in optics to minimize stray light (Fischer, 2008). In the system, the baffles are spaced in such a way that little stray light cannot enter the system without coming into contact with at least three scattering surfaces thus reducing the overall intensity of the stray light.

The optimal baffle geometry design method is described here. In Figure 3-21a, the base baffle case is formed with the critical baffle vane at the entrance to the optical system (-250 mm) and a second vane is located closest to the optical chain. The marginal rays of the optical system are represented by the red line.

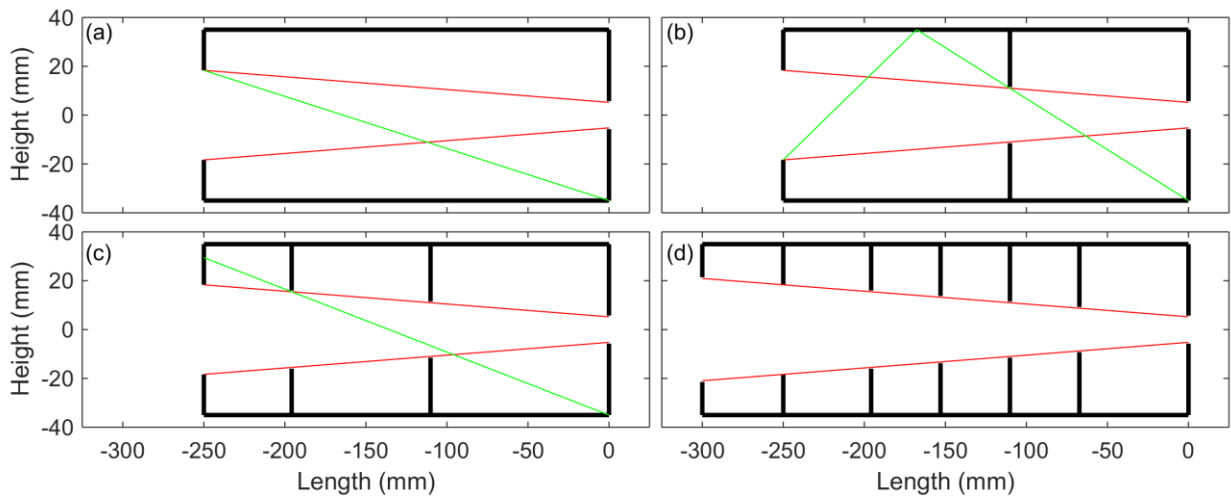


**Figure 3-21:** (a) Start of the optical baffle geometry method. The red lines are the marginal rays and the green line is the first ray that can enter the system without encountering at least three surfaces. (b) The first internal vane has been added and the location of the next vane is being determined. (c) The second internal baffle has been added and since the green line intersects with the critical baffle no more baffles are required. (d) Additional interior vanes and an external vane have been added to ensure a height to pitch ratio of 0.5 to improve the baffle's capabilities to reduce stray light.

Next, an indicator line is drawn from the bottom right corner of the baffle to the opposite tip of the critical baffle, represented by the green line. This line represents the first ray that can enter the

system without coming into contact with at least three surfaces. The next vane is added where the indicator line and marginal ray intersects, and has been added in Figure 3-21b.

The next indicator line goes from the bottom corner to just passing the newly inserted vane and encounters the outer side of the baffle wall. The line goes through a reflection and passes just by the critical baffle once again. The intersection of the second segment of the indicator line and marginal ray is where the second vane is added as in Figure 3-21c.

The process is then repeated to determine the location of any additional vanes. For the ALI baffle, the indicator line no longer is able to reflect upon the top baffle surface and therefore the minimum level of baffles has been achieved. However, two extra internal baffles and one external baffle were added to the design (Figure 3-21d). The exterior baffle was added to help further reduce stray light from surface reflection by shielding the critical baffle from the direct ground reflections. The additional interior baffles were added to achieve a height to pitch ratio greater than 0.5. If the height to pitch ratio is less than 0.5, additional stray light enters the optical system due to the high amount of empty space within the baffle (*Fischer et al., 2008*)

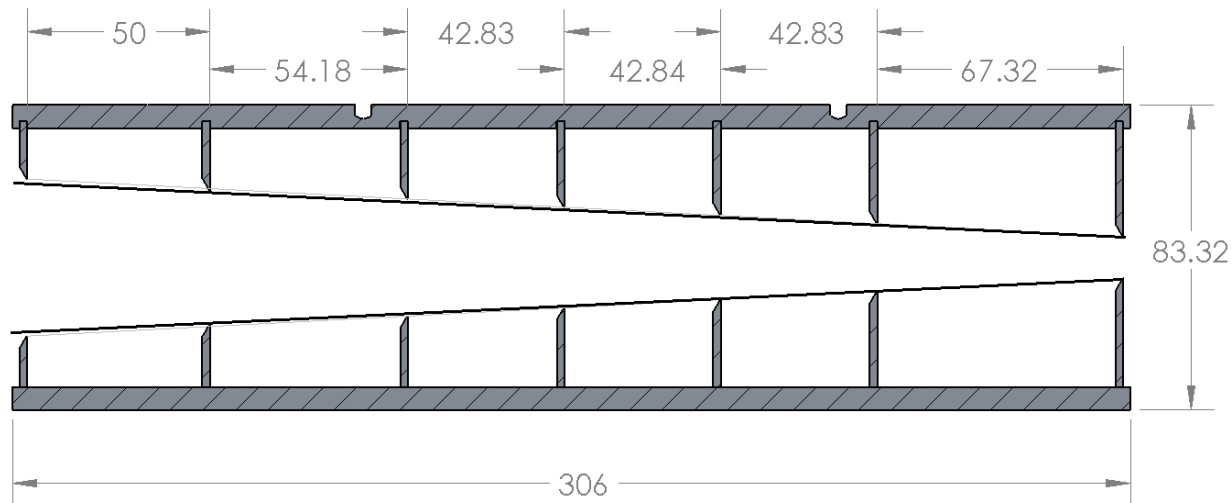


**Figure 3-22:** A cross-section view of the ALI baffle system. All dimensions on the drawing are in millimeters and the sloped black lines represent the 6 degree FOV.

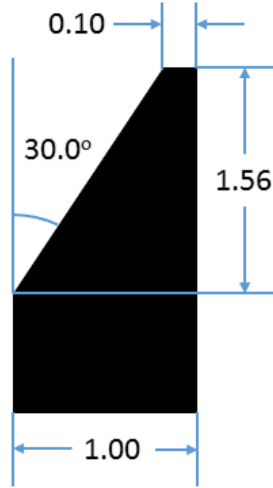


**Figure 3-23:** ALI baffle vain profile. Dimensions are in millimeters.

With the exception of the critical baffle all of the edges of the vanes were reduced in size by 0.5 mm so that they could be produced within possible machining tolerances and not limit the FOV by being too tall. A SolidWorks version of the baffle can be seen in Figure 3-22 which accounts for the thickness of the materials and machining tolerances.

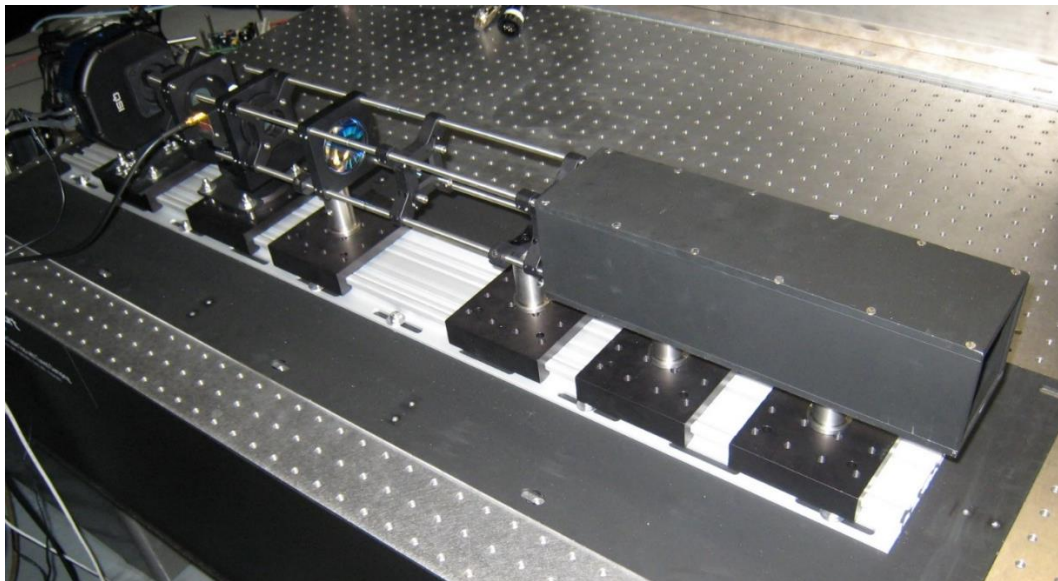


**Figure 3-24:** Final ALI optical and opto-mechanical assembly.

Ideally, the edges of the vanes would be machined to a fine blade. However, this is not practical for two reasons. First, the baffle's edges would be prone to damage causing dents or grooves in the vane cross-section possibly producing unwanted scattering effects. Second, it is only possible to machine the tips so fine with tolerances without reducing the height of the vane. Figure 3-23 shows the profile for the baffle vanes as they were machined. A final assembly of the optical system can be seen in Figure 3-24.

### 3.4.3 Light Tight Case

To complete the opto-mechanical design, a light tight case was required. The case was made out of aluminum and every connection point in the case was overlapped, through interlocking pieces, to ensure the rejection of all light. The light tight case was clamped onto the base plate of ALI and a photograph of the finalized prototype can be seen in Figure 3-25.

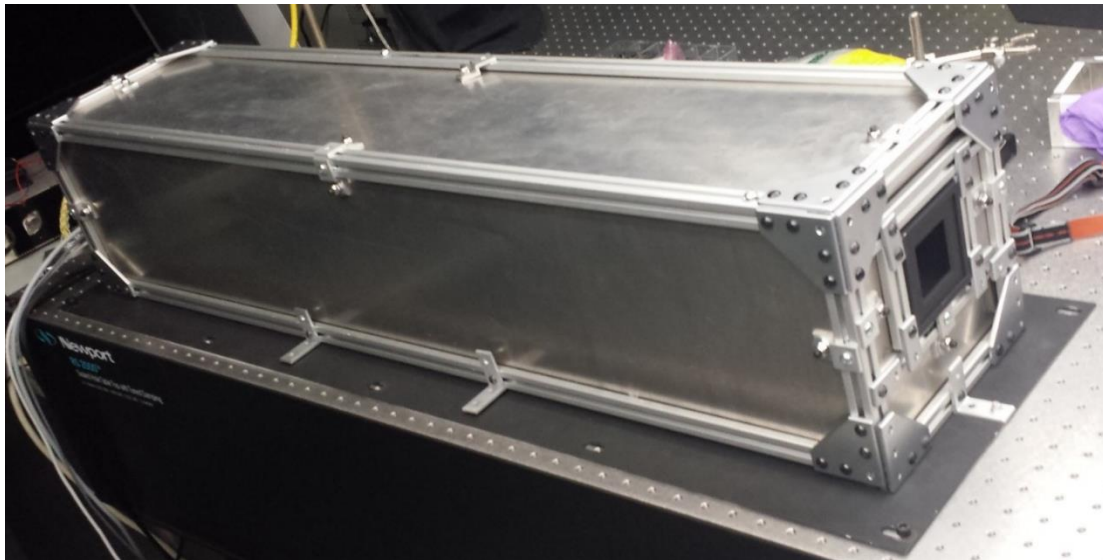


**Figure 3-25:** ALI optical system with light tight case attached. Three degree horizontal tilt not present in this image.

### 3.4.4 Thermal Considerations

An instrument, like ALI, had to survive the possibility of extreme temperatures during the flight on a stratospheric balloon. The extreme temperatures could arise through various processes. First

the instrument must survive the ascent through the tropopause where temperatures can reach -70°C and must survive the float temperatures which can be as cold as -50°C. Conversely, being exposed to direct sunlight causes heating that would result in instrument failure due to overheating. Furthermore, since simple opto-mechanical design were used for ALI there was no active thermal control. With the reduced atmospheric density at approximately a float altitude of 35 km, convective cooling could not be relied upon for thermal control. The following is a discussion of various thermal concerns within ALI.

The electronics were stored within two aluminum cases, a computer case and power supply case. All components within the two cases were rated for an extended thermal range (-40 to 85°C) except the RF driver which had an operational thermal range of 0 to 50°C. The extended range of all other electronic components reduced the concern since this case was not be exposed directly to the elements as they weresheltered via insulation. From consultation with the CSA and CNES teams, the internal temperature of the electronics area from previous missions had reached a coldest temperature of approximately -20°C during normal flight operations.

However, the RF driver does not fall into the specified temperature range, which was a problem. In addition the driver also produced a large amount of heat that was convectively cooled in the laboratory which was not possible at float altitude due to the reduced atmospheric pressure. Since the RF driver was a fundamental piece of hardware, failure in the component would result in a primary system failure.

To mitigate the risk, several considerations were made with regards to the RF driver. First, a RF driver with a cooling plate was purchased to better allow for conductive thermal control. The driver was mounted in thermal contact with the aluminum case such that the cooling plate was in direct contact with the surface of the case, which was then mounted directly against the aluminum

mounting surface on the gondola. This allowed a large amount of heat to be conducted to the gondola to keep the RF driver within the operating range. Reaching too cold of a temperature was not as large of a concern since the driver produced enough heat to sustain its operating temperature. However, as the driver was a power hungry component it was desirable to toggle the power to save battery. In this case, overcooling of this component was a concern. A temperature sensor was used to monitor the driver and the control software was designed with a safety measure such that it would automatically turn the driver off if it reached 50°C or turn it on if the temperature dipped below 0°C.

Another region of concern was the housing of the optical system which would be directly exposed to the elements. The optics can expand and contract based on the temperature. Additionally, the CCD camera had an operating temperature range of -40 to 20°C. Furthermore, the CCD primarily used convection to cool the camera, which was disabled for flight as they would self destruct due to the low atmospheric pressure since the rotation speed is based on air resistance. To mitigate the thermal risk, a twofold approach was taken that is standard for stratospheric ballooning. First, the optical housing was surrounded in foam to thermally insulate it from the cold experienced during darkness and ascent though the tropopause. Second, the foam insulation was covered in a reflective material to reduce direct warming from the radiation from the sun. The small amount of heat generated by the camera within the insulted box was enough to maintain a relatively small temperature swing of the optical chamber during the flight.

# CHAPTER 4

## CALIBRATIONS AND CONTROL SOFTWARE<sup>1</sup>

### **4.1 Introduction**

This chapter focuses on a discussion of the control software developed for the ALI stratospheric balloon flight, as well as the calibration and performance evaluation of the instrument. For the calibration, the AOTF is first characterized separately from the ALI optical system and detector, and then the fully assembled instrument calibration is presented.

### **4.2 Control Software**

During the stratospheric balloon flight, software was required in order to control the instrument from the ground for remote operation. Two separate software packages were developed to accomplish the communication and control systems required for the mission. First, a ground system, commonly known as Ground Support Equipment, or “GSE”, was developed to provide communication to the instrument including the receipt of diagnostic information and images, and the capability to provide control commands. The second software system was the onboard system that controls the instrument operations.

The GSE is responsible for establishing communication with ALI, handling any loss of information during data transfer, decoding the data from the ALI flight software, as well as uploading commands to the instrument. The onboard control system was more complicated with several different modules to handle the different aspects of the hardware and control systems. The onboard computer was a VersaLogic PC-104 OCELOT (Appendix A.2.3), which has fanless operation, a thermal operating range of -40 to 85°C, and runs a Debian Linux operating system. Multi-threaded C++ based software developed specifically for ALI controlled the hardware and ran

---

<sup>1</sup> Portion of sections 4.3.1, 4.3.2, 4.3.3, 4.4.4 and 4.4.5 as well as Figure 4-3, and Figure 4-7 were originally published in *Elash et al. (2016)*

the data collection operating modes. This flight software contained five different modules to handle different functions of the system. The five modules were the main module, communication module, diagnostics module, science module, and local storage represented in Figure 4-1 by blue, green, orange, purple, and yellow respectively. A brief overview of each follows.

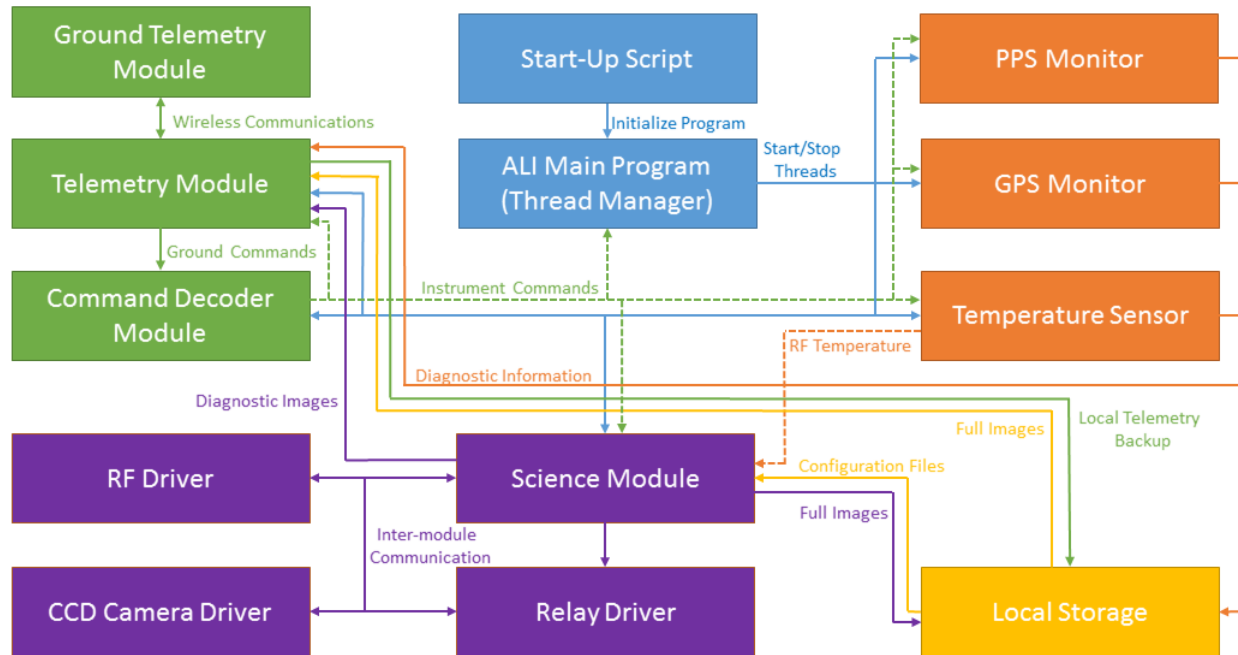


**Figure 4-1:** A complete flow diagram showing interaction between all the modules on board the ALI flight computer.

The main module consists of a BASH script which initiates the ALI C++ flight program during startup and can be restarted from the ground upon a software failure. Once the main program has been started by the script, the thread manager initializes all of the individual threads for the other processes and then waits for a termination command to close the ALI flight software.

The first module started by the thread manager is the communications module which operates the telemetry or communication between other modules as well interactions with the ground control software. The module sends and receives all data packets that are outgoing and incoming through User Datagram Protocol (UPD) as required by the CSA and CNES specifications. Also,

data rate limits were imposed on the instruments to avoid one instrument using all the bandwidth to transfer data from the gondola. For ALI the limit was 100,000 bits per second. The communication module was responsible for verifying that this limit was obeyed when encoding into packets and sending them to the ground. Also, uploaded commands were decoded and sent to the command decoder, which took all the incoming commands from the ground, parsed the information, and sent the commands to the proper modules. A full list of commands can be found in section B.1

The diagnostic module managed the Global Positioning System (GPS) information, pulse per second ping, and voltage and temperature sensors. The GPS monitor recorded the current location and height of the instrument with respect to the front of ALI optical instrument. The pulse per second was a signal that was sent out from the gondola's SIREN module (a proprietary device used for the gondola's communications and telemetry system) every second. It is a constant signal between all instruments on board to synchronize data collection. The voltage sensors provided monitoring to ensure that the voltage levels stayed within the electronics specified ranges. Lastly, the temperature sensor module read all of the temperature sensors from a one-line temperature sensing device, where all temperature sensors were connected with a simple serial connection (known as RS-232). The locations of the temperature sensors are seen in Table 4-1 and the locations attempted to achieve a complete temperature profile of the instrument. All information gathered by the diagnostic module was sent to the telemetry system so the ground user could determine the state of the system and make any required changes. The data was also stored on the local hard drive (solid state) onboard ALI for use when ALI was recovered after the flight.

The science module operated the ALI instrument, the acquisition of data, and directly controlled the relay to the RF driver and the QSI CCD camera. The science module loads program defaults

upon startup from local storage or program settings can be altered from ground control. Each of the modes for data acquisition had its own configuration file and the supported modes were a calibration mode, an aerosol mode, an H<sub>2</sub>O mode, an O<sub>2</sub> mode, a constant exposure time aerosol mode, and a custom mode. The details for these mode can be found in appendix B.2.

**Table 4-1:** Location of ALI temperature sensors.

Number	Sensor Location
1	Aluminum wall of electronics case
2	Cooling plat of RF Driver
3	OCELOT CPU heatsink
4	Aluminum wall of power supply case
5	5 V power supply transducer
6	12 V power supply transducer
7	Front of ALI baffle just inside system
8	On the CCD camera

When the science operations were enabled, ALI loads an operational mode as specified from the ground. The science mode controlled all of the hardware and processed the imaging cycle. Two types of images were created. Full images that contain the entire image were sent to local storage due to bandwidth considerations, and diagnostic images were transmitted to the ground. These contained the required information to achieve minimal level of success from the flight in case the local solid state drive was not recoverable after the balloon flight due to a crash landing, water damage, etc. When the mode was completed the same mode was repeated unless the instrument had received a command to stop acquiring images or was queued to start another mode.

Each diagnostic image contained five complete vertical columns of measurements with statistics on the entire image, including percentages of saturated and under-saturated pixels, as well as the location and time of the measurement and the current state of ALI. The software was configured such that any extra bandwidth that is not allocated to other processes is used to transmit complete images to the ground.

### 4.3 AOTF Calibration

The calibration of the AOTF is presented within this section. As noted previously, the AOTF was purchased from Brimrose of America and the complete specifications can be found in appendix A.1.3. The calibrations preformed on the AOTF were:

- Tuning curve analysis
- Point spread function analysis
- Diffraction efficiency determination.

#### 4.3.1 Tuning Curve Analysis

The tuning curve relates the applied RF wave to the diffracted wavelength, and must be accurately known to determine the wavelength being measured, as this directly affects the aerosol retrieval. The form of the tuning curve was given in Equation 3.32. To determine the tuning curve for the AOTF, a test optical set up was devised in the lab to measure the central diffracted wavelength as a function of the selected RF.

For this analysis, a telecentric test layout was used, the details of which are described in section 3.3.2. An advantage of the telecentric testing layout for the AOTF characterization is that the wavelength dependence of the acousto-effect from the incident angle, noted in Equation 3.32, is removed since all the lines of sight enter the AOTF with the same angular spread. The experimental set up consisted of the AOTF centered between two 100 mm focal length lenses to optimally fill the AOTF aperture. Linear polarizers were inserted before and after the AOTF to remove the unwanted polarization states. An aperture was set up in front and behind the AOTF in the optical chain at the focal length of the front and back lenses respectively and opened to 5 mm to complete the telecentric experimental layout. The high front end f-number of 20 required long integration times to capture sufficient signal but provides a much higher degree of telecentricity. Two prisms were used to compensate for the  $2.7^\circ$  off axis bending to set the light parallel to the optical path. A

standard 100 W tungsten halogen bulb was used as a light source. The front end optics had no magnification and the back optics were used to match the f-number of the spectrometer's input optics. The layout can be seen in Figure 4-2.

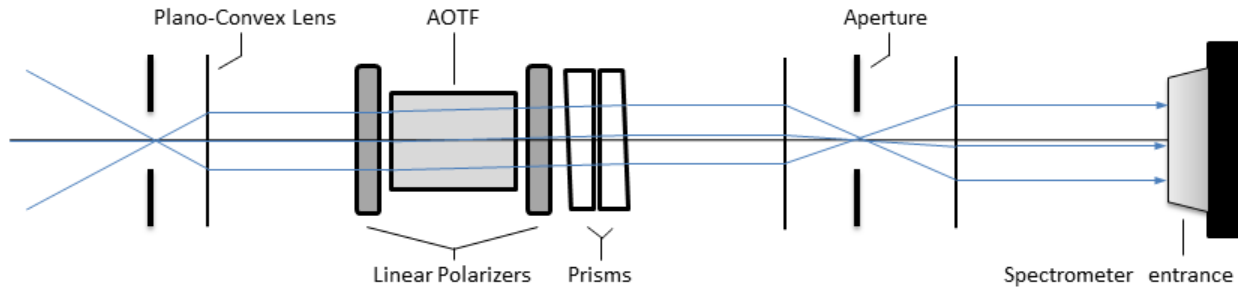


**Figure 4-2:** Telecentric test experiential setup for AOTF parameter determination. All lenses and apertures are represented by the vertical lines.

The output was passed into a HORIBA iHR320 spectrometer with a 1200 lines/mm grating blazed at 750 nm (see Appendix A.3.1) and was imaged on a Synapse 354308 front-illuminated CCD detector with 1024x256 pixels (see Appendix A.3.2). The CCD was thermoelectricity cooled to -75°C to reduce any significant dark current contributions to the measurements. The signal entering the spectrometer optics were well collimated and limited the amount of stray light.

Images were taken at a set of RFs spaced every 150 kHz from 160 MHz to 75 MHz nominally corresponding to a 1 nm resolution. The spectral images were recorded with the spectrometer slit at 0.5 mm making the minimum Full Width Half Max (FWHM) of the spectrometer 1.175 nm, less than the minimum factory specification for the AOTF spectral resolution of 1.6 nm. Note that the final recorded spectra are a convolution of the PSF of the AOTF and spectrometer and this had a small effect on the determined spectral resolution. At each RF, two images were taken with a 15 second exposure time: one with the AOTF in the “on” state and another with the AOTF in the “off” state. The stray light, dark current, and the DC bias are recorded in the image with the AOTF turned off and can be removed from the final image by subtraction. Since the recorded spectra are

spatially aligned in the images all of the rows of the CCD are summed together to get the total count measurement at each wavelength. The maximum value of each spectra is taken to be the central diffracted wavelength through the AOTF at each respective RF. A typical spectral measurement result can be seen in Figure 4-3a.

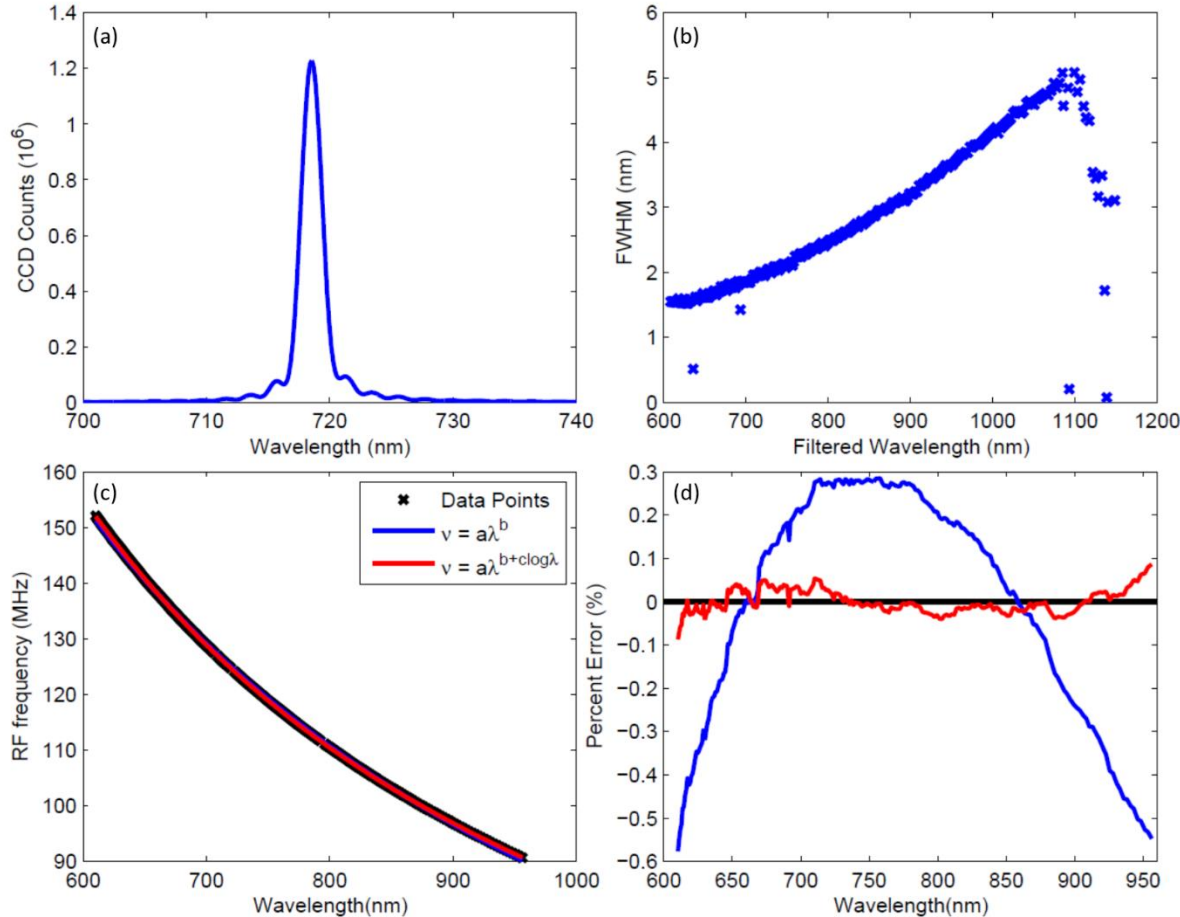


**Figure 4-3:** (a) A row averaged image taken from the AOTF of the point spread function when the tuning frequency of the AOTF was at 124.96 MHz. (b) The FWHM for each of the determined wavelengths for the AOTF. The FWHM at 600 nm is 1.5 nm and as the wavelengths get longer the FWHM increases to 4.9 nm at 1080 nm. (c) The calibration curves for the AOTF RF versus the diffracted wavelength which contains the data points recorded and fit curves. (d) The percent error with respect to the measured frequency for the two best fit curves in the previous panel. Originally published as Figure 6 in *Elash et al. (2016)*.

The maximum values from each of the images were determined along with the corresponding wavelengths. The function form of the tuning curve from section 3.2.4 (Equation 3.32) shows that

the wavelength and the RF are inversely related. Although this was approximately the case with this measured data, it was noted that the curve empirically fit a power function of the form

$$F = a\lambda^b. \quad (4.1)$$

This fit provides an agreement with the measurements across the spectral range to better than 0.6%.

An improved fit was provided by a modified power function in the form of

$$F = a\lambda^{b+c\log\lambda}. \quad (4.2)$$

The results of these fits can be seen in Figure 4-3c and Figure 4-3d. The agreement of this form was better than 0.1% throughout the whole wavelength range and the determined tuning curve was

$$F = \exp(19.793)\lambda^{-3.381+0.168\log\lambda} \quad (4.3)$$

where  $\lambda$  is in nanometers and  $F$  is in megahertz. Note that this relationship was temperature dependent. However, even when considering the potential temperature changes during the balloon flight, this would impact the relation by a maximum wavelength drift of 2.5 nm. This level of uncertainty had a very small impact on the aerosol retrieval due to the slowly varying scattering cross section and it was decided that this relationship would not be actively changed with temperature. Furthermore, it should be noted that even though the AOTF optical range was 600 nm to 1200 nm, our analysis only measured wavelengths from 600 nm to 1080 nm due to the low quantum efficiency of the CCD beyond this range.

### 4.3.2 Point Spread Function

The spectral Point Spread Function (PSF) of the AOTF was also determined using the same set of data that was used for the tuning curve calibration. The spectral PSF was found by determining the FWHM for each wavelength. These results are shown in Figure 4-3b. The sidelobes in Figure 4-3a are a known AO effect discussed in section 3.2.2 as a result of Equation 3.17, and for the Brimrose AOTF this amounts to 8-14% of the total signal depending on wavelength. As noted

in the previous section, the PSF of the AOTF and the spectrometer are convolved in this analysis. Even with this widening bias to the spectral PSF, the AOTF spectral resolution was well within the limits that were required in order to determine aerosol extinction in the upper troposphere and lower stratosphere (see section 2.6.1).

### 4.3.3 Diffraction Efficiency

An additional experiment was performed at several wavelengths to determine the RF power that yielded the highest optical throughput with the AOTF using a collimated light source. It was found that at all wavelengths the maximum throughput occurred when the RF power was at the recommended limit of 2 W. Following this, the diffraction efficiency of the AOTF was determined by using two sets of measurements. The first was the experimental data used to perform the tuning curve analysis, and the second was a set of measurements of the intensity of the incident collimated light beam. The incident light in both measurement sets was linearly polarized and aligned with the polarization axis of the AOTF; to create the second set of measurements, the AOTF was simply removed from the optical chain. It should be noted that the attenuation of the AOTF crystal itself was not determined independently and was combined with the diffraction efficiency. As we were more concerned about signal throughput of the device a measurement of the combination of the effects was acceptable. The incident light source was then measured with the same iHR320 spectrometer and Synapse CCD with identical settings. By taking the ratio of the intensity at the diffracted wavelength to the incident intensity the diffraction efficiency was determined. It was found to vary between 54 and 64% across the measured spectral range. Equation 3.18 was not used to determine a theoretical diffraction efficiency due to the fact that some of AOTF parameters, such as interaction length, were unknown due to the proprietary nature of the device. However, our results agreed with the experimental diffraction efficiencies supplied from Brimrose with the AOTF.

It should be noted that the diffraction efficiency changes also with respect to incoming angle and this experimental determination only measured the diffraction efficiency at normal incidence (*Xu and Stroud, 1992*). It was acceptable to only perform these measurements at normal incidence since the loss of signal was small as long as the incident angle remains within the acceptance angle of the device, which in this case is  $2^\circ$ .

#### **4.4 ALI Calibrations and System Test**

A series of pre-flight laboratory calibrations were performed on the complete ALI instrument. The instrument was characterized as a complete system to provide calibrated radiance and estimate flight exposure times. The following pre-flight tests and calibration measurements were performed on ALI:

- Exposure time determination
- DC offset removal
- Dark current correction
- Stray light calibration
- Relative flat-fielding correction

##### **4.4.1 Exposure Time Determination**

An experiment was performed to determine exposure times for the stratospheric balloon flight, as well as to verify the design of the entrance pupil size of the system. On July 12, 2014 from 13:00 to 16:00, during clear conditions, ALI was placed on the roof of the University of Saskatchewan Physics building ( $52.13^\circ\text{N}$   $106.63^\circ\text{W}$ ) pointing approximately  $90^\circ$  in the azimuth direction from the sun, and measurements were recorded with a range of exposure times (0.01 to 120 seconds) and wavelengths (600 to 1000 nm). These ground based measurements were then used to determine the exposure times that would be required when imaging the atmospheric limb from the float altitude of the stratospheric balloon.

The SASKTRAN-HR radiative transfer model was used to determine the scaling factors that relate the ground-based radiance to the limb radiance. Using the scalar SASKTRAN-HR (*Bourassa et al.*, 2008; *Zawada et al.*, 2015) radiative transfer model, discussed in detail in section 2.4.5, radiance profiles were simulated from the ground-based geometry and a simulated balloon flight geometry. The simulated radiances for the ground based and balloon flight geometry are shown in Figure 4-4. A scaling factor,  $\beta$ , was determined based on the ratio of the ground based and balloon based geometries and was used to adjust the integration times. The scaling factor was used in combination with the ground based determined integration times,  $t_g$  in the following

$$t_b = t_g \beta = t_g \frac{I_b}{I_g}, \quad (4.4)$$

where  $t_b$  is the integration time from the balloon platform, and  $I_b$  and  $I_g$  are the simulated scalar radiances from the balloon and ground, respectively. The scaling factor is shown in black in Figure 4-4 and the estimated balloon geometry exposure times are located in Table 4-2.

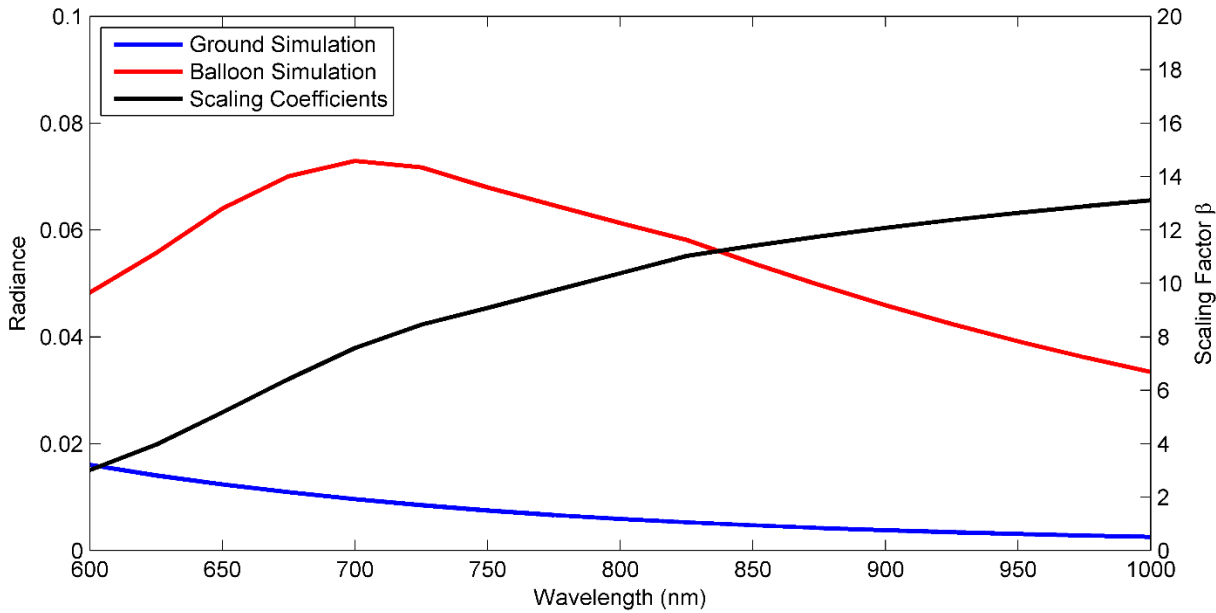


**Figure 4-4:** Simulated scalar radiances from the SASKTRAN-HR in blue and red with the radiance on the left side and the scaling factor in black with the value on the right side.

The exposure times determined were designed to be on the order of a second during the flight which was performed by selecting an appropriate entrance pupil size of 9.91 mm; however, a severe limitation in the measurement frequency capability of the instrument was the read-out speed of the CCD detector. This was very slow compared to the exposure times and on average took 20 second per image, which greatly reduced the measurement density. Nonetheless, with a faster detector read-out, the desired measurement density could be achieved. Approximate exposure times estimate for the balloon flight are listed in Table 4-2. Flexibility was maintained in the control software to adjust these with ease during the flight.

**Table 4-2:** Estimated balloon flight exposure times.

Wavelength (nm)	Exposure Time (s)
650	2.00
675	2.00
700	1.39
725	0.38
750	0.10
775	0.10
800	0.10
825	0.33
850	0.47
875	0.48
900	1.00
925	2.00
950	2.00

#### 4.4.2 DC Offset Removal

The DC offset is a bias that is applied to the analogue to digital converter inside the CCD camera, which causes a bias in the final count values for the image and needs to be removed in order to be able to get the pure measurement counts due to photons. It is usually assumed that the DC offset for a CCD is a constant across the operating temperatures and exposure times of the device; however, the DC offset for the camera used in ALI exhibited a temperature dependence.

Dark images were acquired in the laboratory to be used in the calibration. Additionally, a calibration mode was used on the ascent of the balloon during the campaign that acquired dark images which were used to further calibrate the DC offset. All of the dark images were taken with the shortest possible exposure time of 0.01 s to reduce any dark current contribution from the images. The mean value of the counts for each image was determined and was used to determine the DC offset. The standard deviation of the counts for each image ended up being approximately 2% of the average value. Using this data, a curve was fit to determine the DC offset with respect to temperature. The curve is in the form of

$$\text{DC offset} = 0.00659T^3 - 0.09202T^2 - 3.5368T + 64305127 \pm 2\%, \quad (4.5)$$

where  $T$  is the temperature of the detector in degrees Celsius to determine the offset that needed to be removed and is plotted in Figure 4-5.

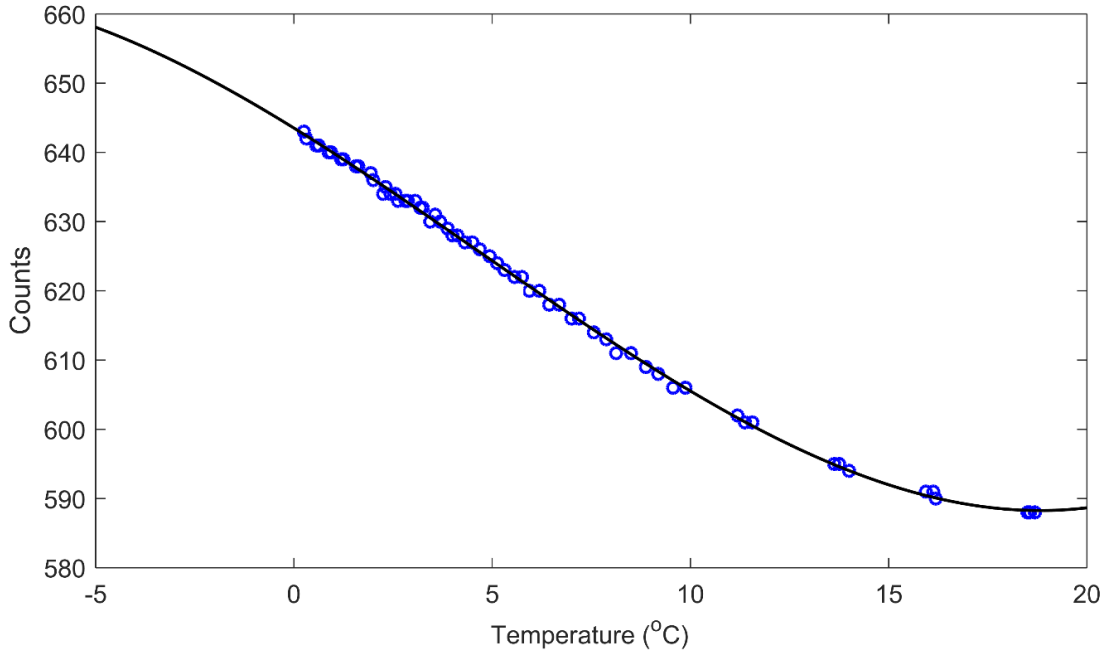


**Figure 4-5:** The DC offset curve (Equation 4.5) is seen in black where the lab and flight calibration data is shown in blue. The counts on the vertical axis are the counts that need to be removed to account for the DC offset.

#### 4.4.3 Dark Current Correction

The dark current is due to thermally generated electron-hole pairs, and grows linearly with exposure time and nonlinearly with temperature. By using images taken in darkness with a variety of exposures time, the dark current can be determined by looking at the residual after the DC offset has been removed using the curve developed in the previous section. The residual of the counts for the calibration dark image can be seen in Figure 4-6. During the campaign, the operating temperature of the camera was less than 10°C throughout the entire flight and most exposure times were less than five seconds leaving a very small dark current contribution in the measurement images, at worst approximately seven counts. This level of dark current was small compared to the other signal levels and was simply considered an additional noise term in the error analysis.

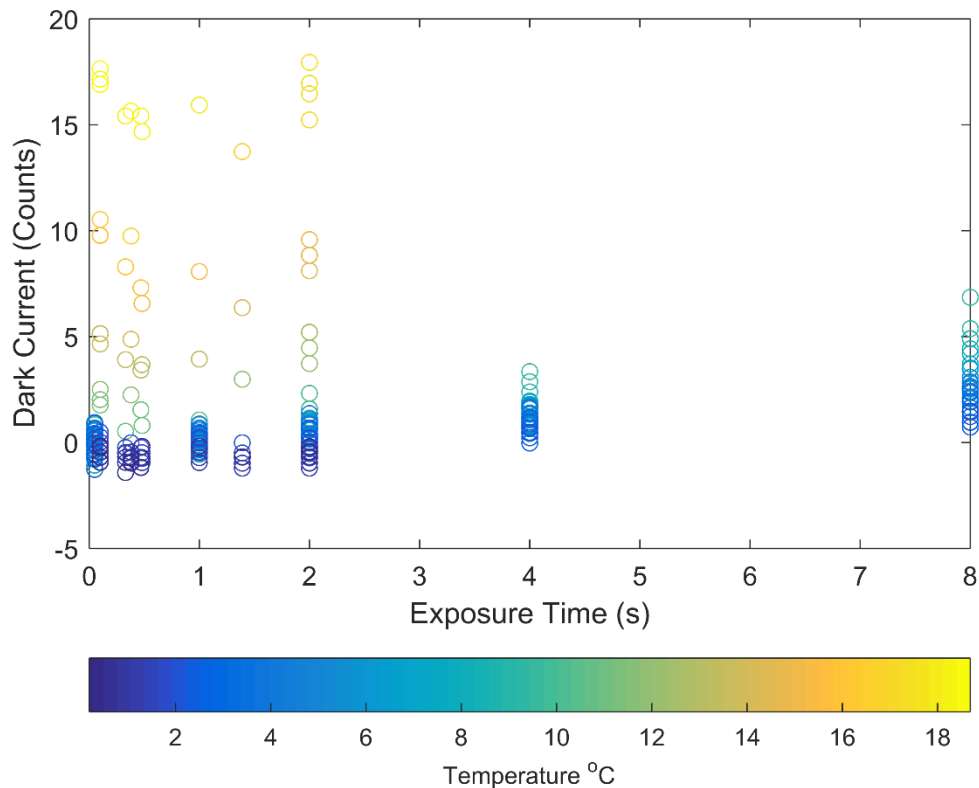


**Figure 4-6:** The dark current from the calibration images over a series of camera temperatures and exposure times.

#### 4.4.4 Stray Light Calibration

A laboratory experiment to characterize the stray light in the ALI system was performed. Two types of stray light exist; the first is out-of-field stray light, *i.e.* signal that enters the optical path that originates outside of the FOV. The second is internal stray light, which is caused by scattering, reflections or other imperfections in the optical elements. As mentioned previously, stray light removal is critical for limb scatter measurements.

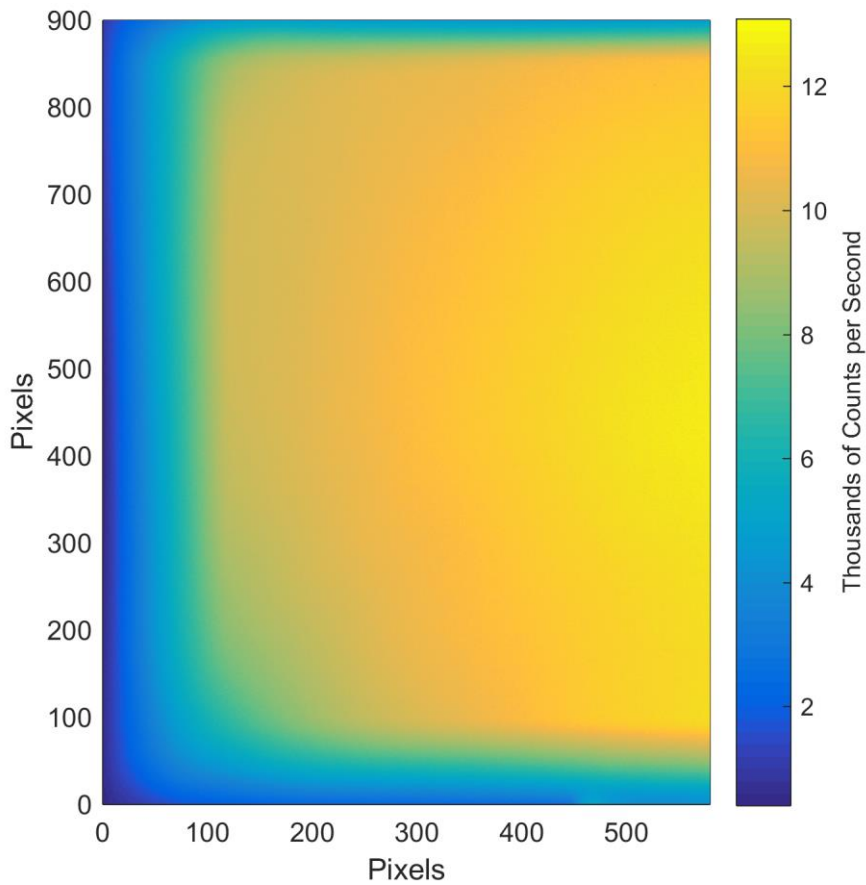


**Figure 4-7:** A calibration image after stray light removal has been performed where the measured wavelength is 750 nm with a 1 second exposure time. Vignetting can be seen as moving away from center of the image. Additionally the last  $1^\circ$  of the horizontal FOV on the right side is lost due to strong contamination from reflections within the system. Originally published as Figure 7 in Elash *et al.* (2016).

The use of the AOTF has potential to increase the amount of internal stray light due to the fact that the undiffracted beam and the unmeasured polarization also propagate through the system.

However, the diffraction interaction only occurs when the acoustic wave signal is applied, so without the acoustic wave the recorded measurement only contains the stray light in the system. Using this unique characteristic of the AOTF, the stray light of the system was measured in the laboratory. A 250 W quartz-tungsten light source was passed through a dispersing screen and onto the entrance aperture of ALI, effectively filling the entire aperture and all angles within the FOV. Using a variety of exposure times, ranging from 0.1 to 60 s and wavelengths from 650 to 950 nm in 25 nm intervals, this diffuse source was imaged twice, once with the AOTF in its off state, with no driving acoustic wave, and once with the AOTF in its on state, with the acoustic wave applied. For each pair of measurements the image with the “AOTF-off” only contains stray light in the system, and the “AOTF-on” image contains the stray light combined with the image of the diffuse source. Subtracting the “AOTF-off” image from the “AOTF-on” image yields a final image that contains only the image of the diffuse source. A typical example of a resulting image is shown in Figure 4-7. The observed vignetting is caused by the aperture of the AOTF, expected from the ray tracing model, and light entering the AOTF outside the acceptance angle. Note that this method also partially removes dark current associated with the detector. This two-image method was used operationally during the balloon measurement campaign such that images captured had a corresponding “AOTF-off” image immediately obtained with the same exposure time. For the calibration images an average stray light to signal ratio of  $2.5 \cdot 10^{-2}$  was noted.

#### **4.4.5 Relative Flat-Fielding Correction**

With the simple optical layout chosen for the prototype, some in-field light gets blocked by the AOTF aperture causing a vignetting of the image. As the FOV is increased, so is the vignetting. Furthermore, at the extreme range of the FOV, approximately the last half degree in each direction, the angles are outside the acceptance angle of the AOTF. This causes a decrease in diffraction efficiency. Both of these effects also needed to be calibrated. The flat-field calibration corrects

optical and detector level differences in the system across the FOV such that a calibrated image of a perfectly diffuse source yields a constant value across the image. The resulting images from the diffuse source described above were used to determine the flat fielding corrections for ALI. These were determined in two steps: spatial and spectral.

The experimental measurements from the stray light calibration mentioned above were also used to perform the relative flat-fielding calibration. For the spatial correction the stray light was removed and for each image at a given wavelength, each pixel was scaled to the mean value of the center 25x25 pixels. These scaling factors were averaged across all images of the same wavelength to determine the flat-fielding coefficient for each wavelength. The flat-fielding scaling coefficient had no more than a 4% standard deviation.

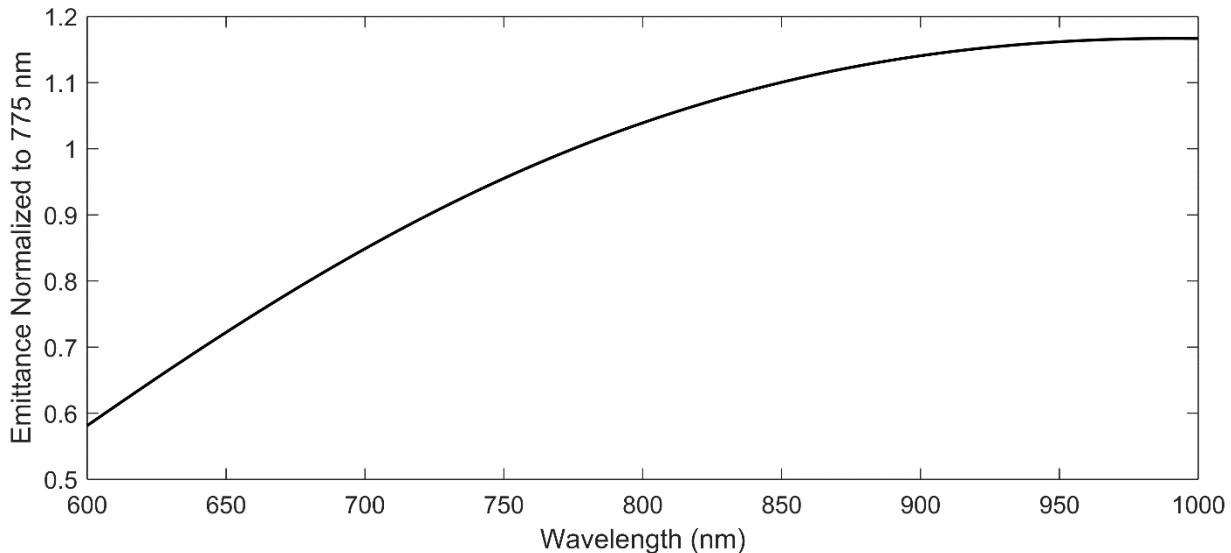


**Figure 4-8:** The blackbody emittance curve from Equation 4.6 normalized to 775 nm.

For the spectral calibration, ALI is most sensitive at 775 nm so this wavelength was chosen as the reference wavelength of a relative spectral calibration. All flat-fielding corrections were then scaled to the blackbody curve of a tungsten halogen bulb normalized to 775 nm assuming an

operating temperature,  $T$ , of 3300 K using a method by *Kosch et al.* (2003). The blackbody emittance,  $E(\lambda, T)$ , of a filament bulb is given by

$$E(\lambda, T) = \varepsilon(\lambda, T) \frac{2\pi c}{\lambda^4} \frac{1}{\exp\left(\frac{hc}{\lambda kT}\right) - 1}, \quad (4.6)$$

where  $\varepsilon(\lambda, T)$  is the emissivity of the tungsten filament,  $c$  is the speed of light,  $h$  is Planck's constant, and  $k$  is Boltzmann's constant. The emissivity values for tungsten were acquired by work done by *Forsythe and Worthing* (1925) and used to compute the spectral emittance of the bulb normalized to 775 nm seen in Figure 4-8.

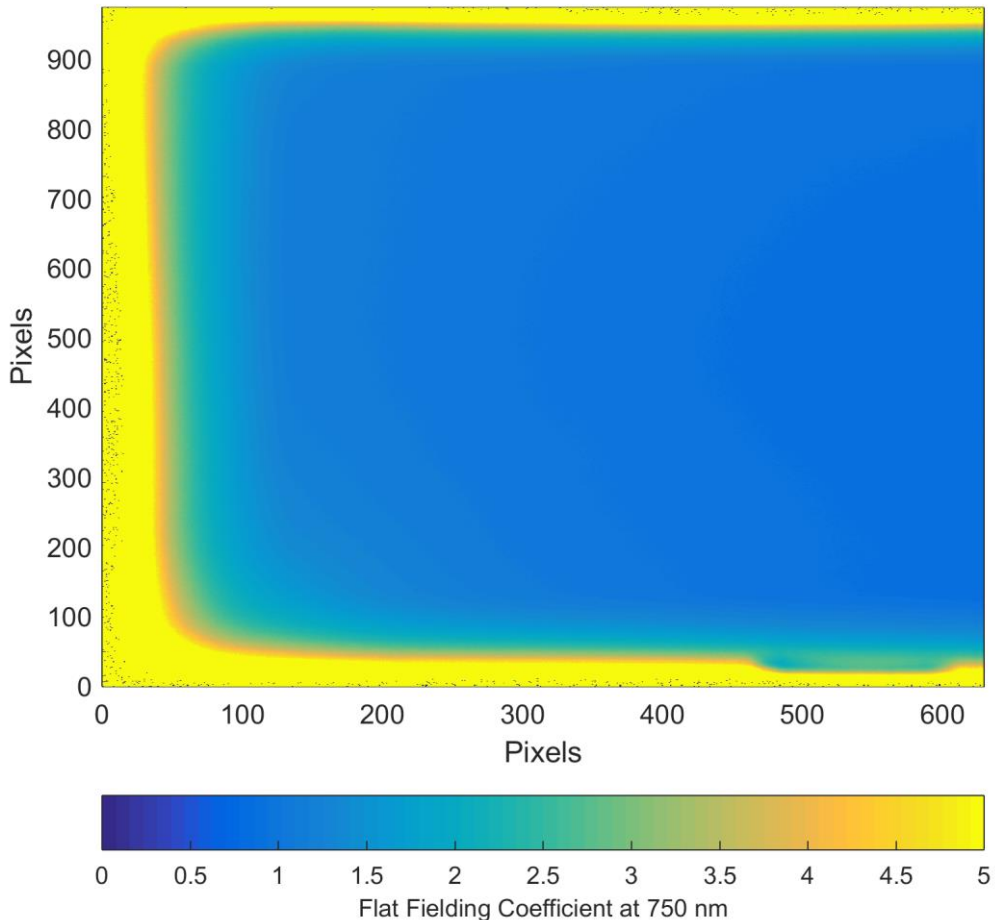


**Figure 4-9:** The flat fielding coefficients for 750 nm.

An example of the flat fielding coefficients for 750 nm can be seen in Figure 4-9. A majority of the coefficients for the central FOV are near unity, yielding good sensitivity throughout most of the image. However, due to the vignetting and the loss of diffraction efficiency near the edges of the image, the flat fielding values in these regions are larger than the more central FOVs. Note that no absolute calibration was performed due to lack of availability of an appropriately calibrated source.

#### **4.5 Integrated Testing**

With the completion of the ALI instrument, including the optical chain, power and electronics hardware, and system software, a full system test was performed, including a mass and power check. ALI was set up in a flight configuration to simulate the launch of the balloon. During the test, ALI was completely controlled from a ground station computer over a local area network to simulate the stratospheric balloon's communication interface. All commands were sent to ALI from the ground station and the simulation performed a full but shortened mission plan, which including pre-flight checks, launch, science measurement acquisition, and mission termination. During the simulation, the temperature and pressure during the flight could not be simulated. However the electronics were pressure tested separately and no issues were noted.

The full integration testing occurred on August 18, 2014, along with a second instrument, the OSIRIS development model (*Kozun 2015; Taylor, 2015*) which was flown alongside ALI during the Timmins campaign. The OSIRIS development model was connected to the same local network, as would be the case during the flight, to be a further test for both ALI and OSIRIS to locate any cross communication problems between multiple instruments.

The testing suite for ALI consisted of testing the pre-flight commands to verify full systems operation, ascent operational mode, science operational mode, and system power down. Each

mode tested the various states of ALI during the balloon mission. Further, all of the possible commands for ALI were also tested in various orders to verify no issues with their operation.

The full integration test found a few minor software bugs that were not found prior, but no major problems were noted with ALI itself or any cross communication problems with the OSIRIS development model. The minor software issues were patched and tested on ALI before a final stable version of the software was loaded onto both the ground and flight computer systems and were considered to be the final flight version for the mission. Finally ALI's power consumption and mass were checked to verify that they were within the requirements as listed in section 2.6.1. The total mass was  $37.4 \text{ kg} \pm 5\%$  and the average power draw was  $70 \text{ W} \pm 10\%$  with a peak draw of  $80 \text{ W} \pm 10\%$ , which were within the requirements of the balloon flight.

# CHAPTER 5

## STRATOSPHERIC BALLOON FLIGHT AND AEROSOL RETRIVALS<sup>1</sup>

### **5.1 Stratospheric Balloon Flight**

After the completion of the calibrations and the system tests on August 18, 2014, ALI was transported to the Canadian Space Agency launch facility in Timmins, Ontario, to prepare for the balloon test flight. Integration and system testing on the gondola occurred from August 25, 2014 until September 18, 2014. During the campaign, there were seven balloon launches, including the ALI flight on the seventh balloon on September 19, 2014.

This chapter explains the procedures used to integrate the instrument onto the gondola for the stratospheric balloon flight. Following, results from the flight are presented including flight path, instrument parameters, and sample calibrated relative radiance images. Finally, scientific results from the flight measurements are presented, including retrieved multi-spectral aerosol extinction profiles, and particle size information.

#### **5.1.1 Preflight Preparations**

The Canadian Space Agency (CSA) balloon launch facility in Timmins, Ontario is located at the Victor M. Power Airport ( $48.47^{\circ}\text{N}$   $81.33^{\circ}\text{W}$ ). The ALI shipment arrived at the base on August 25, 2014 with a scheduled launch window from September 8 to 14, 2014. Before the launch, several tasks were performed including verification of system performance after shipping, removal of a seal on the detector array to allow for low pressure operation, thermal insulation of the case, and integration onto the Centre National d'Etudes Spatiales (CNES) CARMEN-2 gondola.

---

<sup>1</sup> Portion of sections 5.1.1, 5.2, 5.3.1, 5.3.3, 5.3.4 and 5.4 as well as Figure 5-3, Figure 5-6, Figure 5-7, Figure 5-8, Figure 5-13, and Figure 5-15 were originally published in *Elash et al. (2016)*

The system check included verification of automated startup, establishment of telemetry connection, ensuring that the system powered on all components with no errors, and that the science operation program functioned. This test verified that no functional problems occurred to the instrument during transportation, and all temperature and voltage sensors, GPS module, and CCD camera were reporting valid diagnostic values.

An imaging check was performed in the integration hall to verify that no optical components suffered damage or misalignment during transportation. An EIA 1956 resolution target was illuminated by a 250 W tungsten halogen light source and was imaged by ALI to verify the optical layout. The recorded images were very similar to the ones taken in the laboratory before leaving Saskatoon.

An important final item of preparation before integration with CARMEN-2 gondola was removal of the detector seal. The QSI CCD detector was in a vacuum-sealed chamber designed for operation at atmospheric pressure. This seal was removed so as to not develop a pressure gradient between the detector chamber and the low pressure environment of the stratosphere, which could cause permanent catastrophic damage to the detector. Following manufacturer advice, the orange o-ring shown in Figure 5-1 was simply removed and the camera panel replaced. Following this another set of test resolution target images were taken to check for any impact of this operation. Results were very similar to the set of measurements taken before the seal was removed, except for an approximately 5% drop in overall signal level. Although this may have been caused by unsealing the detector it is more likely due to a change in the lighting of the resolution target in the non-optimal conditions of the integration hall. With all optical and electronic verifications complete the thermal insulation discussed in section 3.4.4 were added to ALI.



**Figure 5-1:** The QSI CCD with the panel that covers the vacuum seal removed. The orange o-ring seen in the cavity is removed from the chamber to break the vacuum seal on detector.

The mounting of ALI on the CARMEN-2 gondola is shown in Figure 5-2. ALI used the power and communication subsystems of CARMEN-2. Testing was performed in collaboration with the CARMEN-2 engineering team to verify that there were no issues between ALI and CARMEN-2 systems.

It should be noted that several other instruments were also integrated on the CARMEN-2 gondola alongside ALI including two other Canadian remote sensing instruments: the OSIRIS-DM (Developmental Model) (*Kozun, 2015; Taylor, 2015*) and SHOW (Spatial Heterodyne Observations of Water), which measures water vapour and was developed by a collaboration between ABB, York University, and the University of Saskatchewan.



**Figure 5-2:** The ALI instrument is mounted on board the CARMEN-2 gondola (top shelf on the right). ALI located next to SHOW. ALI has a cover over the optical entrance to protect the instrument from dust and other contaminants. Thermal insulation has been added to the instrument exterior. Some of the reflective covering was blacked out to not cause additional stray light into SHOW optical path.

The CNES gondola is an actively pointed gondola with azimuthal pointing precision better than  $1'$  with the use of an onboard star tracker. ALI was orientated so it would be maintained at  $90^\circ$  from the azimuthal direction of the sun, with an overall southern field-of-view during the flight.

### 5.1.2 Balloon Flight

The flight plan for the CARMEN-2 gondola was to launch near sunrise, and provide at least four hours of sustained sunlit measurements at a float altitude of greater than 35 km before descent. The operational objectives for the ALI flight were operationally simple: to collect a suite of dark (AOTF-off) measurements for calibration purposes, and to collect several full spectrum limb images for aerosol retrieval. A secondary, optional, goal was to test the sensitivity of ALI to solar

scattering angle by recording images at various azimuthal directions by rotation of the gondola with respect to the sun.

The flight of CARMEN-2 was delayed past its launch window of September 8 to 14, 2014 due to poor weather conditions. On September 19, 2014 at 05:35 UTC (01:35 local time) ALI was launched as part of the Nimbus 7 mission from the CSA Timmins balloon launch facility. During the launch, the sky was clear with light winds allowing for a safe and uneventful launch. Due to the very early launch window, the ascent of the gondola occurred in darkness and reached its flight altitude of 36.5 km at 8:17 UTC. First light was observed by ALI over an hour later at 9:39 UTC and spectral images were recorded until 14:42 UTC. ALI was powered off at 17:15 UTC.

A visualization of the flight path with major landmarks noted can be found in Figure 5-3a. Temperature profiles for the ambient atmosphere and instrument are shown in Figure 5-3b. The black curve is the ambient atmospheric temperature at the gondola altitude and location during the flight as obtained from ECMWF reanalysis (*Dee et al.*, 2011). The blue, green, and red are from temperature sensors onboard ALI located on the baffle, camera, and RF driver respectively. The baffle temperature sensor was attached just on the inside of ALI right by the entrance aperture for the system and monitors the temperature at the front of the system. The camera sensor is attached to the back of the CCD camera and the RF driver sensor measures the surface temperature of the RF driver. ALI was thermally insulated to keep the system warm whereas the baffle temperature sensor is relatively uninsulated from the extreme cold of the environment. The effect of the cold tropopause can be seen on the gondola at approximately 6:00 UTC. The cooling effect can even be seen on the interior CCD and RF driver sensors which are thermally isolated from the exterior temperature. After the internal temperature drop, the system reaches an equilibrium temperature until the sun rises and solar radiation comes into contact on the instrument at approximately

10:00 UTC at which point there is a small and gradual increase in the system temperature. All of the temperatures were kept within operating range throughout the flight.

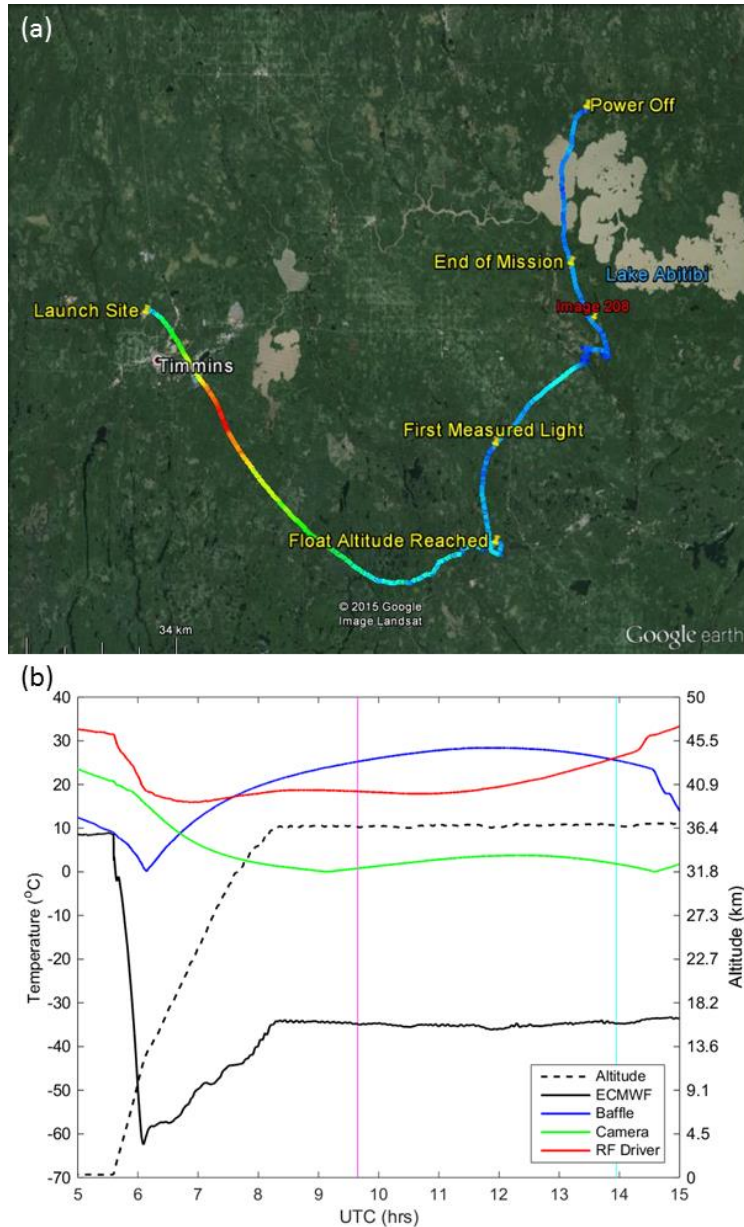


**Figure 5-3:** (a) The GPS data from ALI during the Nimbus 7 mission generated via Google Earth. The colour of the line represents the absolute speed of the gondola during the mission and the blue, green, red colours represent speeds of approximately 10, 70, and 140 km/h. Important landmarks are noted on the image. The end of mission represents the end of the data collection. No GPS data was collected from ALI after power down. The location of image 208 is the red label. (b) The temperature and altitude profiles from the Nimbus 7 flight. The time of image 208 is shown by the cyan vertical line and first light measured by ALI occurs at the magenta vertical line. Originally published as Figure 8 in *Elash et al. (2016)*.

During the flight, ALI was operated in two primary acquisition modes, a calibration mode and a limb imaging mode. The first mode, the calibration mode, was primarily used during ascent when the gondola was in darkness and intermittently between the limb imaging mode during sunlit conditions. During this mode, the AOTF was kept in the “off” state and the system imaged essentially only dark current during the ascent in darkness and dark current plus stray light during sunlit conditions. Eight exposures were taken in the calibration mode with 0.05, 0.1, 0.5, 1, 2, 3, 5, 10 second exposure times.

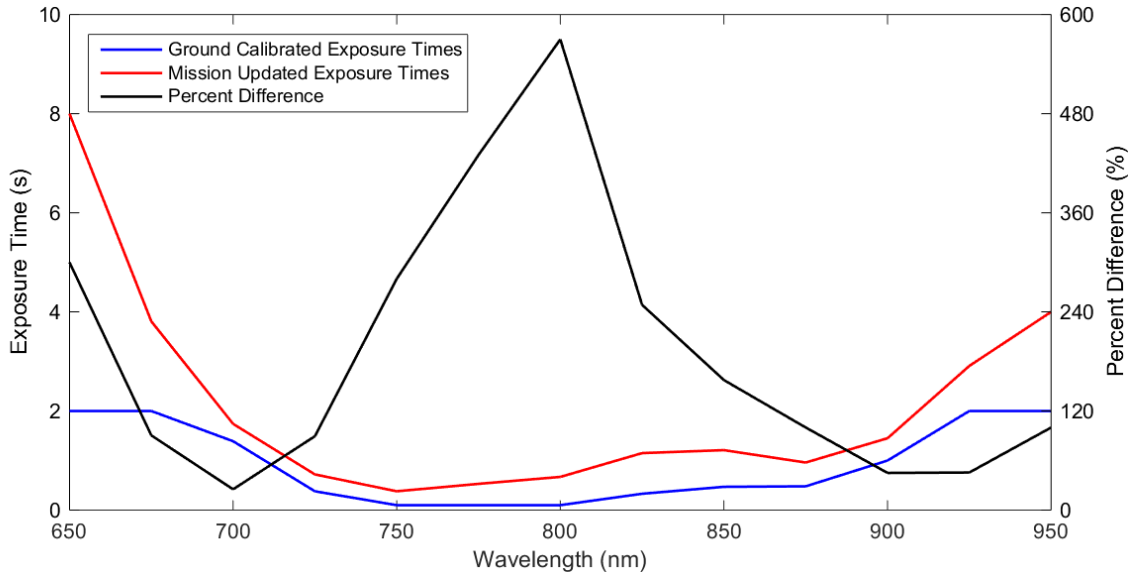


**Figure 5-4:** During the flight the calibrated exposure times was updated. The blue curve represents the exposure times from the ground calibration and the red curve is the recalibration during the flight. The black curve is the percent change in between the pre-flight calibrated results and the during flight calibration.

The second operational mode, the limb imaging mode, recorded measurements in a cycle that contained 13 pairs of images across the spectral range (650-950 nm every 25 nm). Each pair of images included a calibration image with the “AOTF-off” and an image of the limb. Each cycle took approximately 10 minutes with each measurement set taking approximately 45 seconds to acquire with initial exposure times shown in Figure 5-4 in blue. These were the exposure times

determined during the ground based testing of ALI (see section 4.4.1). However, during the flight it was determined that the calculated exposure times were not long enough and the images were somewhat underexposed. The commanding software allowed adjustment of the exposure times during the flight using the image statistics that were sent down with the housekeeping data stream. A comparison of the two exposure time curves with the percent increase can be seen in Figure 5-4. The percent increase is given by

$$\text{Percent Difference} = \left| \frac{t_c - t_u}{t_c} \right| * 100\%, \quad (5.1)$$

where  $t_c$  is the exposure time for the original calibration and  $t_u$  are the updated exposure times calculated from the flight.

The Nimbus 7 flight lasted for 16 hours 19 minutes with a successful landing at 21:54 UTC. During the flight, ALI successfully gathered 216 limb images. The gondola landed 70 km from Amos, Quebec or approximately 250 km from the launch facility. CARMEN-2 was recovered by the balloon recovery team and was returned to the base on September 21, 2015. ALI was removed from the gondola, repacked and transported back to Saskatoon, Saskatchewan.

## 5.2 Limb Measurements

After the successful post-flight recovery, ALI was unpacked and checked for any damage in Saskatoon, SK on September 25, 2014. No obvious damage had occurred to ALI from the flight and the instrument was tested to verify no internal damage had occurred. There was no damage sustained to ALI from the flight. 216 raw limb image pairs were obtained from the flight and the calibration was performed, including the pointing alignment discussed below and the image calibrations detailed in section 4.4.

ALI recorded the position and altitude information of each measurement from the onboard GPS but the pointing, i.e. orientation, information was determined by the gondola system. Azimuth and

zenith directional information are needed to determine the mapping of the line-of-sight of each pixel on the CCD to the atmospheric limb. The CNES team was able to supply the Solar Azimuth Angle (SAA) information at high time resolution and this was correlated to the images using GPS time. The zenith direction was only specified in terms of stability, *i.e.* time periods when no motion was detectable to within  $0.1^\circ$ . These stable periods were used in the following analysis. Therefore some manual calibration of the absolute zenith angle was required. ALI was mechanically tilted at  $3^\circ$  to allow the full  $6^\circ$  field of view to image the limb from the ground to float altitude. Thus the zenith angle of the center of the field-of-view was initially assumed to be  $93^\circ$  assuming a balanced gondola. However, there is no guarantee that the gondola was perfectly balanced so a manual calibration was performed by varying the zenith angle from  $92^\circ$  to  $94^\circ$  in  $0.1^\circ$  intervals and the tangent altitude was calculated for each case. Then the radiance profiles for each zenith angle was compared to find zenith angles where the features were aligned, such as cloud radiance features whose tangent altitudes occur below the tropopause. The zenith angle with the optimal alignment was determined to be  $92.6^\circ$ . An uncertainty of  $0.1^\circ$  was determined from this analysis, which agreed with the stability rating of the gondola.

The calibration techniques discussed in section 4.4 were then applied to the raw images to produce the final calibrated radiance. As an example, image number 208 is used to demonstrate the steps in the calibration on a flight image. Image 208 was recorded with a wavelength of 750 nm and taken at 13:57 UTC with a SZA and SSA of  $63^\circ$  and  $98^\circ$  respectively. The dark current and DC offset have been removed from image 208 using Equation 4.5. Next, the stray light is removed by using the “AOTF-off” or calibration image and removing it from the “AOTF-on” or measurement image. The result of this procedure can be seen in Figure 5-5. In the first panel, abnormal bright spots are noticed in the right side and the top right of the measurement. These

same features are noticed in the stray light image. By subtracting the AOTF-off image from the measurement image, a final smooth measurement image is noted in the last panel. Finally, a flat fielding calibration is performed (see section 4.4.5) and a final calibrated image can be seen in Figure 5-6a. Remember that no absolute calibration was performed on ALI, so the radiance is relative to the 775 nm laboratory calibration in arbitrary units. The error,  $\epsilon$ , on a given pixel for the radiance measurements were given by

$$\epsilon^2 = \epsilon_{read}^2 + \epsilon_{DC}^2 + \epsilon_{dark}^2 + \epsilon_{stray}^2 + \epsilon_{ff}^2, \quad (5.2)$$

where  $\epsilon_{read}$  is the readout uncertainty from the CCD, which is 15 counts at worst,  $\epsilon_{DC}$  is the error in the DC offset calibration,  $\epsilon_{dark}$  is the error from the dark current in the CCD,  $\epsilon_{stray}$  is the error in the stray light calibration, and  $\epsilon_{ff}$  is the error in the flat field corrections. The average error per pixel was approximately 14-21% of the radiance. Most of the error for the radiance is from the flat fielding calibration accounting for approximately three-quarters of the overall error. The last quarter comes from a combination of the other four sources.

From image 208, the horizontal structure across the image is nicely revealed by calculating the mean radiance profile across the image and then removing it from each profile, *i.e.* each column of pixels. This is shown in Figure 5-6b, where thin clouds (2 km vertical extent or less) are clearly seen near and below the tropopause level, with substantial variation in tangent altitude across the horizontal FOV. These clouds were also observed from other instruments on board the gondola during the mission (B. Solheim, private communication, 2014). A brief check on the CALIPSO quick-look plots also shows clouds at a maximum height of approximately 13 km from measurements taken at 08:40 UTC at 47.24°N, 95.25°W, the nearest measurement point to the ALI location and time. Although these images only have a 35 km extent in the horizontal direction, there is also some indication of horizontal variation in radiance significantly above the cloud level,

possibly due to real atmospheric variability in the aerosol layer. It should also be noted that some high altitude stray light is also visible in this mean residual image that was not observed in the laboratory tests. For the high altitudes in the range of 27 to 30 km the expected ratio of signal to stray light was estimated to be between 2-3, but for the campaign the ratio of signal to stray light for some regions dropped down to slightly below one. This may be due to contamination from scattering from a baffle vein or a nearby component of the gondola, although the true cause is unknown.

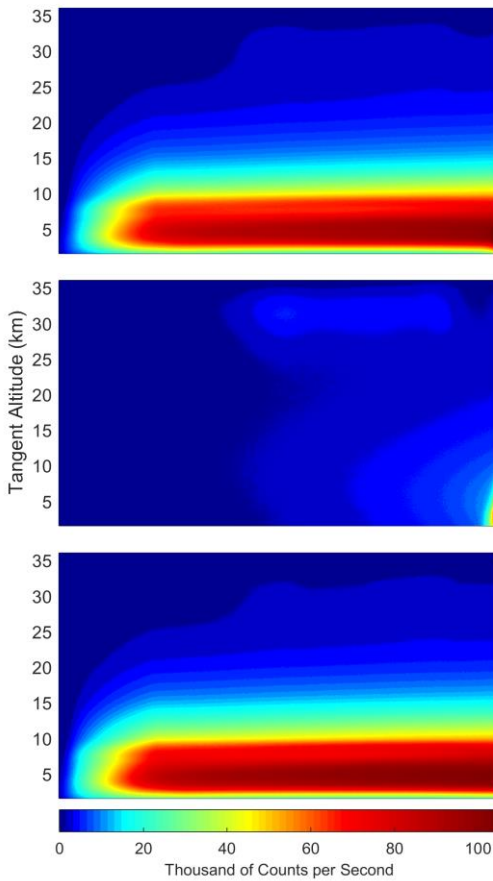


**Figure 5-5:** Stray light removal technique was performed using image 208 which is a 750 nm measurement. The top panel is the image after the DC offset has been removed from the measurement. The middle panel is the associated AOTF-off image and stray light features are seen in the upper right of the image as well as light being registered in the entire right side of the image. The final panel is the first panel minus the second panel and the abnormal gradient has been removed from the final image, leaving a cleaner radiance profile.

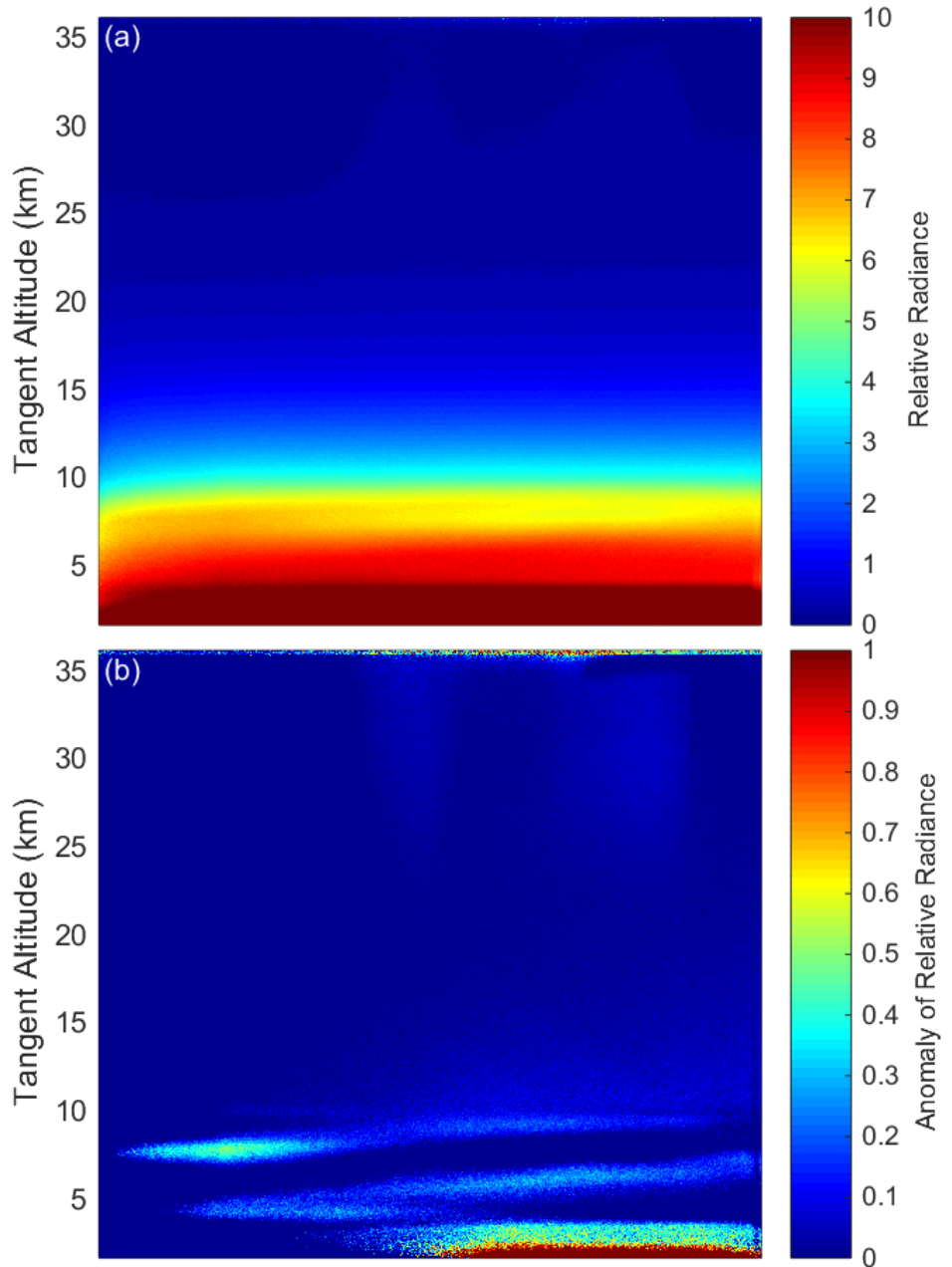


**Figure 5-6:** (a) Final calibrated 750 nm image, taken at 13:57 UTC located at  $48.55^{\circ}\text{N}$ ,  $80.00^{\circ}\text{W}$  with a SZA and SSA of  $63^{\circ}$  and  $98^{\circ}$  respectively. The horizontal FOV is 30 km.(b) The same 750 nm image with the mean of the profile removed from the image leaving the residual signal that shows thin clouds in the troposphere. Originally published as Figure 9 in Elash *et al.* (2016).

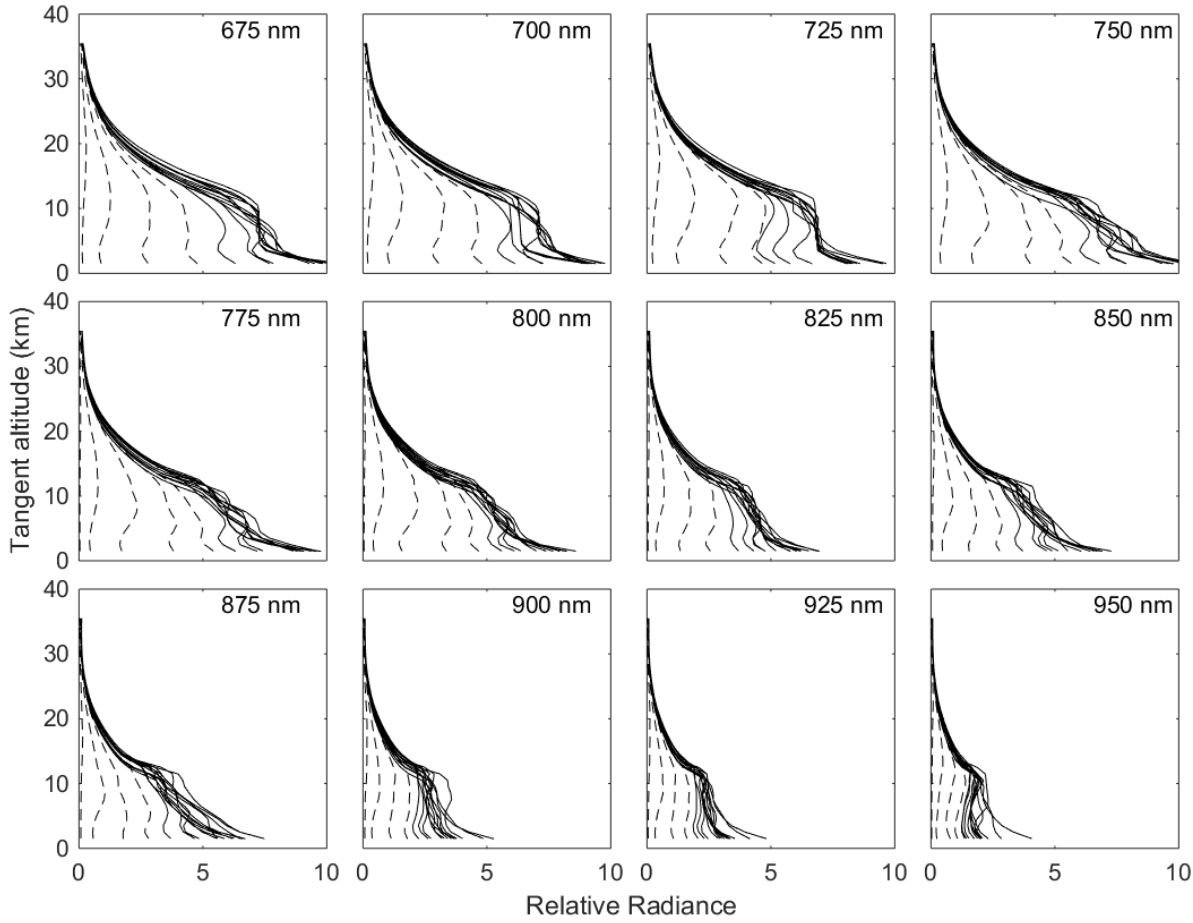


**Figure 5-7:** Averaged ALI relative radiance vectors from 12 of the 13 wavelengths from the Nimbus 7 flight. Each panel presents the radiance vectors from a different wavelength measured which is denoted in the top right corner. The dashed lines are radiance profiles where the SZA is greater than  $90^\circ$  and solid lines are profile where the SZA is less than  $90^\circ$ . Originally published as Figure 10 in Elash *et al.* (2016).

For ease of further analysis, and to decrease the uncertainty of the measurements to a minimum of 0.6 MTF, the images were averaged into cells of 25 pixels horizontally and averaged vertically onto a 1 km tangent altitude grid. The errors for the averaged radiances, E, is given by

$$E = \left( \frac{1}{(N-n)(M-m)} \sum_{i=n}^N \sum_{j=m}^M (\epsilon_{i,j})^2 \right)^{\frac{1}{2}}, \quad (5.3)$$

where the errors for each pixel,  $\epsilon_{i,j}$ , are summed in vertical,  $i$ , and horizontal,  $j$ , directions from the starting pixel,  $n$  for the vertical and  $m$  for the horizontal, to the final pixel in the average,  $N$  for the vertical and  $M$  for the horizontal. For the portions of the image used for aerosol retrievals this ended up being 4-7% of the overall radiance.

The radiance profiles from the center column of the images for all measurements obtained during the flight are shown in Figure 5-7. The first set of profiles, the dashed lines, which start near zero and move toward larger values, are the measurements that were recorded near and during sunrise (*i.e.* SZA greater than  $90^\circ$ ) so the gradual increase is therefore expected. Measurements obtained for SZAs less than  $90^\circ$  are represented by the solid lines. These radiance profiles follow a similar and expected exponential shape, with some variability at tangent altitudes below 12 km corresponding largely to changing cloud conditions.

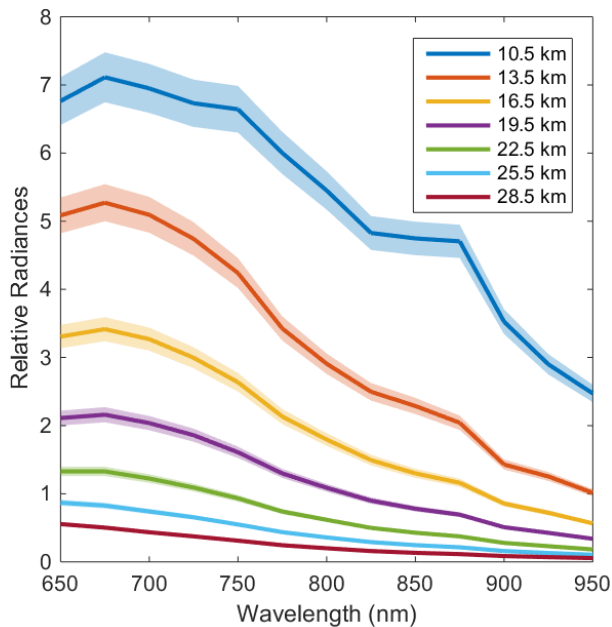


**Figure 5-8:** Relative radiances spectrally from 650 nm to 950 nm as measured from ALI at approximately 14:20 UTC consisting of images number 204 to 216 looking  $90^\circ$  in the azimuth from the sun facing southwards. These spectral profiles are presented at several tangent altitudes with a horizontal look direction of  $0^\circ$ . The shading represents the error on the radiances. Originally published as Figure 11 in Elash *et al.* (2016).

A full cycle of 13 spectral images (numbers 204-216) were used in Figure 5-8 to show the spectrum of relative calibrated radiances at selected tangent altitudes. The estimated uncertainty in the radiance is represented by the shading and was calculated using Equations 5.2 and 5.3. The uncertainty is approximately five percent from 5 to 20 km and increases up to eight percent from 20 to 35 km. The spectra displays the expected and relatively smooth fall off in intensity with increasing wavelength with Chappuis ozone absorption seen at the lower wavelengths; however, the reason for the peak in the spectra at 875 nm is not known and may be due to an inconsistency in the pre-flight calibration.

### **5.3 Aerosol Retrievals**

From the successful flight, radiance measurements from ALI were used to determine aerosol parameters. The following sections describe the Multiplicative Algebraic Reconstruction Technique (MART) retrieval method used to determine aerosol extinction and particle size information. The retrieved aerosol profiles from ALI is presented and is compared to the OSIRIS version 5.07 aerosol extinction product for coincident satellite overpasses. Following, a cycle of aerosol measurements are used to determine a particle size distribution estimate that is compared with particle size parameters from other instruments.

#### **5.3.1 Aerosol Extinction Retrieval Methodology**

The inversion of the ALI radiances used a Multiplicative Algebraic Reconstruction Technique (MART), discussed in section 2.6.3. Specifically we have applied a slightly modified version of the standard OSIRIS stratospheric aerosol extinction retrieval (*Bourassa et al.*, 2007; 2012b). This inversion algorithm, which is applied from the tropopause to 30 km altitude, assumes log-normal distributed hydrated sulphuric acid droplets (see Equation 2.1) in order to calculate the aerosol scattering cross section from the Mie scattering solution. The modeled radiances for the nonlinear

inversion were computed with the SASKTRAN-HR radiative transfer engine using the newly developed vector module for polarization (*Bourassa et al.*, 2008; *Zawada et al.*, 2015; *Dueck et al.*, 2016). The output of SASKTRAN-HR gives the Stokes vectors for the radiance in the model reference frame, which are then rotated into the instrument's coordinate system (see section 2.4.5). Once rotated, the polarization signal required to match the ALI measurement is the vertical polarization given by

$$I_v = \frac{1}{2}(I - Q), \quad (5.4)$$

where  $I$  and  $Q$  are Stokes parameters defined by  $I = \langle E_x^2 \rangle + \langle E_y^2 \rangle$  and  $Q = \langle E_x^2 \rangle - \langle E_y^2 \rangle$ . The variables  $E_x$  and  $E_y$  are the horizontal and vertical component of the electric field in the instrument reference frame.

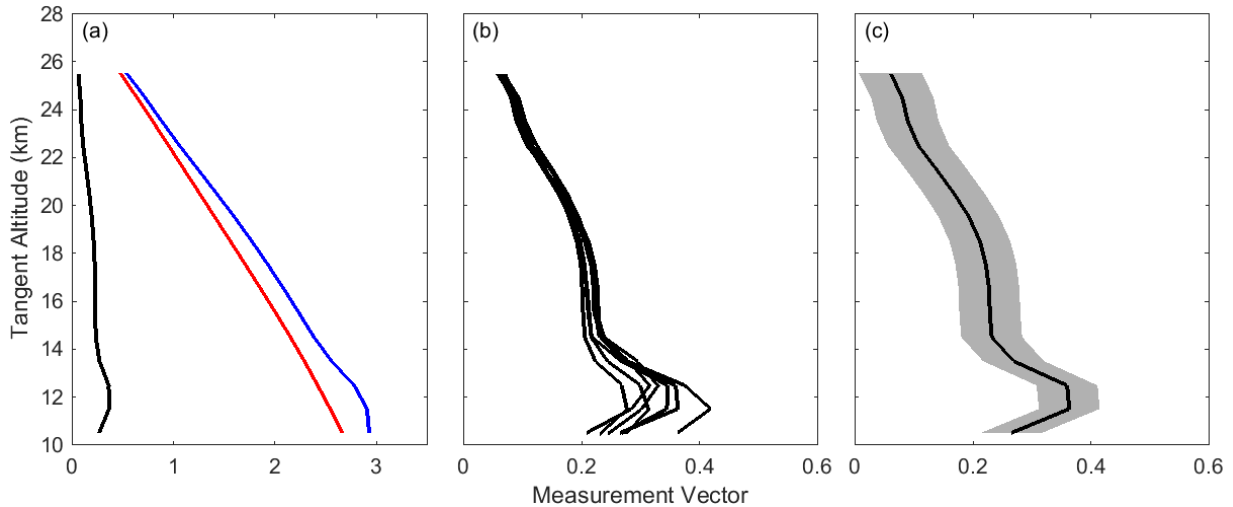


**Figure 5-9:** (a) The black, blue, red curves represent the measurement vector,  $\mathbf{y}$ , first term of Equation 5.5, and second term of Equation 5.5 using image 208 (b) A collection of all of the measurement vectors at 750 nm during the mission with a SZA less than 90°. (c) Image 208 measurement vector with associated error represented by the shading.

The relative radiance measurements from ALI are used to create measurement vectors,  $\mathbf{y}$ , as specified in *Bourassa et al.* (2012b) in the form,

$$\mathbf{y} = \log\left(\frac{\mathbf{I}_v(\mathbf{z}, \lambda)}{I_v(z_{ref}, \lambda)}\right) - \log\left(\frac{\mathbf{I}_{v,ray}(\mathbf{z}, \lambda)}{I_{v,ray}(z_{ref}, \lambda)}\right), \quad (5.5)$$

where  $\mathbf{I}_v(\mathbf{z}, \lambda)$  is the measured relative radiance from ALI at an altitude  $z$  and  $I_v(z_{ref}, \lambda)$  is the relative radiance at a high reference tangent altitude where there is little aerosol contribution. For the ALI measurements, the highest possible tangent altitude where the signal is above the noise threshold is approximately 30 km tangent height and typical values for  $z_{ref}$  were between 27 and 30 km. The second term in Equation 5.5 uses modeled radiances from SASKTRAN-HR with only the molecular atmosphere to approximately remove the Rayleigh signal. This is done to improve the speed of the convergence of the retrieval (Bourassa *et al.*, 2012b). Figure 5-9a shows the measurement vector from a 750 nm image (number 208) from the center column of the CCD. The final measurement vector,  $\mathbf{y}$ , is shown in the black, with the first term of Equation 5.5 in blue and the second term in red. Removing the Rayleigh component of the signal from the measurement vector increases the sensitivity to aerosol, which increases the speed of convergence of the solution. All of the measurement vectors for the 750 nm images from the mission can be seen in Figure 5-9b.

An initial guess state,  $\mathbf{x}_a$ , for the aerosol extinction and an assumed particle size distribution profile are set in the SASKTRAN-HR model. The forward model vector is then constructed similarly to the measurement vector, and used in combination with the measurement vector to update the aerosol extinction coefficient profile using the MART algorithm,

$$\hat{x}_i^{(n+1)} = \hat{x}_i^{(n)} \sum_j \frac{y_j}{F(z_j)} W_{ij} \quad (5.6)$$

where  $\hat{x}_i$  is the aerosol extinction at each model altitude,  $i$  and  $j$  denotes a tangent altitude from the measurements. The forward model result is defined by  $F(z_j)$  and the weighting matrix,  $W_{ij}$ , relates the importance of each element of the measurement vector to each retrieval altitude. It

should be noted that this inversion technique is computationally efficient as it allows for the updating of the atmospheric state without calculating the Jacobian (*Degenstein et al.*, 2009). This iterative process is run until the solution has converged and the value of the summation is approximately one and the final aerosol state is determined.

A precision estimate is also required for the retrieved aerosol profiles, and an uncertainty estimate on the measurement vector is performed. To yield the uncertainty on the measurement vector at a specific tangent altitude,  $j$ , Equation 5.5 is differentiated and terms are summed in quadrature yielding the following result

$$\delta y_j^2 = \left( \frac{\delta I_\nu(z_j, \lambda)}{I_\nu(z_j, \lambda)} \right)^2 + \left( \frac{\delta I_\nu(z_{ref}, \lambda)}{I_\nu(z_{ref}, \lambda)} \right)^2 + \left( \frac{\delta I_{\nu,ray}(z_j, \lambda)}{I_{\nu,ray}(z_j, \lambda)} \right)^2 + \left( \frac{\delta I_{\nu,ray}(z_{ref}, \lambda)}{I_{\nu,ray}(z_{ref}, \lambda)} \right)^2. \quad (5.7)$$

However, the only uncertainty that is considered here is due to the measurement and calibration errors and systematic biases from the SASKTRAN-HR model are ignored. Since the Rayleigh components are modeled, they are dropped from the uncertainty, simplifying the above result to

$$\delta y_j^2 = \left( \frac{\delta I_\nu(z_j, \lambda)}{I_\nu(z_j, \lambda)} \right)^2 + \left( \frac{\delta I_\nu(z_{ref}, \lambda)}{I_\nu(z_{ref}, \lambda)} \right)^2 \quad (5.8)$$

An example of the uncertainty on a measurement vector for image 208 is located on Figure 5-9c.

Once a retrieval has been completed for a measured radiance profile, the result and the uncertainty estimate is then used to estimate the precision in the retrieved extinction. For each altitude, a gain matrix is defined as

$$\mathbf{G} = \frac{d\hat{\mathbf{x}}}{d\mathbf{y}} \quad (5.9)$$

where  $d\hat{\mathbf{x}}$  is the change in the retrieved aerosol extinction and  $d\mathbf{y}$  is the change in the measurement vector. The gain matrix is calculated through successive numerical perturbation of the measurement vector and re-retrieval (*Rodgers*, 2000). A much faster method is to use the Jacobian

to determine the uncertainty has been performed (*Bourassa et al.*, 2012a), but makes an assumption that the gain matrix is equal to the inverse of the Jacobian, as typically the averaging kernel is close to the identity matrix. However, this method adds additional uncertainty to the precision estimate and was deemed unsuitable for the balloon campaign. Instead, with a limited set of balloon data, it is feasible to calculate the gain matrix directly. The uncertainty at each retrieved altitude is then given by

$$\mathbf{E} = \mathbf{G} \mathbf{S}_\epsilon \mathbf{G}^T \quad (5.10)$$

where  $\mathbf{S}_\epsilon$  is the covariance matrix of the measurement vector and  $\mathbf{E}$  is the covariance of the retrieved aerosol profile (*Rodgers*, 2000). The covariance matrix is given by

$$\mathbf{S}_\epsilon = \begin{pmatrix} S_{11} & S_{12} & \cdots & S_{1n} \\ S_{21} & S_{22} & \cdots & S_{2n} \\ \vdots & \vdots & \ddots & \vdots \\ S_{m1} & S_{m2} & \cdots & S_{mn} \end{pmatrix} \quad (5.11)$$

where the individual terms are given by

$$S_{\epsilon,ij} = \begin{cases} \left( \frac{\delta I_\nu(z_j, \lambda)}{I_\nu(z_j, \lambda)} \right)^2 + \left( \frac{\delta I_\nu(z_{ref}, \lambda)}{I_\nu(z_{ref}, \lambda)} \right)^2 & i = j \\ \left( \frac{\delta I_\nu(z_{ref}, \lambda)}{I_\nu(z_{ref}, \lambda)} \right)^2 & i \neq j. \end{cases} \quad (5.12)$$

The reported precision for ALI aerosol extinction retrievals is the square root of the diagonal of  $\mathbf{E}$ .

Ideally, the ALI measurements would be used independently to also retrieve ozone in the Chappuis band (600-700 nm range for ALI). However, due to the spectral range of the prototype, only a small fraction of the long wavelength side of the absorption band was captured. For this analysis, we have not retrieved the ozone profile but have set the ozone profile in SASKTRAN-HR to an average of the five closest coincident ozone profiles measured by OSIRIS at the ALI location and time. The ozone cross sections were determined by *Burrows et al.* (1999). The surface albedo used is also from the OSIRIS scans since the two instruments share a similar measurement

method and should determine a similar albedo for the cloudy conditions. Preferably, albedo would be determined from ALI following the method of *Bourassa et al.*, 2012b, however due to the lack of an absolute calibration this was not possible.

### **5.3.2 Particle Size Retrieval Methodology**

Work done by *Rieger et al.* (2014) has shown that different particle size distributions can affect the aerosol measurement vectors, thus yielding some sensitivity to the distribution. In this study, they used an OSIRIS geometry and calculated the respective measurement vectors for a series of particle sizes. This is recreated in Figure 5-10. In panel A, three different log-normal distributions were used to calculate the measurement vectors using a simulated atmosphere through SASKTRAN. The three profiles were: a single fine mode particle size distribution with a mode radius and width of 0.08  $\mu\text{m}$  and 1.6 respectively shown in blue, bimodal particle size distribution that simulates volcanic conditions with the mode radius and width of 0.08  $\mu\text{m}$  and 1.6 for the fine mode and 0.4  $\mu\text{m}$  and 1.2 for the coarse mode, which is shown in black, and lastly the red curve is a representative size distribution with mode radius and width of 77  $\mu\text{m}$  and 1.75. Panel B shows the measurement vectors calculated with the three distributions across a series of wavelengths. The third panel, panel C, shows the difference of the measurement vectors compared to the bimodal distribution. Sensitivity to particle size is only seen past 800 nm measurements but great sensitivity does not occur until measurement are recorded out to 1200 nm. Furthermore, a 1% error in the radiance yields a relative error in the bimodal distribution measurement vector shown by the gray shading in panel C.

For ALI, measurements were only gathered between 650 and 950 nm in wavelength, due to the low sensitivity of the CCD camera in the NIR. As such, it is not be possible to determine both the mode radius and mode width of an assumed log-normal distribution. Instead, the data from ALI was used to determine an Angström exponent, which is essentially one piece of information about

the particle size distribution. The Angström exponent is an approximation to the Mie scattering solution where the value of the Angström exponent,  $\alpha$ , is related to the spectral change in scattering cross section, which depends on particle size (Angström, 1964):

$$\frac{n\sigma}{n_0\sigma_0} = \left(\frac{\lambda}{\lambda_0}\right)^{-\alpha}. \quad (5.13)$$

Lower Angström exponents correspond to larger particle sizes and vice versa for small particle sizes. Thus the relation between retrieved extinction at various wavelengths can be used to gather an understanding of aerosol particle size in the form of Equation 5.13, where  $n$  is the aerosol concentration, and  $\sigma$  is the scattering cross section, and their product is the extinction coefficient. An example of how the scattering cross section changes with particle size is shown in Figure 5-11 for the 750 nm wavelength where the Mie scattering cross section was calculated for a variety of mode radii and widths.

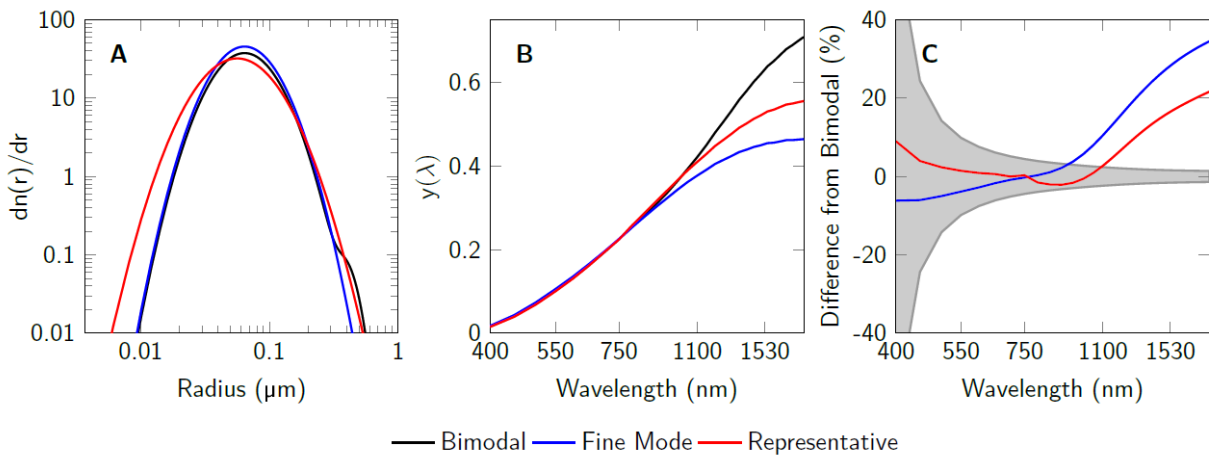


**Figure 5-10:** Reproduced from Figure 4 of Rieger *et al.* (2014). For OSIRIS scan 6432001 aerosol measurement vectors were calculated at 22.5 km. (A) The three size distributions used in the study. (B) The measurement vectors calculated via the SASKTRAN simulation (C) The relative percent difference of the fine and representative distributions with respect to the bimodal distribution. A 1% error is the radiance yields an uncertainty in the bimodal measurement vector shown by the grey shading.

Since the ALI measurements observe essentially the same atmosphere over the time of one complete spectral imaging cycle (one set of images from 650 to 950 nm), the particle size should be essentially the same for each imaged wavelength. The Angström exponent can then be determined by fitting a line through a series of spectral points in retrieved extinction by rearranging Equation 5.13 into the following

$$\alpha = -\frac{\log(n\sigma) - \log(n_0\sigma_0)}{\log(\lambda) - \log(\lambda_0)}. \quad (5.14)$$

The rearrangement demonstrates that the Angström exponent is a slope, i.e. the log of the extinction over the log of the wavelengths.

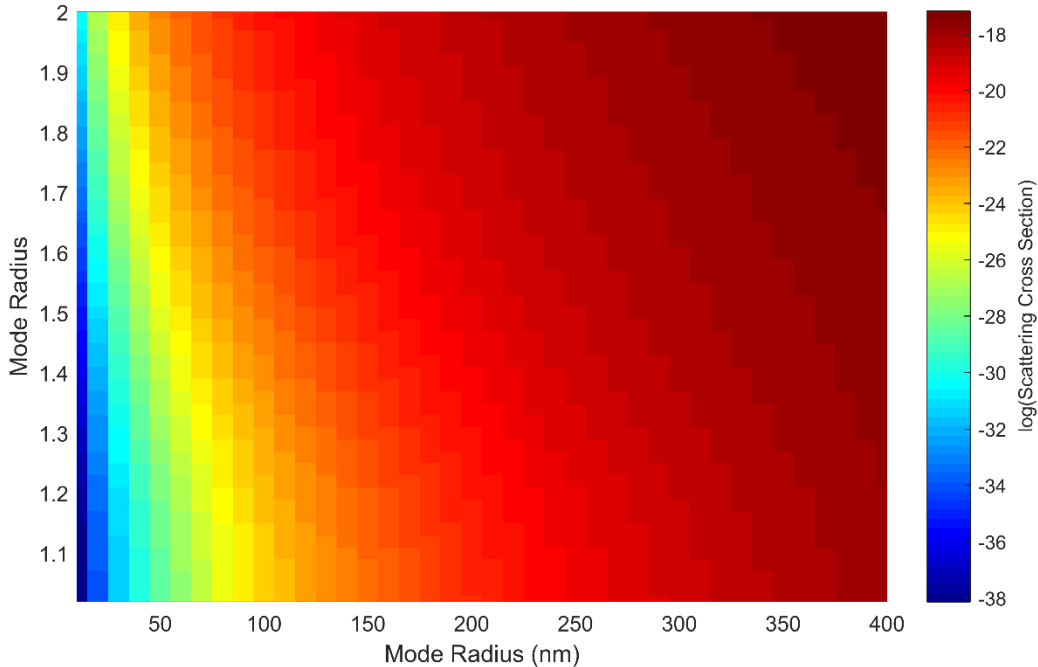


**Figure 5-11:** Mie scattering cross section at 750 nm computed with the optical properties of the SASKTRAN-HR engine. This variation of the cross section with respect to the mode radius and width allows for some determination of the particle size distribution through the Angström exponent.

Using the retrieved extinction profiles for the complete spectral range, we have attempted a determination of the Angström exponent using a method similar to that outlined by *Rault and Loughman* (2013) for the OMPS-LP analysis. In this method, the independently retrieved

extinction profiles at each wavelength and altitude are fit with a straight line in log-wavelength, log-extinction space using a least squares fit. The slope of this line corresponds to the Angström exponent. This is then used to find the best match to the spectral dependence of the Mie scattering cross section in order to update the particle size distribution. With only one piece of information, the mode-width of the log-normal distribution is fixed to 1.6 and the mode radius is updated. The extinction retrievals are then performed again at each wavelength and the process is iterated until the Angström exponent, corresponding to the determined mode radius, converges.

A precision estimate was also required for the Angström exponent. The method used is the standard method to calculate uncertainty from the least squares fit (*York*, 1966). Assuming no uncertainty in the measurement points, the error in the slope is given by

$$\delta\alpha = \frac{s}{SS_{xx}}, \quad (5.15)$$

where  $s$  is

$$s = \sqrt{\frac{SS_{yy} - \alpha SS_{xy}}{n - 2}}, \quad (5.16)$$

and  $SS_{xx}$ ,  $SS_{yy}$ , and  $SS_{xy}$  are the sum of squares of the wavelength, aerosol extinction, and cross term between the wavelength and aerosol extinction and  $n$  is the number of points. However, there is an associated error with each aerosol extinction profile as outlined in section 5.3.1. So to determine the precision of the Angström exponent, accounting for the uncertainty in the aerosol extinction, a Monte Carlo method was used. The uncertainty of the Angström exponent was calculated millions of times and for each calculation a random amount of the error from the known range was added to the extinction. Finally, the mean from all of the uncertainty calculations of all of the least squares fits was used as the precision estimate on the Angström exponent.

### 5.3.3 Aerosol Extinction Retrievals

The complete flight data set consisted of 216 image pairs that were recorded in illuminated conditions. The MART retrieval method was performed on a select complete cycle for the purpose of the analysis, specifically the set of images from 204-216 over the wavelength range of 650 to 950 nm. For the purpose of the retrieval an *a priori* particle size distribution was used with a mode radius of 0.08  $\mu\text{m}$  and a mode width of 1.6 (Deshler *et al.*, 2003). A sample of the retrievals can be observed in Figure 5-12 which shows the 750, 850, and 950 nm retrievals. The left panels show the measurement vector from ALI in black with the calculation of the measurement vector using SASKTRAN-HR in blue. For each of the wavelengths, the algorithm determines altitudes where the value of the measurement vector is less than the known noise and does not allow aerosol extinction to be retrieved in those regions. Instead, the scaling factor,  $\gamma$ , given by the summation term in Equation 5.6 is scaled to the aerosol profile above and below the last retrieved point to keep the aerosol profile smooth, as discontinuities are non-physical. The middle panel shows the convergence between the measurement vector and the forward model result. The right column of Figure 5-12 is the retrieved aerosol profiles in blue with the associated uncertainty calculated using the method described in the previous section.

The retrieved aerosol extinction profiles for the analysis cycle can be seen in the left panel of Figure 5-13, note the log scale. For the full range of wavelengths, a difference of less than 2% between the measurement vector and forward model is seen throughout the retrieval altitude from approximately 13 to 29 km. Note the behavior of decreasing extinction with increasing wavelength as expected due to the dependence of the cross section with respect to particle size.

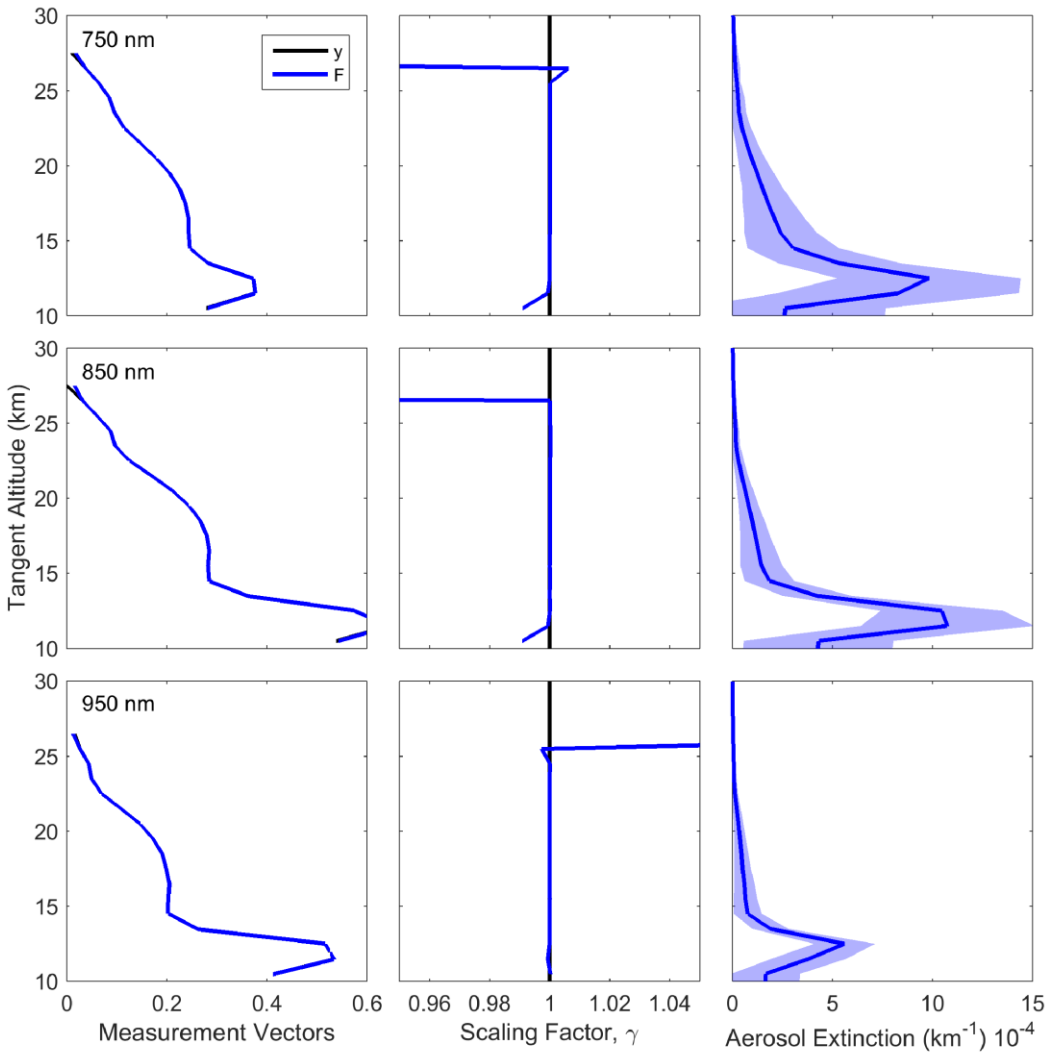


**Figure 5-12:** An example of three aerosol retrievals from images 206, 208, and 214, with center wavelengths of 750, 850, and 950 nm respectively are vertically displayed in the figure from top to bottom. The left column shows the measurement vector,  $y$ , in black with the retrieved forward model,  $F$ , in blue. The center column shows the ratio of the measurement vector over forward model known as  $\gamma$  and is the scaling factor between the ALI measurement and the forward model. For both of the first two columns, the black line is barely visible due to the very good agreement of the forward model. The final column is ALI aerosol extinction in blue with the associated error represented by the light blue shading.

The ALI 750 nm aerosol extinction profile is shown in the right panel of Figure 5-13 with the shading representing the precision of the retrieval. The error is strictly based on measurement and instrument uncertainty and neglects any model and atmospheric state uncertainties as previously outlined. The red curve is the average 750 nm aerosol extinction profiles of the same five

coincident OSIRIS scans used for the ozone profile. The retrieved extinction profiles from ALI and OSIRIS are within the total retrieval uncertainty. It is encouraging that the instruments follow the same overall profile shape including the stratospheric layer and the steep increase below 15 km. Aerosol is notoriously difficult to validate in remote sensing with various technique and instrument geometries, and yet the SAGE II, SAGE III and OSIRIS differences are generally below 20-30% up to 30 km (*Bourassa et al.*, 2012b; *Rieger et al.*, 2015). However, the comparisons between the OSIRSI and ALI are acceptable. There are also several possible systematic errors not accounted for in the inversion including the choice of retrieval altitude ranges, particle size composition and distributions, stray light, and the high altitude aerosol load.

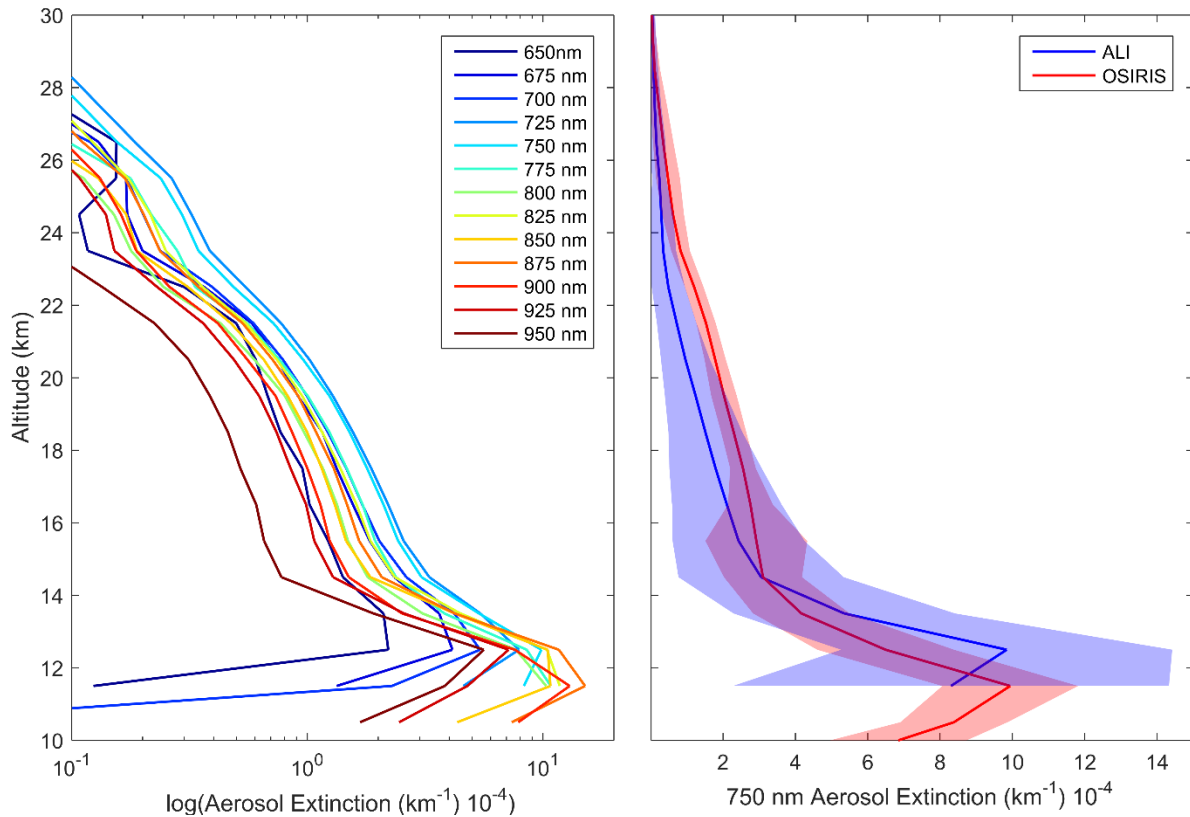


**Figure 5-13:** Left is the retrieved aerosol extinction profiles from the last complete imaging cycle consisting of images 205 to 216 from the 0.0° horizontal line-of-sight. Right is the 750 nm ALI aerosol extinction in blue with its error represented by the shading compared to the 750 nm extinction measured by OSIRIS in red with its error represented by the shading. Originally published as Figure 12 in *Elash et al.* (2016).

As a further note, other issues may have resulted in the disagreement between OSIRIS and ALI, mainly the estimation of the albedo and pointing inaccuracies. For the albedo, vertically linear polarized aerosol retrievals have a much larger sensitivity to albedo. For a scalar retrieval, changing the albedo from zero to one results in approximately a 30% increase in the aerosol extinction, but for a linear polarized measurement this change in albedo can be as large as a 100% increase in aerosol. The retrieval was performed again on image 208 using an albedo of zero and one and the results shown in Figure 5-14a. Once again, note the log scale. The albedo used from OSIRIS was 0.79. It should be noted that increasing the albedo higher than the OSIRIS values does not greatly increase the aerosol extinction. However, the retrieved aerosol profile varies by almost a factor of two just from a change in albedo. A similar reanalysis was performed using the error in the zenith pointing discussed in section 5.2. The results of the alteration of the pointing can be seen in Figure 5-14b. From decreasing the zenith angle, the aerosol extinction is increased which could account for the largest discrepancies between the OSIRIS and ALI results at the 20 km range, but moves the aerosol peak to a higher altitude causing a further discrepancy with OSIRIS at lower tangent altitudes. However, due to a lack of pointing information from the gondola this is the best estimation that could be performed.

Another source of systematic error could arise from sensitivity to the solar scattering angle in the retrieval algorithm due to the relationship between particle size distribution and the scattering phase function. For the ALI image the solar scattering angle is 98° and for the five OSIRIS scans they are 77°, 89°, 90°, 91°, 92°, and 93°. With the exception of the forward scatter angles of 77° and 89° from OSIRIS, the scattering angles between OSIRIS and ALI are similar and should not cause a large effect on the retrieved profiles. However, as noted from the study detailed in Chapter 6, a strong sensitivity to particle size distribution occurs near solar scattering angles of 90 degrees for

the vertical polarized measurements. Regardless, the comparison of the OSIRIS and ALI results are encouraging.

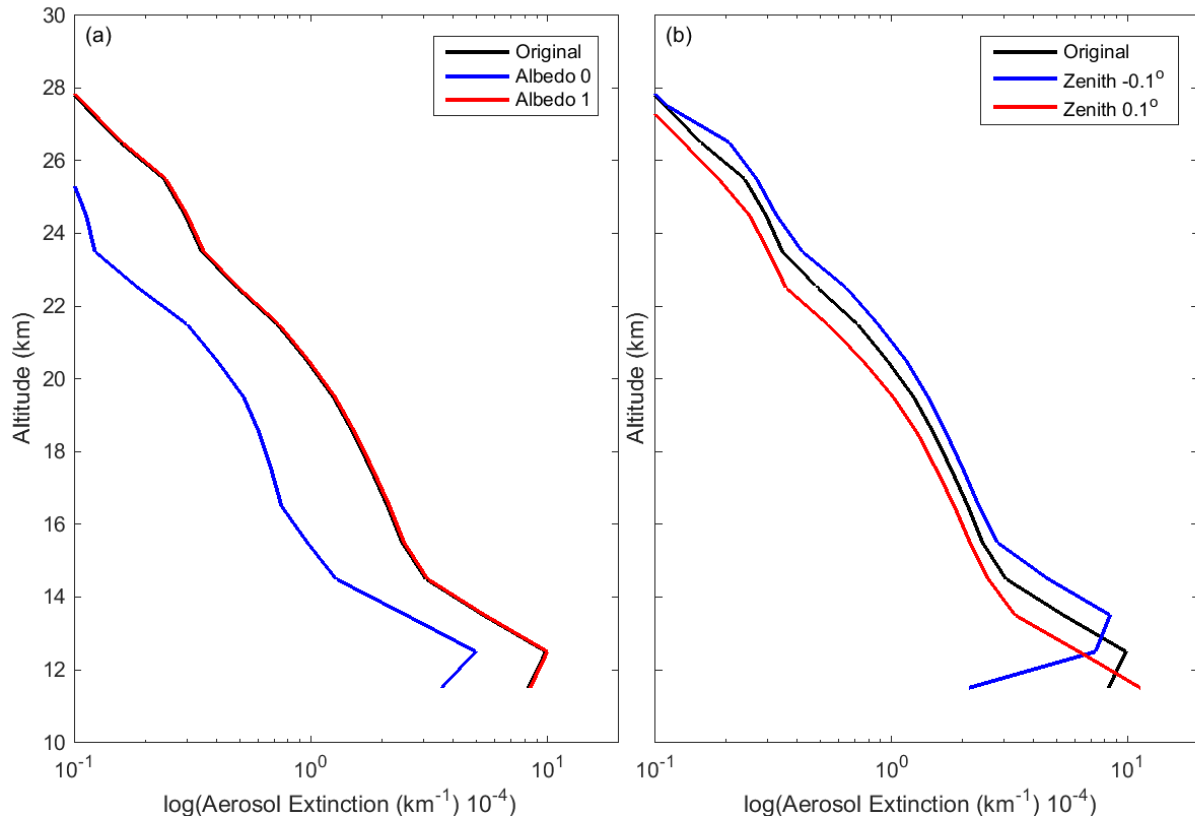


**Figure 5-14:** (a) Image 208 (750 nm) re-retrieved using an albedo of 0 and 1 compared to the original albedo used from OSIRIS. (b) Using the determined zenith pointing error from section 5.2, image 208 is retrieved again using the maximum possible pointing error compared to the original.

### 5.3.4 A Sample Particle Size Retrieval

The particle size method outlined above to determine the Angstrom exponent was also applied to this measurement set consisting of images 204 to 216. The retrieved extinction at a given altitude was rejected from the straight line fit if the converged forward model radiance at that altitude was not within 2% of the measurement vector. In the case shown in right of Figure 5-15, at the 14.5 km altitude point, only 10 of the 13 possible wavelengths contributed to the determination of the Angström exponent. The left panel of Figure 5-15 shows the median Angström exponent that was determined after each iteration and convergence can be seen after a couple iterations. The results

are shown in the middle panel of Figure 5-15, where the Angström exponent is between 2 and 3 throughout the altitude range from 13 to 22 km. Assuming a mode width of 1.6 yields a median mode radius of 0.077  $\mu\text{m}$ . In comparison to typical levels of background aerosol from the Laramie, Wyoming OPC data (*Deshler et al.*, 2003), the retrieved particle size parameters are certainly within the expected range, although there is a relatively large error bar on the retrieved value, limiting the usefulness of the retrieved particle size information for background aerosol. However, with these error bars, even this limited spectral range would have the sensitivity to detected particle size changes as seen by OSIRIS and SAGE II over recent decades due to small volcanic perturbations (*Rieger et al.*, 2014).

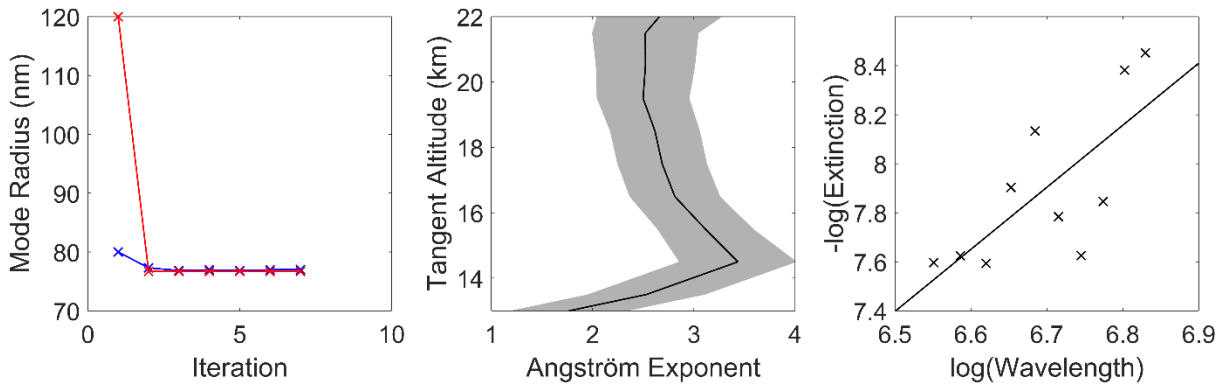


**Figure 5-15:** The left panel shows the convergence of two sample particle size retrievals, blue and red represent an initial state of 0.08 and 0.12  $\mu\text{m}$  mode radius respectively. Both initial states converge to the same value over approximately 3 iterations in the particle size retrieval method. The middle panel shows the final Angström exponents determined from images 204-216. The shading represents the error associated with the least squares fit. The right panel shows a typical least squares fit of the retrieved extinction values over wavelength to determine the Angström exponent at model altitude of 14.5 km. Originally published as Figure 13 in *Elash et al.* (2016).

# CHAPTER 6

## THE SENSITIVITY TO POLARIZATION IN STRATOSPHERIC AEROSOL RETRIEVALS FROM LIMB SCATTERED MEASUREMENTS

With the success of the ALI stratospheric balloon mission, a satellite feasibility study funded by the Canadian Space Agency through Honeywell Aerospace is currently underway. In addition, the next generation of the ALI prototype is under development at the University of Saskatchewan for a second stratospheric balloon test flight in 2017. As previously mentioned, a similar instrument is currently being developed in Belgium, called ALTIUS (*Dekemper et al.*, 2012, *Fussen et al.*, 2016), which also uses an AOTF for spectral filtering. However, this new method of measuring aerosol has a fundamental difference compared to previous and current limb scatter instruments in that it measures linearly polarized light and not the total radiance.

The modelling study presented in this chapter looks at the effect of polarized radiance measurements from a low earth orbit geometry, similar to that of OSIRIS (*Llewellyn et al.*, 2004) and SCHAMACY (*Bovensmann et al.*, 1999), on the ability to retrieve stratospheric aerosol information. Although it has been previously shown that the retrieval of stratospheric aerosol extinction profiles from polarized scattered sunlight measurements are possible (as shown in Chapter 5 and *Elash et al.*, 2016, as well as *McLinden et al.*, 1999), the full impact of the polarized measurement has not been systematically studied. In this work we perform an analysis with simulated polarized measurements to determine first if there are any clear advantages or disadvantages to making the linearly polarized measurements. Further, we investigate which linear polarization and viewing geometries have the largest sensitivities to aerosol, and how the polarized measurements affect the accuracy and precision of the retrieved aerosol product.

## 6.1 Background and Forward Model

In order to investigate the effect of polarization on the sensitivity to aerosol, an accurate model of the polarized limb radiance must be employed. Additionally, a large number of scenarios, including various atmospheric states and viewing geometries, are required to fully probe the solution space. In this section, the basic background describing the polarization state of the limb signal is developed, and the SASKTRAN-HR model and the various model scenarios used for the analysis are described. Based on the useful spectral range for limb scatter observations of stratospheric aerosol, we have limited our discussion to wavelengths from 500-1500 nm.

### 6.1.1 Polarized Scattered Sunlight and Stratospheric Aerosols

All full description of scattering interactions within the atmosphere can be found in section 2.4.2 to 2.4.4. This section will briefly cover the theory and then use it to analyze the polarization state of earth's atmosphere in regards to look direction.

The time-averaged polarization state of partially polarized, incoherent light can be fully characterized by a Stokes vector,

$$\mathbf{I} = \begin{bmatrix} I \\ Q \\ U \\ V \end{bmatrix}. \quad (6.1)$$

where the terms of the Stokes vector, defined in a reference frame, are measures of the total radiance,  $I$ , the difference between horizontal polarization to vertical polarization,  $Q$ , the difference between  $+45^\circ$  diagonal polarization to  $-45^\circ$  polarization,  $U$ , and the difference between the counter clockwise circular polarization to clockwise polarization,  $V$ . Scattering events modify the polarization state of scattered light. This modification is described by a scattering matrix, which is valid for Stokes vectors defined in a scattering frame. Using a reference frame where the x-axis

is defined to be the horizontal polarization and where x and y axes are orthogonal leads to the following definition for the Stokes parameters

$$\begin{aligned} I &= \langle E_x \rangle^2 + \langle E_y \rangle^2 \\ Q &= \langle E_x \rangle^2 - \langle E_y \rangle^2 \\ U &= 2\text{Re}(\langle E_x \rangle \langle E_y^* \rangle) \\ V &= -2\text{Im}(\langle E_x \rangle \langle E_y^* \rangle). \end{aligned} \quad (6.2)$$

The polarization state of light propagating along a ray is stored as a Stokes vector defined in some reference frame. When a scattering event is modelled the Stokes vector is rotated into the scattering frame, multiplied by the scattering matrix, and then rotated into a reference frame in which the scattered Stokes vector is stored and is represented by the following operation,

$$\mathbf{I}^{\text{sca}} = \mathbf{L}(\theta_2)\mathbf{P}(\Theta)\mathbf{L}(\theta_1)\mathbf{I}^{\text{inc}}. \quad (6.3)$$

The outgoing, or scattered, and incoming radiances are represented 4 by 1 matrices, *i.e.* Stokes column vectors, given by  $\mathbf{I}^{\text{sca}}$  and  $\mathbf{I}^{\text{inc}}$ , the rotation matrices are denoted  $\mathbf{L}$  and rotate the incoming ray and scattered ray by rotation angles  $\theta_1$  and  $\theta_2$ . The scattering matrix is a 4 by 4 matrix represented by  $\mathbf{P}(\Theta)$  and is related to the probability that an incoming ray will be scattered at a scattering angle,  $\Theta$ . It also describes the change in polarization state through the elements of the matrix. . The product  $\mathbf{L}(\theta_2)\mathbf{P}(\Theta)\mathbf{L}(\theta_1)$  is sometimes referred to as the phase matrix.

For this work, two primary scattering interactions induce and/or modify the polarization state of the light propagating in the atmosphere. These are scattering by the molecular air density and by stratospheric sulfate aerosols. The molecular atmosphere interaction is referred to as Rayleigh scattering, and has a scattering matrix that is determined from the Rayleigh-Gans approximation (*Mishchenko et al.*, 2002) given by

$$\mathbf{P}(\Theta)_{\text{ray}} = \frac{3}{4} \begin{bmatrix} 1 + \cos^2 \Theta & -\sin^2 \Theta & 0 & 0 \\ -\sin^2 \Theta & 1 + \cos^2 \Theta & 0 & 0 \\ 0 & 0 & 2\cos\Theta & 0 \\ 0 & 0 & 0 & 2\cos\Theta \end{bmatrix} \quad (6.4)$$

where  $\Theta$  is the scattering angle.

For randomly orientated or spherical particles, such as stratospheric aerosol, only six unique elements of the scattering matrix are required (*van de Hulst, 1957*) which are the following

$$\mathbf{P}(\Theta) = \begin{bmatrix} P_{11}(\Theta) & P_{12}(\Theta) & 0 & 0 \\ P_{12}(\Theta) & P_{22}(\Theta) & 0 & 0 \\ 0 & 0 & P_{33}(\Theta) & P_{34}(\Theta) \\ 0 & 0 & -P_{34}(\Theta) & P_{44}(\Theta) \end{bmatrix} \quad (6.5)$$

Additionally, for spherical particles like stratospheric aerosol only four unique terms are required since  $P_{11} = P_{22}$  and  $P_{33} = P_{44}$ . Spherical aerosol scattering at visible and near-infrared wavelengths is fully described by Mie theory (*Mie, 1908*), for which several standard codes have been developed to calculate scattering cross sections and scattering matrices based on the particle size distribution and index of refraction (*i.e. Wiscombe, 1980*). A more detailed discussion can be found in section 2.4.4.

The basic polarization state of the scattered light in the Earth's atmosphere can be understood by first considering a single scattering event of the unpolarized incoming sunlight in a molecular atmosphere. It can be easily seen from the form of the Rayleigh scattering matrix (Equation 6.4) that a single scattering event causes the sky to develop a distinct polarization at a solar scattering angle (SSA) of 90 degrees from the incoming solar beam. The scattered sunlight is linearly polarized in the horizontal orientation, which is parallel to the horizon. The degree of polarization gradually decreases at scattering angles greater than or less than 90 degrees (broadly referred to as back-scatter and forward-scatter geometries, respectively). In this single scattering scenario, the radiance is completely unpolarized at solar scattering angles of 0 and 180 degrees. If multiple

scattering events are taken into account, the degree of polarization is decreased at 90 degrees SSA, and conversely does not become completely unpolarized at SSAs of 0 and 180 degrees assuming horizontal atmospheric unity. Simulations with the SASKTRAN-HR radiative transfer model using an atmosphere of molecular air density show that at 90 degrees SSA, the degree of linear polarization of the limb radiance is approximately 95% for a wavelength of 750 nm. This linear polarization effect is strongest at longer wavelengths (*i.e.* approaching 1500 nm) and decreases, on average by 10%, as the wavelength become shorter (*i.e.* down to 500 nm). This is directly related to the greater contribution from multiple scattering at shorter wavelengths. As the SSA increases from 90 degrees, the degree of linear polarization decreases. It is approximately 20% for a back scatter geometry of 180 degrees, and 30% for a scattering angle of 45 degrees. The ratio of the horizontal polarization over the total radiance and the vertical polarization over the total radiance is shown in the top of Figure 6-1. The strong polarized nature can be noted around SSA of 90 degrees where the radiance is almost completely horizontally polarized.

For an atmosphere that contains both the molecular air density as well as a typical background state of stratospheric sulfate aerosol, both Rayleigh and Mie scattering occur in a weighted fraction according to the optical depth of air and aerosol. Compared to the pure Rayleigh scattering case, the addition of aerosol causes a decrease in the degree of linear horizontal polarization for wavelengths shorter than approximately 750 nm. The bottom two panels of Figure 6-1 show the difference in the ratio of the polarized over the total radiance for the atmosphere with aerosol and one without. This effect has a weak dependence on solar scattering angle, with the most depolarization occurring in forward scatter geometries for short wavelengths. Interestingly, for longer wavelengths in back-scatter geometries, the opposite occurs. This is due to the changing fraction of scattering from the molecular air density and aerosol because the Rayleigh scattering

cross section falls off much more quickly with wavelength than the aerosol cross section (see section 2.4.4). The magnitude of the observed change in linear polarization from a pure Rayleigh atmosphere to that with typical background aerosol is approximately 5-10%, but it obviously varies depending on aerosol loading and the microphysical parameters of the aerosol.

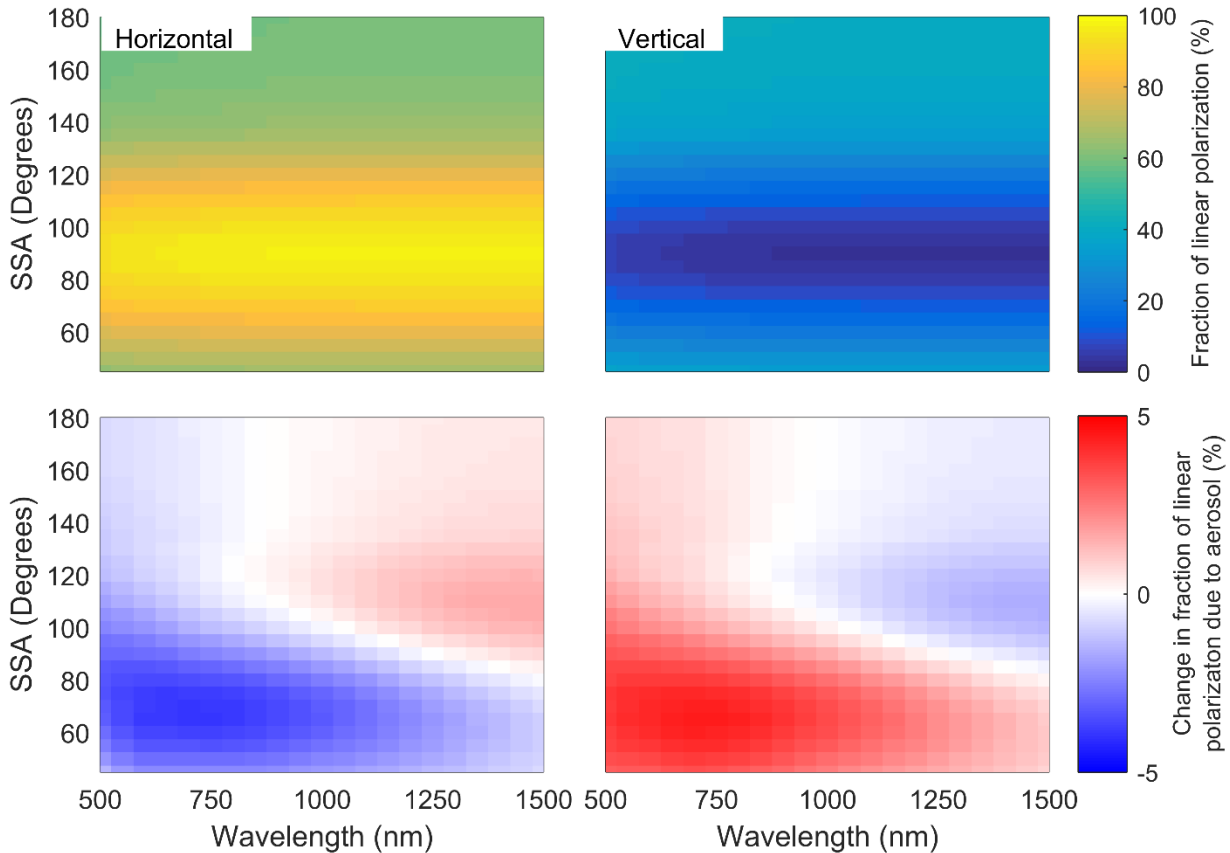


**Figure 6-1:** (Top) The fraction of a linear polarization (left is horizontal and right is vertical) over the total radiance for molecular air density. (Bottom) The change in the fraction of linear polarization between an atmosphere that contains aerosol and one with only molecular air density.

### 6.1.2 SASKTRAN-HR Model

The model used for this work is the SASKTRAN-HR (*Bourassa et al.*, 2007; *Zawada et al.*, 2015) radiative transfer model discussed in section 2.4.5 and a brief overview will follow. The High Resolution module of the SASKTRAN radiative transfer framework (*Bourassa et al.*, 2007;

*Zawada et al., 2015*) was used in this study. The SASKTRAN framework handles built-in and user-specified atmospheric species optical properties and number density profiles, and uses a fully 3D spherical geometry to solve the radiative transfer equation. The High Resolution module uses a successive orders of scattering technique, and solves either the scalar or vector (polarized) radiative transfer equations to arbitrarily many orders of scatter. In this study, the HR module is configured so that for any photon trajectory the first two scatters in the atmosphere (from the Sun) and the final scatter into the instrument line of sight are treated in a fully polarized sense; any intervening scatters treat the photon as randomly polarized. For example: If a photon scatters three times to enter the line of sight, each scatter is treated in a fully polarized sense; if a photon scatters five times to enter the line of sight, the first two scatters are polarized, the photon is then depolarized and scattered twice, and finally undergoes a polarized scatter from its randomly polarized state into the line of sight. This pseudo-polarized approximation has been shown, through comparison against the highly accurate and fully polarized Monte Carlo module of the SASKTRAN-HR framework (*Dueck et al., 2016*), to approximate the full solution of the vector radiative transfer equation to sufficient accuracy for the wavelengths and geometries of interest in this work. All calculations performed with SASKTRAN-HR in this study assume randomly polarized incident sunlight, and dry air and Mie ( $\text{H}_2\text{SO}_4$ ) scattering events only to model the interaction with the molecular air density and stratospheric aerosol, respectively. Scattering events from the Earth's surface are assumed to be Lambertian and fully depolarizing.

### 6.1.3 Model Scenarios

The impact of using polarized radiance measurements on stratospheric aerosol retrievals is systematically studied with the radiative transfer model by exploring a set of distinct cases that approximately cover the expected range of aerosol parameters, including both particle size and concentration (or extinction) profiles, and viewing geometries. Viewing geometry is an important

parameter as even in the case of the total radiance measurements, the geometry can have a substantial effect on the sensitivity of the measurement to aerosol due to the asymmetry of the Mie scattering phase function, *i.e.* element  $P_{11}(\Theta)$  of the scattering matrix (*Rieger et al.*, 2014). There is strong aerosol scattering in the forward direction and so this results in a weaker relative aerosol signal in the back scatter direction.

To probe the space of possible aerosol measurement scenarios, two aerosol extinction coefficient profiles and four particle size distributions were used. The two extinction profiles, nominally specified at 750 nm, correspond to a background aerosol case, typical of the volcanically quiet period of the early 2000's (*Deshler et al.*, 2003), and a volcanically enhanced case which was taken from OSIRIS measurements two months after the Nabro eruption in 2012 (*Bourassa et al.*, 2012c). Both profiles are shown in Figure 6-2. The four particle size distributions were also chosen to represent typical background and volcanically enhanced cases. The background cases are both single mode lognormal distributions with somewhat different, but still typically observed, size parameters. A bi-modal lognormal particle size distribution was used for the volcanically enhanced cases, with one fine mode and one coarse mode, each comprising an equal fraction of the total extinction. All of the parameters of the size distributions are detailed in Table 6-1. These selected distributions are based on in-situ balloon particle counter measurements from Laramie, Wyoming (*Deshler et al.*, 2003). The size distributions were used for translating the extinction profiles, which are specified at 750 nm, to other wavelengths by scaling the extinction by the ratio of the Mie scattering cross sections corresponding to the size distribution at the two wavelengths.

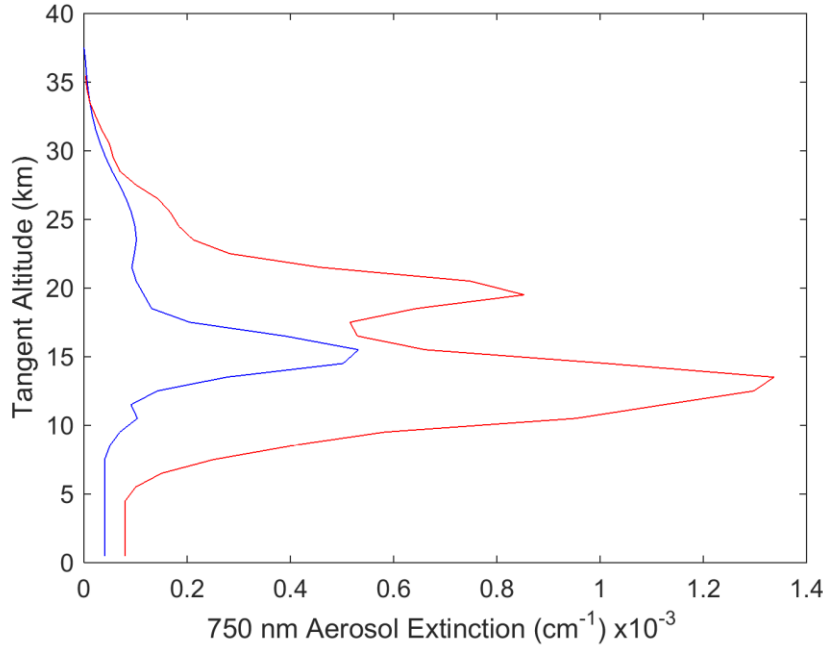


**Figure 6-2:** The two aerosol profiles used in this study. The blue is a background aerosol extinction levels, and the red curve is a representative aerosol profile after the Nabro eruption.

**Table 6-1:** Different particle size distributions used to test the sensitivity of the aerosol retrieval.

Particle size distributions	Fine mode radius ( $\mu\text{m}$ )	Fine mode width	Coarse mode radius ( $\mu\text{m}$ )	Coarse mode width	Percent extinction coarse mode (%)
1	0.04	1.8	--	--	0
2	0.12	1.25	--	--	0
3	0.04	1.8	0.30	1.15	50
4	0.12	1.25	0.30	1.15	50

To probe the range of possible viewing geometries from low earth orbit, a range of Solar Zenith Angles (SZAs) and Solar Scattering Angles (SSA) were selected. The ranges give representative selections of the possible geometries of a limb scatter instrument in low earth orbits at a range of local times. The selected values for SZA are  $15^\circ$ ,  $45^\circ$ , and  $75^\circ$  and for SSA of  $30^\circ$ ,  $60^\circ$ ,  $90^\circ$ ,  $120^\circ$ ,  $150^\circ$ , and  $180^\circ$ .

Simulated measurements were performed at wavelengths of 500, 750, 1000, 1250, 1500 nm, which approximately cover the spectral range commonly used for aerosol retrievals from limb instruments. For example, OSIRIS and SCHIAMACHY aerosol products use the ratio of 750 nm

to 470 nm for the aerosol retrieval (*Bourassa et al.*, 2012b; *Ernst et al.*, 2012). Additional longer wavelengths have been shown to provide particle size information from limb scatter measurements (*Rieger et al.*, 2014) and so the 1000-1500 nm wavelength range was also included in this study. Finally, we also performed simulations for Earth surface albedo values of 0 and 1 in order to cover the full range of potential impact.

## 6.2 Methodology

For the purposes of this study, we have assumed an instrument capable of measuring only the linearly polarized radiance with either a vertical or horizontal orientation. This is representative of newly proposed instruments like ALTIUS (*Dekemper et al.*, 2012, *Fussen et al.*, 2016) and ALI that use an AOTF and by nature only measure one orientation of linearly polarized radiance. We want to answer the question: If the linear polarization is measured, is this an advantage or a disadvantage over a measurement of the total radiance for aerosol retrievals? Further, is there a preferred orientation of linear polarization?

The polarization states used here are defined as the following: the linearly polarized radiance aligned with the horizon is referred to as the horizontal polarization, and the linearly polarized radiance that is perpendicular to the horizon is referred to as the vertical polarization. We also use the total radiance, or alternatively the scalar radiance, as the reference case. Note that the scalar radiance is not precisely equal to the total radiance. For the work presented here the term “total radiance” refers to the first term in the Stokes vector, which is calculated by the SASKTRAN-HR model when solving the vector radiative transfer equation. The term “scalar radiance” refers to the radiance calculated by the SASKTRAN-HR model when solving the scalar transfer equation. Using the Stokes parameter formulation, the horizontal polarization is given by  $0.5(I + Q)$  and the vertical polarization is given by  $0.5(I - Q)$ , which can be easily shown from the definitions given in Equation 6.2.

Our study further breaks down this problem into three questions. First, how does the fraction of the limb scatter signal that is due to aerosol vary with aerosol load and viewing geometry for both scalar and polarized measurements? Second, does the polarized measurement increase sensitivity to assumptions in the retrieval algorithm and therefore increase potential for biased results? Third, how does the polarized measurement affect the uncertainty estimate of the retrieved profile?

To explore the first question, simulated measurements were calculated with SASKTRAN-HR using the scenarios described in section 6.1.3, including various wavelengths, geometries, aerosol loading and particle size distributions. These simulated measurements were then used to determine the approximate fraction of the limb signal that was due to aerosol. In each case the model was run with a nominal atmosphere that consists of molecular air density, and climatological ozone and nitrogen dioxide profiles.

The fraction of the limb signal due to aerosol was determined by calculating the radiance without aerosol in the model atmosphere, *i.e.* that due to Rayleigh scattering only,  $I_R$ , and the radiance including aerosol,  $I_A$ . To find the fraction,  $\delta$ , in percentage, of the signal that is attributed to aerosol, the following formulation is used:

$$\delta = \frac{I_A - I_R}{I_A} * 100\%. \quad (6.6)$$

Due to non-linearities from multiple scattering, it is not strictly true that this is the fraction of the signal due to aerosol; however, at most stratospheric tangent altitudes, the wavelengths under study were quite optically thin and this simple percent difference provides an intuitive approximation of the fraction of the signal due to aerosol.

We explore the second question about the effect of the polarized measurement on the aerosol retrieval using simulated measurements and a retrieval method that was essentially similar to that

developed by *Bourassa et al.* (2012b) for OSIRIS. A minor change to the algorithm was made where the measurement vector for this study was not normalized by a shorter wavelength. Although it was advantageous in a retrieval scenario to limit sensitivity to particle size, for this study we explore the worst case scenario under possible limitations of future technology, given that not all instruments may cover a wide enough spectral range for short wavelength normalization.

The limb radiance was calculated using SASKTRAN-HR, again with climatological ozone and NO<sub>2</sub> profiles, for each of the scenarios listed in section 6.1.3. This was taken as a simulated measurement and was then used to retrieve aerosol extinction profiles using the *Bourassa et al.* (2012b) technique. This was done similarly for the total radiance and for each orientation of the linearly polarized radiance. Additionally, a retrieval was performed with the scalar SASKTRAN-HR model to see if there was any substantial difference between using the scalar radiance and the total radiance from the vector model. For each aerosol retrieval, the ozone, NO<sub>2</sub>, and albedo are fixed to the values used in the simulation of the measurement. All four particle size distributions from Table 6-1 were used in the simulations, but following *Bourassa et al.* (2012b), the aerosol particle size was fixed in the retrieval to a single mode log-normal with 0.08 μm mode radius and mode width of 1.6. The assumption of a fixed particle size distribution was common in limb scatter retrieval algorithms and this was used to explore sensitivity of the polarized measurements to particle size distributions, and test if the uncertainty in this assumption greatly effects the retrieved extinction.

Lastly, to answer the third question, an uncertainty estimate was performed on these retrievals in order to check the precision of the retrieved aerosol profile. The precision was determined by mapping the covariance of the measurement vector,  $\mathbf{S}_\epsilon$  through the gain matrix,  $\mathbf{G}$ , which describes

the sensitivity of the retrieval to the measurement and the respective noise through the following (*Rodgers*, 2000)

$$\mathbf{E} = \mathbf{G}\mathbf{S}_\epsilon \mathbf{G}^T. \quad (6.7)$$

where  $\mathbf{E}$  is the co-variance matrix for the retrieved aerosol profile. However, the direct calculation of the gain matrix is computationally intensive and numerically requires a retrieval for each measured altitude. A method presented by *Bourassa et al.* (2012a) uses the Jacobian,  $\mathbf{K}$ , to approximate the gain matrix by assuming the problem is linear near the solution state, which is largely a good assumption for limb scatter aerosol retrievals. Using these assumptions, the gain matrix can be determined simply through the inverse of the Jacobian,

$$\mathbf{G} \cong \mathbf{K}^{-1}. \quad (6.8)$$

Rather than specifying an assumed measurement co-variance to study the behavior of the retrieval precision, we simply replace the measurement co-variance in Equation 6.7 with the identity matrix. Thus the resulting terms of  $\mathbf{E}$  are not absolute quantities but are related to the amplification of the measurement noise when mapped to the retrieved state (*i.e.* the larger the values of  $\mathbf{E}$  the larger the uncertainty for the retrieval). The square root of the elements of the diagonal of the aerosol covariance, typically used to represent the error bars on the retrieved profile, are taken as the amplification of the measurement noise.

This method assumes that the radiance measurements regardless of polarization state have exactly the same signal to noise performance, *i.e.* all measurements have the same co-variance. We also consider the case where the instrument is not compensated such that the magnitude of the various polarization states directly scales the signal to noise performance, *i.e.* the instrument is not compensated to equalize the measurement co-variance when the signal drops due to the measured polarization state. In this scenario the above method must be modified by replacing the identity

matrix with the matrix,  $\mathbf{R}$ , to represent the change in signal strength for the various polarizations relative to the scalar case. This matrix is defined as

$$R_{ij} = \begin{cases} \frac{I_{ref,i}}{I_{pol,i}} & \text{for } i = j \\ 0 & \text{for } i \neq j \end{cases} \quad (6.9)$$

The diagonal of the  $\mathbf{R}$  matrix is effectively scaled by the inverse of the magnitude of ratio of the polarized radiance,  $I_{pol,i}$ , to the reference scalar case,  $I_{ref,i}$ , for the measurement altitude,  $i$ .

### 6.3 Analysis

#### 6.3.1 Difference in Scalar Retrievals using a Scalar or Vector Model

First, we investigate if there is any significant difference between the use of the scalar radiance and the total radiance for retrievals on measurements of the total radiance. As mentioned above, retrieval algorithms for current limb scatter data sets such as OSIRIS and SCIAMACHY use a scalar radiative transfer model with general success; however, as the total radiance is not generally equal to the scalar radiance, this may lead to biases in the retrieved extinction profile under certain scenarios. Accounting for the vector component in the model alters the overall total radiance from the scalar solution due to multiple scattering interactions between the various polarization states of each successive order of scattering.

The total radiance was simulated with SASKTRAN-HR in vector mode for the full set of wavelengths and viewing geometries, and for the range of aerosol loading scenarios. These were used as input measurements to the retrieval algorithm, which was then performed using both the scalar and vector models. A case-by-case comparison between the retrieved extinctions for the scalar and vector models was performed using a simple percentage difference at each retrieved altitude a can be seen as the grey lines in Figure 6-3. Furthermore, the mean of the bias for each particle size distribution is shown in solid black. These results, given in Figure 6-3, show that

across all wavelengths, the mean percent difference is less than 2% from 15 to 37 km. It should be noted that some of the differences between the two models are removed due to the high altitude normalization in the retrieval. A small number of outlier cases occur where the difference between the retrievals is greater than 7%. All of these cases occur for back scatter geometries and short wavelengths. The reason for this discrepancy is not well understood, although it certainly arises from the differences between the scalar and total radiance due to polarization interactions from the relatively larger contribution of multiply scattered light at shorter wavelengths. These discrepancies are enhanced by the reduced sensitivity to aerosol in the back scatter geometries. Generally, however, any differences between the use of the scalar and vector model for the retrieval are negligible. In fact, any form of discrepancy essentially vanishes for wavelengths past 1000 nm. Since the use of the vector model can increase calculation times by a factor of at least two, it is certainly justifiable to use the scalar model for the overwhelming majority of scenarios. For the rest of the work presented, any reference to the radiance will only refer to the total radiance,  $I$ , from the vector model.

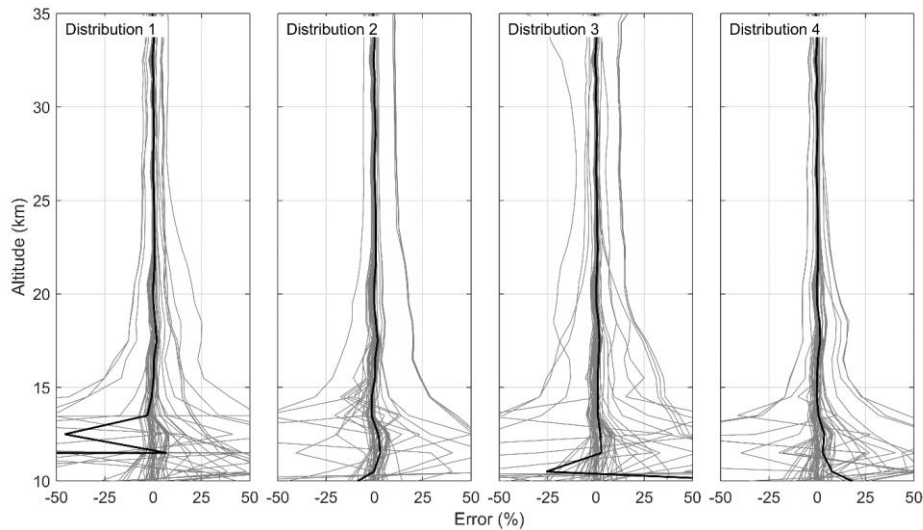


**Figure 6-3:** Percent differences between the vector retrieved aerosol extinction profiles and the scalar retrieval from simulated total radiance measurements. Each column represents a different particle size distribution (see Table 6-1).

### 6.3.2 Fraction of Limb Signal due to Aerosol

For a typical background aerosol state, the fractional contribution to the total limb radiance from aerosol was calculated from modelled radiances over a series of stratospheric tangent altitudes using the background aerosol profile and particle size distribution 1, given in Table 6-1. Figure 6-4 shows the percent change in this fraction for horizontally and vertically polarized measurements compared to the total radiance. The viewing geometry, which is a typical low earth orbit scenario, is SZA=45° and SSA=60°, and the albedo is set to 0 to remove depolarization from the Lambertian Earth. The top of Figure 6-4 shows the percentage of signal that is attributed to aerosol for both horizontal and vertical linear polarizations,  $\delta$ . As can be seen from the bottom of Figure 6-4, most of the change in the aerosol fraction of the polarized limb signal compared to the total radiance (i.e.  $\Delta\delta = \delta_{tot} - \delta_{pol}$ ) occurs for wavelengths between 500-1000 nm. At these wavelengths the horizontal polarization has a smaller fraction of signal due to aerosol and the vertical polarization has a larger fraction due to aerosol. Overall the change is small and essentially limited to less than 10%.

Similar calculations were performed for the range of viewing geometries using the same atmospheric state. Figure 6-5 shows the fraction of limb signal due to aerosol for the total radiance, and both orientations of the linearly polarized radiance. This calculation was performed for 15 km tangent altitude, and other stratospheric tangent altitudes show very similar patterns. An important difference is noted between the forward and back scattering geometries. Remembering the horizontal polarization is given by  $0.5(I + Q)$ , the total and horizontal polarization cases have a similar dependence on viewing geometry, with the strongest aerosol signal from long wavelengths in the forward scatter direction. The vertical polarization, given by  $0.5(I - Q)$ , has a strong aerosol signal contribution for forward scattering directions, especially at visible wavelengths, in

comparison to the total and horizontal polarization cases. For back scattering geometries, somewhat less aerosol signal is observed. For reference, the magnitude of the limb radiance in each case is shown in the right hand column of Figure 6-5 taking note that the high end of the scale is saturated to emphasize the smaller values. It is important to note that the vertical polarization has a very low magnitude at scattering angles near 90 degrees, making vertically polarized measurements in this geometry particularly susceptible to signal-to-noise problems.

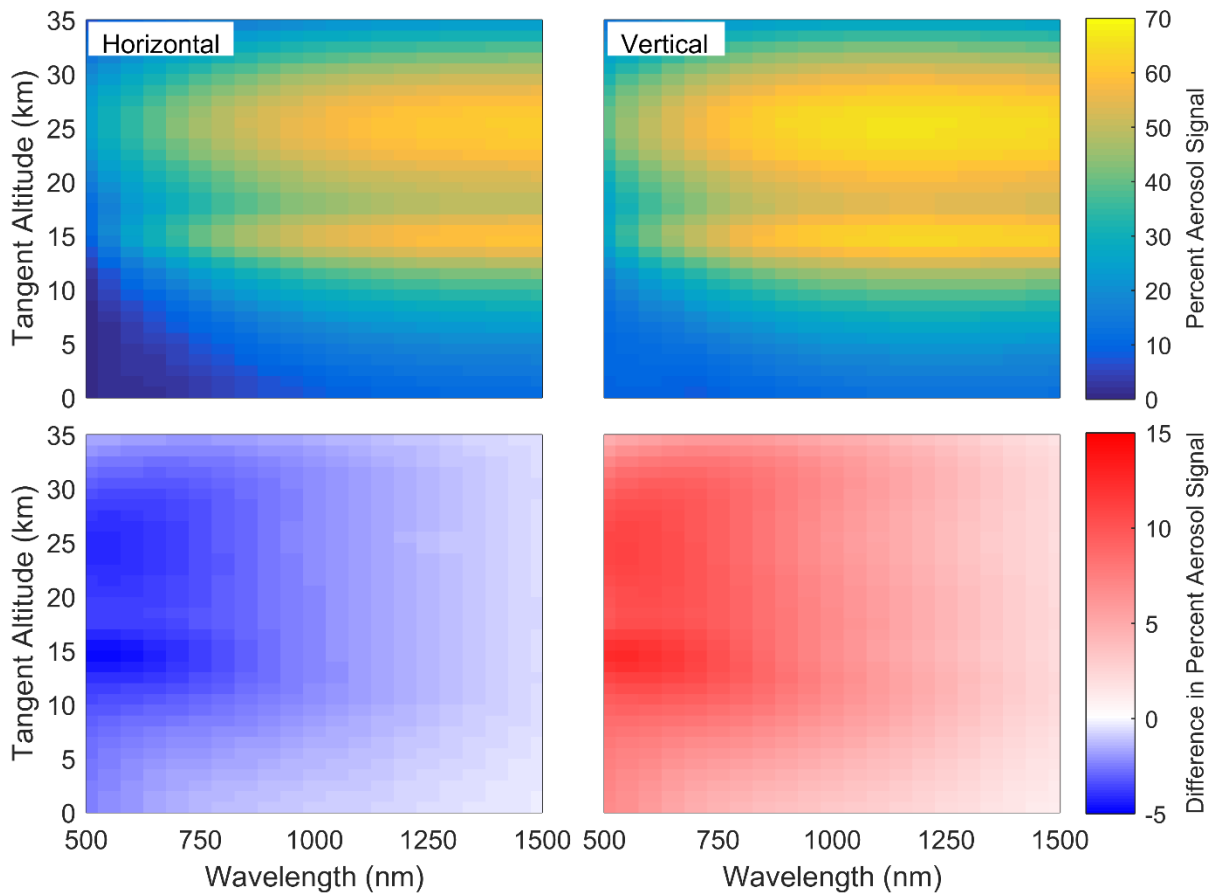


**Figure 6-4:** (Top) For a horizontal (left) or vertical (right) linear polarization the percent of the signal that is attributed to aerosol,  $\delta$ . (Bottom) The change in the fraction of the limb signal due to aerosol when compared to the total radiance for the horizontal (left) and vertical (right) polarization ( $\Delta\delta$ ). The simulation uses a geometry of SZA=45° and SSA=60°, with the albedo being 0 and the aerosol state the background profile with particle size distribution 1. Take note the red-blue scale is non-symmetric.

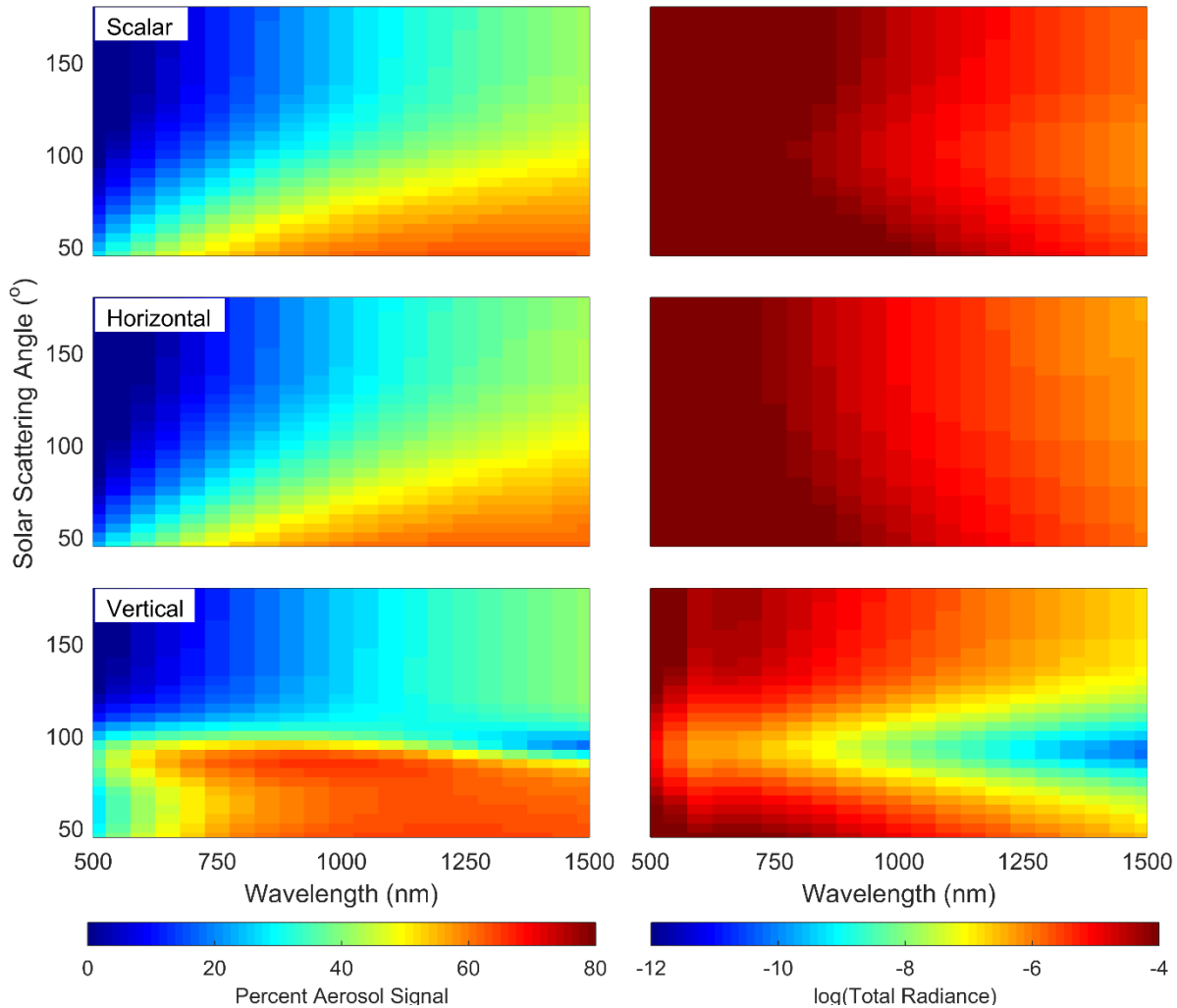


**Figure 6-5:** Dependence of the fraction of the limb spectra due to aerosol on solar scattering angle (left panels) for total radiance (top), horizontal polarization (middle) and vertical polarization (bottom), and the magnitude of the radiance for each case (right panels). Note the low signal near SSA of 90 degrees for the vertical polarization which would be problematic for terminator orbits.

These same calculations were performed for the full range of SZAs and found that the SZA affects the fraction of the signal due to aerosol by only less than 1%. Also, when the albedo is changed from 0 to 1, the aerosol signal decreases for all polarizations and wavelengths thus reducing overall sensitivity to aerosol as albedo increases in all cases. Note, however, that the SASKTRAN-HR model assumes that all ground reflection is randomly polarized; the addition of

a polarized bidirectional reflectance distribution function model may change the sensitivity to aerosol with higher albedo.

This same analysis was also performed for two other additional polarization orientations, the +45 degree and -45 degree linear polarizations (*i.e*  $0.5(I + U)$  and  $0.5(I - U)$ ) to investigate sensitivity to aerosol. It was found that these two polarization orientations had similar aerosol contribution to the total radiance case with approximately two thirds of the overall signal when compared to the total radiance case.

In general, the contribution to the limb radiance from aerosol for the horizontally polarized and total radiance cases is approximately the same. The vertical polarization has more asymmetry in aerosol signal between forward and back scattering geometries with very low signal magnitude near 90 degrees scattering angle. Given that essentially all low earth orbit scenarios will cover forward and backward scattering angles, including 90 degrees scattering angle, it is clear that the horizontal orientation overall shows a more favorable response to aerosol. This is particularly true for a terminator orbit such as that of OSIRIS.

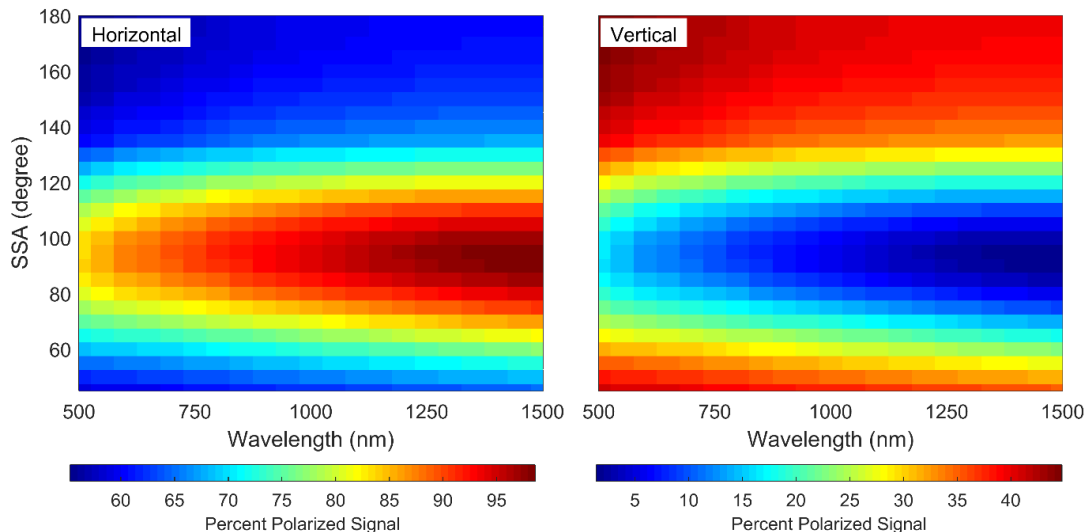


**Figure 6-6:** The ratio of the linearly polarized radiance to the total radiance for horizontal (left) and vertical (right) orientations. Note that the scale for each plot is different. The simulation was performed with a SSA of 60 degrees with volcanic aerosol loading for a tangent altitude of 20 km.

A distinct disadvantage of measuring a linear polarization rather than the total radiance is the loss of overall signal magnitude. In Figure 6-6, the ratio of the polarized radiance to the total radiance is shown for a series of SSAs for a tangent altitude of 20 km, but in this case using the volcanic aerosol extinction profile, which serves to enhance the fraction of signal due to aerosol. Measuring the horizontal polarization results in observing signal levels approximately one half to two thirds of the total radiance, with the greatest effect at the shorter wavelengths. The other forward scatter geometries are similarly affected. For back scatter geometries, the signal levels are also approximately half of the total radiance, but with less spectral dependence. For solar scattering angles near 90°, the horizontal polarization encompasses a large fraction of the total radiance resulting in signals of 80-95% of the total. Across the full parameter space of viewing geometries, wavelengths, and aerosol loading scenarios, the magnitude of the horizontal polarization is on average 60-70% of the total radiance.

Although the vertical polarization shows a relatively larger fraction of the signal due to aerosol particularly in forward scatter geometries, the overall signal levels are substantially lower. For forward scatter geometries, the magnitude of the vertically polarized radiance is only approximately one third of the total radiance across the spectral range. Back scatter geometries are only slightly better with slightly less than half of the total radiance. Again, near solar scattering angles of 90° the limb radiance is almost fully horizontally polarized and the vertically polarized signal is only 5-20% of the total. On average across the entire parameter space, the vertical polarization component typically accounts for 30-40% of the total signal.

It is clear from this relatively simplistic analysis of the aerosol signal in polarized limb radiance that there are trade-offs between viewing geometries and instrument polarization sensitivity, and changing sensitivity across the spectral range. While there is not an overwhelming case to be made

for one particular option over the wide range of scenarios that can be considered, the overall response of the horizontally polarized radiance is essentially similar to the total radiance, but with somewhat reduced magnitude that can most likely be mitigated through instrument design considerations. The vertical polarization has much more widely varying sensitivity to aerosol with very low signal levels near 90 degrees scattering angle, and is a much more challenging choice in terms of instrument performance for aerosol measurements.

### **6.3.3 Potential for Retrieval Bias**

In this section we directly explore the effect of the polarized measurements on the results of a typical retrieval algorithm through application of the algorithm to simulated measurements across the full parameter space.

We explore the potential of an effect of polarization on the bias in retrieved extinction caused by uncertainty in the assumed particle size distribution. The set of radiances for all cases across the parameter space were again used as simulated input measurements to the retrieval algorithm. This time, retrievals were performed on the horizontally polarized radiance, the vertically polarized radiance, and the total radiance. The radiance calculations in the iterations of the retrieval were set to match the polarization states of the input radiance, but the total solution was used to approximate the total radiance. In all cases, the retrieval was performed using an assumed particle size distribution, which was log-normal with a mode radius and width of  $0.08 \mu\text{m}$  and 1.6 respectively. Note that this assumed size distribution is different than all four of the size distributions used as the “true” state for the simulated input radiances. For the total radiance case, this uncertainty is well known to cause biases of up to 20-30% in retrieved extinction (*Rieger et al.*, 2014). A summary of the differences between the retrieved and true aerosol extinction for 750 nm and 20 km altitude is shown in Figure 6-7 and is similar for altitudes from 17 to 35 km. Errors bars on each point represent one standard deviation of the variability in the

results for the range of viewing geometries. These results are representative of the level of agreement also found for other wavelengths and altitudes. There is no substantial difference between the results for the background and volcanic extinction profiles. It should be noted that cases with solar scattering angles of  $90^\circ$  have been removed for the vertical polarization due to the very low values of signal, which manifests as a large dependency on the particle size distribution and a highly biased retrieval. This large bias is very sensitive to scattering angle and is nearly eliminated for even  $85^\circ$  or  $95^\circ$ .

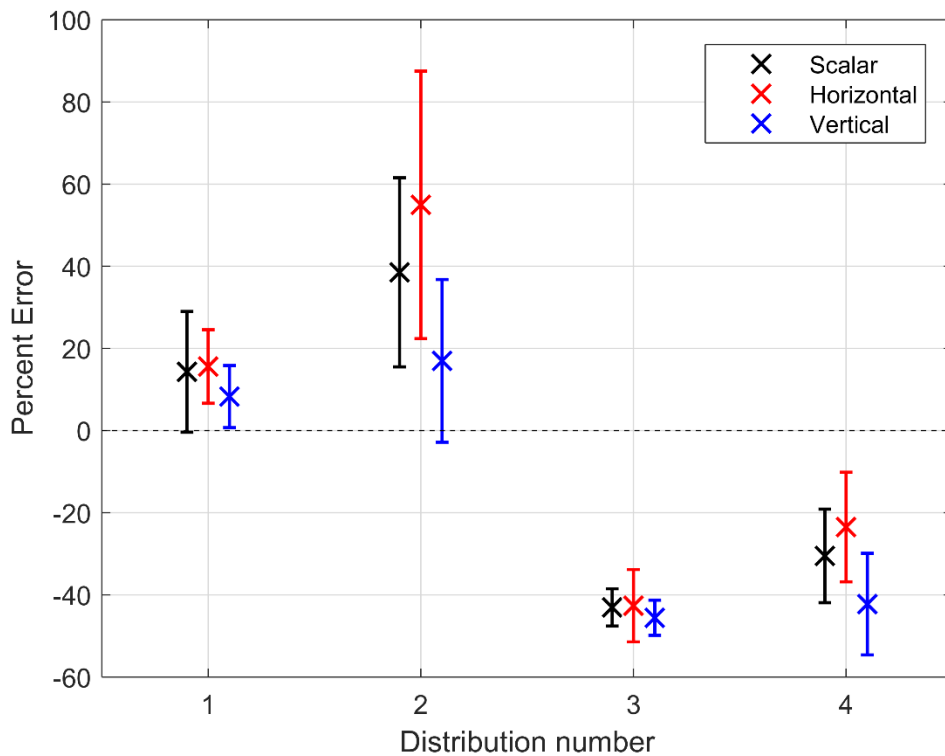


**Figure 6-7:** The mean percent difference between the retrieved aerosol extinction profile with an assumed particle size distribution and the true state corresponding to the indicated particle size distribution (see Table 6-1). Error bars represent one standard deviation of the variability across all viewing geometries. Results shown are for 750 nm and 20 km altitude.

It is clear that the major element of observed bias is simply the difference between the true and assumed particle size distribution. In all four cases there is some difference between the solutions for the various polarization states; however, for each particle size distribution the biases between

the polarization states are essentially the same within the variability observed across the various viewing geometries. Neither of the linearly polarized states perform consistently better than the total radiance case; however, they do not perform any worse either (excepting the vertical polarization near 90 degree solar scattering angle), which is an equally important result.

### 6.3.4 Precision Analysis

Finally, we study the effect of the polarized measurement on the performance of the retrieval in terms of the precision of the results. We again use simulated measurements across the full range of input parameters as input to the standard retrieval algorithm. Following the methodology outlined in section 6.2, using SASKTRAN-HR the Jacobian matrices were calculated for each retrieved state and used to determine the gain matrices, which were then applied as in Equation 6.7 to determine the retrieval precision. It should be noted that not all of the Jacobian matrices could be inverted due to small sensitivity of the lower tangent altitudes (see discussion in *Bourassa et al.*, 2007) and these were removed from the data set (approximately 9% of total cases). This affected a large fraction of the 500 nm cases, so this wavelength was removed from this section of the analysis. As discussed in section 6.2, we approach this problem from two perspectives: (1) an instrument that is compensated in design and/or operation such that measurements regardless of polarization state or geometries have the same signal to noise ratio, and (2) an uncompensated instrument such that the changing signal level with polarization state and viewing geometry affects the signal to noise ratio of the observation.

For the first case, where the signal to noise ratio is compensated such that it is equal for all cases, the measurement co-variance matrix in Equation 6.7 is replaced with the identity matrix, and the relative size of the square root of the diagonal of the resulting aerosol co-variance represents the amplification of the measurement noise. To compare the performance of the various polarization states, the resulting retrieval co-variances for the linearly polarized measurements

were normalized by the retrieval co-variances from the total radiance case. The dependence of the results on the various input parameters, such as wavelength and viewing geometry were examined. Very little altitude dependence was observed and so the results were averaged across the retrieved altitude range.

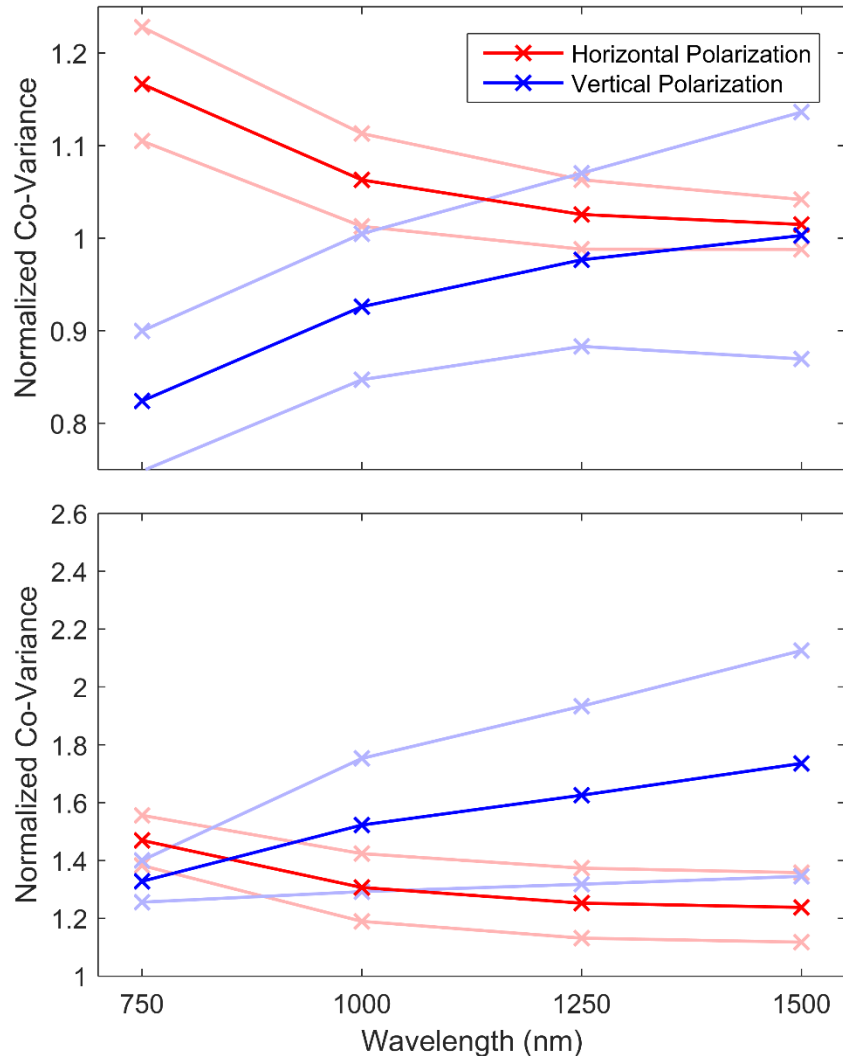


**Figure 6-8:** The wavelength dependence of the co-variance for the horizontal and vertical polarization retrievals normalized to the total radiance case. The faded line represent one standard deviation of the variability encountered across all input parameters. The top panel is for an instrument design and/or operation that compensates for changing signal levels with polarization and viewing geometry, and the bottom panel is for uncompensated measurements.

In Figure 6-8 the normalized co-variances cases were sorted by wavelength using all geometries and atmospheric states. These bins were then averaged for each wavelength shown by the red and blue points for the horizontal and vertical polarization states respectively. The faded colours are one standard deviation from the mean. Each of the means in Figure 6-8 contains between 186 to 229 unique data points and values less than one represent co-variance better than the total radiance case and the opposite for values larger than one.

The resulting normalized co-variances have a substantial dependence on wavelength. The situation where the signal to noise ratio is compensated such that it is equal for all cases is shown in the top panel of Figure 6-8, where the vertical polarization has a smaller co-variance, i.e. better precision, by approximately 20% at the shorter wavelengths than the total radiance retrieval. As wavelength increases to 1500 nm, the precision of the vertical polarization case is approximately equal to that of the total radiance case. The horizontal polarization essentially mirrors the vertical case with higher co-variances than total radiance at short wavelengths and approximately equal at 1500 nm. Recall, however, that the vertical polarization has significantly lower magnitude signal levels and in order for the measurement to be compensated to obtain equal signal to noise levels, an increase in instrument sensitivity or exposure time would be required.

**Table 6-2:** The SSA dependence of the normalized co-variance for the horizontal and vertical polarization retrievals. The given numbers are the mean with the standard deviation for each geometry across all wavelengths. Note that the SSA of 90° for the vertical polarization has been removed due to the poor signal in this region.

Polarization	60°	90°	120°	150°	180°
Horizontal (Compensated)	1.072±0.051	1.090±0.082	1.047±0.078	1.027±0.048	1.023±0.042
Vertical (Compensated)	0.861±0.084	--	0.968±0.157	0.977±0.063	0.980±0.051
Horizontal (Uncompensated)	1.289±0.075	1.225±0.158	1.261±0.165	1.341±0.098	1.360±0.085
Vertical (Uncompensated)	1.576±0.167	--	1.852±0.559	1.527±0.170	1.490±0.130

Across the range of solar scattering angles, the vertical polarization has slightly lower co-variance than the other two cases, except at 90 degrees, which is due to the lack of sensitivity in this region noted previously. Table 6-2 shows the calculated means and standard deviations across SSA for the horizontal and vertical polarizations. Note the SSA of 90° is missing due to the poor signal, and retrieval quality noted in previous sections which results in poor co-variances for this geometry. Furthermore, the variability of the result across all of the other input parameters increases dramatically as the scattering angle approaches 90 degrees. The precision of the retrieval shows very little dependence on the other input parameters such as solar zenith angle, albedo, particle size distribution, and extinction level. On average across all parameters, the retrieved co-variance from the vertical polarization is approximately 15% smaller than the horizontally polarized retrieval.

In the case of an uncompensated instrument, for example where a linear polarizer is added to the optical chain with no other changes in observation, the scaling of the diagonal of the measurement co-variance is used as outlined in section 6.2. Due to the larger magnitude of the signal in the horizontal polarization compared to the vertical polarization, the horizontal cases generally have lower retrieval co-variance, and this effect increases with longer wavelength as seen in the lower panel of Figure 6-8. Note that in this uncompensated case, since the linear polarizations are always some fraction of the total radiance, the co-variance is always larger than the total radiance case (i.e. the normalized co-variances are always greater than 1). Once again very little dependence on solar zenith angle, albedo, size distribution or extinction level was observed. There was also little dependence on solar scattering angle, except for vertical polarization at 90 degrees. On average across all parameters, vertical and horizontal polarizations have approximately a 60% and 30% larger uncertainty than the total radiance case, respectively.

This analysis shows that the main driver of retrieval precision is the signal to noise level of the observation, as would be expected. Again, this leads to instrument design and/or operational considerations in order to maintain retrieval precision at the same level as the total radiance measurement. A main scientific goal of both the ALI and ALTIUS instruments is obtaining high spatial resolution observations, both vertically and horizontally along, and across, the satellite track. This generally means that images must be collected rapidly and long exposure times are not an affordable luxury. Once more, the relatively higher magnitude signal levels of the horizontal polarization point to this as the more appealing choice of orientation; however, compared to the total radiance case the decreased precision is exaggerated at shorter wavelengths.

#### **6.4 Conclusions of the modelling study**

We have attempted to address the question of whether or not the measurement of linearly polarized radiance rather than total limb radiance is an advantage or disadvantage with respect to retrievals of stratospheric aerosol. The sensitivity of the polarized limb radiance to aerosol is complex with respect to many parameters, and there are trade-offs in the orientation of the polarization and the orbital viewing geometry. One important point is the very low magnitude of signal observed in the vertical polarization for scattering angles near 90 degrees, which are encountered for a large fraction of observations in low earth orbit, particularly sun-synchronous near-terminator orbits such as for OSIRIS, and the most likely orbit orientation for an ALI satellite mission. More generally, it is important to consider the overall lower magnitude of the linearly polarized radiance, which by definition is a fraction of the total radiance. The horizontal polarization has, on average, higher signal levels than the vertical polarization. It also has a weaker dependence on solar scattering angle that is more similar to the total radiance than the vertical polarization, which is more strongly skewed in the forward scatter direction.

One critical bias in limb scatter retrievals of stratospheric aerosol is due to uncertainty in particle size parameters. We tested four different particle size distribution scenarios, representing background and volcanically perturbed conditions, over a large range of other parameters such as wavelength, viewing geometry, and extinction level and found that there is no significant change in the observed bias for polarized or total radiance measurements. So, with respect to this bias in stratospheric aerosol retrievals, the linearly-polarized measurement can be used to achieve approximately equal results with only minor advantages and disadvantages between the polarization states.

The polarized measurement can have an effect on the precision of the retrieval, where again the main driver is the magnitude of the signal. The polarization can either increase or decrease the precision and there is an apparent trade-off between signal levels and performance of the vertical or horizontal polarization. This is mostly important at shorter wavelengths since at longer wavelengths the differences are negligible.

In conclusion, we have found no clear advantage to the linearly polarized measurement over the total radiance for aerosol retrievals; however, there are also no clear disadvantages assuming the somewhat lower overall signal levels can be handled in the instrument design or operation. With careful choice of the orientation of the measured polarization with respect to the orbital geometry and desired coverage, an instrument such as ALI or ALTIUS is fully capable of obtaining retrieved aerosol products of very similar quality to an equivalent instrument that measures the total radiance.

# CHAPTER 7

## CONCLUSION

### 7.1 Summary

Space-based remote sensing measurements of stratospheric aerosol have been performed since the 1970's, and have provided valuable insight into aerosol process and trends, including a key record of the "persistently variable" effect of volcanic eruptions. Due to their impact on climate through the scattering of incident solar radiation back to space, the continued monitoring of stratospheric aerosol is critical (*Solomon et al.*, 2012). However, there are very few operational or even planned satellite missions with stratospheric aerosol measurement capability, and the scientific requirements for further understanding the transport of both anthropogenic and volcanic aerosol source gases into the stratosphere present challenges in terms of spatial resolution and coverage of the measurements.

In this thesis, the design, test flight and first results from a new prototype satellite instrument specifically tuned for stratospheric aerosol measurement was presented. The Aerosol Limb Imager, or ALI, instrument was designed to capture hyperspectral images of limb scattered sunlight to determine aerosol extinction and particle size information. The hyperspectral imaging nature of the instrument provides the capability to measure both in altitude and in the cross-track horizontal dimension. Global coverage of the stratosphere can then be obtained by successive measurement along the satellite track. The limb scattering technique, combined with the hyperspectral imaging design of the instrument, provides a powerful combination of global coverage, high spatial resolution, along with the capability to retrieve high quality stratospheric aerosol information, as proven by the ground-breaking OSIRIS algorithms (*Bourassa et al.*, 2007; 2012). In this work, a prototype version of the ALI instrument was developed specifically for a test flight from a stratospheric balloon. This platform provided low cost access to the space

environment, including altitudes that are sufficiently high to image the stratospheric limb, which was the critical factor for this project.

The ALI prototype was designed using an imaging quality, large-aperture AOTF to rapidly filter selected narrow wavelength bands from 650 to 950 nm in two dimensional images of the limb radiance with exposure times on the order of one second. Commercial off-the-shelf components were used for the prototype, consisting of a simple linear optical system with telescopic front-end optics, a focusing lens for the back-end optics, and a scientific grade CCD detector. The system had a large field-of-view of  $6^\circ$  to image the entire limb from the ground to the balloon float altitude (approximately 35 km). This field-of-view was substantially larger than that required for a space-craft version of the instrument owing to the difference in viewing geometries between low earth orbit and stratospheric balloon. This requirement resulted in some optical aberrations in the outer one degree of the field-of-view, a region which was also partially outside of the acceptance angle of the AOTF. From laboratory testing and through simulations in Code V modelling software, the spatial resolution of the instrument was nominally 210 m at the limb tangent point, both in the vertical and horizontal directions, which was well within the sub-kilometre spatial resolution requirement for thin aerosol structures. A systematic calibration of the instrument was performed in the lab, accounting for dark current, stray light, flat fielding, and a relative spectral calibration. An absolute calibration was not performed due the lack of an appropriate lab source; however, ground based testing of the instrument provided an opportunity to compare blue sky measurements of the scattered sunlight radiance with forward model calculations and verify the instrument sensitivity.

The stratospheric balloon test flight for ALI was performed in Timmins, Ontario, from the CSA balloon launch facility. ALI was mounted onboard the CNES CARMEN-2 gondola, and the launch

occurred at 05:35 UTC on September 19, 2014, with a flight duration of 16 hours and 14 minutes. From float altitude at 36.5 km, ALI captured 216 two dimensional images of the limb radiance over five hours. Analysis of this hyperspectral data set shows that the measured radiances are of high quality, and show both vertical and horizontal features of the cloud and aerosol layers. These were used to retrieve aerosol extinction coefficient profiles that show reasonable agreement with coincident OSIRIS satellite measurements. Furthermore, rudimentary particle size distribution information was also retrieved from the ALI measurements. Due to the limited spectral range of the prototype, the retrieval of the particle size distribution was noisy, but still yielded sensitivity to the larger perturbations typically seen after a volcanic eruption.

The birefringent nature of the AOTF means that the ALI measurements were of the linearly polarized limb radiance, whereas historically limb scattered sunlight measurements from space use total radiance. While some preliminary work had already shown that stratospheric aerosol information could be retrieved from a measurement of the polarized radiance observed from aircraft (*McLinden et al.*, 1999), this is a significant difference from previous generations of space-craft instruments and a thorough, systematic study of the potential impact of this change was performed as part of this work. The results of this study show that for most observation geometries and with compensation for the signal levels, there is no disadvantage to these polarized measurements.

## **7.2 Contributions of This Work**

The work in this project has provided several contributions to the field of atmospheric remote sensing, through both advancements in technology, and the modelling and algorithm development that are inherently linked to the technological improvements. These contributions are:

- The first sub-orbital demonstration of an atmospheric remote sensing imaging system using ATOF technology. Although *Dekemper et al.* (2012) showed ground-based

measurements of a factory emission plume using a custom AOTF-based imager, this is the first successful sub-orbital demonstration of this technology that we are aware of.

- An AOTF-based imager design specifically for aerosol measurements. The spectral sensitivity of the AOTF in terms of range and resolution was essentially a perfect match for the requirements of measuring aerosol using limb scattered sunlight. This work provides the ground-work for a future satellite instrument that leverages the combination of the AOTF technology and the limb scattering remote sensing technique.
- The first retrieval of aerosol extinction profiles and particle size information from 2D hyperspectral images of the limb radiance. Although the retrievals presented here were an adaptation of existing algorithms that use radiance profile measurements from scanning spectrometers, this advancement demonstrates the potential to achieve both vertical and cross-track dimensions from a future satellite-based version of ALI, which would vastly improve upon the existing capability for obtaining global coverage.
- The first study on the impact of measuring the polarized radiance, rather than the total radiance, on the ability to retrieve stratospheric aerosol information from limb scattered sunlight measurement. This is important not only for the future of ALI, but also for other instruments under study and development, notably the Belgian ALTIUS instrument, which also uses AOTF technology and will similarly measure the linearly polarized radiance.

### **7.3 Outlook, Recommendations and Future Challenges**

This thesis work has provided for a successful demonstration flight of a prototype ALI instrument, including the foundational hardware design work and scientific analysis of the flight

measurements. This success has provided for opportunity to further pursue the ALI as a space-based mission concept for micro- or small-satellite deployment. Recently, the Canadian Space Agency has provided funding through the FAST program to develop a second, higher fidelity prototype, again for stratospheric balloon test flight, but which incorporates several important functional improvements discussed below. In parallel to this, the CSA has also provided funding to Honeywell Aerospace through the competitive Space Technology Development Program in order to perform a design and feasibility study for a satellite version of the ALI instrument, including an advanced optical design suitable for the geometry of low-earth orbit, and all of the thermal and mechanical accommodations required for space flight.

The most important design improvement to ALI from a scientific perspective is the extension of the spectral range. The capability to retrieve particle size information vastly increases with the inclusion of measurements from the 1000 to 1500 nm near infrared spectral range. Although this could be done with a second hardware channel, i.e. a second AOTF and detector designed for this spectral range, it could be elegantly accomplished with two key technological advances: 1) The use of a dual-transducer AOTF with the capability to tune over the entire spectral range, i.e. over more than one octave in wavelength. These are just now becoming commercially available. 2) The use of an extended range “vis-GaAs” detector, also just recently commercially available, to provide good sensitivity across the full visible and near infrared range.

A second important functional improvement to the instrument from a scientific perspective is the capability to measure both orientations of the linear polarization. This would provide a measurement to discriminate between aerosol and cloud particles through the distinct differences in the scattering phase matrix. One could imagine several approaches that would provide this functionality, including a twin hardware channel with the AOTF oriented in the orthogonal

direction, or a second set of back-end optics oriented to measure the diffracted beam generated from the other axial direction of the birefringent crystal. A more elegant approach that could be explored involves incorporating an element to actively rotate the selected polarization direction in the front-end optics, by moving a wave plate, or possibly with a voltage-controlled liquid crystal rotator.

For future work involving ALI prototype testing on balloons and possibly aircrafts, several recommendations can be made from the lessons learned in this work.

- Careful attention should be paid to the orientation of the measured polarization and the planned flight geometry to avoid the problematic lack of sensitivity of the vertical polarization for scattering angles near 90 degrees.
- Even with the detailed baffle design and the robust method of removing stray light with the cycling of the AOTF, some stray light was still observed in the obtained images. Impact and mitigation of this should be tackled in future iterations of the instrument. Two design changes could particularly help with this. Glan-Taylor prism polarizers (*Archard and Taylor, 1948*) should replace the nanoparticle linear polarizers. The advantage to the Glan-Taylor prism is rather than attenuate the unwanted polarization it is reflected though total internal reflection approximately 90 degrees from the optical axis where it can be absorbed away from the imaging plane reducing the stray light contamination. Further, the addition of a back-end telescope between the AOTF and the camera could be used to help further separate the desired diffracted signal from the zeroth order beam in physical space to reduce stray light further.

- An absolute calibration would improve the retrieval quality by allowing the direct determination of surface albedo. This is simply a matter of having access to the necessary calibration equipment.
- The addition of a shutter or masked pixels on the detector would be useful to calibrate the temperature dependent DC offset and dark current changes. Additionally, a faster readout would greatly increase the number of measurements that can be made with the system.
- A folded optical design would provide a much easier footprint to accommodate on the gondola and potentially help with thermal considerations by minimizing the size of the optical chain.

All of these improvements will help to improve the image quality, scientific return and ultimately the space feasibility of the ALI instrument.

Overall, the test flight of the ALI prototype developed in this work was a success and provides an important demonstration of the technology in a space environment, which is a key step in the path to a satellite mission. The design concept of matching the novel AOTF capability to the strengths of the limb scattering remote sensing technique makes for an innovative, low-cost approach to high quality, high resolution global stratospheric aerosol measurements. With continued work, ALI has potential to fulfill the aerosol monitoring needs of the future and both continue, and improve upon, this important data record for understanding our changing climate.



## LIST OF REFERENCES

- Andersson, S. M., B. G. Martinsson, J.-P. Vernier, J. Friberg, C. A. Brenninkmeijer, M. Hermann, P. F. van Velthoven, and A. Zahn (2015), Significant radiative impact of volcanic aerosol in the lowermost stratosphere, *Nature communications*, 6, doi:10.1038/ncomms8692.
- Andrews F. G. (1987), *Middle atmospheric dynamics*, Academic Press Inc.
- Angstrom, A. (1964), The parameters of atmospheric turbidity, *Tellus*, 16(1), 64 – 75, doi: 10.1111/j.2153-3490.1964.tb00144.x.
- Archard, J. F. and A. M. Taylor (1948), Improved Glan-Foucault Prism, *Journal of Scientific Instruments*, 25(12), 407, doi:10.1088/0950-7671/25/12/304.
- Barth, C. A., D. W. Rusch, R. J. Thomas, G. H. Mount, G. J. Rottman, G. E. Thomas, R. W. Sanders, and G. M. Lawrence (1983), Solar Mesosphere Explorer - Scientific objectives and results, *Geophysical Research Letters*, 10, 237-240, doi:10.1029/GL010i004p00237.
- Beuttell, R. G., and A. W. Brewer (1949), Instruments for the measurement of the visual range, *Journal of Scientific Instruments*, 26, 357.
- Bickel, W. S., and W. M. Bailey (1985), Stokes vectors, Mueller matrices, and polarized scattered light, *American Journal of Physics*, 53, 468-478 (1985), doi:10.1119/1.14202
- Bingen, C., D. Fussen, and F. Vanhellemont (2004), A global climatology of stratospheric aerosol size distribution parameters derived from sage ii data over the period 1984-2000: 1. methodology and climatological observations, *Journal of Geophysical Research*, 109, doi: 10.1029/2003JD003518.
- Boucher O. (2015), *Atmospheric Aerosols: Properties and Climate Impacts*, Springer.
- Bourassa, A. E., D. A. Degenstein, R. L. Gattinger, and E. J. Llewellyn (2007), Stratospheric aerosol retrieval with optical spectrograph and infrared imaging system limb scatter measurements, *Journal of Geophysical Research*, 112, D10217, doi:10.1029/2006JD008079.
- Bourassa, A. E., D. A. Degenstein, and E. J. Llewellyn (2008), SASKTRAN: A spherical geometry radiative transfer code for efficient estimation of limb scattered sunlight, *Journal of Quantitative Spectroscopy and Radiative Transfer*, 109, 52-73, doi:10.1016/j.jqsrt.2007.07.007.

- Bourassa, A. E., C. A. McLinden, A. F. Bathgate, B. J. Elash, and D. A. Degenstein (2012a), Precision estimate for Odin-OSIRIS limb scatter retrievals, *Journal of Geophysical Research: Atmospheres*, 117, D04303, doi:10.1029/2011JD016976.
- Bourassa, A. E., L. A. Rieger, N. D. Lloyd, and D. A. Degenstein (2012b), Odin-OSIRIS stratospheric aerosol data product and SAGE III intercomparison, *Atmospheric Chemistry & Physics*, 12, 605{614, doi:10.5194/acp-12-605-2012.
- Bourassa, A. E., A. Robock, W. J. Randel, T. Deshler, L. A. Rieger, N. D. Lloyd, E. T. Llewellyn, and D. A. Degenstein (2012c), Large volcanic aerosol load in the stratosphere linked to Asian monsoon transport, *Science*, 337, 78-81, doi:10.1126/science.1219371.
- Bourassa, A. E., A. Robock, W. J. Randel, T. Deshler, L. A. Rieger, N. D. Lloyd, E. Llewellyn, and D. A. Degenstein (2013), Response to comments on "large volcanic aerosol load in the stratosphere linked to Asian monsoon transport", *Science*, 339, 647-647, doi:10.1126/science.1227961.
- Bovensmann, H., J. Burrows, M. Buchwitz, J. Frerick, S. Noël, V. Rozanov, K. Chance, and A. Goede (1999), SCIAMACHY: Mission objectives and measurement modes, *Journal of the Atmospheric Sciences*, 56, 127-150, doi:10.1175/1520-0469(1999)056<0127:SMOAMM>2.0.CO;2.
- Brasseur G. P. and S. Solomon (2005), *Aeronomy of the Middle Atmosphere: Chemistry and Physics of the Stratosphere and Mesosphere*, 3<sup>rd</sup> edition, Springer.
- Brock, C. A., P. Hamill, J. C. Wilson, H. H. Jonsson, and K. R. Chan (1995), Particle Formation in the Upper Tropical Troposphere: A Source of Nuclei for the Stratospheric Aerosol, *Science*, 270, 1650-1653, doi:10.1126/science.270.5242.1650.
- Canty, T., N. Mascioli, M. Smarte, and R. Salawitch (2013), An empirical model of global climate—Part 1: A critical evaluation of volcanic cooling, *Atmospheric Chemistry and Physics*, 13(8), 3997–4031, doi:10.5194/acp-13-3997-2013.
- Carn, S. A., K. D. Froyd, B. E. Anderson, P. Wennberg, J. Crounse, K. Spencer, J. E. Dibb, N. A. Krotkov, E. V. Browell, J. W. Hair, G. Diskin, G. Sachse, S. A. Vay (2011), In situ measurements of tropospheric volcanic plumes in Ecuador and Colombia during TC4, *Journal of Geophysical Research*, 116, D00J24, doi:10.1029/2010JD014718.
- Chahine, M. T. (1970), Inverse Problems in Radiative Transfer: Determination of Atmospheric Parameters, *Journal of Atmospheric Science*, 27, 960-967, doi:10.1175/1520-0469(1970)027<0960:IPIRTD>2.0.CO;2.

- Chang, I. C. (1977), Noncollinear tunable acousto-optic filter. Patent.
- Charlson, R. J., N. Ahlquist, H. Selvidge, and P. MacCready Jr. (1969), Monitoring of atmospheric aerosol parameters with the integrating nephelometer, *Journal of the Air Pollution Control Association*, 19, 937-942, doi:10.1080/00022470.1969.10469360.
- Chazette, P., C. David, J. Lefrere, S. Godin, J. Pelon, and G. Mégie (1995), Comparative lidar study of the optical, geometrical, and dynamical properties of stratospheric postvolcanic aerosols, following the eruptions of El Chichon and Mount Pinatubo, *Journal of Geophysical Research*, 100, 23-195, doi:10.1029/95JD02268.
- Chuang, T., P. Burns, E. B. Walters, T. Wysocki, T. Deely, A. Losse, L. Le, B. Drumheller, T. Schum, M. Hart, K. Puffenburger, B. Ziegler, and F. Hovis (2013), Space-based, multi-wavelength solid-state lasers for NASA's Cloud Aerosol Transport System for International Space Station (CATS-ISS), *Proceedings SPIE*, 8599, 85990N. doi:10.1117/12.2005545.
- Cisewski, M., J. Zawodny, J. Gasbarre, R. Eckman, N. Topiwala, O. Rodriguez-Alvarez, D. Cheek, and S. Hall (2014), The stratospheric aerosol and gas experiment (SAGE III) on the international space station (ISS) mission, *Proceedings SPIE*, 9241, 924,107-924,107-7, doi:10.1117/12.2073131.
- Clarissee, L., P.-F. Coheur, N. Theys, D. Hurtmans, and C. Clerbaux (2014), The 2011 Nabro eruption, a SO<sub>2</sub> plume height analysis using IASI measurements, *Atmospheric Chemistry and Physics*, 14, 3095-3111, doi:10.5194/acp-14-3095-2014.
- Crutzen, P. J. (1976), The possible importance of CSO for the sulfate layer of the stratosphere, *Geophysics Research Letters*, 3, 73-76, doi:10.1029/GL003i002p00073.
- Damadeo, R. P., J. M. Zawodny, L. W. Thomason, and N. Iyer (2013), SAGE version 7.0 algorithm: application to SAGE II, *Atmospheric Measurement Techniques*, 6, 3539-3561, doi:10.5194/amt-6-3539-2013.
- Dee, D. P., S. M. Uppala, A. J. Simmons, P. Berrisford, P. Poli, S. Kobayashi, U. Andrae, M. A. Balmaseda, G. Balsamo, P. Bauer, P. Bechtold, A. C. M. Beljaars, L. van de Berg, J. Bidlot, N. Bormann, C. Delsol, R. Dragani, M. Fuentes, A. J. Geer, L. Haimberger, S. B. Healy, H. Hersbach, E. V. Hlm, L. Isaksen, P. Kllberg, M. Khler, M. Matricardi, A. P. McNally, B. M. Monge-Sanz, J.-J. Morcrette, B.-K. Park, C. Peubey, P. de Rosnay, C. Tavolato, J.-N. Thpaut, and F. Vitart (2011), The ERA-interim reanalysis: configuration and performance of the data

assimilation system, *Quarterly Journal of the Royal Meteorological Society*, 137, 553-597, doi:10.1002/qj.828.

Degenstein, D. A., A. E. Bourassa, C. Z. Roth, and E. J. Llewellyn (2009), Limb scatter ozone retrieval from 10 to 60 km using a multiplicative algebraic reconstruction technique, *Atmospheric Chemistry and Physics*, 9, 6521-6529, doi:10.5194/acp-9-6521-2009.

Dekemper, E., N. Loodts, B. V. Opstal, J. Maes, F. Vanhellemont, N. Mateshvili, G. Franssens, D. Pieroux, C. Bingen, C. Robert, L. D. Vos, L. Aballea, and D. Fussen (2012), Tunable acousto-optic spectral imager for atmospheric composition measurements in the visible spectral domain, *Applied Optics*, 51, 6259-6267, doi:10.1364/AO.51.006259.

Deshler, T., M. Hervig, D. Hofmann, J. Rosen, and J. Liley (2003), Thirty years of in situ stratospheric aerosol size distribution measurements from Laramie, Wyoming (41 N), using balloon-borne instruments, *Journal of Geophysical Research*, 108, doi:10.1029/2002JD002514.

Deshler T. (2008), A review of global stratospheric aerosol: Measurements, importance, life cycle, and local stratospheric aerosol, *Atmospheric Research*, 90, 2–4, 223-232, doi:10.1016/j.atmosres.2008.03.016.

Dueck, S., A. E., Bourassa, and D. A. Degenstein (2016), Polarization Additions SASKTRAN Radiative Transfer Model, In Preparations.

Elash, B. J., A. E. Bourassa, P. R. Loewen, N. D. Lloyd, and D. A. Degenstein, (2016), The Aerosol Limb Imager: acousto-optic imaging of limb-scattered sunlight for stratospheric aerosol profiling, *Atmospheric Measurement Techniques*, 9, 1261-1277, doi:10.5194/amt-9-1261-2016.

Ernst, F., C. von Savigny, A. Rozanov, V. Rozanov, K.-U. Eichmann, L. A. Brinkho, H. Bovensmann, and J. P. Burrows (2012), Global stratospheric aerosol extinction profile retrievals from SCIAMACHY limb-scatter observations, *Atmospheric Measurement Techniques*, 5, 5993-6035, doi:10.5194/amtd-5-5993-2012.

Fairlie, T. D., J.-P. Vernier, M. Natarajan, and K. M. Bedka (2014), Dispersion of the Nabro volcanic plume and its relation to the Asian summer monsoon, *Atmospheric Chemistry and Physics*, 14, 7045-7057, doi:10.5194/acp-14-7045-2014.

Fischer, R. E., B. Tadic-Galeb, and P. R. Yoder (2008), *Optical System Design*, 2nd ed., McGraw-Hill.

Fiocco, G., and G. Grams (1964), Observations of the aerosol layer at 20 km by optical radar, *Journal of the Atmospheric Sciences*, 21, 323-324.

Forsythe, W. E., and Worthing, A. G. (1925). The properties of tungsten and the characteristics of tungsten lamps. *The Astrophysical Journal*, 61, 146, doi:10.1086/142880.

Fromm, M., G. Nedoluha, and Z. Charvt (2013), Comment on "Large volcanic aerosol load in the stratosphere linked to Asian monsoon transport", *Science*, 339, 647, doi:10.1126/science.1228605.

Fromm, M., G. Kablick, G. Nedoluha, E. Carboni, R. Grainger, J. Campbell, and J. Lewis (2014), Correcting the record of volcanic stratospheric aerosol impact: Nabro and sarychev peak, *Journal of Geophysical Research*, 119, 10,343-10,364, doi:10.1002/2014JD021507.

Fussen, D., E. Dekemper, Q. Errera., G. Franssens, N. Mateshvili, D. Pieroux, and F. Vanhellemont (2016): The ALTIUS mission (in review), *Atmospheric Measurement Techniques Discussions*, doi:10.5194/amt-2016-213, in review.

Fyfe, J. C., N. P. Gillett, and F. W. Zwiers (2013), Overestimated global warming over the past 20 years, *Nature Climate Change*, 3, 767-769, doi:10.1038/nclimate1972.

Gass, P. A., and J. R. Sambles (1991), Accurate design of a non-collinear acousto-optic tunable filter, *Optics Letters*, 16, 429-431, doi:10.1364/OL.16.000429.

Gilbert, K., D. Turnbull, K. Walker, C. Boone, S. McLeod, M. Butler, R. Skelton, P. Bernath, F. Chateauneuf, and M.-A. Soucy (2007), The onboard imagers for the Canadian ACE SCISAT-1 mission, *Journal of Geophysical Research*, 112, doi:10.1029/2006JD007714.

Guenther, R. (1990), *Modern Optics*, 1st edition ed., Wiley and Sons, Inc.

Hamill P., E. J. Jensen, P. B. Russell, and J. J. Bauman (1997), The Life Cycle of Stratospheric Aerosol Particles, *Bulletin of the American Meteorological Society*, 78, 1395–1410, doi:10.1175/1520-0477(1997)078<1395:TLCOSA>2.0.CO;2.

Hansen, J. E., and L. D. Travis (1974), Light Scattering in Planetary Atmospheres, *Space Science Reviews*, 16(4), 527-610, doi:10.1007/BF00168069.

Hansen, J., R. Ruedy, and M. Sato (1996), Global surface air temperature in 1995: Return to pre-Pinatubo levels, *Geophysical Research Letters*, 23(13), 1665-1668, doi:10.1029/96GL01040.

Harris, S. E., and R. W. Wallace (1969), Acousto-Optic Tunable Filter, *Journal of the Optical Society of America* (1917-1983), 59, 744, doi: 10.1364/JOSA.59.000744.

Haywood, J. M., A. Jones, and G. S. Jones (2014), The impact of volcanic eruptions in the period 2000-2013 on global mean temperature trends evaluated in the HadGEM2-ES climate model, *Atmospheric Science Letters*, 15, 92-96, doi:10.1002/asl2.471.

Hofmann D. J. and J. M. Rosen (1983), Stratospheric sulfur acid fraction and mass estimate for the 1982 volcanic eruption of El Chichon, *Geophysical Research Letters*, 10(4), 313-316, doi: 10.1029/GL010i004p00313.

Hofmann, D., J. Barnes, M. O'Neill, M. Trudeau, and R. Neely (2009), Increase in background stratospheric aerosol observed with lidar at Mauna Loa observatory and Boulder, Colorado, *Geophysical Research Letters*, 36, doi:10.1029/2009GL039008, l15808.

Hoinka, K. (1997), The tropopause: Discovery, definition and demarcation, *Meteorologische Zeitschrift*, 6, 281-303, doi:10.1175/1520-0493(1998)126<3303:SOTGTP>2.0.CO;2.

Holton, J. R., P. H. Haynes, M. E. McIntyre, A. R. Douglass, R. B. Rood, and L Pfister (1995), Stratosphere-troposphere exchange, *Review of Geophysics*, 33, 403–439, doi:10.1029/95RG02097.

Jäger, H., and D. Hofmann (1991), Midlatitude lidar backscatter to mass, area, and extinction conversion model based on in situ aerosol measurements from 1980 to 1987, *Applied optics*, 30, 127-138, doi:10.1364/AO.30.000127.

Junge, C. E., C. W. Chagnon, and J. E. Manson (1961), Stratospheric aerosols, *Journal of Atmospheric Science*, 18, 81–108, doi:10.1175/1520-0469(1961)018<0081:SA>2.0.CO;2.

Kettle, A. J., U. Kuhn, M. von Hobe, J. Kesselmeier, M. O. Andreae, (2002) The global budget of atmospheric carbonyl sulfide: Temporal and spatial variations of the dominant sources and sinks, *Journal Geophysical Research*, 107, D22, 4658, doi:10.1029/2002JD002187.

Kiehl, J. T., and B. P. Briegleb (1993), The relative roles of sulfate aerosols and greenhouse gases in climate forcing, *Science*, 260, 311-314, doi:10.1126/science.260.5106.311.

Kosch, M., S. Mäkinen, F. Sigernes, and O. Harang (2003), Absolute optical calibration using a simple tungsten light bulb: Experiment, *Proceedings of the 30th Annual European Meeting on Atmospheric Studies by Optical Methods*, 50-54.

Kovilakam, M., and T. Deshler (2015), On the accuracy of stratospheric aerosol extinction derived from in situ size distribution measurements and surface area density derived from remote SAGE II and HALOE extinction measurements, *Journal Geophysical Research Atmospheres*, 120, 8426–8447, doi:10.1002/2015JD023303.

Kozun M. N. (2015), *Optical Pointing System For Stratospheric Balloon-Borne Multi-Slit OSIRIS-DM*, Master's Thesis, University of Saskatchewan.

Kremser, S., L. W. Thomason, M. von Hobe, M. Hermann, T. Deshler, C. Timmreck, M. Toohey, A. Stenke, J. P. Schwarz, R. Weigel, S. Fueglstaler, F. J. Prata, J.-P. Vernier, H. Schlager, J. E. Barnes, J.-C. Antuña-Marrero, D. Fairlie, M. Palm, E. Mahieu, J. Notholt, M. Rex, C. Bingen, F. Vanhellemont, A. Bourassa, J. M. C. Plane, D. Klocke, S. A. Carn, L. Clarisse, T. Trickl, R. Neely, A. D. James, L. Rieger, J. C. Wilson, and B. Meland (2015), Stratospheric aerosol—Observations, processes, and impact on climate, *Reviews of Geophysics* 54, doi:10.1002/2015RG000511.

Lacis, A., J. Hansen, and M. Sato (1992), Climate forcing by stratospheric aerosols, *Geophysical Research Letters*, 19, 1607–1610, doi:10.1029/92GL01620.

Levenberg, K. (1944), A method for the solution of certain non-linear problems in least squares, *Quarterly of Applied Mathematics*, 2(2), 164-168.

Llewellyn, E., N. D. Lloyd, D. A. Degenstein, R. L. Gattinger, S. V. Petelina, A. E. Bourassa, J. T. Wiensz, E. V. Ivanov, I. C. McDade, B. H. Solheim, J. C. McConnell, C. S. Haley, C. von Savigny, C. E. Sioris, C. A. McLinden, E. Griffioen, J. Kaminski, W. F. J. Evans, E. Puckrin, K. Strong, V. Wehrle, R. H. Hum, D. J. W. Kendall, J. Matsushita, D. P. Murtagh, S. Brohede, J. Stegman, G. Witt, G. Barnes, W. F. Payne, L. Piche, K. Smith, G. Warshaw, D. L. Deslauniers, P. Marchand, E. H. Richardson, R. A. King, I. Wevers, W. McCreath, E. Kyrölä, L. Oikarinen, G. W. Leppelmeier, H. Auvinen, G. Megie, A. Hauchecorne, F. Lefevre, J. de La Noe, P. Ricaud, U. Frisk, F. Sjoberg, F. von Scheele, and L. Nordh (2004), The OSIRIS instrument on the Odin spacecraft, *Canadian Journal of Physics*, 82, 411-422, doi:10.1139/p04-005.

Marquardt, D. W. (1963), An algorithm for least-squares estimation of nonlinear parameters, *Journal of the society for Industrial and Applied Mathematics*, 11(2), 431-441.

McLinden, C. A., J. C. McConnell, C. T. McElroy, and E. Griffioen (1999), Observations of Stratospheric Aerosol Using CPFM Polarized Limb Radiances, *Journal of the Atmospheric Sciences*, 56:2, 233-240, doi:10.1175/1520-0469(1999)056<0233:OOSAUC>2.0.CO;2.

McCormick, M. P., and T. J. Swissler (1983), Stratospheric aerosol mass and latitudinal distribution of the El Chichon eruption cloud for October 1982, *Geophysical Research Letters*, 10(9), 877–880, doi:10.1029/GL010i009p00877.

McCormick, M. P. and R. E. Veiga (1992), SAGE II measurements of early Pinatubo aerosols, *Geophysical Research Letters*, 19(2), 155-158, doi:10.1029/91GL02790.

McCormick, M. P., L. W. Thomason, and C. R. Trepte (1995), Atmospheric effects of the Mt Pinatubo eruption, *Nature*, 373(6513), 399-404, doi:10.1038/373399a0.

McElroy, C. T., C. R. Nowlan, J. R. Drummond, P. F. Bernath, D. V. Barton, D. G. Dufour, C. Midwinter, R. B. Hall, A. Ogyu, A. Ullberg, D. I. Wardle, J. Kar, J. Zou, F. Nichitiu, C. D. Boone, K. A. Walker, and N. Rowlands (2007), The ACE-MAESTRO instrument on SCISAT: description, performance, and preliminary results, *Applied Optics*, 46, 4341-4356, doi:10.1364/AO.46.004341.

Mie, G. (1908), Considerations on the optics of turbid media, especially colloidal metal solutions, *Annalen der Physik (Leipzig)*., 42, 377.

Mishchenko, M. I., L. D. Travis, and A. A. Lacis (2002), *Scattering, Absorption, and Emission of Light by Small Particles*, 3<sup>rd</sup> edition, Cambridge, UK: Cambridge University Press.

Murphy, D. M., K. D. Froyd, J. P. Schwarz, and J. C. Wilson (2014), Observations of the chemical composition of stratospheric aerosol particles, *Quarterly Journal of the Royal Meteorological Society*, 140, 1269-1278, doi:10.1002/qj.2213.

Neely, R. R., P. Yu, K. H. Rosenlof, O. B. Toon, J. S. Daniel, S. Solomon, and H. L. Miller (2014), The contribution of anthropogenic SO<sub>2</sub> emissions to the Asian tropopause aerosol layer, *Journal of Geophysical Research*, 119, 1571-1579, doi:10.1002/2013JD020578.

Notholt, J., Z. Kuang, C. P. Rinsland, G. C. Toon, M. Rex, N. Jones, T. Albrecht, H. Deckelmann, J. Krieg, C. Weinzierl, H. Bingemer, R. Weller and O. Schrems (2003), Enhanced Upper Tropical Tropospheric COS: Impact on the Stratospheric Aerosol Layer, *Science*, 300, 307-310, doi:10.1126/science.1080320.

Oikarinen, L., E. Sihvola, and E. Kyrölä (1999), Multiple scattering radiance in limb-viewing geometry, *Journal of Geophysical Research*, 104, 31,261-31,274, doi:10.1029/1999JD900969.

Plumb, R. A. and J. Eluszkiewicz, (1999), The Brewer–Dobson Circulation: Dynamics of the Tropical Upwelling, *Journal of Atmospheric Science*, 56, 868–890, doi:10.1175/1520-0469(1999)056<0868:TBCDO>2.0.CO;2.

Prata, A. J., G. Gangale, L. Clarisse, and F. Karagulian (2010), Ash and sulfur dioxide in the 2008 eruptions of Okmok and Kasatochi: Insights from high spectral resolution satellite measurements, *Journal of Geophysical Research*, 115, D00L18, doi:10.1029/2009JD013556.

Rault, D. F., and R. P. Loughman (2013), The OMPS limb profiler environmental data record algorithm theoretical basis document and expected performance, *IEEE Transactions on Geoscience and Remote Sensing*, 51, 2505-2527, doi:10.1109/TGRS.2012.2213093.

Rayleigh, F.R.S. (1899), XXXIV. On the transmission of light through an atmosphere containing small particles in suspension, and on the origin of the blue of the sky, *Philosophical Magazine Series 5*, 47, 287, 375-384, doi:10.1080/14786449908621276.

Ridley, D. A., S. Solomon, J. E. Barnes, V. D. Burlakov, T. Deshler, S. I. Dolgii, A. B. Herber, T. Nagai, R. R. Neely, A. V. Nevezorov, C. Ritter, T. Sakai, B. D. Santer, M. Sato, A. Schmidt, O. Uchino, and J. P. Vernier (2014), Total volcanic stratospheric aerosol optical depths and implications for global climate change, *Geophysical Research Letters*, 41, 7763-7769, doi:10.1002/2014GL061541, 2014GL061541.

Rieger, L. A., A. E. Bourassa, and D. A. Degenstein (2014), Stratospheric aerosol particle size information in Odin-OSIRIS limb scatter spectra, *Atmospheric Measurement Techniques*, 7, 507-522, doi:10.5194/amt-7-507-2014.

Rieger, L. A., A. E. Bourassa, and D. A. Degenstein (2015), Merging the OSIRIS and SAGE II stratospheric aerosol records, *Journal of Geophysical Research*, doi:10.1002/2015JD023133, 2015JD023133.

Rodgers, C. (2000), *Inverse Methods for Atmospheric Sounding: Theory and Practice, Series on atmospheric, oceanic and planetary physics*: 1999, World Scientific, River Edge, NJ, USA.

Rogers, R. R., C. A. Hostetler, J. W. Hair, R. A. Ferrare, Z. Liu, M. D. Obland, D. B. Harper, A. L. Cook, K. A. Powell, M. A. Vaughan, and D. M. Winker (2011), Assessment of the CALIPSO lidar 532 nm attenuated backscatter calibration using the NASA LARC airborne high spectral resolution lidar, *Atmospheric Chemistry and Physics*, 11, 1295-1311, doi:10.5194/acp-11-1295-2011.

Rosen J. M. (1971), The Boiling Point of Stratospheric Aerosols, *Journal of Applied Meteorology*, 10, 1044–1046, doi:10.1175/1520-0450(1971)010<1044:TBPOSA>2.0.CO;2.

Russell, P., and M. McCormick (1989), SAGE II aerosol data validation and initial data use: An introduction and overview, *Journal of Geophysical Research*, 94, 8335-8338 doi:10.1029/JD094iD06p08335.

Saito K., A. W. and T. Yano (1976), Acousto-optic filter. Patent.

Sawamura, P., J. P. Vernier, J. E. Barnes, T. A. Berko, E. J. Welton, L. Alados-Arboledas, F. Navas-Guzmn, G. Pappalardo, L. Mona, F. Madonna, D. Lange, M. Sicard, S. Godin-Beckmann, G. Payen, Z. Wang, S. Hu, S. N. Tripathi, C. Cordoba-Jabonero, and R. M. Ho (2012), Stratospheric AOD after the 2011 eruption of Nabro volcano measured by lidars over the northern hemisphere, *Environmental Research Letters*, 7, 034,013, doi:10.1088/1748-9326/7/3/034013.

Schutz, B., H. Zwally, C. Shuman, D. Hancock, and J. DiMarzio (2005), Overview of the ICEsat mission, *Geophysical Research Letters*, 32, doi:10.1029/2005GL024009.

Sioris, C. E., C. D. Boone, P. F. Bernath, J. Zou, C. T. McElroy, and C. A. McLinden (2010), Atmospheric chemistry experiment (ACE) observations of aerosol in the upper troposphere and lower stratosphere from the Kasatochi volcanic eruption, *Journal of Geophysical Research*, 115, doi:10.1029/2009JD013469, d00L14.

Smith, W. J. (2000), *Modern Optical Engineering*, New York: McGraw-Hill.

Sneep, M., and W. Ubachs (2005), Direct measurement of the Rayleigh scattering cross section in various gases, *Journal of Quantitative Spectroscopy and Radiative Transfer*, 92(3), 293-310, doi:10.1016/j.jqsrt.2004.07.025.

Soden, B. J., R. T. Wetherald, G. L. Stenchikov, and A. Robock (2002), Global cooling after the eruption of Mount Pinatubo: A test of climate feedback by water vapor, *Science*, 296(5568), 727–730, doi:10.1126/science.296.5568.727.

Solomon, S., D. Qin, M. Manning, Z. Chen, M. Marquis, K. B. Averyt, M. Tignor, and H. L. Miller (2007), Contribution of Working Group I to the Fourth Assessment Report of the Intergovernmental Panel on Climate Change, *Tech. rep.*

- Solomon, S., J. S. Daniel, R. R. Neely, J.-P. Vernier, E. G. Dutton, and L. W. Thomason (2011), The persistently variable background stratospheric aerosol layer and global climate change, *Science*, 333, 866-870, doi:10.1126/science.1206027.
- Solomon, S., D. J. Ivy, D. Kinnison, M. J. Mills, R. R. Neely, and A. Schmidt (2016), Emergence of healing in the Antarctic ozone layer, *Science*, 353, 269-274, doi:10.1126/science.aae0061.
- Stocker, T. F., D. Qin, G.-K. Plattner, M. M. Tignor, S. K. Allen, J. Boschung, A. Nauels, Y. Xia, V. Bex, and P. M. Midgley (2013), *Climate Change 2013 The Physical Science Basis*, Cambridge University Press, Cambridge, UK, and New York, NY, USA.
- Suhre, D. R., L. J. Denes, and N. Gupta (2004), Telecentric confocal optics for aberration correction of acousto-optic tunable filters, *Applied Optics*, 43, 1255-1260, doi:10.1364/AO.43.001255.
- Taylor B. J. A. (2015), *The Upgrade, Calibration, and Evaluation of the Multi-Slit OSIRIS-DM for Stratospheric Balloon Flight*, Master's Thesis, University of Saskatchewan.
- Thomason, L. W., and G. Taha (2003), SAGE III aerosol extinction measurements: Initial results, *Geophysical Research Letters*, 30, doi:10.1029/2003GL017317.
- Thomason, L. W. and T. Peter (2006), Assessment of Stratospheric Aerosol Processes (ASAP), *World Climate Research Program*, 1–322.
- Thompson, D. W., J. M. Wallace, P. D. Jones, and J. J. Kennedy (2009), Identifying signatures of natural climate variability in time series of global-mean surface temperature: Methodology and insights, *Journal of Climate*, 22(22), 6120–6141, doi:10.1175/2009JCLI3089.1.
- Thomason, L. W., and J.-P. Vernier (2013), Improved SAGE II cloud/aerosol categorization and observations of the Asian tropopause aerosol layer: 1989-2005, *Atmospheric Chemistry and Physics*, 13, 4605-4616, doi:10.5194/acp-13-4605-2013.
- Uchida, N. (1971), Optical properties of single-crystal paratellurite ( $\text{TeO}_2$ ), *Physics Review B*, 4, 3736-3745, doi:10.1103/PhysRevB.4.3736.
- Van de Hulst, H. C. (1962), *Light Scattering by Small Particles*, New York: Wiley and Sons Inc.
- Vanhellemont, F., C. Tetard, A. Bourassa, M. Fromm, J. Dodion, D. Fussen, C. Brogniez, D. Degenstein, K. L. Gilbert, D. N. Turnbull, P. Bernath, C. Boone, and K. A. Walker (2008),

Aerosol extinction profiles at 525 nm and 1020 nm derived from ACE imager data: comparisons with GOMOS, SAGE II, SAGE III, POAM III, and OSIRIS, *Atmospheric Chemistry and Physics*, 8, 2027-2037, doi:10.5194/acp-8-2027-2008.

Vernier, J.-P., L. Thomason, and J. Kar (2011a), CALIPSO detection of an Asian tropopause aerosol layer, *Geophysical Research Letters*, 38, doi:10.1029/2010GL046614.

Vernier, J.-P., L. W. Thomason, J.-P. Pommereau, A. Bourassa, L. Blanot, C. Trepte, D. Degenstein, and F. Vargas (2011b), Major influence of tropical volcanic eruptions on the stratospheric aerosol layer during the last decade, *Geophysical Research Letters*, 38, L12807, doi:10.1029/2011GL047563.

Vernier, J.-P., L. W. Thomason, T. D. Fairlie, P. Minnis, R. Palikonda, and K. M. Bedka (2013), Comment on "Large volcanic aerosol load in the stratosphere linked to Asian monsoon transport", *Science*, 339, 647, doi:10.1126/science.1227817.

Volk, C. M., J. W. Elkins, D. W. Fahey, G. S. Dutton, J. M. Gilligan, M. Loewenstein, J. R. Podolske, K. R. Chan, and M. R. Gunson (1997), Evaluation of source gas lifetimes from stratospheric observations, *Journal of Geophysical Research*, 102(D21), 25543–25564, doi:10.1029/97JD02215.

Voloshinov, V. (1996), Spectral and polarization analysis of optical images by means of acousto-optics, *Optics Laser Technology*, 28, 119-127, doi:10.1016/0030-3992(95)00079-8.

Voloshinov, V. B., and J. C. Mosquera (2006), Wide-aperture acousto-optic interaction in birefringent crystals, *Optics and Spectroscopy*, 101, 635-641, doi:10.1134/S0030400X06100225.

Voloshinov, V. B., K. B. Yushkov, and B. B. J. Linde (2007), Improvement in performance of a TeO<sub>2</sub> acousto-optic imaging spectrometer, *Journal of Optics A: Pure and Applied Optics*, 9, 341-347, doi:10.1088/1464-4258/9/4/006.

von Savigny, C., F. Ernst, A. Rozanov, R. Hommel, K.-U. Eichmann, V. Rozanov, J. P. Burrows, and L. W. Thomason (2015), Improved stratospheric aerosol extinction profiles from SCIAMACHY: validation and sample results, *Atmospheric Measurement Techniques*, 8, 8353-8383, doi:10.5194/amtd-8-8353-2015.

Wang, P.-H., M. P. McCormick, T. J. Swissler, M. T. Osborn, W. H. Fuller, and G. K. Yue (1989), Inference of stratospheric aerosol composition and size distribution from SAGE II

satellite measurements, *Journal Geophysical Research*, 94(D6), 8435–8446, doi:10.1029/JD094iD06p08435.

Winker, D. M., W. H. Hunt, and M. J. McGill (2007), Initial performance assessment of CALIOP, *Geophysical Research Letters*, 34, doi:10.1029/2007GL030135.

Wiscombe, W. J. (1980), Improved Mie scattering algorithms, *Applied Optics*, 19, 1505-1509, doi:10.1364/AO.19.001505.

Xu, J., and R. Stroud (1992), *Acousto-optic devices: principles, design, and applications*, Wiley-Interscience.

York, D. (1966), *Least-Square Fitting of a Straight Line*, Canadian Journal of Physics 44, 1079-1086.

Young, S. A., and M. A. Vaughan (2009), The retrieval of profiles of particulate extinction from cloud-aerosol lidar infrared pathfinder satellite observations (calipso) data: Algorithm description, *Journal of Atmospheric and Oceanic Technology*, 26, 1105-1119, doi:10.1175/2008JTECHA1221.1.

Zawada, D. J., S. R. Dueck, L. A. Rieger, A. E. Bourassa, N. D. Lloyd, and D. A. Degenstein (2015), High resolution and Monte Carlo additions to the SASKTRAN radiative transfer model, *Atmospheric Measurement Techniques*, 8, 3357-3397, doi:10.5194/amtd-8-3357-2015.

## APPENDIX A

# HARDWARE COMPONENTS

The section will list and give specifications for all of the major hardware components. Each section will have a brief description followed by a table of the specifications.

### A.1 ALI Optical Components

#### A.1.1 Optical Lenses

All lenses used in the ALI system were purchased from Newport and were coated with anti-reflective coating AR.16 which covers 650-1000 nm range with an average reflectance of 0.5% and a maximum of 1.5%. All the lens in the system were made from N-BK7 glass and the specification and model number of each lens is located in Table A-1.

**Table A-1:** Lens used in ALI and their specifications.

Model Number	Effective Focal Length (mm)	Diameter (mm)	Center Thickness (mm)	Radius (mm)	Type of Lens
KPX100AR.16	150.0±1.5	25.4+0/-0.1	4.0±0.1	77.520	Plano-Convex
KPX187AR.16	100.0±1.0	50.2+0/-0.1	9.7±0.1	51.680	Plano-Convex
KBX052AR.16	50.2±0.5	25.4+0/-0.1	6.2±0.1	50.806	Bi-Convex

#### A.1.2 Polarizers

ALI needed two linear polarizers to help remove unwanted signal and reduce stray light in the system. These polarizers required a high extinction ratio over the range of the CCD sensitivities. The polarizers chosen were model number LPVIS100 from Thorlabs. The extinction ratios and transmission of the device can be seen in Figure A-1.

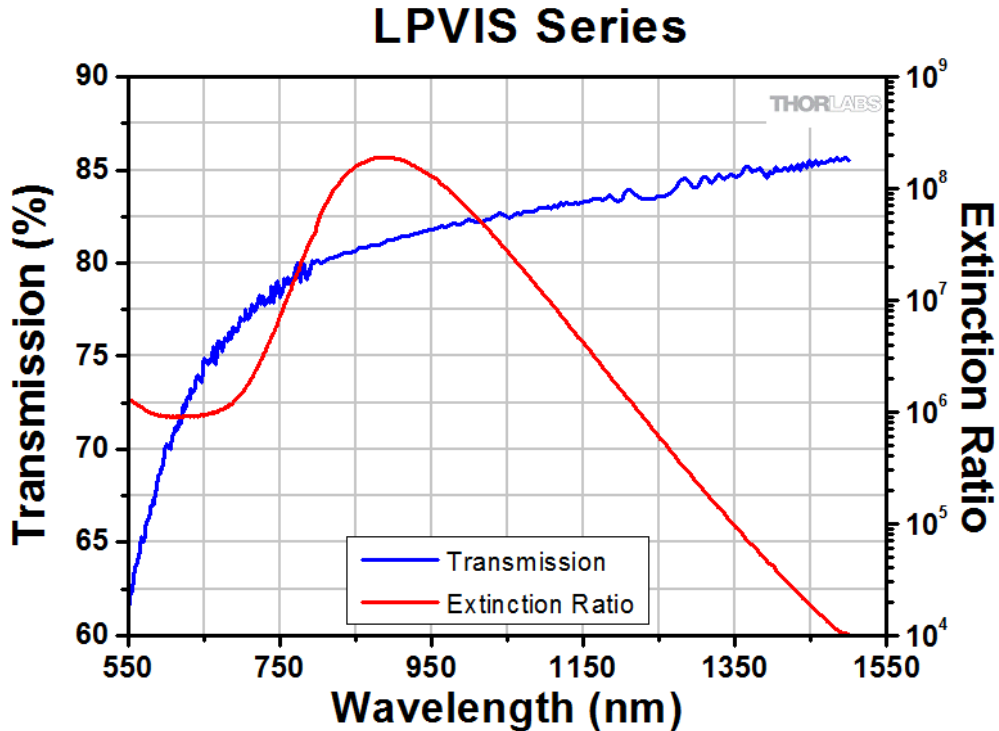


**Figure A-1:** The transmission and extinction ratios of the LPVIS100 used in ALI.

### A.1.3 AOTF

The AOTF in ALI is made by Brimrose of America (model number TEAFI10-0.6-1.0-MSD).

The specifications of the device can be seen in Table A-2. The separation angle is defined as the angle between the input source and the desired refracted polarization and the acceptance angle is measured from the normal of the face of the crystal.

**Table A-2:** AOTF Specifications.

Parameter	Value	Parameter	Value
Material	$\text{TeO}_2$	Polarization	Linear vertical
RF Range (Mhz)	75-156	Tunable Range (nm)	600-1200
Optical Aperture (mm)	10x10	Angular Aperture ( $^\circ$ )	4.0
Acceptance Angle ( $^\circ$ )	2.0	Separation Angle ( $^\circ$ )	6.4
Output Angle ( $^\circ$ )	2.7	Diffraction Efficiency (%)	~60
RF Power (W)	2.0	Damage Threshold (W)	5.0

## A.2 ALI Opto-Mechanical and Electrical Components

### A.2.1 RF Driver

The driver for ALI is made by Gooch and Housego (model number 64020-200-2ADMDFS-A). It had no internal control mechanism and required additional control hardware to operate the device. In order to pick the frequency, a 30-bit digital value is inputted into the device to pick a frequency as well as manage several control lines to the device. The control word is used to determine a specific frequency which is given by

$$K_{10} = \frac{F2^{n+1}}{F_{clk}} \quad (\text{A.1})$$

where  $K_{10}$  is the 30-bit control word in base 10 rounded to the nearest integer,  $F$  is the desired RF to be outputted by the driver,  $F_{clk}$  is the internal clock of the driver which is 1000.059 MHz for ALI, and  $n$  is the number of bits in the control word for ALI (*i.e.*  $n = 30$ ). The control word is converted to binary and sent to the device to get the desired RF.

### A.2.2 QSI CCD Camera

The CCD camera was a QSI 616s with a Kodak KAP-1603ME sensor with a mechanical shutter and a 16-bit digital readout. The spectral response of the device can be seen in Figure 3-8 and the camera specification can be seen in Table A-3.

**Table A-3:** QSI CCD camera specifications.

Parameter	Value	Parameter	Value
Imager Size (mm)	13.8 x 9.2	Imager Size (pixels)	1536 x 1024
Pixel Size ( $\mu\text{m}$ )	9 x 9	Read Noise RMS (electrons)	15
Mass (kg)	0.95	Power Consumption (W)	24
Operating Temperature ( $^{\circ}\text{C}$ )	-20 to 30	Full Well Depth (electrons)	100,000

### A.2.3 OCELOT Computer

The on board computer for the ALI instrument was the Ocelot VL-EPMs-21 computer made by VersaLogic. Its architecture is based on the Intel Atom Z5 processor and had 2 GB of DDR2

memory. It had low power draw and fanless operation. It had a temperature range of -40 to 85 °C.

The system run a bare-bone version of Debian Linux.

#### A.2.4 Opto-Mechanical Pieces

In this section is a brief list of all the opto-mechanical components used within the final version of ALI. Listed is the model number of the components and the quantity in the design with a short description. All components were purchased from Thorlabs.

**Table A-4:** Opto-mechanical components used in ALI

Model Number	Quantity	Description
XT95SP-1000	1	1000 mm length optical rail, 95 mm width
XT95P11/M	4	95 mm width optical rail drop-on carriage
RS2P4M	2	Pedestal post, 50 mm long, 25.4 mm width, metric, M4
RS2P/M	2	Pedestal post, 50 mm long, 25.4 mm width, metric, M6
RS2M	2	Pedestal post spacer, 2 mm long, 25.4 mm width
RS7M	2	Pedestal post spacer, 7 mm long, 25.4 mm width
LCP01B	2	60 mm cage clamp
CP02T/M	1	30 mm cage plate, 1" lens holder, square, metric
CP07	3	60 mm cage plate, 1" lens holder, round, metric
LCP01/M	1	60 mm cage plate, 2" lens holder, square, metric
LCP02/M	4	30 mm to 60 mm cage converter, metric
ER1-P4	3	Cage assembly rod, 1" long, 4 pack
ER2-P4	2	Cage assembly rod, 2" long, 4 pack
ER4-P4	1	Cage assembly rod, 4" long, 4 pack
ER8-P4	2	Cage assembly rod, 8" long, 4 pack
LC1A/M	1	Swivel mount, 60

### A.3 Calibration Equipment

#### A.3.1 Horiba iHR 320 Spectrometer

Below are the specification for the Horiba iHR 320 spectrometer used for the calibration of the ALI instrument with a 1200g/mm diffraction grating.

**Table A-5:** Horiba iHR 320 spectrometer specifications

Parameter	Value	Parameter	Value
Focal Length (mm)	320	Aperture (F/#)	4.1
Spectral Range (nm)	150-1500	Grating Size (mm)	68x68
Flat Field Size (mm)	30x12	Resolution (nm)	0.06
Wavelength Accuracy (nm)	$\pm 0.20$	Repeatability (nm)	$\pm 0.075$
Spectral Dispersion (nm/mm)	2.35	Magnification	1.1
Stray Light	0.0005	Scan Speed (nm/s)	159
Step Size (nm)	0.002	Dimensions (mm)	417x422x192

#### A.3.2 Synapse CCD Detector

Below are the specifications and spectral dependence on the Synapse CCD detector used in some calibration experiments of ALI.

**Table A-6:** Synapse CCD Detector Specifications

Parameter	Value	Parameter	Value
CCD Size (pixls)	1024x256	Pixel Size ( $\mu\text{m}$ )	26x26
Image Area (mm)	26.6x6.7	Dynamic Rage (bits)	bits
Readout Noise – mean ( $e^-$ )	3.4	Readout Noise – max ( $e^-$ )	5.0
Pixel Well – min ( $ke^-$ )	350	Pixel Well – mean ( $ke^-$ )	500
Dark Current ( $e^-/\text{pixel/s}$ )	0.002		

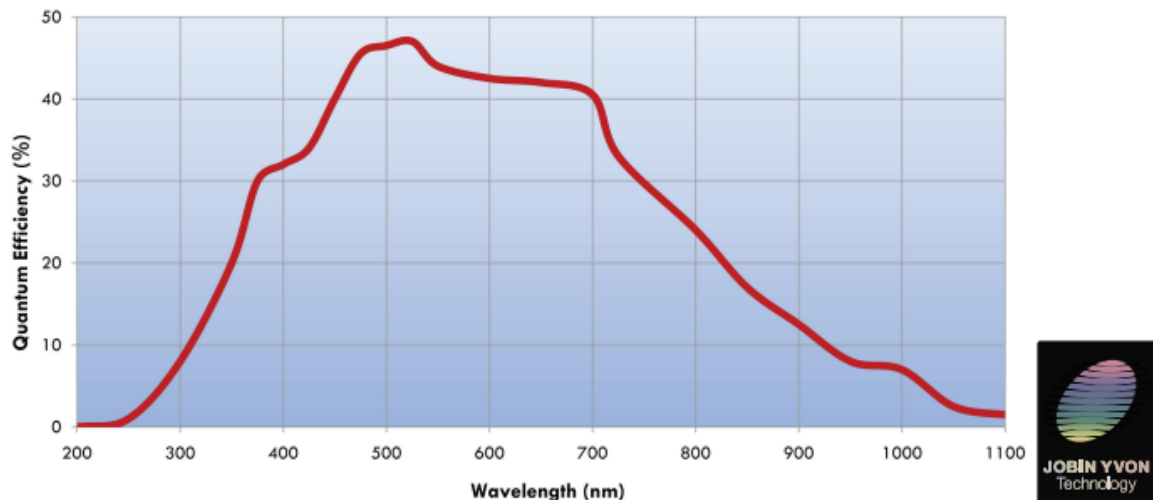


**Figure A-2:** Typical Spectral response of a Synapse CCD Detector as provided by Jobin-Yvon.

## APPENDIX B

### ALI SOFTWARE COMMANDS

#### **B.1 List of Commands for ALI Software**

Following is a list of the commands that can be used in the ALI software for operational control during flight through the ground based communication program. A complete list will be presented then a description of each function will follow, all are case sensitive.

- `EnableScience`
- `DisableScience`
- `EnableRF`
- `DisableRF`
- `EnableAutoSendStats`
- `DisableAutoSendStats`
- `SetScienceMode`
- `ReloadConfig`
- `LdCusCnf`
- `LdCusExp`
- `GetFile`
- `EndCurrentScienceCycle`
- `SetExposureScaleFactor`
- `UpdateExposureTimeCurve`
- `EnableCheckRfTemps`
- `DisableCheckRfTemps`
- `ResetHousekeeping`

- `DumpConfig`
- `SetBitsPerSecond`
- `EnableAutomation`
- `DisableAutomation`
- `SetAutomationTimeout`
- `EnableGps`
- `DisableGps`
- `EnablePulse`
- `DisablePulse`

### **B.1.1 EnableScience**

Full Command: `EnableScience`

This command enables science data acquisition and enables the RF driver. If the current mode is invalid, the system reports the error to the user. By default, science mode data acquisition is disabled and must be enabled.

### **B.1.2 DisableScience**

Full Command: `DisableScience`

This command disables science data acquisition at the end of the current science mode cycle. This mode does not disable the RF driver. Disabling the RF driver only pauses the cycle and does not terminate it. By default, science data acquisition is disabled.

### **B.1.3 EnableRF**

Full Command: `EnableRF`

This command turns on the RF driver by enabling the relay that controls the power to the device. It has a heavy power draw and by default is disabled.

### **B.1.4 DisableRF**

Full Command: **DisableRF**

Disables the RF driver during science mode acquisition. This only pauses the science acquisition cycle mode and will continue once the driver is enabled again. By default, the RF driver is disabled due to the high power draw.

### **B.1.5 EnableAutoSendStats**

Full Command: **EnableAutoSendStats**

Enables the sending of statistics for each image taken and includes five vertical columns of measured data and housekeeping information. By default, this is enabled.

### **B.1.6 DisableAutoSendStats**

Full Command: **DisableAutoSendStats**

Disables the sending of statistics for each image taken. It is not recommended to disable sending the statistics. .

### **B.1.7 SetScienceMode**

Full Command: **SetScienceMode scienceMode,exposureMode**

Parameter: **scienceMode** is a numerical value of the science mode to be run.

Parameter: **exposureMode** is a numerical value of the science mode to be run.

Allows the user to change science mode and exposure modes that ALI is performing. The science mode is a predetermined cycle of images to perform a specific scientific goal and Table B-1 contains a list of all of the modes available and a complete description of each cycle is presented in section B.2. The exposure mode is a predetermined exposure time length to be used for each wavelength and Table B-6 contains a list of all of the modes available and a complete description of each mode is presented in section B.3. The next mode will be loaded once the current mode is complete. By default the program is set in Invalid Mode.

### **B.1.8 ReloadConfig**

Full Command: **ReloadConfig**

Upon completion of the current science cycle, the science mode cycle will be reloaded from the configuration files.

### **B.1.9 LdCusCnf**

Full Command: **LdCusCnf IsOneExp,NumExp,wavelength,RFPower...**

Parameter: **IsOneExp** is either a 0 or a 1. A 0 states that the exposure time will be scaled to the calibration curve. A value of 1 states the exposure time will be constant.

Parameter: **NumExp** is the number of images in the custom science mode.

Parameter: **wavelength,RFPower...** is a pair of values for each image in the cycle as defined by **NumExp** consisting of a wavelength in nanometers and a RF power ranging from zero to one.

This function uploads values for a custom science mode. The first value is whether a constant or varying exposure time is to be used for the cycle followed by the number of exposures. For each exposure, a pair of values that consists of a wavelength in nanometers and RF power are required for the specifications. There is no check on the values of the wavelength and RF powers and the user must verify that the wavelength range is in between 600 and 1000 nm and the RF power is between zero and one.

### **B.1.10 LdCusExp**

Full Command: **LdCusExp numTimes,time...**

Parameter: **numTime** is the number of exposure times to be entered.

Parameter: **time...** is a series of times in seconds separated by commas to match the number of exposure times loaded into the custom mode.

This function uploads values for a custom exposure time series. The first value is the number of exposure times followed by a series of time in seconds. If custom exposure time is used, the number of exposures must match the number of exposure times or an error is sent to the user.

### **B.1.11 GetFile**

Full Command: **GetFile filename**

Parameter: **filename** is the image file to be downloaded from ALI with the full path.

Sends a filename into the queue to be downloaded from ALI if the filename exists. This entered file is added to the top of the queue.

### **B.1.12 EndCurrentScienceCycle**

Full Command: **EndCurrentScienceCycle**

Ends the current science operation mode immediately.

### **B.1.13 SetExposureScaleFactor**

Full Command: **SetExposureScaleFactor scaleFactor**

Parameter: **scaleFactor** is a number greater than zero that scales the default calibrated exposure time curve seen in Table 4-2.

Sets a scaling factor for the exposure times. Value must be greater than zero or an error is returned. Default is 1.0.

### **B.1.14 UpdateExposureTimeCurve**

Full Command: **UpdateExposureTimeCurve time...**

Parameter: **time...** is a series of 13 times separated by commas with minimum values of 0.05 seconds and a maximum of 60 seconds. The 13 values correspond to exposure times for wavelengths from 650-950 nm in 25 nm intervals.

This function changes the default values in the calibrated exposure time curve. Default values can be seen in Table 4-2.

### **B.1.15 EnableCheckRfTemps**

Full Command: `EnableCheckRfTemps`

Enables a check to verify that the RF driver is not operating outside its rated temperature range.

At 0 degrees Celsius the RF driver is powered on and at 50 degrees it is powered off. By default the check is enabled.

### **B.1.16 DisableCheckRfTemps**

Full Command: `DisableCheckRfTemps`

Disables the temperature check for the RF driver. By default the check is enabled and it is not recommended to disable the check unless an issue with the temperature sensors arises.

### **B.1.17 ResetHousekeeping**

Full Command: `ResetHouseKeeping`

Resets the housekeeping module to reacquire the voltage and temperature sensors. To only be used if there is a problem occurs with the housekeeping module.

### **B.1.18 DumpConfig**

Full Command: `DumpConfig`

Prints the current configuration loaded into the science module. It is used for debugging purposes.

### **B.1.19 SetBitsPerSecond**

Full Command: `SetBitsPerSecond bitsPerSecond`

Parameter: `bitsPerSecond` is the value to change the download speed during operation in bits per second.

Changes the bitrate limit for the ALI operation program. Minimum value is 32000 bits per second and the default is 50000 bits for second.

**B.1.20 EnableAutomation**

Full Command: **EnableAutomation**

Enables the automatic timeout process in case of a loss of communication during the launch.

Enabled by default and after 90 minutes of inactivity it puts the system in aerosol mode.

**B.1.21 DisableAutomation**

Full Command: **DisableAutomation**

Stops the process that automatically starts ALI in an aerosol mode science operation after 90 minutes. This process should be disabled if the user has control of the system at float altitude.

**B.1.22 SetAutomationTimeout**

Full Command: **SetAutomationTimeout time**

Parameter: **time** is the new time in minutes to set the timeout value.

Changes the default timeout time to the time given in minutes. Default is 90, minimum is 5 and maximum is 240 minutes.

**B.1.23 EnableGps**

Full Command: **EnableGps**

Starts the GPS process if it is not already started.

**B.1.24 DisableGps**

Full Command: **DisableGps**

Stops the GPS process if it is not currently running.

**B.1.25 EnablePulse**

Full Command: **EnablePulse**

Starts the pulse per second process if it is not already started.

**B.1.26 DisablePulse**

Full Command: **DisablePulse**

Stops the pulse per second process if it is not currently running.

## B.2 List of ALI Science Modes

The following section will give a brief description of each of the programmed science operational modes that exist on the ALI platform. A complete table of the modes can be seen in Table B-1.

**Table B-1:** ALI operational science modes.

Mode Number	Mode Name
0	Invalid Mode
1	Calibration Mode
2	Aerosol Mode
3	H <sub>2</sub> O Mode
4	O <sub>2</sub> Mode
5	Custom Mode
6	Aerosol Constant Exposure Time Mode

### B.2.1 Invalid Mode

This mode is a nonexistent mode that has no operational function and will not allow the science module to operate. No images in the mode.

Mode Number: 0

Number of Images: N/A

### B.2.2 Calibration Mode

This mode runs with the shutter opened and the AOTF off. The scaling factor does not work on this function and the values are hard coded into the system. This mode does not use any wavelength values and the RF power is set at 0.

Mode: 1

Number of Images: 8

**Table B-2:** ALI calibration science mode specifications.

Image Number	Exposure Time (s)	Image Number	Exposure Time (s)
1	0.05	5	2.00
2	0.10	6	3.00
3	0.50	7	5.00
4	1.00	8	10.00

### B.2.3 Aerosol Mode

This mode runs with the standard aerosol mode. An AOTF off image is taken between each exposure. Custom exposure times and scale factor can be used. Exposure time is based off the standard calibration curve which can be seen in Table 4-2.

Mode Number: 2

Number of Images: 26

**Table B-3:** ALI aerosol science mode specifications.

Image Number	Wavelength (nm)	RF Power	Image Number	Wavelength (nm)	RF Power
1	650	0.0	14	800	1.0
2	650	1.0	15	825	0.0
3	675	0.0	16	825	1.0
4	675	1.0	17	850	0.0
5	700	0.0	18	850	1.0
6	700	1.0	19	875	0.0
7	725	0.0	20	875	1.0
8	725	1.0	21	900	0.0
9	750	0.0	22	900	1.0
10	750	0.9	23	925	0.0
11	775	0.0	24	925	1.0
12	775	0.9	25	950	0.0
13	800	0.0	26	950	1.0

### B.2.4 H<sub>2</sub>O Mode

This mode is used to measure water vapor lines. An AOTF off image is taken at the start and end of each cycle. Custom exposure times can be used, as well as a scale factor can be used. Exposure times are based off of the standard calibration curve for the first wavelength of the cycle and is constant for every image.

Mode Number: 3

Number of Images: 28

**Table B-4:** ALI H<sub>2</sub>O science mode specifications.

Image Number	Wavelength (nm)	RF Power	Image Number	Wavelength (nm)	RF Power
1	920	0.0	15	946	1.0
2	920	1.0	16	948	1.0
3	922	1.0	17	950	1.0
4	924	1.0	18	952	1.0
5	926	1.0	19	954	1.0
6	928	1.0	20	956	1.0
7	930	1.0	21	958	1.0
8	932	1.0	22	960	1.0
9	934	1.0	23	962	1.0
10	936	1.0	24	964	1.0
11	938	1.0	25	966	1.0
12	940	1.0	26	968	1.0
13	942	1.0	27	970	1.0
14	944	1.0	28	970	0.0

### B.2.5 O<sub>2</sub> Mode

This mode is used to measure O<sub>2</sub> lines. An AOTF off image is taken at the start and end of each cycle. Custom exposure time and scale factor can be used. Exposure times are based off of the standard calibration curve for the first wavelength of the cycle and are constant for every image.

Mode Number: 4

Number of Images: 20

**Table B-5:** ALI O<sub>2</sub> science mode specifications.

Image Number	Wavelength (nm)	RF Power	Image Number	Wavelength (nm)	RF Power
1	755	0.0	11	764	1.0
2	755	1.0	12	765	1.0
3	756	1.0	13	766	1.0
4	757	1.0	14	767	1.0
5	758	1.0	15	768	1.0
6	759	1.0	16	769	1.0
7	760	1.0	17	770	1.0
8	761	1.0	18	771	1.0
9	762	1.0	19	772	1.0
10	763	1.0	20	772	0.0

### B.2.6 Custom Mode

This mode lets the user upload a configuration to an extra configuration file on the ALI platform. The command is sent up via the `LdCusCnf` command. Details can be located in section B.1.9.

Mode Number: 5

Number of Images: N/A

### B.2.7 Aerosol Constant Exposure Time Mode

This function is the same as the aerosol science mode (section B.2.3) except the exposure time has been set to two seconds for all exposures. The scaling factor is applied to this mode. A table of the specifications can be seen in Table B-3.

Mode Number: 6

Number of Images: 26

## B.3 List of ALI Exposure Modes

ALI had two usable exposure modes during the campaign, a calibrated mode and a custom mode which can be configured by the user. An automatic exposure mode was planned but due to time constraints was never implemented. A brief description of the modes will follow.

**Table B-6:** ALI operational exposure time modes.

Mode Number	Mode Name
0	Invalid Mode
1	Calibrated Exposure Mode
2	Automatic Exposure Mode ( <i>Not Implemented</i> )
3	Custom Exposure Mode

### B.3.1 Invalid Mode

This mode is a nonexistent mode that has no operational function and will not allow the science module to operate. No exposure times are associated with this mode.

Mode Number: 0

### B.3.2 Calibrated Exposure Mode

Using the method outlined in section 4.4.1, a table of calibrated exposure times were determined for a stratospheric balloon geometry. Table 4-2 contains the calibrated exposure times. For any wavelength requested that is between two of the calibrated wavelengths, the exposure time is linearly interpolated between the two wavelength's exposure times. For wavelengths less than 650 nm the exposure time for 650 nm is used, and for wavelengths greater than 950 nm the exposure time for 950 nm is used.

Mode Number: 1

### B.3.3 Custom Exposure Mode

This mode lets the user upload a series of exposure times on the ALI platform to be used instead of the calibrated exposure mode. The command is sent up via the LdCusExp command. Details can be located in section B.1.10.

Mode Number: 3